Operando X-ray diffraction during laser 3D printing: from machine design to experiments and computer simulations

Samy HOCINE

Acknowledgements

Acknowledgements

Abstract

The importance of additive manufacturing, also known as 3D printing, has grown exponentially in the recent years thanks to its high flexibility to manufacture intricate parts. This process can be divided into many different sub-categories, depending on the feedstock form and the source used. However, the principle stays the same: building the part one layer after another.

Selective Laser Melting (SLM) is one of them, combining a fine metallic powder bed and a laser beam scanning the surface to selectively fuse the particles together. SLM is already used in the medical field where custom shapes implants are needed, or in the automotive and aerospace industries where it eases the production time of certain parts. SLM exhibits very high heating and cooling rates, up to 10^5-10^6 K/s as demonstrated in this work. Therefore, it poses several challenges such as the formation of pores, the accumulation of residual stresses and the creation of metastable phases in the microstructure. Post-processing techniques such as long heat treatments are used to counter the effect of these problems. A better way to address these different issues would be to adapt the processing parameters to reduce or remove the generation of such unwanted features. To do so, it is necessary to understand the underlying causes creating these defects. *Ex situ* characterisation of SLM-printed parts can be done using microscopy techniques. It consists of exploring the microstructure changes for a certain range of parameter values (laser power, scanning speed, etc). However, this is very time consuming. Simulations could be used as a prediction tool, but the degree of complexity needed here is quite high, which makes them computationally expensive.

This PhD thesis is part of the CCMX-Challenge AM[3] (Additive Manufacturing and Metallic Microstructures) and is dedicated to the development of a new device reproducing the SLM manufacturing process to characterise the phase evolution of metallic microstructures in real time, or *operando*, by X-ray diffraction (XRD) techniques. A Ti-6Al-4V (wt%) alloy is used to demonstrate the capabilities of this new device, thanks to its compatibility with the X-ray energies available at the Swiss Light Source (SLS) synchrotron beamlines of the Paul Scherrer Institut (PSI).

This dissertation introduces the design of the machine and its software, as well as a characterisation of the printed Ti-6Al-4V samples to determine the optimum printing parameters. To demonstrate the measurement capabilities of the machine, different *operando* XRD experiments will then be presented, giving new insights into the phase evolution during SLM processing. These observations will be linked to the sample microstructure after printing. Additionally, the unique properties of this setup allow to capture the rapid temperature evolution within the probed materials during the XRD measurement. The obtained temperature profile will be compared to some results derived by Finite Elements Method (FEM) analysis on already existing models established for Ti-6Al-4V.

Abstract

Keywords: Additive manufacturing, selective laser melting, 3D printing, operando, X-ray diffraction, XRD, Ti-6Al-4V, phase evolution, simulation

Résumé

L'importance de la fabrication additive, ou impression 3D, a augmenté de façon exponentielle ces dernières années grâce à sa grande flexibilité pour fabriquer des pièces complexes. Ce processus peut être divisé diverse catégories, selon la forme de la matière première et la source utilisée. Le principe reste cependant le même : construire la pièce une couche après l'autre.

La fusion sélective par laser (de l'anglais Selective Laser Melting - SLM) est l'une d'entre elle, combinant un lit de poudre métallique et un faisceau laser scannant la surface pour faire fondre les particules. Le processus SLM est déjà utilisé dans le domaine médical où des implants de formes personnalisées sont nécessaires, ou dans les industries automobile et aérospatiale où il raccourci le temps de production de certaines pièces. Le processus SLM présente des vitesses de chauffe et de refroidissement très élevés, jusqu'à 10^5-10^6 K/s, comme démontré dans ce travail. Cela pose donc plusieurs défis tels que la formation de pores, l'accumulation de contraintes résiduelles et la création de phases métastables dans la microstructure. Des techniques telles que de longs traitements thermiques sont utilisées après le processus de fabrication pour palier à l'effet généré par ces problèmes. Une alternative pour résoudre ces différents problèmes serait d'adapter les paramètres d'impression afin de réduire ou supprimer la génération de ces anomalies. Pour cela, il est nécessaire de comprendre les causes sous-jacentes à l'origine de ces défauts. La caractérisation *ex situ* des pièces imprimées via SLM peut être effectuée à l'aide technique de microscopie. Cela consiste à analyser les variations de la microstructure pour certains paramètres (puissance du laser, vitesse de scan, etc.). Cependant, cela prend beaucoup de temps. Les simulations pourraient être utilisées comme outil de prédiction, mais le degré de complexité devient assez élevé, ce qui les rend coûteuses en puissance de calcul.

Cette thèse fait partie du projet CCMX-Challenge AM[3] (Additive Manufacturing and Metallic Microstructures) et est dédiée au développement d'un nouveau dispositif reproduisant le processus de fabrication SLM pour caractériser l'évolution des phases métalliques en temps réel, ou *operando*, en utilisant la diffraction des rayons X (DRX). Un alliage Ti-6Al-4V (%m) est utilisé pour démontrer les capacités de ce nouveau dispositif, grâce à sa compatibilité avec les énergies de rayons X disponibles sur les lignes d'expérience du synchrotron Swiss Light Source (SLS) de l'Institut Paul Scherrer (PSI).

Cette thèse présente la conception de la machine et de son logiciel, ainsi qu'une caractérisation des échantillons de Ti-6Al-4V imprimés pour déterminer les paramètres d'impression optimaux. Pour démontrer les capacités de mesure de la machine, différentes expériences *operando* DRX seront présentées, donnant de nouvelles informations sur l'évolution des phases pendant le traitement SLM. Ces observations seront liées à la microstructure de la pièce imprimée. De plus, les propriétés uniques de cet instrument permettent de capturer l'évolution rapide de la température dans le matériau sondé par la mesure DRX. Le profil de

température obtenu sera comparé à certains résultats obtenus par méthode des éléments finis (MEF) sur des modèles déjà établis pour l'alliage Ti-6Al-4V.

Mots clés : Fabrication additive, fusion sélective par laser, impression 3D, operando, diffraction des rayons-X, DRX, Ti-6Al-4V, évolution de phases, simulation

List of Figures

List of Tables

Acronyms

Notation	Description
A_{XR}	X-ray probed surface region
AM	Additive Manufacturing
AM^3	Additive Manufacturing and Metallic Microstructures
BCC	Body-Centred Cubic
CAD	Computer-Aided Design
EBSD	Electron Back Scatter Diffraction
EDS	Energy-Dispersive X-ray Spectroscopy
EDXRD	Energy-Dispersive X-Ray Diffraction
ELI	Extra Low Interstitial
EMPA	Swiss Federal Laboratories for Materials Testing and Research
EPFL	École Polytéchnique Fédérale de Lausanne
FCC	Face-Centred Cubic
FCT	Face-Centred Tetragonal
FEA	Finite Element Analysis
FEM	Finite Element Method
FWHM	Full-Width at Half-Maximum
HAZ	Heat Affected Zone
HCP	Hexagonal Closed-Packed
IPF	Inverse Pole Figure
KB	Kirkpatrick-Baez
PSI	Paul Scherrer Institute

Acronyms

Notation	Description
SAXS	Small Angle X-ray Scattering
SEM	Scanning Electron Microscope
SLM	Selective Laser Melting
SLS	Swiss Light Source
TEM	Transmission Electron Microscope
XRD	X-Ray Diffraction

Contents

Contents

Contents

Thesis Part I

1 Introduction

Additive Manufacturing (AM), also commonly known as 3D printing, has become a part of our daily life. It has tremendous capabilities in terms of design flexibility as it can produce intricate shapes within a single build part. It has revolutionised the way rapid prototyping is done, and offers now the possibility to realise custom design for single unit or small scale production. This is particularly attractive for the medical field were custom-shaped implants are needed; or in the industrial field where it eases the production time of parts that are complicated to manufacture with traditional techniques. It has even found a way in our homes, since polymer-based 3D printers are now very affordable and user friendly.

Additive manufacturing technologies

TECHNOLOGY	MATERIALS	TYPICAL MARKETS	RELEVANCE FOR METAL
Powder bed fusion – Thermal energy selectively fuses regions of a powder bed	Metals, polymers	Prototyping, direct part	●
Directed energy deposition – Focused thermal energy is used to fuse materials by melting as the material is deposited	Metals	Direct part, repair	◑
Sheet lamination – Sheets of material are bonded to form an object	Metals, paper	Prototyping, direct part	◕
Binder jetting – Liquid bonding agent is selectively deposited to join powder material	Metals, polymers, foundry sand	Prototyping, direct part, casting molds	◕
Material jetting – Droplets of build material are selectively deposited	Polymers, waxes	Prototyping, casting patterns	○
Material extrusion – Material are selectively dispensed through a nozzle or orifice	Polymers	Prototyping	○
Vat photopolymerization – Liquid photopolymer in a vat is selectively cured by light-activated polymerization	Photopolymers	Prototyping	○

AM technologies for metal objects

Figure 1.1 – Summary of existing AM technologies. Figure taken from [1]

AM is defined as a layer-by-layer technique to create intricate 3-dimensional shapes generated by Computer-Aided Design (CAD). The first plastic-based AM system was commercialised in 1987. Metal-based systems were introduced a bit later, in 1995 [1]. Depending on the processing source and the feedstock, AM can be divided into several groups. A pertinent summary of the technique is done in figure 1.1, and an extensive presentation can be found in the book of Gibson, Rosen and Stucker [2].

AM has already more than 30 years of history with polymers, but is less mature in the metallurgical field. This means that there is still room for development and improvement. General Electric's recent \$1.4bn investment

[3] shows that industries have started to include AM among their manufacturing processes. In fact, they already produce parts such as the fuel nozzle for the LEAP (Leading Edge Aviation Propulsion) aero engine [4].

The work presented in this thesis is part of the CCMX-Challenge Additive Manufacturing and Metallic Microstructures (AM³) project between the Paul Scherrer Institute (PSI), the École Polytéchnique Fédérale de Lausanne (EPFL), the Swiss Federal Laboratories for Materials Testing and Research (EMPA) and is backed by the Swiss watch and precious metals industry. It focuses on the laser powder bed fusion process identified as Selective Laser Melting (SLM), which is defined in the following section. It consists of developing a new device that replicates SLM processing conditions, coupled with X-ray investigation techniques to investigate the material evolution in real time, or *operando*, during printing. To demonstrate the capabilities of such a device, titanium-aluminium based alloys are primer candidates as benchmark materials, mainly because these materials have excellent X-ray transmission properties for the X-ray energies available at PSI beamlines. Ti-6Al-4V processed under SLM conditions has been extensively studied [5–11] and is therefore perfect to explore the capabilities of this new setup.

1.1   Selective laser melting
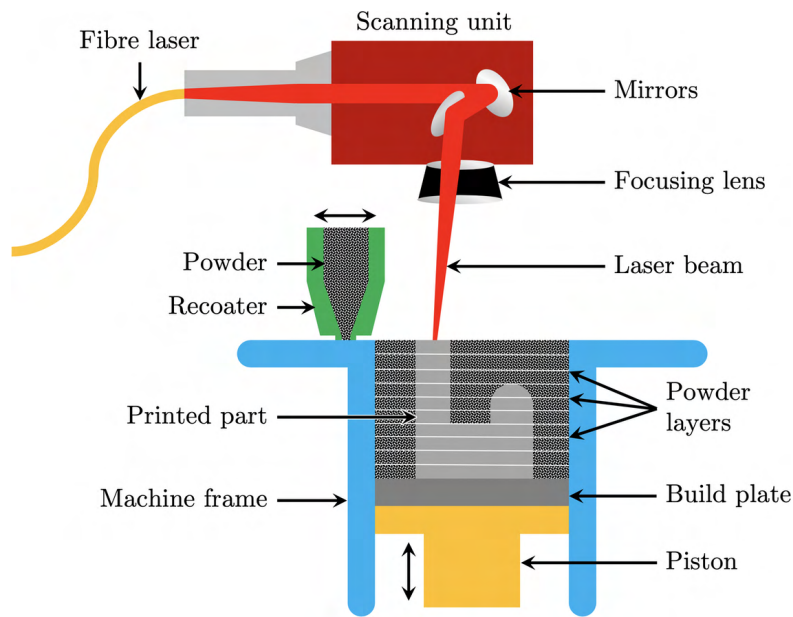
Figure 1.2 – Schematic of SLM processing

SLM is an AM technique combining a metallic powder bed as feedstock material, and a laser beam scanning its surface to locally melt and bind the particles into a solid material. An illustration of the process is given in figure 1.2 indicating the important components [2, 12]. The build plate acts as binding support for the part generated during the printing process, defining the bottom of the powder bed. It is mounted on a piston which can move vertically to create a gap between the powder bed surface and the machine frame, corresponding to the desired layer thickness. The new layer is deposited by the recoater which translates horizontally above the powder bed, and the gap is filled by the powder falling down. A high power fibre laser

collimated into a scanning unit scans the powder bed surface to selectively melt the particles together and produce a dense structure. The laser beam is steered by mirrors which allows to reach high scanning speeds, and is focused to a very small spot size to increase the energy density. By iterating this cycle several times, 3-dimensional parts can be created embedded within the powder bed.

The typical layer thicknesses for laser powder bed-based processes are between 20 μm - 100 μm, with a typical particle diameter distribution within this range [13]. However, a small particle size can be detrimental to the powder bed quality, since below 10 μm diameter the particles tend to agglomerate and form satellites, which reduces the fflowability of the powder [14], and hence the density of the powder bed after recoating.

To prevent material oxidation, the printing chamber is usually filled with inert gas such as argon, nitrogen, or kept under vacuum. Moreover, the addition of a laminar flow over the build surface can reduce the amount of porosity in Ti-6Al-4V processing [15]. In general, pores are unwanted features and are one of the main reasons of failure of the printed part [16]. Without laminar flow, a plume carrying fumes and spatters formed by the laser beam attenuates considerably the incident energy to the powder bed and creates redeposits around the melt pool [17].

Laser-material interaction can be a source of porosities through the ejection of material during the melting process (spattering) due to convection or vaporisation of the metal [18]. If the laser power is high enough, the melt pool becomes too deep and can generate keyhole by increasing the vaporisation rate of the material [19]. A keyhole is when the laser goes too deep in the material, creating pores under the metal surface. These pores are entrapped as they cannot resurface before the melt pool solidifies. Pulse shaping of the laser beam has been proposed as a potential solution to better manage the input power of the beam inside the metal [20]. Porosity can also be induced by artefacts already present in the powder during its fabrication (gas trapped inside the particles) [18]. Surface irregularities generated by laser scanning can also be a source of porosity depending on how well the following layer is processed [21]. This can be avoided with an appropriate scanning strategy [22].

High-density parts are desirable in SLM, but tend to have more residual stresses than porous ones, because cavities act as open surfaces that relax constraints inside the material [23]. Post-process heat treatments such as annealing [24] and hot isostatic pressing [25] have been reported as good ways to improve mechanical characteristics of SLM parts by reducing the tensile residual stresses and improving overall density.

SLM is a very brutal processing technique and poses a multitude of challenges, since it involves a long welded track arranged in a specific geometry to create a part in 3D. The material can experience high cooling rates ranging from 10^3 K/s to 10^8 K/s [26]. This leads to non-equilibrium microstructures with high residual stresses. The mechanical properties of the printed parts also are significantly affected: the tensile and yield strengths are different along the building direction and perpendicular to it, which creates a strong anisotropy inside the material [27, 28]. In order to have the best part quality, a processing window (laser power vs. scan speed) should be established to avoid melting defects like balling or porosity [29].

The aim of this thesis is to develop a new machine mimicking SLM conditions to understand the microstructure of metallic materials processed. *Ex situ* material analysis techniques such as optical microscopy, Scanning Electron Microscope (SEM) and Transmission Electron Microscope (TEM) observations are already extensively used to investigate microstructures at different scales. X-ray and neutron diffraction are also

employed for more specific purposes such as residual stresses measurements using diffraction techniques, and porosity mapping using imaging [30–35].

Thanks to the new device developed during this project, the microstructural evolution of the part is followed through X-Ray Diffraction (XRD) measurements with high-energy synchrotron X-rays during SLM processing in real time. The machine design and construction presented in this thesis offer a new perspective on how metals behave during SLM processing. It provides an extensive, but necessary amount of data to know how to adapt the processing parameters to control the phase evolution as well as the heating and cooling rates which can lead to the formation of residual stresses, which have an impact on the final mechanical properties. Additionally, the temperature evolution within the X-ray probed region is compared to recent Finite Element Method (FEM) models, revealing that *operando* XRD measurements have the potential to contribute to the validation process of computer simulation analysis.

1.2 *In situ* monitoring under SLM processing conditions

Highlights from literature

In order to understand the complexity of the SLM process, *in situ* monitoring has been seen as a way to gather data during the part manufacturing. The use of thermocouple has been reported as a technique to record the temperature evolution in the sample during the printing process. This method gives a direct input on the temperature evolution over time. A simple way to perform temperature recording is to connect a thermocouple directly onto the build plate before printing [36, 37]. A more complex way to use this contact monitoring method is to place a thermocouple within the sample during the printing process [38]. This requires to open the machine during the printing process. However, the temperature values provided by this method may be more reliable.

It is also possible to have a direct information on the printing process using high-speed camera to observe the melt pool with visible light [39, 40]. Matthews et al. [41] used this principle to reveal the denudation process happening during laser scanning of the powder bed. This study was completed by Ly et al. [42] highlighting the liquid ejection process caused by the laser recoil pressure, and Trapp et al. [43] revealing the change of absorptivity of the laser light in the material depending on the laser parameters.

In addition to observation made in the visible spectrum, high-speed cameras can also be used to capture the infrared emissions coming from the high-temperature and molten material. By calibrating properly the emission spectrum, it is possible to record the temperature evolution at the surface of and around the melt pool. Lane et al. [44] performed thermal imaging measurements of the hot material, including ejected particle of an Inconel 625 during powder bed laser scanning. A high degree of spatial accuracy was achieved by Hooper [45] who performed a mapping of the temperature distribution at the surface of the melt pool with a resolution of 20 μm.

Another imaging technique investigating the powder bed quality during recoating using a high-resolution scanner was repored by Tan-Phuc et al. [46], revealing the variation in the powder levelling caused by the layer deposition system. Lastly, more exotic techniques like the use of acoustic emission coupled with artificial intelligence has shown industrial potential to control defects during the laser scanning process [47].

In situ setups at other large scale facilities

In recent years, several research groups reported novel experimental stations to investigate metallic materials during SLM processing, using X-ray radiations. Bidare et al. [48] developed a compact open-architecture for metal powder bed fusion compatible with high speed X-ray and schlieren imaging. They revealed the vapour and plasma flow above the melt pool, entraining particle during laser scanning using the change of refractive index of the hot gases [49].
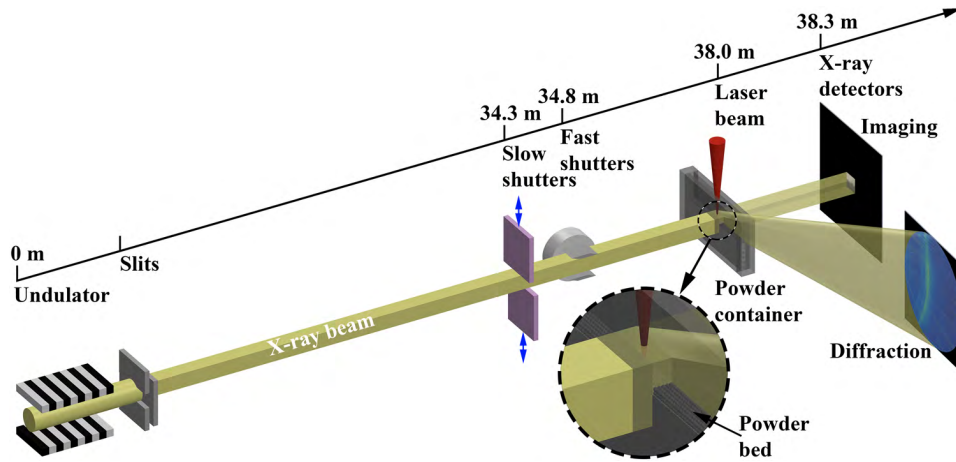
Figure 1.3 – *In situ* X-ray setup at the Advanced Photon Source. Image taken from [50].

However the first results on *in situ* X-ray diffraction and imaging were announced by Zhao et al. [50] at the Advanced Photon Source in Argonne (IL, USA). This experiment requires a particular setup that allows the X-ray beam to pass through the powder and solidified material. The powder is sandwiched between two plates that are transparent to X-rays. A static laser beam positioned above the plates melts the top part of the loose powder, whereas the X-ray beam impinges on the sample horizontally.
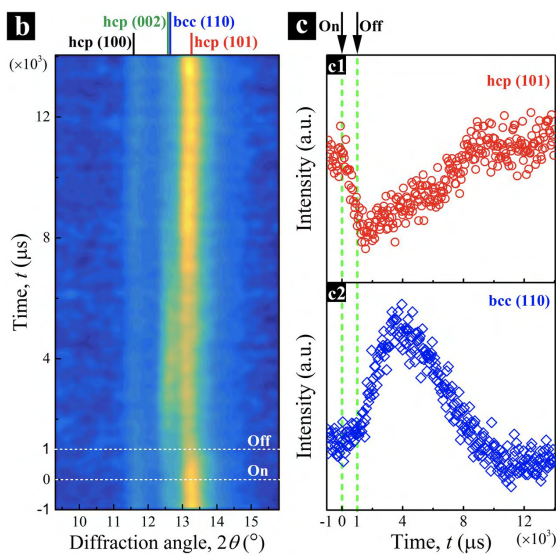
Figure 1.4 – *In situ* XRD results on the phase transformation of a Ti-6Al-4V alloy. Image taken from [50].

Figure 1.3 shows an illustration of this setup. Depending on measurement configuration, data can either be collected through imaging or diffraction. For the imaging part, these experiments provided information on the formation of keyhole porosities and spatters. They presented the melt pool dynamic evolution in radiography recorded at a frame rate of 50 kHz, revealing the formation of pores and spatters on a Ti-6Al-4V alloy.

The phase transformation of the material upon melting and solidification was also observed by XRD experiments, as shown in figure 1.4. This result reveals the phase transformation of Ti-6Al-4V from the β phase (bcc) at high temperature to the α phase (hcp) during cooling down. Since the laser is static above the powder bed, a short pulse of 1 μs was emitted to

7

observe the phase evolution, which leads to a β phase present for around 8 µs. This setup was subsequently upgraded to reach a frame rate of up to 6.5 MHz in radiography, and include laser scanning capabilities to study the melt pool shape [51].
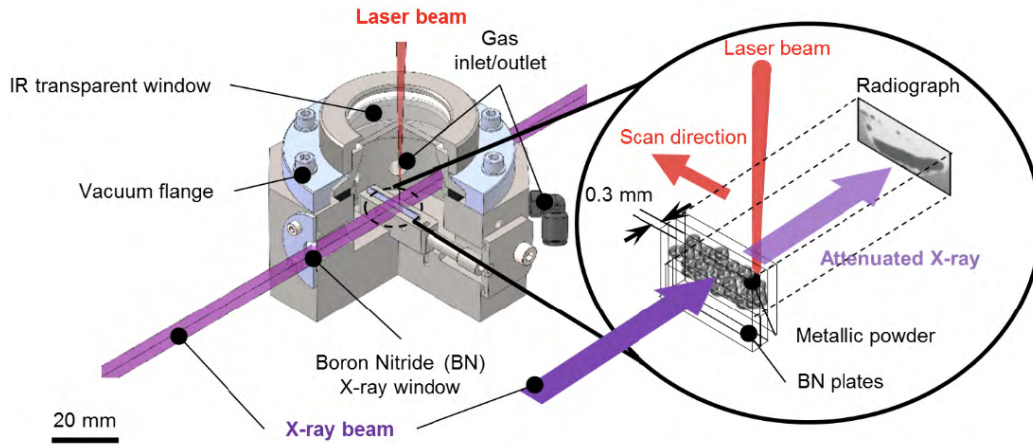
Figure 1.5 – *In situ* X-ray setup at the Diamond Light Source. Image taken from [52].

Leung et al. [52] developed a similar system named laser additive manufacturing process replicator (LAMPR) at the Diamond Light Source in the UK. This setup is shown in figure 1.5. Here, the laser can scan the top surface of the powder, thus creating an elongated melt pool. By doing so, they were able to inspect the formation of pores within the melt pool with high speed *in situ* X-ray imaging on a Invar 36 alloy. A scanning speed of 13 mm/s was used here, which is quite slow compared to the average speed used in SLM processing. Additionally, the laser scanning was performed on loose powder without a printing substrate, similar to overhanging conditions in SLM. This generated a local coarsening of the melt pool entering in contact with the X-ray transparent plates, which might not be representative of the situation in SLM machine.
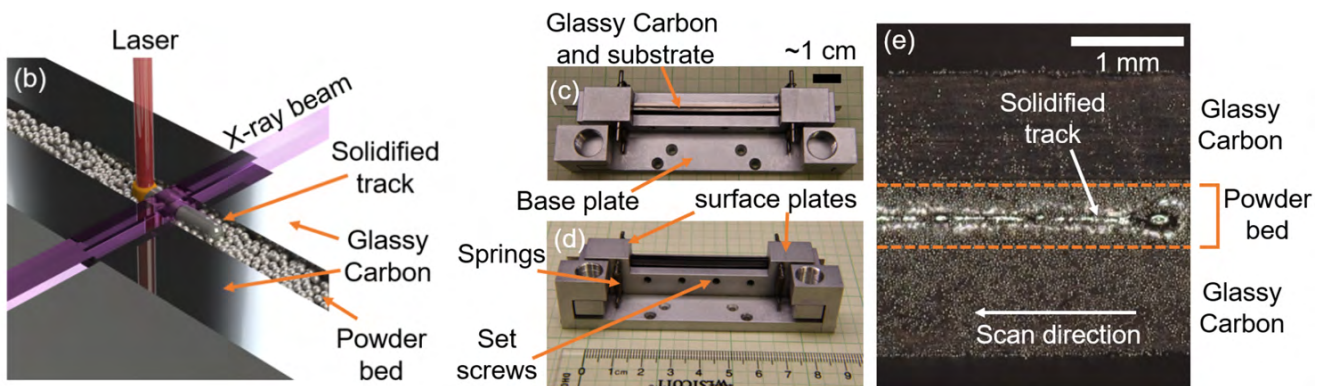
Figure 1.6 – *In situ* X-ray setup at the Stanford Synchrotron Radiation Lightsource. Images taken from [53].

Calta et al. [53] reported the development of a comparable setup, combining both X-ray diffraction and imaging on Ti-6Al-4V. Figure 1.6 shows an illustration of this setup used in diffraction mode to observe the phase transformation of Ti-6Al-4V, in a similar manner as done by Zhao et al. [50]. A scanning speed of 576 mm/s was used for XRD at a 1 kHz acquisition rate. Due to the setup geometry, the phase transformation in Ti-6Al-4V was presented for a single line only.
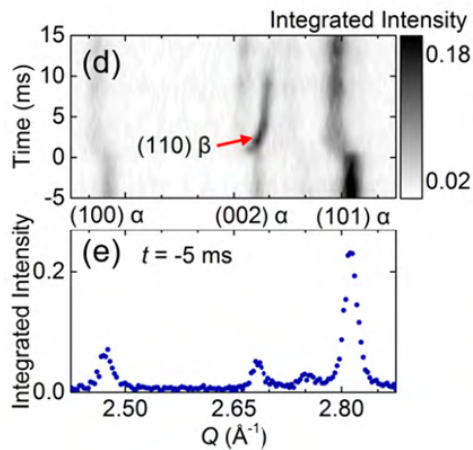
Figure 1.7 – *In situ* XRD results on the phase transformation of a Ti-6Al-4V alloy. Image taken from [53].

This result is presented in figure 1.9, where the phase transformation from the β phase to the α phase is observed. Here the β phase is present for a around 10 ms, which is way longer than in the result presented by Zhao et al. [50] (figure 1.4). This can be explained by the longer interaction between the laser beam and the X-ray probed volume.

However, none of these setups allow to use complex scanning strategies for XRD measurements since the distance between the two X-ray transparent plates ranges from 0.3 mm to 0.5 mm. Furthermore, there is no powder recoating system allowing the deposition of new layers during measurements.

Recently, Uhlmann et al. [54] performed XRD experiments Petra III synchrotron in Hamburg, Germany. They probed the sample in depth using the same configuration, but with a width of 3 mm between the two X-ray transparent plates, which allows to scan multiple lines on the powder bed surface. Figure 1.8 shows an illustration of this setup.

(a) Details of the setup   **(b)** XRD experiment
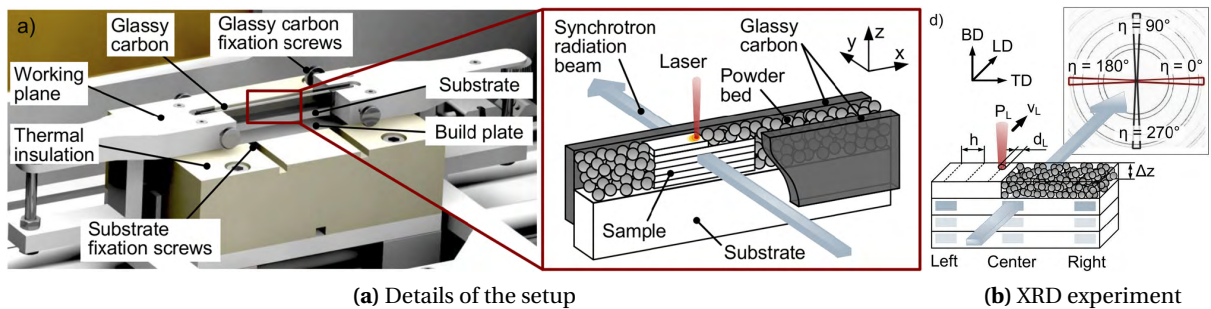
Figure 1.8 – *In situ* X-ray setup at Petra III. Images taken from [54].

They added a recoating system to deposit new layer, enabling to build elevated structure during measurement. As a result, they could probe the previous printed layers to measure the evolution of residual stresses and texture in the sample during laser melting. However the measurements were done at a sampling rate of 10 Hz, which is too slow to measure the influence of the rapid heating and cooling rates on the microstructure.
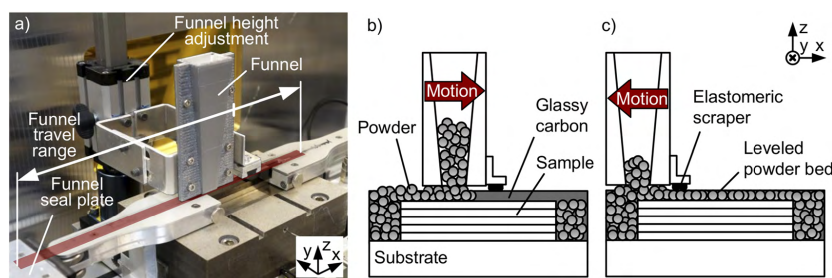
Figure 1.9 – Layer deposition on the *in situ* X-ray setup at Petra III. Images taken from [54].

To summarise, the three first quasi-2D setups do not capture the 3D character of a conventional laser powder bed system, and the full complexity of the layer scanning process. Ulhmann et al. [54] managed to get closer to a 3D powder bed, with more complex scanning strategy and a recoating system to deposit new layers. However, they are not able to follow the influence of the laser scanning strategy on the microstructure evolution and record the rapid thermal gradient within the material due to the slow acquisition rate.

Laser-based XRD setup at PSI

A previous laser-based setup at PSI was developed at the TOMCAT beamline of the Swiss Light Source (SLS) synchrotron. Kenel et al. used this setup to mimic the rapid solidification conditions happening during AM processing. They performed *in situ* XRD experiments at the microXAS beamline of PSI on Ti-48Al [55, 56]. The setup consists of two infrared (980 nm) lasers focused on a spherical sample of about 1 mm diameter positioned on a copper support.

(a) Laser setup CAD design   **(b)** Sample during *in-situ* XRD experiment
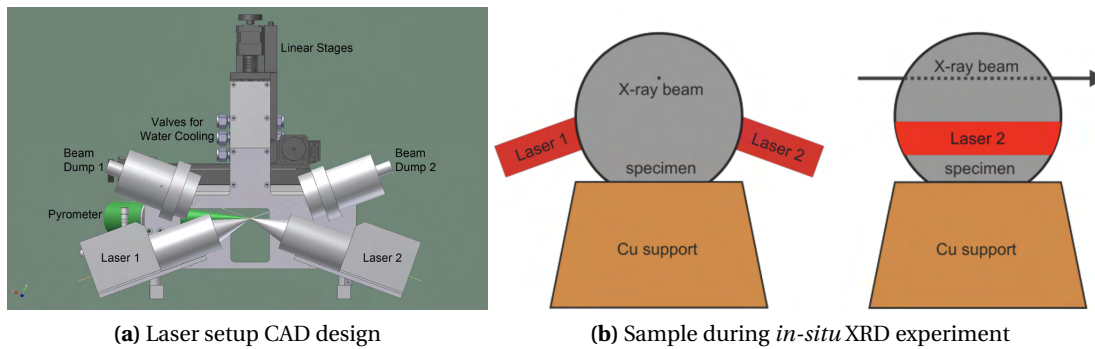
Figure 1.10 – Laser-based setup from TOMCAT beamline at PSI. Image taken from [55]

Figure 1.10a shows a 3D representation of this laser setup used for synchrotron XRD measurements. Linear stages are used to bring the spherical sample at the focal point of the two laser beams (figure 1.10b). While the lasers are turned on, the X-ray beam is aimed at the top of the sample to perform XRD measurement through the reduced thickness at the top of the sphere (figure 1.10c). The laser is then shutdown to record the rapid solidification event.

The diffracted intensities were collected by a PILATUS 100K detector operated at a frame rate of 100Hz. The phase formation during the solidification was observed over time and is represented in figure 1.11. Thanks to the high detector frame rate compatible with the solidification rates, it was possible to detect the chronological order of appearance for intermetallic phases in Ti-48Al. A cooling rate of 1.25×10^3 K/s was reported in this study, which is on the lower end of what is expected in SLM processing.

Figure 1.11 – Phase evolution inside a Ti-48Al sample from the liquid phase under rapid solidification conditions. Images taken from [55]

Mimicking SLM processing at PSI

The initial strategy adopted to mimic SLM processing conditions was to use the laser-based setup already existing at PSI, and improve it in order to get closer to the real manufacturing method. Figure 1.12 shows one possible improvement, with components similar to the TOMCAT design (figure 1.10a). This time, the sample would consist of a flat capillary (1) with a thickness of a few hundreds microns filled with powder. The laser (2) would be turned on to melt the powder inside the capillary. At the same time, the X-ray beam (3) would go through the capillary to capture the melting event. The laser would then be turned off, and the solidification process would then be observed. A beam dump (4) would be positioned on the other end of the laser trajectory to collect any radiation going between the powder particles, and a pyrometer (5) would monitor the temperature. This design would have been very similar to the quasi-2D setups presented previously.
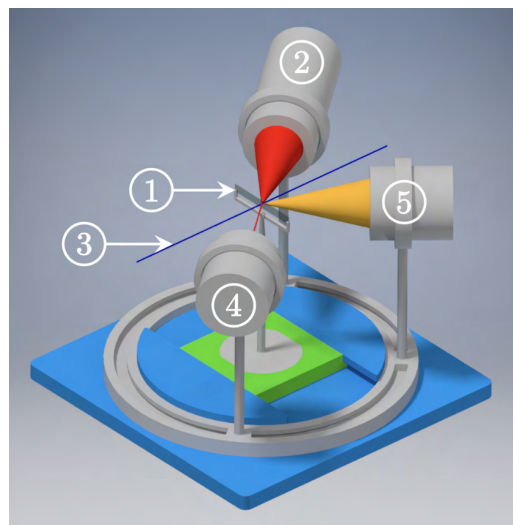
Figure 1.12 – First tentative of CAD design for the new setup: 1) powder capillary; 2) laser; 3) X-ray beam; 4) laser beam dump; 5) pyrometer.

However, this approach was discontinued for two main concerns:
- The filling of a very narrow and fragile capillary with metallic powder in a controlled manner is very challenging
- In order to be X-ray transparent, the thickness of the powder capillary would only include a couple of powder particles, which would not be representative of SLM conditions

Thus, a different approach was taken. In order replicate SLM conditions, one would have to go from a thin powder container to a larger one in order to be able to build and study 3-dimensional samples. One main issue that arises from this modification is that the thickness of the powder bed prevents the transmission of the X-ray beam. Given that a synchrotron X-ray beam is following a horizontal path, the only option available is to tilt the powder bed to probe the surface and perform XRD measurements in reflection mode. This change of direction led to the conception of a miniaturised device for *operando* XRD experiments.

1.3 A new design

Following the observations made in the previous section, the main focus of this dissertation is to design a machine reproducing the SLM processing conditions accurately. Such a machine should include all the capabilities of commercially available SLM systems, in a miniaturised format in order to perform *operando* XRD experiments. This new instrumentation, named MiniSLM, was designed to include four design specifications:

- Replicate the SLM manufacturing process (DS1)
- Enable access to the powder bed for X-ray beam for diffraction measurements (DS2)
- Be compact enough to fit at different beamlines (DS3)
- Respect the safety regulations at PSI and other large scale facilities (DS4)

The design of the MiniSLM device is largely based on conventional powder bed fusion devices that are commercially available. This includes key components such as 1) a build plate to act as a support for the printed part mounted on a vertical piston to define the layer thickness, 2) a recoating system to deposit a new layer of powder and 3) a high-power laser source coupled to a scanning unit to selectively fuse the powder with the previously solidified layer. All this is confined in a printing chamber under inert gas atmosphere [2]. However, further considerations had to be taken when selecting the possible components to satisfy the design considerations as discussed below.

Replicate the SLM manufacturing process (DS1)

The build plate is the first essential component of the MiniSLM. This is where the samples are printed. Preheating is often recommended to reduce the accumulation of residual stresses within the sample [57]. A ceramic silicon-nitride based resistor is an adequate choice for the preheating system thanks to their compactness and high temperature up to 500°C.

The layer thickness of SLM-made samples is of the same order of magnitude as the powder particle diameter, which is few tens of microns [13]. Displacement systems based on stepper motors are often a good compromise between cost and accuracy. However, if the motor is positioned too close to the heating element, heat conduction can happen from the build plate to the motor. In general, standard stepper motor cannot support more than 50°C for the working environment temperature [58]. Therefore, attention must be paid to the location of the motor, and proper cooling to avoid heat damage.

After solving the displacement of the build plate, a recoating system is needed. There are many combinations based on gravity feeding or a double piston with a scrapper, which can be shaped in various ways such as a roller or a rigid blade [2]. The easiest and most convenient system is a funnel shape with a blade to deposit and scrape of the excess powder since it does not necessitate any additional mechanically moving part like the roller system.

To achieve laser melting of metal, a high energy input is needed. Nowadays, infrared fibre lasers offer a high-power output at affordable prices. Ti-6Al-4V and precious metals such as gold and copper based alloys are materials of interest for this project. Unfortunately, the family of precious metals (gold, copper, silver) possesses a high reflectivity to infrared wavelengths [59]. To overcome this issue, a laser power up to 1kW would be needed [60, 61]. However, such a laser power would raise safety concerns regarding the setup, and thus would prevent us to address DS4 (safety regulations) properly. Furthermore, the dimensions of the scanning head are constrained by the maximum laser output power: the higher the output power, the bigger the scanning head needs to be. After extended considerations, and to keep flexibility in both the scanning parameter window and the machine design, it was decided that the maximum acceptable laser power output should be 500W.

Enable access to the powder bed for X-ray beam for diffraction measurements (DS2)

In order to perform XRD measurements, synchrotron X-ray beams must interact with the powder bed. Given that synchrotron X-rays follow a horizontal path which is parallel to the surface of the powder bed, the simplest solution here was to slightly tilt the whole machine to create this interaction. An important

consideration is that the scanning head must move together with the machine to keep the laser scanning coordinate system on the printing area at all times. Moreover, the scanning head must be attached to a support stiff enough to avoid any possible vibrations that might otherwise perturb the laser scanning.

The printing chamber is required to be a closed environment, thus X-ray transparent windows were placed on opposite sides of the chamber. One window serves as an entrance for the X-ray beam to probe the powder bed during laser scanning, and the other one as an exit to let the diffracted X-ray beam be collected by a detector. To avoid any harmful laser radiation to escape, glassy carbon is a good candidate for the material of the X-ray transparent windows as it is heat resistant and opaque to visible and infrared light [62]. Therefore, the users and the beamline sensitive equipments such as X-ray detectors are shielded from potential laser radiation that might escape the chamber during laser scanning.

Be compact enough to fit at different beamlines (DS3)

Some beamlines have very little space to accommodate large setups within the X-ray beam path. Some beamlines using focusing optics such as Kirkpatrick-Baez (KB) mirrors possess a focal plane of the order of 10-20 cm. Moreover, the device has to be light enough to be manually transportable to ease the installation process at the experimental station, which puts another limitation on the maximum size of the printing chamber.

Several critical pieces of equipment are also required to operate the machine, such as the laser and its cooling system, different power supplies, controllers and a workstation to pilot everything. The location of each part had to be anticipated and the cable length planned accordingly.

Respect the safety regulations at PSI and other large scale facilities (DS4)

Several safety rules must be enforced for the proper operation of a device using such a high power laser. First of all, there should be no open gap along the path of the laser beam to ensure the protection of users and the sensitive equipment of synchrotron beamlines. Secondly, an interlock system must positioned in an adequate position to disarm the laser when the printing chamber is opened. Finally, an emergency button must be easily reachable to manually disable the laser in case an unpredicted event occurs.

1.4 SLM of Ti-6Al-4V

Titanium based alloys are the workhorse of the aerospace, automotive and medical industries. They are desirable for their good mechanical properties, with a high strength-to-weight ratio and an excellent corrosion resistance. However, titanium costs more than other conventional metals: 10 times more expensive than aluminium and 50 times more expensive than steel. Titanium is also more difficult to form than its counterparts with traditional manufacturing techniques. Because AM offers more flexibility in the manufacturing process and a reduced amount of waste, it has been regarded as a new way to efficiently produce titanium parts. The material investigated in this work is Ti-6Al-4V, which represents 70% of the total worldwide production of titanium alloys. [63]

As-processed Ti-6Al-4V made by SLM exhibits very fine α' martensitic needles due to the high cooling rates in the material [9]. The α' martensitic phase is often considered an unwanted brittle phase and is decomposed into $\alpha + \beta$ through heat treatments to achieve better mechanical properties [24, 64, 65]. However recent studies shown that a fully α' martensitic [66] or dual $\alpha + \alpha'$ [67] microstructures can achieve high ductility, contradicting the general the α' is detrimental to the mechanical properties of Ti-6Al-4V. Additionally, the mechanical properties of Ti-6Al-4V are also affected by the printing orientation of the part [8]. Because of the thermal gradients are oriented from the top to the bottom of the part, Ti-6Al-4V exhibits a columnar structure along the build direction [6, 68]. This gives rise a strong anisotropy in the material, with better tensile properties when the part is oriented perpendicular to the building direction [8, 69].

Hot isostatic pressing (HIP) is the preferred method to decomposed the α' martensitic phase into an $\alpha + \beta$ microstructure [64, 70]. However, this process requires to keep the printed part few hours at high pressure and temperature values. Zafari et al. [71] reported another possible way to decompose *in situ* the martensite α' within the part during SLM processing by adapting the printing parameters. In addition, Ali et al. [57] shown that using preheating temperature of 570°C also contributes to the $\alpha' \rightarrow \alpha + \beta$ phase decomposition during the printing process.

The SLM processing of Ti-6Al-4V can be delicate if the parameters are not properly optimised. Song et al. [72] reported severe cracking and high porosity in the material. Gong et al. [7] reported the formation of pores induced by a too large hatch spacing or during the layer deposition process, where pits are creating when the recoating blade remove partially welded particles. To improve the sample quality, Li et al. [73] suggested a parameter optimisation based on a regressive analysis to improve the surface roughness and therefore the sample density, reaching a maximum of 99.8%. Finally, Thijs et al. [6] reported that rotating the scanning pattern by 90° between layers contributes to reducing the sample porosity and allows to reach a relative density of 99.9% for Ti-6Al-4V. However, obtaining a dense sample induces residual stresses within the material, which not only affect the mechanical properties of the part, leading to early failure, but also the part geometry by causing warping after printing [74, 75]. Recently, a new method called 3D laser shock peening has shown promising results to reduce *in situ* the formation of residual stresses in Ti-6Al-4V during SLM fabrication [76].

There is a strong interest in Finite Element Method (FEM) as a tool to help predicting residual stresses by modelling the temperature and phase evolution in Ti-6Al-4V parts during laser scanning. Zhang et al. [36] developed a phase field analysis to predict the resulting phases in Ti-6Al-4V based on the temperature evolution in the sample. Mirkoohi et al. [77] reported a predictive analysis of the temperature distribution within the melt pool. Lastly, Ali et al. [78] reported an enhanced thermal conductivity approach with an improved melt pool depth using a cylindrical heat source with parabolic penetration in the material in order to simulate the residual stresses in the sample after printing.

1.5   Thesis objectives

This thesis aims at the creation of a new tool to perform XRD experiments under SLM conditions, demonstrating its capabilities and exploring the new possibilities given by the unique type of data obtained. The goals of this dissertation are to:

- Develop a new miniaturised device and its software to replicate SLM processing conditions, and perform *operando* XRD measurement on metallic powders at PSI
- Develop the data analysis procedure to interpret the information collected during *operando* XRD experiments
- Study how the phase evolution in the material is affected by the laser scanning process, and link it to the final microstructure
- Determine the temperature evolution within the sample from the lattice strain measured during *operando* XRD experiments
- Examine the potential of this measurement technique for the validation of computational models

In the thesis part, the second chapter will first focus on the design of the MiniSLM with the selection of the different components. An overview of the software design will also be provided, with an explanation of the important functions.

The material studied for this work is Ti-6Al-4V. Information on the crystallographic phases and microstructure under SLM condition will be presented in the third chapter, together with a characterisation of the powder used to produce samples. The methods to measure the sample porosity by optical imaging will be introduced, followed by the techniques employed to acquire and analyse X-ray data that were developed specifically for the measurement technique.

To demonstrate the capabilities of the machine, chapter four presents various results, starting with the processing window determination of the alloy. Here processing window refers to the laser power (P) and scanning speed (v) combination which generate samples of good quality. The printing of the first samples and their porosity content will then be investigated to find the best parameters to use for *operando* XRD experiments. Different *operando* XRD experiments will be presented, giving new insights into the phase and temperature evolution of Ti-6Al-4V during SLM processing. This will be followed by the observation of the microstructure after printing.

In chapter five, the unique data acquired during *operando* measurements will be compared to already existing models on Ti-6Al-4V via FEM computer simulation. An in-depth description of the methods used for the models will be shown, with a comparison between the temperature profile and melt pool dimensions.

Several discussion points will come in chapter six, beginning with the possibility of transfering parameters from the literature to the MiniSLM and its measurement configurations during XRD *operando* experiments. Improvements made to the routine used for data analysis will be briefly commented, followed by the important of the X-ray detector. The phase evolution in the material depending on the scanning geometry and its impact on the final microstructure will then be shown. The importance of the size of the X-ray beam is described afterwards. Finally, the outcome of the simulations is compared to the experimental data.

The last chapter concludes this work, summarising the on the capabilities of the MiniSLM and the new possibilities it offers as an end user station at PSI. It will also give an outlook on the possible improvements to bring to the machine and the experiments.

In the appendices part, additional results on experiments performed on precious metals will be presented. The SLM processing of two alloys, bronze and red gold, has been investigated.

2 Machine design

In this chapter, an extended description of the design of the MiniSLM and its components is given. In the first section, the specifications of the final version of the machine and its components is explained in more detail. Later on, a detailed presentation of the software design and its functions.

2.1 MiniSLM design and components

The design of the MiniSLM has gone through several improvement steps to ensure that the device is compact enough to fit in a synchrotron beamline, and that all the parts needed to be machined can be manufactured by a workshop. Furthermore, the different mechanical and optical components have been properly integrated into the design, while making sure that they can operate in the conditions specified by their manufacturers and that the user safety is ensured during the machine operation.

2.1.1 General presentation

In order to use such a device at synchrotron beamlines, several constraints need to be considered. First, the incoming X-ray beam needs access to the powder bed and the divergent diffracted X-ray beam needs to be able to reach a detector placed outside the printing chamber. Therefore, X-ray transparent openings are needed on the printing chamber. Furthermore, the whole setup has to be transportable to be installed at a beamline for the experiment. The device itself has to fit on the beamline stage in between other beamline components. For instance, the distance between certain focusing optics, such as KB mirrors, and the focal plane can be of the order of 10-20 cm, which puts strong limitations on the maximum size of the printing chamber. The other SLM components, such as the laser, the controllers and various power supply must fit around without obstructing the other end-station components. The SLM device needs to be controlled from outside the experimental hutch, which is not accessible during an X-ray experiment. Any person present in the hutch while X-ray diffraction measurement are ongoing will be subject to intense and lethal radiation exposure. Finally, the data acquisition at the synchrotron beamline and the laser scanning must be synchronised with high accuracy.

Figure 2.1 shows a 3D CAD model of the MiniSLM constructed to to satisfy the goals laid out in this thesis. For the X-ray beam to have access to the powder bed, the complete device needs to be tilted. The inclination

angle should be such that the powder does not flow from the build plate. A powder starts flowing on an inclined surface when the angle exceeds the angle of repose, which is defined by the angle at the base of the cone formed by the powder when poured on a flat surface. For most powders this angle is usually above 20° [79]. Therefore, the device is mounted on a heavy load tilting stage (Huber, Germany) that allows a rotation of ±20° around a horizontal axis (figure 2.1 - (1)).

(a) Front view   **(b)** Rear view
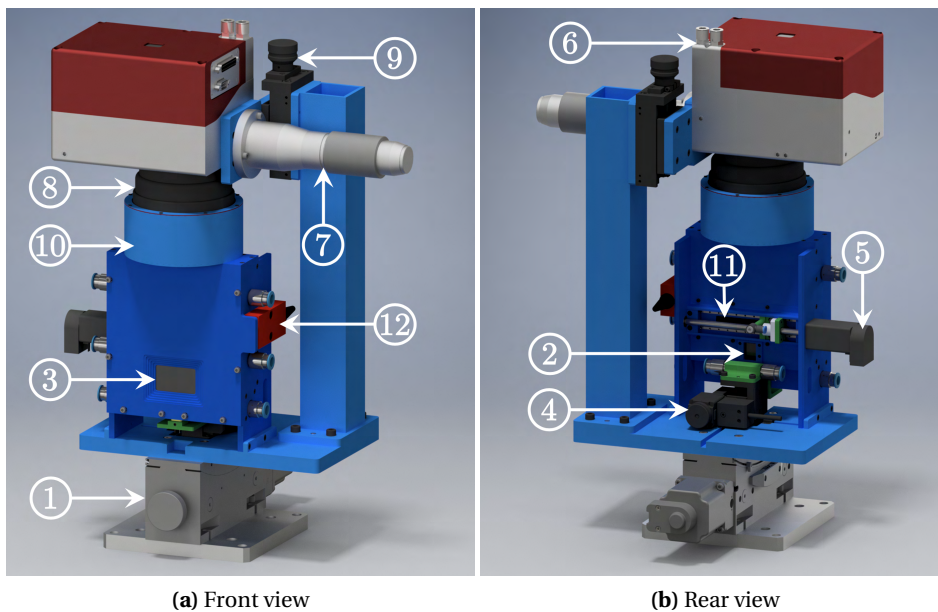
Figure 2.1 – Rendered 3D model of the MiniSLM: 1) tilt stage, 2) entrance window, 3) exit window, 4) motor build stage, 5) motor recoater, 6) scanning head, 7) laser collimator, 8) F-theta lens, 9) vertical stage to change focal length, 10) top cover, 11) back cover, 12) door interlock.

The MiniSLM has a height of 520 mm and its lateral dimensions are 280 mm and 260 mm, parallel and perpendicular to the direction of the X-ray beam, respectively. The overall weight (including the tilting stage) is 25 kg. Figures 2.1, 2.3 and 2.4 depict in detail the different parts of the device. The components are labelled by numbers and explained in the following paragraphs. The printing chamber includes two openings at the back (figure 2.1 - (2)) and front (figure 2.1- (3)) for, respectively, the entrance and exit of the X-ray beam. The incoming beam enters the backside through a 100 µm glassy carbon window (HTW, Germany), interacts with the build stage area where the printing is done and exits through a 500 µm thick window, also made of glassy carbon. As previously stated, glassy carbon was selected because of its high transparency to hard X-rays and opacity to visible and infrared light. Figure 2.2 shows the transmission curves for glassy carbon plates for thicknesses of 100 µm and 500 µm for different X-ray energies. At PSI, the measurements have been done with energies above 12 keV giving a transmission of at least 85% for the 500 µm thick

Figure 2.2 – Glassy carbon X-ray transmission [80]

window and at least 95% for the 100 μm thick window. Because it is amorphous, glassy carbon adds a background contribution to the diffraction pattern and is not suitable to perform Small Angle X-ray Scattering (SAXS) experiments. The width and height of the entrance window were chosen such that the X-ray beam has access to the whole build plate surface when the machine is tilted to up to 20°. The width and height of the exit window were chosen such that diffraction angles up to 70° can be achieved.

Due to the fact that glassy carbon is completely opaque to infrared light, *operando* diffraction experiments can be performed without letting the laser beam escape the chamber and damage the surrounding equipment at the beamline. To ensure the user's and equipment's protection, all the open paths along the laser beam trajectory have been closed. Two covers have been placed on top (figure 2.1 - (10)) and at the back (figure 2.1 - (11)) of the printing chamber. An interlock (figure 2.1 -(12)) has been coupled the front panel of the printing chamber so that the laser cannot be turned on if the machine is open.

2.1.2 Printing chamber

The printing chamber constitutes the core of the MiniSLM device. The build plate (2.3 – (13)) has a surface area of 12x12 mm² and is mounted on a high precision motorised vertical stage (2.1 – (4)) with a step resolution of 21 nm (8MVT40-13-1, Standa Ltd, Lithuania) and a travel range of 12 mm. The total build height is restricted to about 5 mm depending on the powder quality, layer thickness and losses during the recoating. Due to the lack of space inside of the chamber, the recoater could not be made large enough to ensure the complete filling of the theoretical build volume. However this is enough to perform *operando* XRD experiments.

(a) Printing chamber **(b)** Build stage
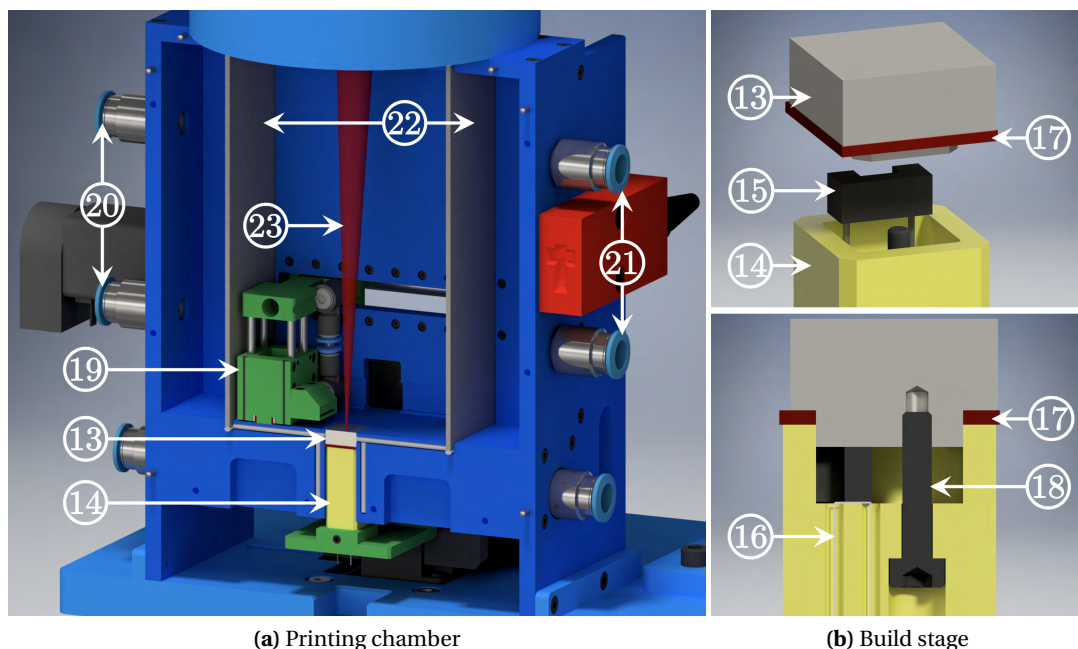
Figure 2.3 – a) 3D rendering of the printing chamber of the MiniSLM; b) exploded view and cross-section of the build stage; 13) build plate, 14) ceramic holder, 15) heater, 16) thermocouple, 17) sealing, 18) clamping screw, 19) recoater, 20) gas inlet, 21) gas outlet, 22) steel filters, 23) laser beam.

A custom-made zirconia ceramic holder serves as a support and link between the plate and the motorised stage (figure 2.3 – (14)). Inside of the ceramic holder, a silicon-nitride resistive heater (Bach RC, Germany, figure 2.3 – (15)) is placed directly in contact with the build plate (figure 2.3 – (13)). The contact surface is relatively small (1.5x7 mm²) and can reach up to 500°C. A fine gage unsheathed type K thermocouple (OMEGA Engineering, INC., US, figure 2.3 – (16)), is placed under the resistor. The temperature is controlled by a conventional PID closed-loop control protocol. A silicon joint surrounding the plate (figure 2.3 – (17)) prevents the powder from falling in the clearance gap between the ceramic holder and the frame of the machine. A crew holds the the assembly together (figure 2.3 – (18)), using the build plate as clamp to press everything together. In the current design, the maximum temperature on top of the base plate is only 100°C. The most important factors that prevent reaching higher temperatures are: 1) loss of contact during heating because of different thermal expansion of the various components, 2) the small size of the ceramic heater compared to the size of the base plate and 3) heat losses.
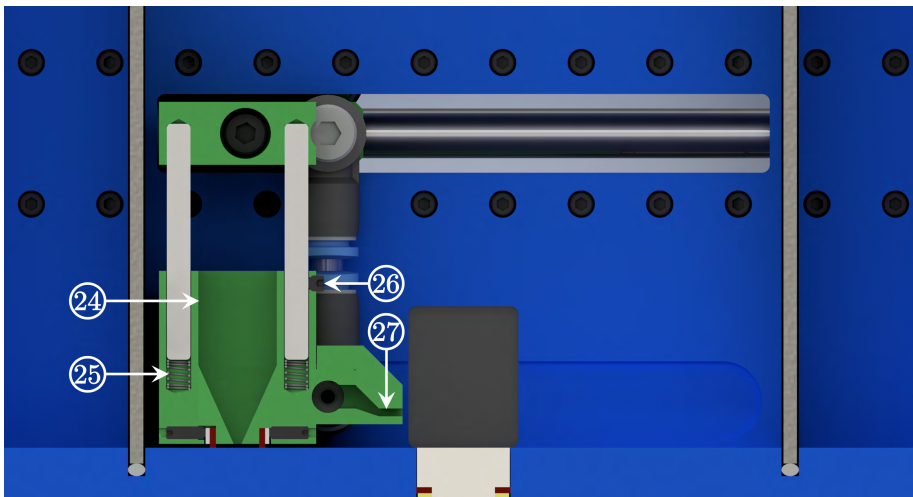
Figure 2.4 – Cross-section of the printing chamber showing the recoater design. 24) recoater funnel, 25) spring, 26) screws, 27) gas nozzle.

The powder delivery system is a hopper-based design with a doctor blade [2]. The powder is stored in a funnel-like cavity (figure 2.3 – (19) and figure 2.4 – (24), in green). Before recoating, the build plate is moved down to a height corresponding to one-layer thickness. This creates a gap between the top of the plate and the frame of the machine. A motor-spindle assembly (Igus® Schweiz GmbH, figure 2.1 – (5)) drives the recoating system above the newly formed gap, while the linearity of the movement is ensured by two miniature linear guides (Chieftek Precision Co., Ltd, Taiwan). The powder falls in the gap during the first passage of the recoater, and the excess of powder is scrapped by the blade on its way back, creating the freshly deposited layer. The recoater was designed so that no excessive force is applied on the powder bed during the recoating process. This is accomplished using four springs (figure 2.4 – (25)) to ensure that the silicon blades are in contact with the base of the machine before locking them into position with two screws (figure 2.4– (26)) to avoid any vertical movements during the recoating.

It is known that the flowability of metallic powders can be poor [81]. This is particularly critical for gravity-based recoating systems like the MiniSLM has, since the powder tends to stick on the walls or agglomerate at the bottom of the funnel. To overcome this, a vibration system has been installed on the beam holding the

recoater (Seeed Studio, China). The vibration is activated during the recoating process in order to enhance the flowability of the powder.
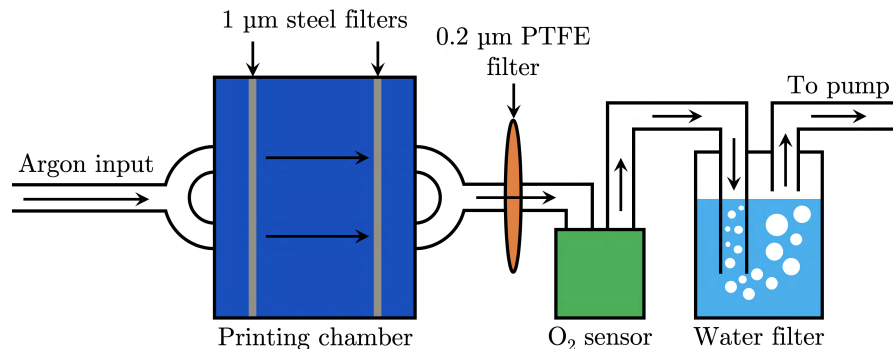
Figure 2.5 – Schematic of the particle filtering circuit of the MiniSLM. The gas flow is indicated by the arrows.

Because the chamber is not air-tight, it is continuously flushed with high purity argon gas (99.998% Ar, Carbagas) from the gas inlets (figure 2.3 – (20)). A vacuum pump (KNF Neuberger AG) is connected to the outlets (figure 2.3 – (21)) to ensure a unidirectional flow. Additionally, a local argon flow is generated above the powder bed through a nozzle mounted on the recoater (figure 2.4 – (27) in green). The input, output and nozzle flows are controlled with manual flowmeters (Vögtlin Instruments AG). The inlet and outlet flows are adjusted to create a small overpressure in the chamber. This avoids oxygen contamination from the outside atmosphere. A small oxygen monitoring module (Pewatron AG) monitors the oxygen level at the outlet with an 0.2% accuracy below 10% oxygen. Filters are placed along the inert gas circuit to sieve ejected particles generated during printing. In the chamber, 1 µm opening stainless steel filters (TWP Inc., US, figure 2.3 – (22)) are mounted. For sub-micron particles, an 0.2 µm opening PTFE hydrophobic filter (Merck & Cie, CH) is placed before the oxygen sensor to protect it, and a simple water-based filter is placed after the pump to catch any residual particles. The complete flow schematic is illustrated in figure 2.5.

2.1.3 Recoater upgrade

(a) Top front view   **(b)** Bottom view
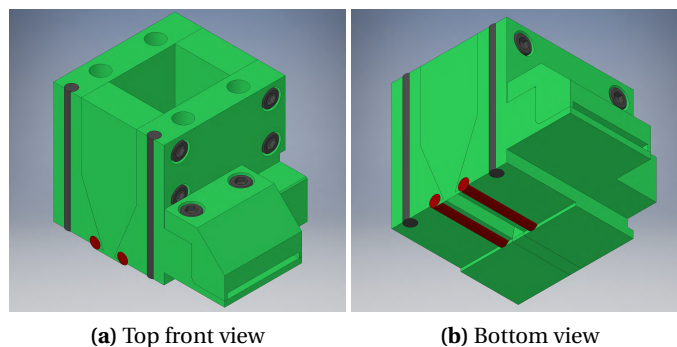
Figure 2.6 – 3D representation of the old recoater

The first version of the recoater was designed to have cylindrical silicon pads to act as a blade during the recoating process (figure 2.6). These pads (dark red) were held in place in a cylindrical groove and could be replaced by sliding them in and out from the front part of the recoater. When the silicon pads needed to be

replaced, new ones were made by cutting a silicon cord at the appropriate length. However, after careful observation, the silicon pad was not straight once inserted in the recoater but slightly convex, due to an inferior holding configuration. In addition, the diameter of the silicon cord varied along its length. Together, these made the pads stick out farther than they should and exerted excessive pressure on the powder bed during the recoating. (see section 4.2).

(a) Top front view   **(b)** Bottom view
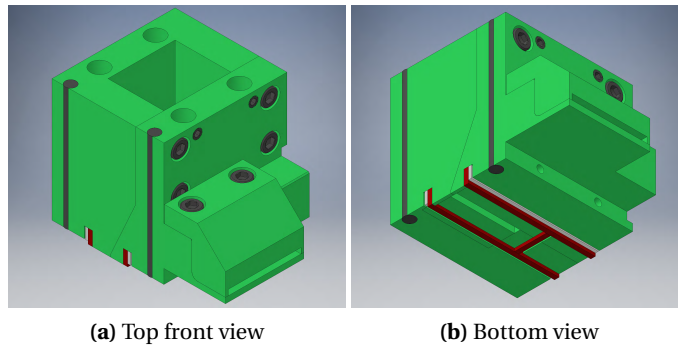
Figure 2.7 – 3D representation of the new recoater

For that reason, a second version of the recoater was made as shown in figure 2.7. The design and holding configuration of the silicon pads (dark red) were improved to reduce the pressure on the powder bed as much as possible during the recoating process. The new pads have a rectangular shape and are cut from a silicon sheet by high precision water jet cutting. Even if the silicon sheet has some variation in its thickness, the side of the pads in contact with the powder bed is defined by the cutting process which reduces the risk of having an uneven surface. Moreover, aluminium side supports (grey) clamp the pads in place by tightening screws on the side of the recoater. This ensures that the surface stays flat during the recoating.

2.1.4 Laser and optics

A high-energy laser beam (redPOWER, SPI Lasers Ltd, UK) with maximum power of 500W and a wavelength of 1070±10 nm is directly collimated as a parallel Gaussian beam (ø9.6mm at $\frac{1}{e^2}$, figure 2.1 – (7)) into a 2-axis deflection scanning unit (SuperScan III, Raylase GmbH, Germany, figure 2.1 – (6)). The whole setup (laser, scanning unit and printing chamber) is cooled down with a closed-loop air-water exchanger chiller (Termotek GmbH, Germany). The laser and chiller are mounted on a standard 19 inches rack housing on wheels, to facilitate transport. Two fused silica mirrors galvanometer (di-electric coating, reflectivity >99.5% at 1064 nm) pilot the laser beam in the two horizontal directions of the printing area. The laser beam is focused through a F-Theta lens (Sill Optics, Germany, figure 2.1 - (8)) to a minimum spot size of 25 µm at the focal plane of the lens. The name "F-Theta" is commonly used because the position of the laser spot is proportional to the focal length "F" of the lens and the deflection angle "Theta" of the laser beam [82]. In the case of the MiniSLM, the positioning of the F-Theta lens needed additional precaution to prevent any interaction between the laser beam and the frame of the machine.

Figure 2.8a and b illustrate the positioning of the F-Theta lens compared to the powder bed, and the position of the MiniSLM powder bed within the object focal plane of the lens. The optical axis of the lens lies in the centre of the object focal plane. To avoid interaction between the machine frame and the laser beam, the

condition that must be respected is α>0. To obtain that, the minimum distance ΔY was determined to be 15 mm to have an angle value of α=0.3°. At this distance, the laser beam has an opening angle of β=5.4°. These values were calculated and communicated by the Raylase after the selection of the scanning head and the F-Theta lens. A distance ΔY=20 mm was chosen for the positioning of the optical axis of the lens compared to the front panel of the printing chamber.

(a) F-Theta lens positioning

(b) Object focal plane, taken from [83]
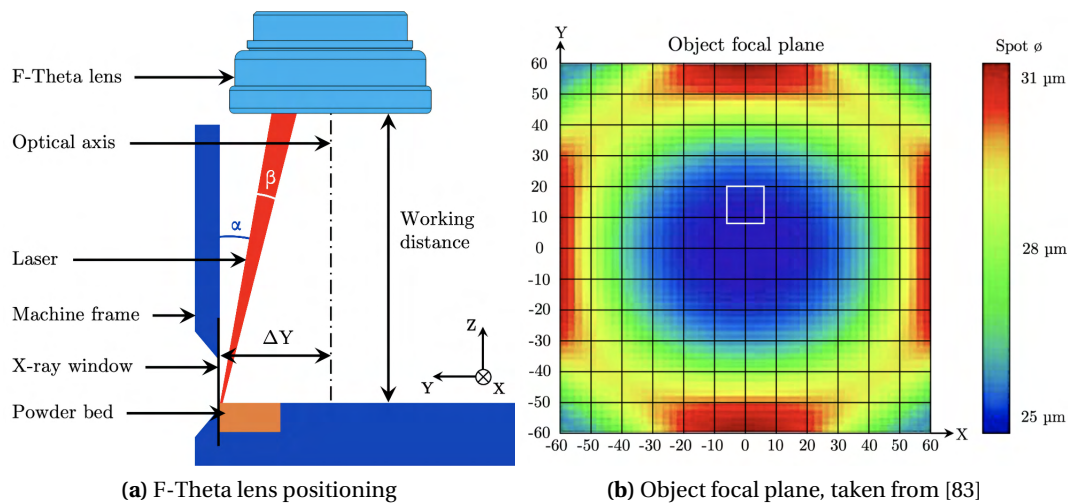
Figure 2.8 – Schematic of the positioning and object focal plane of the F-Theta lens, the highlighted area corresponds to the position of the MiniSLM powder bed (axis in mm)

The laser spot diameter distribution within the object focal plane of the lens is given by the manufacturer [83]. Figure 2.8b shows the total object focal plan of our lens, with the powder bed area of the MiniSLM highlighted after offsetting. The powder bed lies in a region where the laser spot diameter does not experience significant variations, and as a result it can be considered constant during laser scanning.
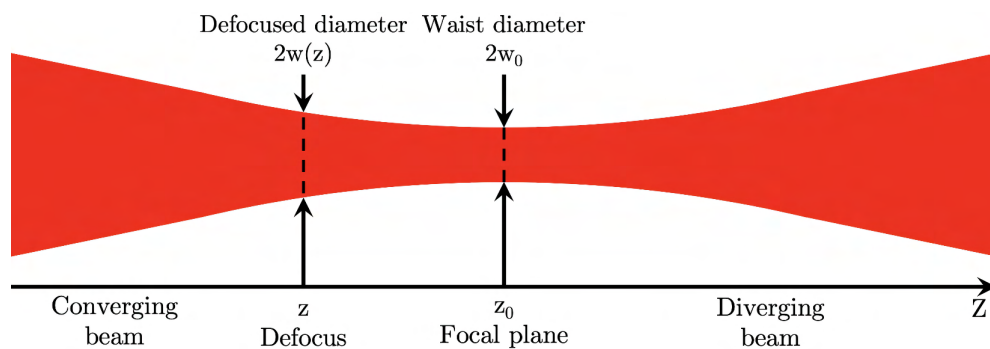
Figure 2.9 – De-focusing of the laser beam, the Z-axis corresponds to the working distance

Larger spot sizes can be achieved by defocusing using a micrometric precision linear stage (OWIS LT 60-25, figure 2.1 – (9)) and changing the working distance of the F-Theta lens (figure 2.8a). By doing so, the plane of the powder bed is intersecting the laser beam at a higher position, resulting in an effectively larger spot. Figure 2.9 illustrates the change of beam diameter. The new defocused beam diameter $2w(z)$ can be obtained

using the equation [12]:

$$w(z) = w_0 \sqrt{1 + \left(\frac{z - z_0}{z_0}\right)^2} \qquad (2.1)$$

Where w_0=12.5 μm is given by the manufacturer of the scanning head, and:

$$z_0 = \frac{\pi w_0^2}{\lambda M^2} \qquad (2.2)$$

With λ=1064 nm the wavelength of the laser and M^2=1.1 the laser beam quality factor

Based on the CAD design, the necessary displacement to be in focus on the micrometric vertical stage is 15.02 mm from the top edge of the stage (position 0). By using equation 2.1, one can then derive the different stage positions corresponding to the desired laser spot diameter as shown in table 2.1.

Table 2.1 – Laser spot diameter and defocus

Vertical stage position [mm]	Defocus [mm]	Laser spot diameter [μm]
15.02	0	25
15.75	0.73	50
16.21	1.19	75
16.65	1.63	100

The laser beam (figure 2.3 – (23)) enters the printing chamber through a 500 μm thick fused quartz window (UQG Optics, UK) with an anti-reflection coating (R<0.50%) on both sides. Since we are working with a high-power laser, the goal of this coating has two function: 1) to prevent back reflection of the laser beam in the optics and thus maximising the light transmission to the powder bed; and 2) reduce the amount of light absorbed by the glass and avoid thermal damage to the window. In addition to this coating, a physical shielding element is placed along the laser beam path between the lens and the chamber window to protect the user from any possible back reflections.

2.2 Software design

The complete setup is managed by a single computer. The laser and scanning head are steered via a SP-ICE-3 board that can be controlled by the WeldMARK software (Raylase GmbH, Germany). This an engraving software that offers different scanning strategies: unidirectional and bidirectional raster scanning (with or without meander) and cross-hatch scanning. The scanning vector can be rotated at any angle value within the printing plane. All the motors are steered with USB controllers (Standa Ltd, Lithuania). In this thesis, an in-house written LabVIEW-based software package was developed to control and synchronise all components. The communication between WeldMARK and LabVIEW is achieved over a standard ActiveX communication protocol. One of the advantages of this method is that LabVIEW can call independently any of the functions embedded in WeldMARK, which makes it very flexible. For instance, it allows to print complex 3D structures or combine various scanning strategies.
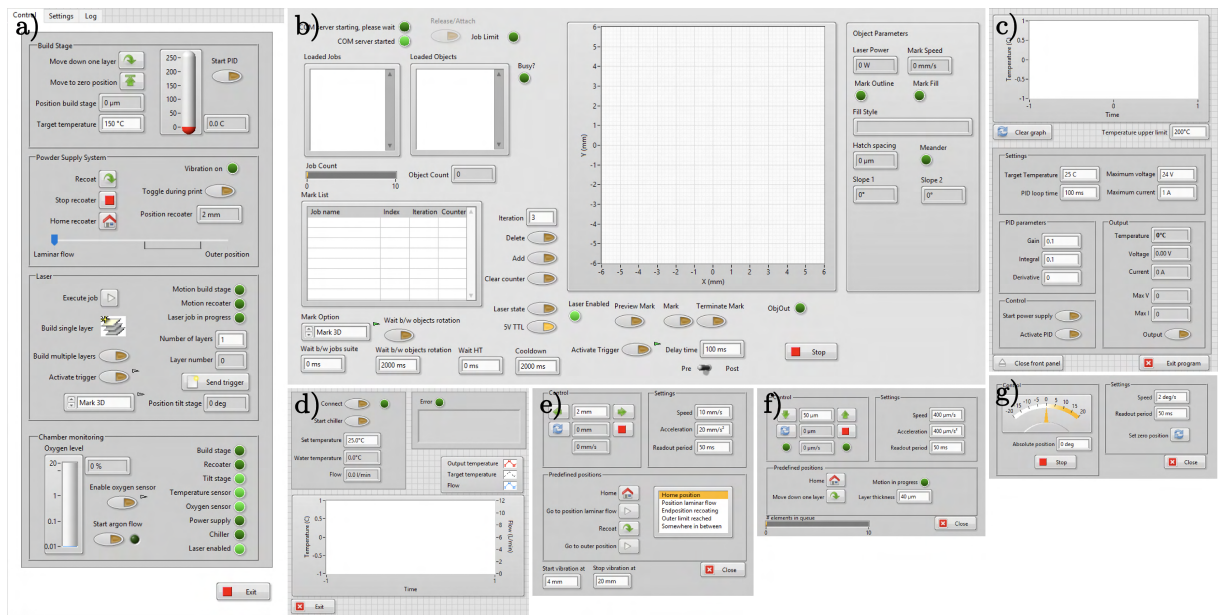
Figure 2.10 – In house LabVIEW interface to control the different component of the MiniSLM. a) Main panel to control the machine; b) Laser scanning unit module; c) Preheating module; d) Chiller module; e) Build stage module; f) Recoater module; g) Tilt stage module

During *operando* measurements, the control computer is placed inside the experimental hutch, which is not accessible during X-ray experiments, and remotely controlled from the control room. Since the experiment is very fast, the synchrotron beamline and laser must be synchronised with high accuracy to ensure efficient data acquisition. This is achieved by combining a soft- and hardware trigger.
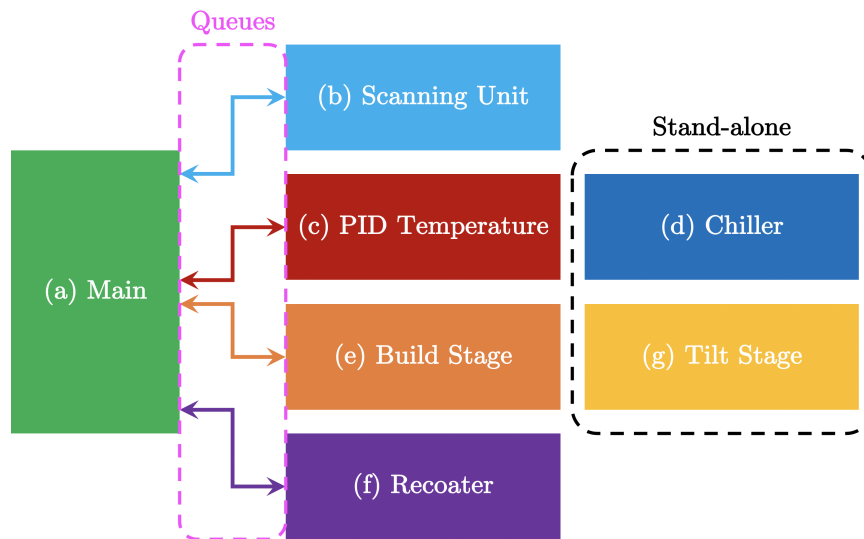
Figure 2.11 – LabVIEW QSM-PC communication from figure 2.10

Our in-house developed software is based on a LabVIEW "Queued State Machine - Producer Consumer" (QSM-PC) architecture [84]. Figure 2.10 shows the different modules used to pilot the MiniSLM. The main panel (a) is the centre of this network system, distributing the tasks to the different modules through a

queue-based system. Each module has its own queue, from where information is read and written between the main panel and the other modules. The module (b) controls the scanning head and the laser through the SP-ICE-3 card. The module (c) controls the power supply of the resistor heating and read the temperature of the thermocouple in the preheating cell to regulate the PID loop. The module (d) controls the chiller used to cool down the laser, printing chamber, scanning head and laser collimator. The module (e) steers the build stage while the module (f) pilots the recoater. Finally, the module (f) controls the angle of the tilt stage.

Figure 2.11 illustrates the communication arrangement of the software from figure 2.10. The modules of the laser scanning unit, temperature, build stage, and recoater can be used separately or synchronized through the main panel. The modules of the chiller and tilt stage are stand-alones and do not interface with the other part of the software. The following paragraph will provide more detail on the functions of each module.

2.2.1 Main panel

Figure 2.12 shows the different sections of the main panel window (a). The first section (b) is dedicated to the communication with the build stage and the PID temperature control. In this section, it is possible to move the build stage down by the value corresponding to the thickness of one layer ("Move down one layer", value specified in the build stage module). This is only used during manual operation like, for instance, during an *operando* XRD measurement (see also further). Additionally, one can move the build stage back to the zero position ("Move to zero position"). Furthermore, it is possible to see the build stage position ("Position build stage"). The PID temperature control consists of a button to start or stop the PID loop ("Start PID"), a field to enter the desired target temperature at the thermocouple ("Target temperature"), and a temperature indicator (red level).
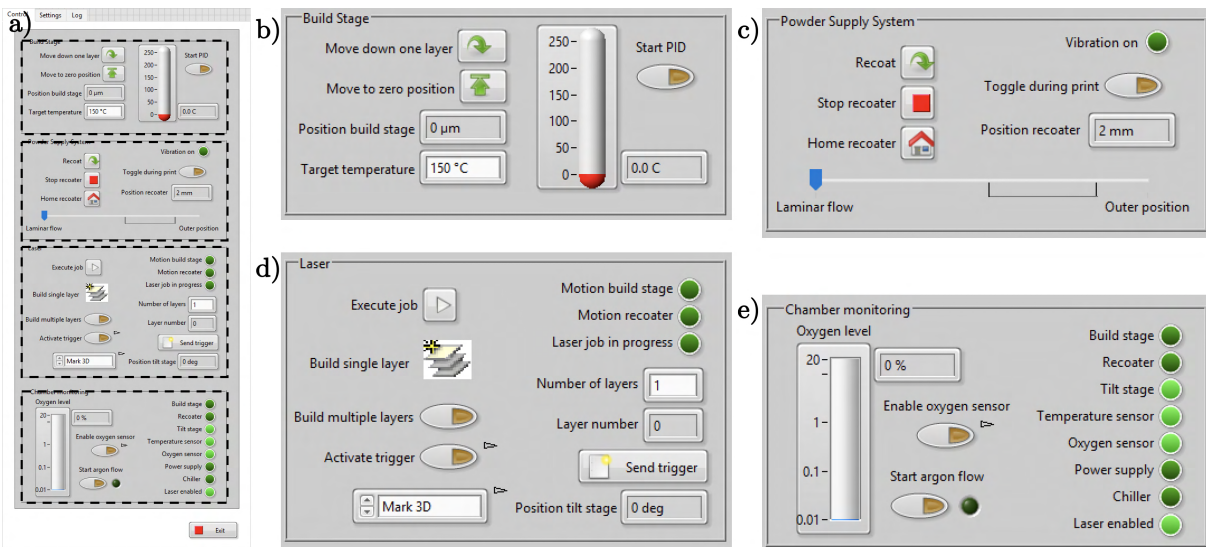
Figure 2.12 – a) Main panel window; b) Build stage and temperature section; c) Recoating section; d) Laser and scanning unit section; e) Oxygen sensor, inert gas and connection section

The second section (c) is for the communication with the recoating module and enabling the vibration system. In this section, it is possible to manually recoat the powder bed ("Recoat") or stop the motion of the recoater during its translation ("Stop recoater"). A third option moves the recoater back to its home position

("Home recoater") if necessary. If the recoater is not at its home position, it will either be in "Laminar flow" position (near the powder bed to blow the local inert gas shielding), in "Outer position" (maximum position during recoating before traveling back) or somewhere in between. A field ("Position recoater") and a cursor allow to monitor the recoater position during printing. An option is available to enable vibrations during the recoating ("Toggle during print") to enhance the powder deposition in case of bad flowability. A small indicator is available to see whether the motor vibrates or not ("Vibration on").

The third section (d) concerns the interaction with the laser, laser scanning unit module and all the information related to the printing process. In this section, the main interface can send basic commands to the laser scanning unit module, such as executing a printing job ("Execute job"). A "job" is the name given by WeldMARK to the object container file for scanning. There is also the possibility to send the command to build a single layer ("Build a single layer") which consists in 1) moving the build stage of one-layer thickness, 2) recoating of the powder bed to deposit the new powder layer and 3) laser scanning of the powder. It is possible to loop this section to build 3D parts by building multiple layers ("Build multiple layers"). Depending on the option selecting in the scanning strategy menu (field "Mark 3D"), the number of desired layers will have to be specified in this section of the main panel ("Number of layers") or directly in the laser scanning unit module. A field ("Layer number") allows to follow the progression of the printing of multiple layer by displaying the layer number. Some monitoring indicators are displaying the operation status by signaling if the motion of the build stage ("Motion build stage"), the recoater ("Motion recoater") or the laser ("laser job in progress") is happening. During *operando* XRD measurements, it is possible to monitor the angle of the tilt stage ("position tilt stage"), activate the detector trigger for data acquisition ("Activate trigger") or send a trigger to test the synchronisation ("Send trigger").

Finally, the fourth section (e) is to control the oxygen level in the chamber and monitor the connection state of each components. The oxygen level is monitored by a sensor in the gas circuit after the printing chamber and displayed in the "Oxygen level" field. Two buttons are there to remotely turn on or off the oxygen sensor ("Enable oxygen sensor") and to open or close the argon flow ("Start argon flow"). On the right side, several indicators display the connection state of each component to troubleshoot in case of problems.

2.2.2   Laser scanning unit module

The laser scanning unit module relies on the ability of LabVIEW to use the ActiveX Component Object Model (COM) automation server of the WeldMARK software from Raylase. The goal of this section is to detail the role of the different elements of the laser scanning unit module. For more information regarding the creating of scanning objects or the functions linked to these, all the information can be found in the WeldMARK manual [85].

Figure 2.13 shows the configuration for the communication between the laser, scanning head, and computer. The laser and scanning head are both connected to the SP-ICE-3 board which is piloting and synchronizing both of the components. WeldMARK is communicating with the SP-ICE-3 board by sending instructions through different software functions. All these functions are also available in an ActiveX COM automation server that is created when WeldMARK is installed on the computer. LabVIEW can start the server and use the different functions to send instructions to the SP-ICE-3 trough WeldMARK. The advantage of doing so is that the functions can be called separately and in any order, which gives a lot more flexibility for users in

LabVIEW than in WeldMARK.
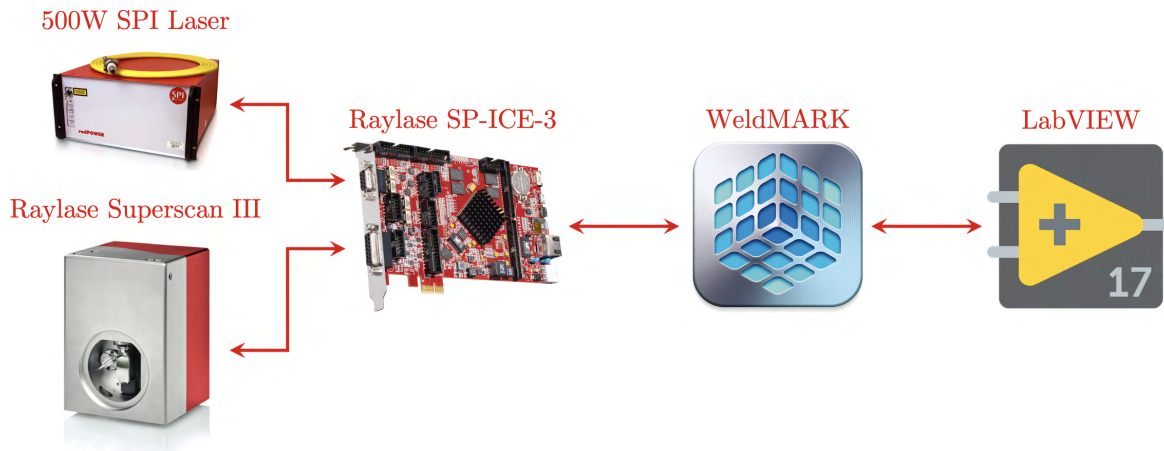
Figure 2.13 – Laser and scanning head communication configuration (pictures taken from [85–87])

Figure 2.14 shows the LabVIEW laser scanning unit module which is used to communicate with the scanning head and the laser through the WeldMARK Active COM automation server. Once the module is started, a connection is opened to the COM server, which first needs to launched. During this time, the indicator "COM server starting, please wait" is on and any actions in the module cannot be performed. Furthermore, the items allowing interaction with the COM server are greyed out. Once the COM server has started, the waiting indicator is off, the indicator "COM server started" turns on and the interface can be used. Once the interface is started, it is possible to load job files in the interface with the "Job" menu on the top left corner of the window. The job files are the objects containers generated by WeldMARK. To prevent any file corruption risk, the job files can only be read and executed on the LabVIEW laser scanning unit module. To generate job files, one has to use the WeldMARK software to ensure that the data is written properly. Before being loaded in the LabVIEW scanning module, a verification step occurs to be sure that the calibration of the job file is correct. Here calibration refers to the limits of the scanning area in WeldMARK compared to the powder bed dimensions of the MiniSLM. The size and positioning of this scanning area have been initially calibrated and hardcoded in the LabVIEW laser scanning unit module. When WeldMARK generates a job file, this information is present in the header of the file and is compared to the hardcoded values. A good calibration means that the objects will be scanned within the printing area in the object focal plane (figure 2.8b). If the calibration is wrong for some reason, the file is rejected by the interface to prevent any mistake during printing.

Once a job file is loaded, it will appear in the "Loaded Job" list and the counter "Job count" will be incremented. WeldMARK and its COM server only allow to load a maximum of 10 job files. A job file in the LabVIEW interface can be either closed under the "Job" menu and removed from the list or explored by simply clicking on it in the "Loaded Job" list. Once the selected job is highlighted, the objects contained inside the file will be displayed in the "Loaded Objects" list and the number of objects will appear in the "Object Count" field. All the objects will automatically be displayed in the printing area field at their respective position (X-Y graph field). If an object inside the job is out of the printing area, the indicator "ObjOut" will light up and it will not be possible to print. Once an object is selected in the "Loaded Objects" list, it will be highlighted in the printing area field and its object parameters will be displayed in the "Object Parameters" area showing the

values entered during its creation in WeldMARK. The parameters displayed are the laser power; scanning speed ("Mark Speed"); if the outline ("Mark Outline"), or filling ("Mark Fill") of the object is active; the scanning strategy ("Fill Style") and the hatch spacing. In the case of bi-directional scanning, an indicator shows if the scanning is continuous ("Meander") or stops at the end of each scanning vector. If the filling is done with a certain angle, the rotation value is displayed in "Slope 1" for simple scanning and additionally in "Slope 2" for bi-directional scanning.
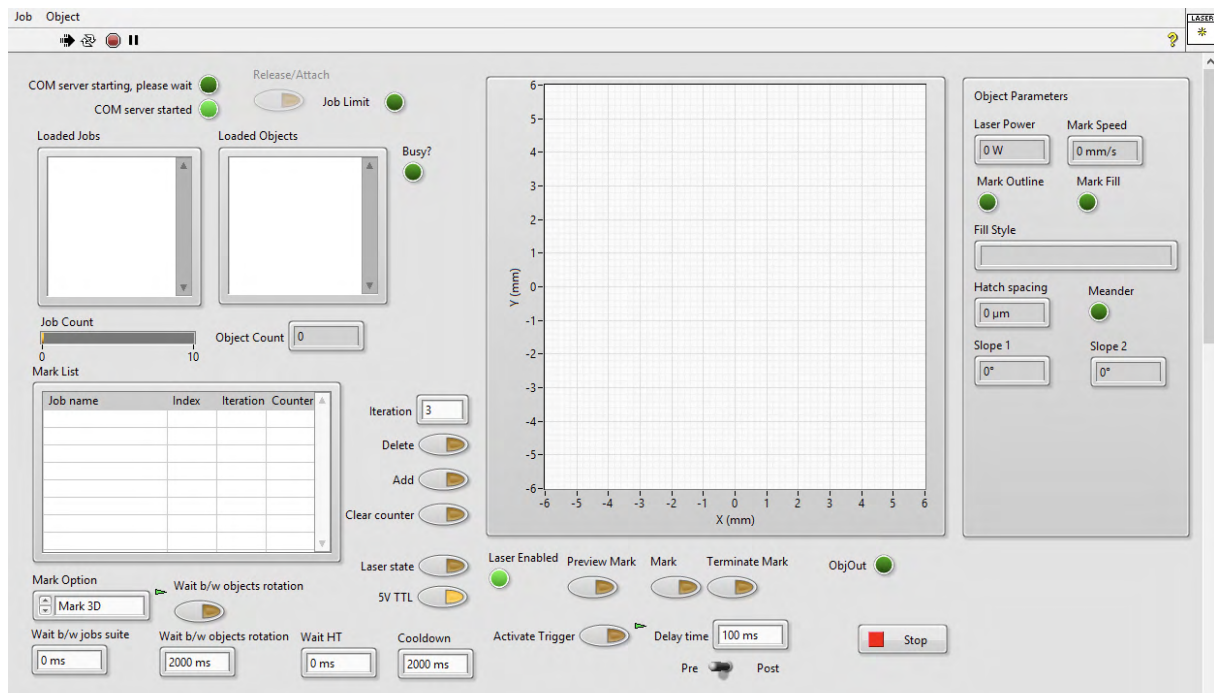
Figure 2.14 – Laser scanning unit module on LabVIEW

From this interface, it is only possible to send the marking command to print the current layer via the "Mark" button. To couple the marking process with the recoating of new layers, it is necessary to start the printing process from the main panel (figure 2.12d). This will result in a marking trigger sent from the main panel to the laser scanning unit module, emulating the action of clicking on the "Mark" button. A "Mark List" can be used depending on the adopted printing strategy. In this list, it is possible to queue the desired jobs by selecting them in the "Loaded Jobs" list and click on the "Add" button. The number of iterations has to be specified beforehand in the "Iteration" field to indicate how many times the job has the be executed in the list. The list has four columns: "Job name", "Index", "Iteration" and "Counter". The first two are the job identifiers, the third column is specified when adding the job as previously explained, and the last one is the counter for the number of times the "Mark" command has been executed. When the counter equals the number of iterations, the "Mark" command cannot be executed for this job anymore.

Several printing options are available in the laser scanning unit module in the "Mark Option" menu. The "Mark Option" menu in the laser scanning module and main panel (figure 2.12d) are synchronised for safety reasons. Once the "Mark" command is sent, the laser scanning module will perform the following depending on the marking option selected:

- "MarkObj" will only print the selected object in the "Loaded Objects" list.
- "MarkAllObj" will print all the objects of the selected job in the "Loaded Jobs" list.
- "Mark List" will print all the jobs in the list until the last line, starting from the selected line in the list and with one iteration per layer. Before going to the next line, all the iterations of the current line have to be completed.
- "Mark Suite" will print all the jobs of the list once in the top-bottom order.
- "Mark 3D" will print the highlighted object in the "Loaded Objects" list and highlight the next one after the marking is done. This option allows the printing of complex structures. The open-source software Slic3r [88] is used to slice an STL file ("Standard Triangle Language" or "Standard Tessellation Language") into layers with a defined thickness. These are exported into an SVG file (Scalable Vector Graphics), which can be used in the WeldMARK environment and our in-house written software. The SVG file has to be rewritten using an external module into a job file containing one layer per object, the bottom layer being the first object. The 3D part is printed by loading object at the corresponding layer height tanks to the "Mark 3D" option. Figure 2.15 shows a STL model of the well-known Matterhorn mountain in (a) that has successfully gone through this conversion process to a SVG file and ultimately 3D printed as shown in (b).
- "Mark HT" will print all the jobs in the list for the same layer, completing all the iterations for each line after sending one time the "Mark" command. The label "HT" stands for heat treatment. This option was made available for local heat treatment with the laser on the sample after printing. For example, the printing job is in the first line with one iteration, and a heat treatment job (laser scanning at low power) is in second position with 100 iterations. The first job will be printed normally and directly after the surface will be scanned 100 times at a lower power.
- "Pattern rotation" will print all the jobs in the list until the last line, starting from the selected line in the list. The module will go to the next line automatically after printing the current line. For example, if 4 jobs are present in the list with 20 iterations each, the printing sequence will be 1-2-3-4-1-2-3-4-etc. This option has been made to enable rotation of the printing pattern between each layer, given that the jobs have been rotated properly.

In addition to the different marking strategies, it is possible to adjust the waiting time for certain options. This was made available to produce *ex situ* samples in the same condition as during *operando* measurements where the whole printing process is controlled manually: the build stage displacement, the recoating, and the laser scanning are done by physically clicking on the different buttons. Moreover, one layer is not printed directly on top of the other one because some other manipulations are necessary between each layer, which means the whole sample has time to cool down. Therefore, within the laser scanning unit module it is possible to specify different cooling times:

- "Wait b/w jobs suite" will make the software wait between each job in "Mark Suite" mode.
- "Wait b/w objects rotation" will make the software wait between each object in "Pattern rotation" mode.
- "Wait HT" will make the software wait between each job in the "Mark HT" mode
- "Cooldown" will make the software wait at the end of a "Mark" command in any mode.

Finally, some advanced options are available to interact directly with the laser, scanning head, or X-ray detector:

- "Laser state" will enable or disable the laser for printing. When the laser is disabled, a low-power laser pointer is visible on the build stage to see the position of the laser spot. The indicator "Laser Enabled" indicates the status of the laser.
- "Preview Mark" will scan repetitively the contour of the selected object in the "Loaded Objects". This option is to be used in combination with the laser pointer when the laser is disabled to control the position of the object on the build plate. This has been made for calibration purposes.
- "Terminate Mark" will immediately terminate any marking happening in case of an emergency.
- "Activate Trigger" will activate the trigger sent to the X-ray detector when the "Mark" command is sent to the scanning head. The delay time between the trigger and command can be adjusted in the "Delay time" field. It is also possible to choose if the trigger has to be sent before ("Pre") or after ("Post") the mark command. The "Activate Trigger" button in the laser scanning module and main panel (figure 2.12d) are synchronized for safety reasons.

(a) STL model   **(b)** 3D printed model
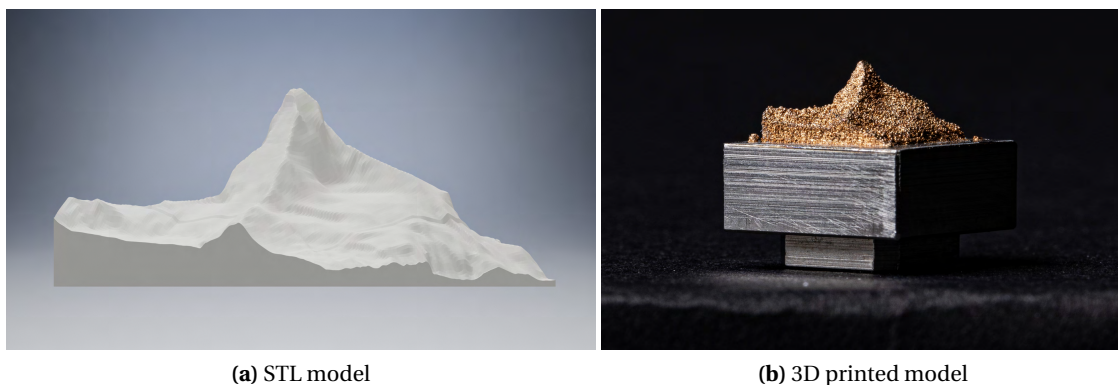
Figure 2.15 – 3D model of the Matterhorn, bronze on stainless steel plate (sample height: 5 mm)

2.2.3 PID loop temperature

The preheating temperature is set by the ceramic resistor which is powered by a programmable benchtop power supply (RND 320-KD3005P). The temperature is measured by using a thermocouple in contact with the resistor (figure 2.3b). A PID loop temperature module is used, and based on a standard LabVIEW PID controller which regulates the voltage and current input at the resistor based on the temperature reading at the thermocouple. Figure 2.16 shows the LabVIEW module that is used to control the PID loop.

In the "Settings" section, the temperature can be set in the "Target Temperature" field, which is synchronised with the field in the main panel (figure 2.12b). One can adjust the frequency at which the PID loop is executed in the field "PID loop time" and specify the maximum voltage and current that the power supply can reach in the fields "Maximum voltage" and "Maximum current" respectively. These values are provided by the manufacturer of the resistor. The PID loop parameters can be adjusted in the fields "Gain", "Integral" and "Derivative".

When the power supply is turned on the first time with a connection to the computer, it is in configuration mode where the maximum voltage and current can be entered manually. With the PID temperature module, the power supply can be initialized with the maximum voltage and current values using the "Start power
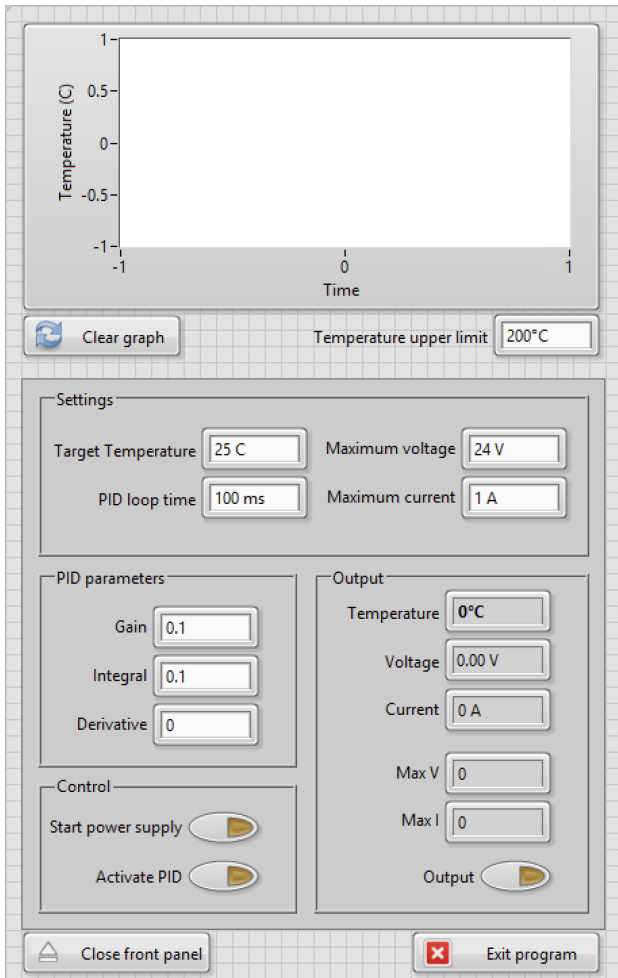
Figure 2.16 – PID temperature module on LabVIEW
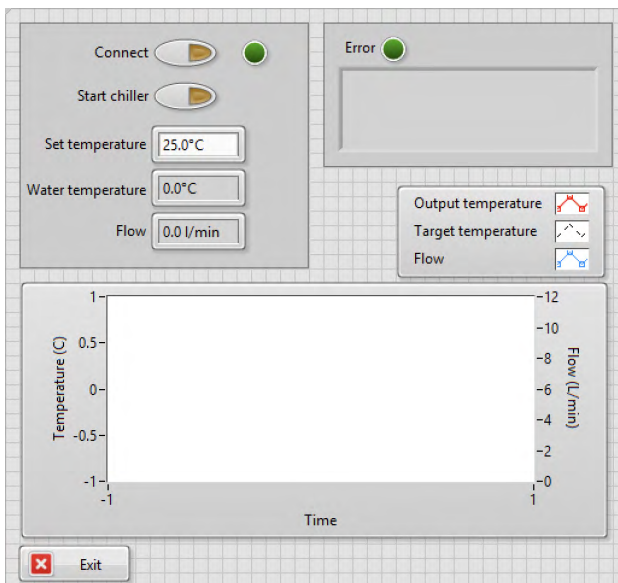
Figure 2.17 – Chiller module on LabVIEW

supply" button, but no output will be provided. When clicking on the "Activate PID", the power supply is initialised, and an output is provided starting the PID loop control. The readout values area displayed in the "Output section and the "Output" button is on. In case the PID loop stops working properly, it is possible to turn the output off by clicking the "Output" button.

2.2.4 Chiller

The chiller module controls the cooling system of the MiniSLM. The communication based on the RS-232 (Recommended Standard) exchange protocol. The commands to change parameters or read information are sent to the chiller as encoded bits based on the index list provided by Termotek. This list includes an extensive amount of commands to communicate with the chiller, but only few were hand-picked to be able to control and monitor the cooling properly from the computer. Figure 2.17 shows the LabVIEW module used to control the chiller.

The "Connect" button is here to start the connection to the chiller. Once the connection is enabled, the indicator next to it lights up. The "Start chiller" button allows to start or stop the chiller remotely. Once the chiller is started, the water temperature and flow will be displayed in the field "Water temperature" and "Flow" respectively. It is possible to adjust the target temperature in the "Set temperature" field. Note that it is only possible to enter temperature values between 20°C and 30°C. The output temperature of the water and the target temperature are displayed in the graph, with the units on the left axis. The flow of water is also displayed with values on the right axis. In case any error happens, the "Error" indicator will illuminate, and the error message will be displayed in the field below it.

2.2.5 Recoating system
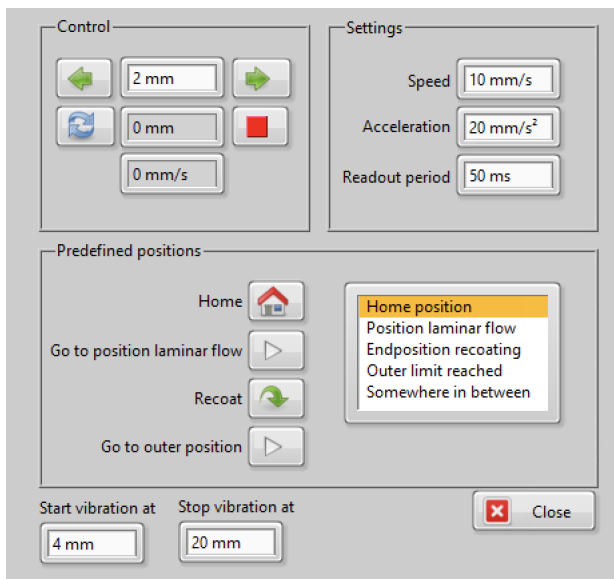
Figure 2.18 – Recoating system module on LabVIEW

The recoater is powered by a standard spindle and stepper motor assembly with linear guides. Additionally, a vibration motor has been added on the displacement system to enhance powder deposition during the recoating process. Figure 2.18 shows the recoating system module made in LabVIEW. In the "Control" section, the first field and the two arrows are for the displacement of the recoater. By clicking on the left or right arrow, the recoater will move in the left or right direction relative to the value specified in the field between them. The second field displays the current position of the recoater. The two blue arrow on the left side of the second field are to reset the home position of the recoater and the red square button on the right side is to stop its displacement. The third field is to display the displacement speed of the recoater. In the "Settings" section it is possible to adjust the speed of the recoater, its acceleration when starting or stopping and the readout period of the position and speed.

In the "Predefined positions" section, it is possible to move the recoater to positions already saved in the module. The "Home" button will move the recoater to its zero value. The "Go to position laminar flow" button will put the recoater in place to shield the powder bed with the argon flow. The "Go to outer position" will move the recoater to a position on the other side of the powder bed. The "Recoat" button will make the recoater move from the flow position to the outer position and come back, producing the deposition of a new layer of powder. On the right side of the section, a list highlights the current status of the recoater. In the "Build single layer" or "Build multiple layers" mode (figure 2.12d) the main panel always checks that the recoater is back to the flow position before sending the "Mark" command to avoid that the laser hits the recoater.

Finally at the bottom of the recoating system module, two fields labeled "Start vibration at" and "Stop vibration at" enable to define the position range in which the vibration motor will be activated when the recoater is moving from the flow position to the outer position, if the "Toggle during print" option has been activated in the main panel (figure 2.12c).

2.2.6 Build stage

The build stage module is based on the same configuration as the recoating system module. Figure 2.19 shows the build stage module made in LabVIEW.

In the "Control" section, the first field and the two arrows are for the displacement of the build stage. By clicking on the up or down arrow, the build stage will move up or down relative to the value specified in the

field between them. The second field displays the current position of the build stage. The two blue arrows on the left side of the second field are to reset the home position of the build stage and the red square button on the right side is to stop its displacement. The third field is to display the displacement speed of the build stage. In the "Settings" section it is possible to adjust the speed of the build stage, its acceleration when starting or stopping and the readout period of the position and speed.
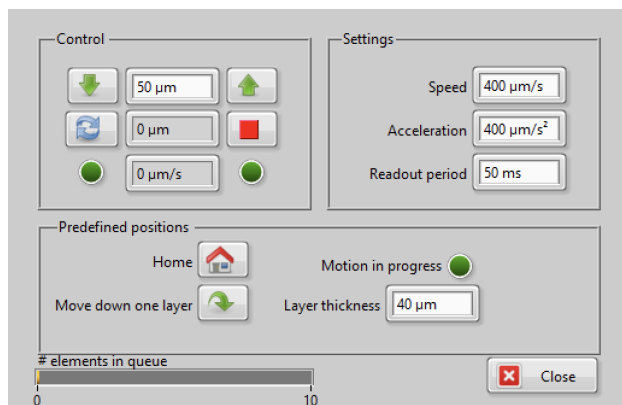
Figure 2.19 – Build stage module on LabVIEW position, in order to avoid collisions.

In the "Predefined positions" section, it is possible to move the build stage to positions already saved in the module. The "Home" button will move the recoater to its zero value. "Move down one layer" will move the build stage down of the value entered in the field "Layer thickness". Finally, when the build stage is moving, the indicator "Motion in progress" is lit up. In the "Build single layer" or "Build multiple layers" mode (figure 2.12d) the build stage will not move before sending the recoating command to the recoater. Additionally, the build stage cannot be moved if the recoater is not in the "laminar flow"

2.2.7 Tilting stage
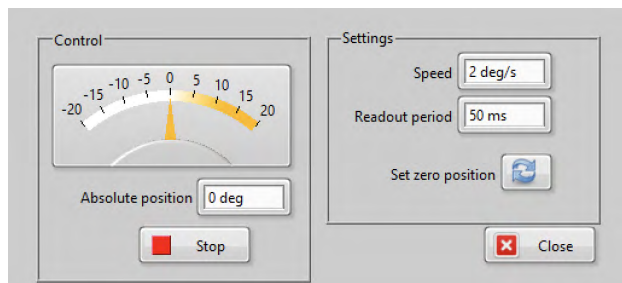
Figure 2.20 – Tilt stage module on LabVIEW

The tilt stage is only used during *operando* XRD measurements, when the machine needs to be inclined so that the X-ray beam has access to the powder bed. Figure 2.20 shows the tilt stage module made in LabVIEW. In the "Control" section, it is possible to change the position of the tilt stage by entering the desired inclination angle in the "Absolute position" field. Once entered, the tilt stage will position itself directly to this value.

Above the field, an indicator shows the position of the tilt stage in real-time. A "Stop" button is also available to interrupt the movement of the stage. In the "Settings" section, it is possible to adjust the rotation speed of the stage in the "Speed" field. One can change the zero position of the stage with the "Set zero position" button. The readout period can also be adjusted if necessary.

3 Experimental and methods

General information regarding the crystallographic and micro- structures of Ti-6Al-4V are introduced in this chapter, followed by the method used to determine the sample porosity by optical imaging. The different setup used at the SLS beamline are then presented before showing how *operando* X-ray data are acquired and analysed for this work.

3.1   Ti-6Al-4V

3.1.1   Material

Crystallography

(a) α-HCP lattice   **(b)** β-BCC lattice   **(c)** Ti-alloy distribution [89]
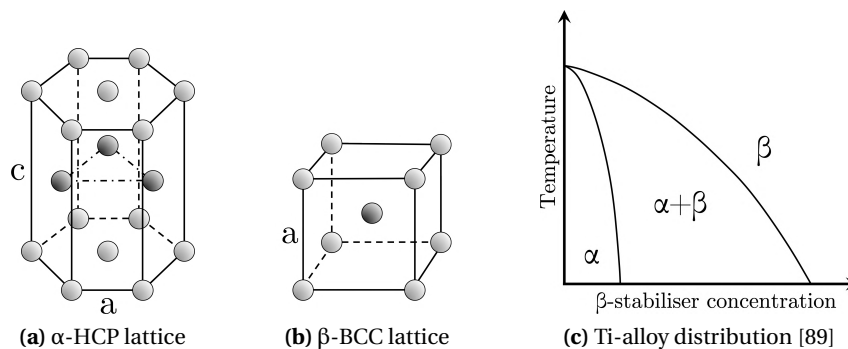
Figure 3.1 – Crystallographic lattices and phase distribution of titanium alloys

Pure titanium has two crystallographic phases: the Hexagonal Closed-Packed (HCP) α phase, stable at room temperature; and the Body-Centred Cubic (BCC) β phase, stable at high temperature (figures 3.1a and b). When heated up, it experiences the phase transformation $\alpha \rightarrow \beta$ at the β transus temperature $T_{\alpha \rightarrow \beta}$ = 1155.65K. Titanium based alloys are classified into three different categories, depending on the alloying elements presents in the mixture: α alloys, β alloys and $(\alpha + \beta)$ alloys (figure 3.1c). The first category - α alloys - includes pure Ti, or Ti alloys with addition of Al, Sn, Ga, Zr, C, O and N. Such elements are called α-stabilisers since they increase the β transus temperature when added to titanium. The second category - β alloys -

includes Ti alloys with addition of V, Mo, Nb, Ta and Cr. These chemical elements are called β-stabilisers as they decrease the β transus temperature. When added in proper amounts, they can make the β phase stable at room temperature. Finally when combining α and β stabilisers with Ti, both phases coexist at room temperature making it an (α + β) alloy type [89, 90].

Ti-6Al-4V belongs to the last category, with a β transus temperature $T_{\alpha \to \beta}$ = 1268.15K [91]. The α + β microstructure combination of this alloy is desirable since it combines the high strength of the α phase (Al enriched), and the ductility of the β phase (V enriched). Heat treatment are often necessary to achieve this phase distribution [64]. After being heated above the β transus temperature, several hours of heat treatment with slow cooling rates are needed to allow the diffusion of Al and V into the α and β phases, respectively [65]. If the cooling rate from the β phase is above 410 K/s, a diffusion-less transformation $\beta \to \alpha'$ alpha occurs creating the martensitic α' phase, a V enriched α phase [92]. Table 3.1 presents the physical properties Ti and Ti-6Al-4V, with their crystal lattice constants (see figures 3.1a and b). The α and α' phase have very close lattice parameters, which will lead to an overlap of their XRD patterns.

Table 3.1 – Physical properties of pure titanium and Ti-6Al-4V

Phases	Pure Ti	Ti-6Al-4V
α (HCP)	a = 2.95030 Å, c = 4.68312 Å [93]	a = 2.921 Å, c = 4.665 Å [94]
α' (HCP)		a = 2.9313 Å, c = 4.6813 Å [6]
β (BCC)	a = 3.32 Å at 1173.15 K [93]	a = 3.208 Å [94]
$T_{\alpha \to \beta}$	1155.65K [89]	1268.15K [91]

Microstructure

(a) α + β microstructure   **(b)** Zoom
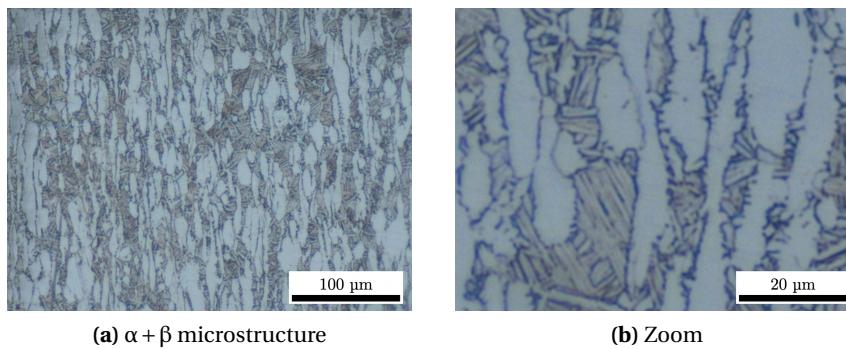
Figure 3.2 – Standard α + β microstructure for Ti-6Al-4V

Figure 3.2 shows the standard Ti-6Al-4V, composed of a mixture of α and β grains. This image was taken from a commercially available Ti-6Al-4V rod, manufactured by extrusion. A cross section of the sample was made along the extruded direction, and mechanically polished until obtaining a mirror finish. Etching was performed using Kroll's reagent, revealing the α + β microstructure. The samples were observed using a standard light microscope. The microstructure consists in large primary α grains in light grey, surrounded by the β phase and secondary α lamellae with darker contrast [95]. The vertical grain elongation indicates the extrusion direction.

(a) Columnar structure inherited from the prior-β grains

(b) Zoom on the α/α' lamellae
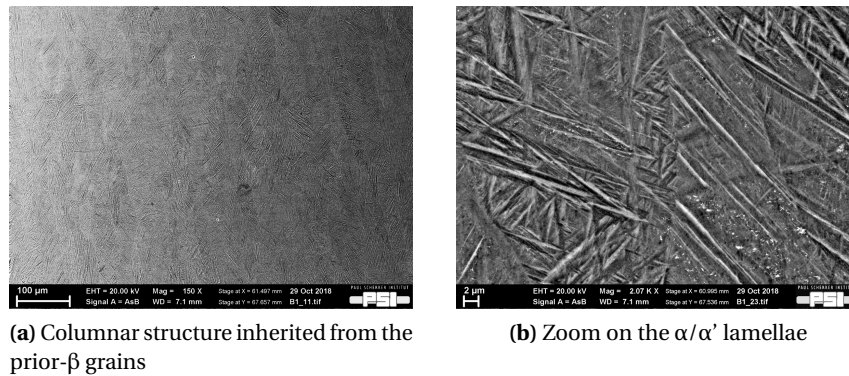
Figure 3.3 – Microstructure of SLM-made Ti-6Al-4V sample

During AM processing, cooling rates are of the order of 10^4-10^6 K/s, which is faster than the minimum cooling rate needed to induce martensitic transformation. As a result, the typical microstructure of SLM-made samples is composed of a mixture of fine α and α' lamellae arranged within columnar prior-β grains as shown in figure 3.3. The columnar prior-β grains have tendency to grow epitaxially with a [001] crystallographic orientation along the build direction due to directional heat gradient in the sample [9, 69, 96].

3.1.2 Powder characterisation

Titanium Based Powders

Process				Chemical Composition (wt %)						Contact LPW directly for similar specifications eg				
Selective Laser Melting	Electron Beam Melting	Laser Metal Deposition	Alloy	Element	Min	Max	Element	Min	Max	UNS	DIN	ASTM	AMS	Similar Grades
✓	✓	✓	**LPW Ti64 Gd23**	Al	5.5	6.5	O		0.13	R56407		B348 gr 23	4956	ISO 5832-3
			Different compositions available for optimised flow or mechanical properties	C		0.08	Res Each		0.1			F136		
				Fe		0.25	Res Total		0.4			F3001		
				H		0.0125	Ti	Bal	Bal					
				N		0.03	V	3.5	4.5					

Figure 3.4 – Ti-6Al-4V data sheet from LPW

The powder studied is a Ti-6Al-4V Extra Low Interstitial (ELI) Grade 23, manufactured by LPW Technology Ltd. (Widnes, United Kingdom). ELI means that this alloy has a lower oxygen content than other Ti-6Al-4V grades. Figure 3.4 shows the chemical composition given by the manufacturer. In SLM processing, the typical layer thickness used for Ti-6Al-4V is between 30 μm and 50 μm [6, 13, 31, 97]. This powder is produced using gas atomisation resulting in a particle size distribution of 15-45 μm, which is within the appropriate range for SLM processing compared to the layer thickness used [98]. For 3D printing the quality of the powder is crucial, and the information provided by the powder manufacturer may not always be accurate. Prior to printing, the powder is first investigated by various techniques. The particle shape and size ranges are assessed by SEM imaging and the size distribution is measured using laser diffraction as described below. Furthermore, XRD and EDS measurements were used to check the phase and chemical composition.

SEM images

To investigate the powder characteristics, a field emission gun scanning electron microscope (FEG SEM) Zeiss NVision-40 was used on a sample of powder deposited on a conductive carbon tape. Figure 3.5 shows an SEM image of the powder (a) with a zoom on few particles (b). These images reveal that the powder particles are spherical, as expected from a gas atomisation process [13].

(a) Ti-6Al-4V powder particles   **(b)** Zoom 10x
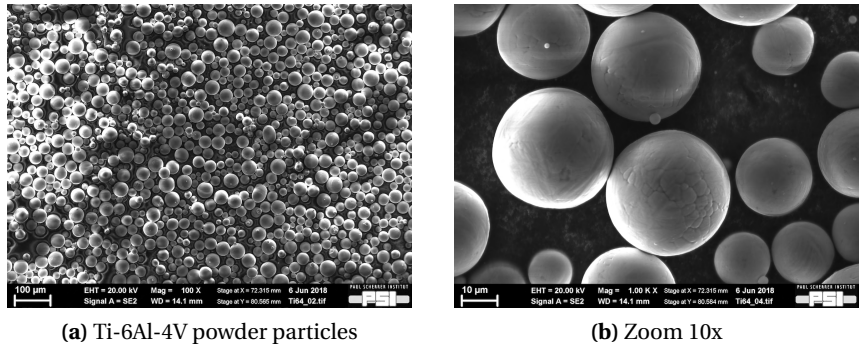
Figure 3.5 – SEM imaging of the Ti-6Al-4V powder

Particle size distribution
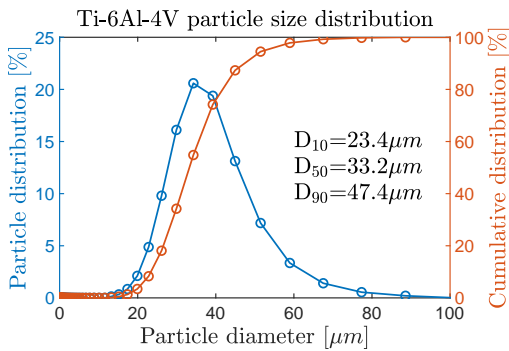
Figure 3.6 – Ti-6Al-4V particle size diameter

The particle size distribution was measured by a laser diffraction particle size analyser Partica LA-950 V2 system (Horiba, Tokyo, Japan). Figure 3.6 shows the particle distribution on the left vertical axis and the cumulative distribution on the right axis. From this distribution, the D_{10}, D_{50} and D_{90} were measured to determine the size repartition in this Ti-6Al-4V powder. The D_{10}, D_{50} and D_{90} represent the diameter values at which the cumulative distribution is equation to 10%, 50% and 90% respectively. The size distribution in figure 3.6 has a D_{10} value at 23.4 µm, which means that 10% of the particles have a diameter smaller than this value. In the same way, the D_{50} and the D_{90} are at 33.2 µm and 47.4 µm respectively. The particle size distribution of this powder corresponds well to the range provided by the manufacturer.

XRD measurements

Phase determination was performed by conventional XRD measurements on a D8 ADVANCE (Bruker Corporation) with a Cu-Kα radiation source. Figure 3.7 shows the diffraction pattern of the powder and corresponding Rietveld analysis by TOPAS [99]. The powder consists of a mixture of hexagonal α (62 wt%) and α′ (38 wt%) Ti-phases. No cubic β-phase was observed. One can notice the overlap of the α and α′ peaks as mentioned earlier.
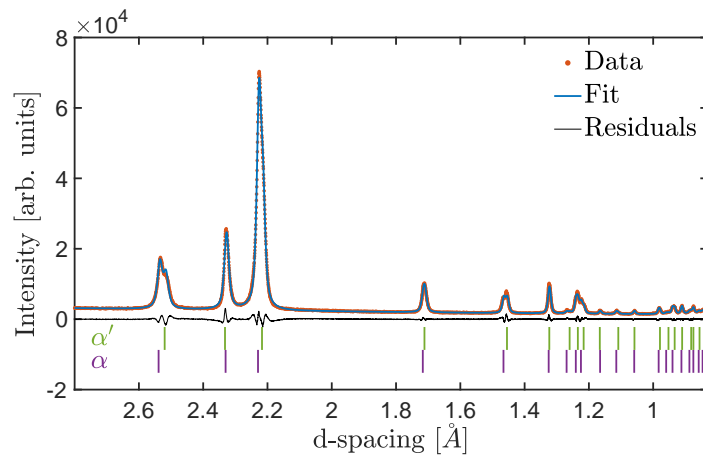
Figure 3.7 – Ti-6Al-4V powder diffraction pattern

EDS measurements
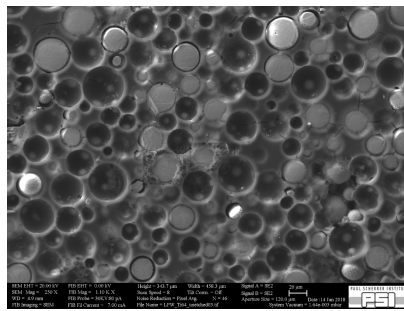
(a) Powder particle cross sections
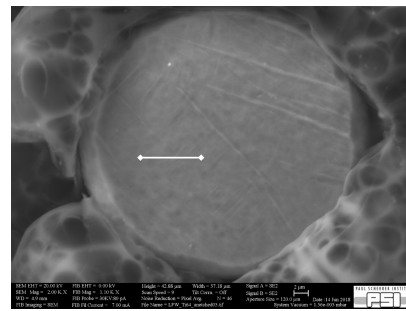
(b) EDS measurement on one particle (white line)

Figure 3.8 – Embedded Ti-6Al-4V particles after polishing, revealing the particle cross section for measurements

Table 3.2 – EDS measurements results

Measurement	Al (wt%)	Ti (wt%)	V (wt%)	Fe (wt%)
1	6.41%	90.07%	3.34%	0.19%
2	6.35%	90.03%	3.50%	0.12%
3	6.35%	90.02%	3.46%	0.16%
4	6.29%	90.14%	3.42%	0.14%
5	6.32%	90.20%	3.38%	0.10%
6	6.38%	89.95%	3.52%	0.15%
7	6.27%	90.15%	3.41%	0.17%
Average	6.34%	90.08%	3.43%	0.15%
Standard deviation	0.05%	0.09%	0.06%	0.03%

To investigate the powder chemical composition, an energy dispersive X-ray spectrometer (EDS) analysis system from Oxford Instruments was used. A sample of powder was embedded and polished to obtain cross sections of the powder particles. Figure 3.8 shows the embedded particles after polishing (a). Some of the particles got removed from the embedding matrix due to friction while polishing, leaving empty cavities.

An EDS scan was performed along a line where 7 points were selected measurement of concentration in Ti, Al, V and Fe in wt% (figure 3.8b). Table 3.2 shows the obtained results for each measurement

point, the average for each chemical element and the standard deviation.

The low standard deviation indicates that the measurement is acceptable. By comparing with data provided by LPW (figure 3.4), it appears that the V content is slightly below the reported minimum. The concentration of the other elements is within the expected range. Finally, the powder was inspected for elemental segregation within the particles. Figure 3.9 shows an EDS mapping for the particle shown in figure 3.8b, revealing a homogeneous distribution of Ti, Al and V within the cross section area.

(a) Powder particle cross section

(b) Ti content

(c) Al content

(d) V content
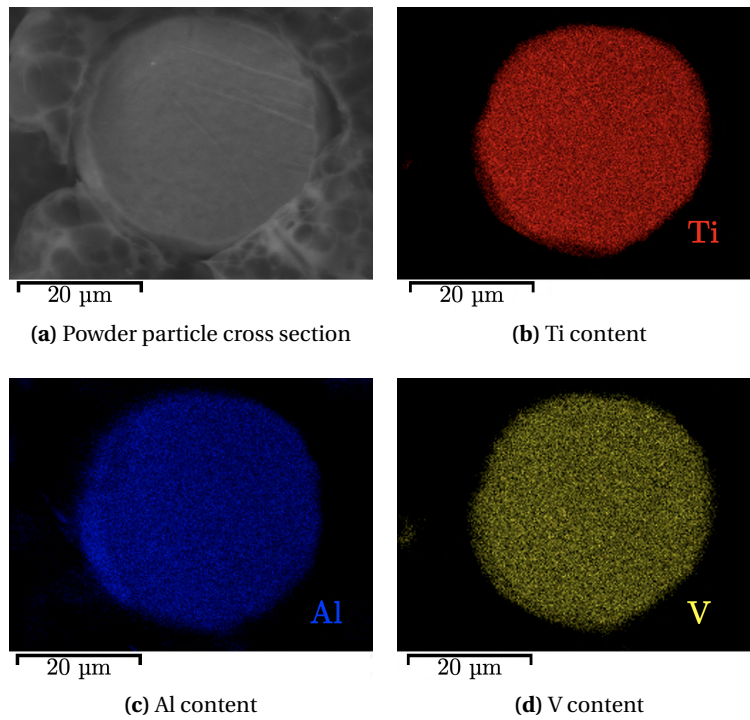
Figure 3.9 – EDS mapping of one particle cross section

3.2 Porosity measurements methodolodgy

The porosity measurements of the printed samples are done via optical imaging to assess the density, that will be referred to as optical density. This porosity measurement method will be demonstrated on the sample 34 from the study described later in section 4.2. This sample is a Ti-6Al-4V cuboid with a volume of 4x4x4 mm^3. After SLM processing, the sample is cut and polished to reveal the inner pores.

Figure 3.10a shows a light microscope image from a cross section along the building direction, here oriented vertically. One can notice the horizontal pattern of the different layers revealed after polishing. In order to measure the inner porosity, it is necessary to crop a region of interest within the sample as shown in figure 3.10b. The sample surface should be as clean as possible since dark residual traces after polishing may also be counted as pores. If the sample surface is not perfectly clean, these traces should be cut out of the picture to not give a wrong estimate of the porosity content.

The cropped image in figure 3.10b is then post-processed with Fiji, a software based on imageJ with an

extensive package library [100]. The first step is to convert the cropped section into a grey scale image. The result is displayed in figure 3.11a.

(a) Sample cross section

(b) Cropped area from (a)
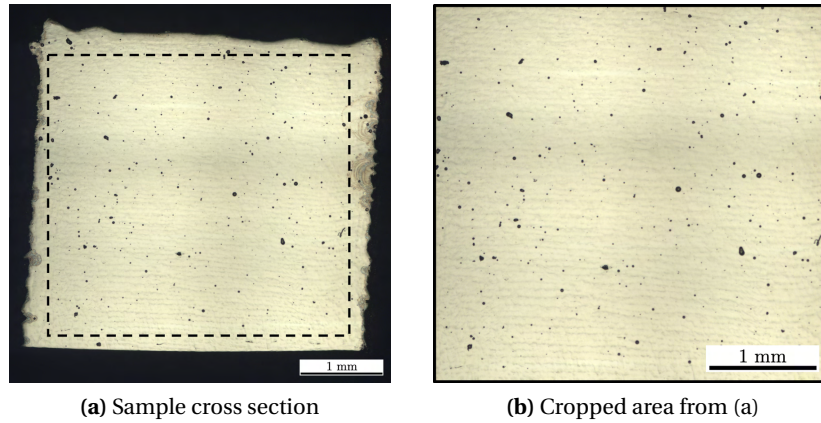
Figure 3.10 – Ti-6Al-4V cross section for porosity inspection

Once converted into a grey scale image, the pores have to be isolated from the dense material. This is done by setting a threshold on the image. Figure 3.11b shows the region of interest from sample 34 after applying the threshold function. The pores have been converted into black pixels, and the rest of the sample into white pixels. The last step to determine the porosity of the sample is to make the ratio of black pixel over the total image surface area. For sample 34, the measured optical density is 99.56%, meaning that pores cover just under 0.5% of the cross-sectional area.

(a) Grey scale image from figure 3.10b

(b) Threshold image from (a)
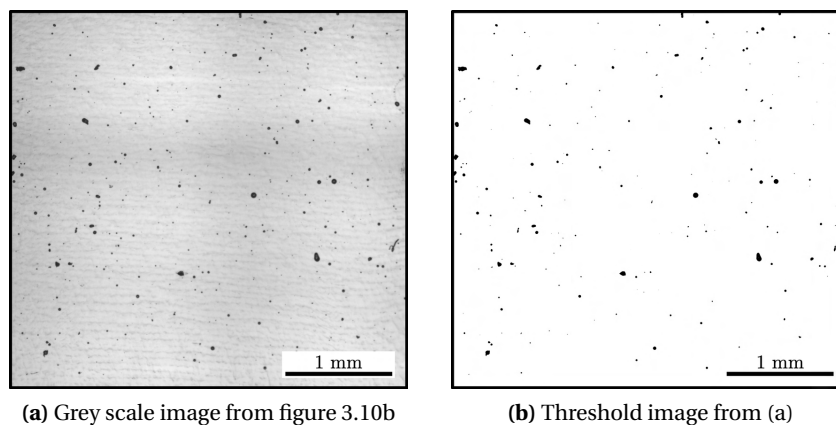
Figure 3.11 – Image post-processing with Fiji to measure the optical density

To process multiple sample, a macro was written in Java script. The complete list of commands used in this section, and the macro are available in section C.1 of the appendices.

3.3 *Operando* X-ray diffraction setup

3.3.1 Measurement configurations

The MiniSLM can be used in both transmission and reflection mode. In transmission mode (figures 3.12a and 3.12b), the X-ray beam (in yellow) is aimed near the edge of the build plate and goes through the sample, hence the term "transmission". In the reflection mode (figures 3.12c and 3.12d), the X-ray beam is located further away from the edge and only the reflected part of the beam with diffraction angles larger than the tilt of the machine can reach the detector.

(a) Transmission mode   **(b)** Zoom on (a)

(c) Reflection mode   **(d)** Zoom on (c)
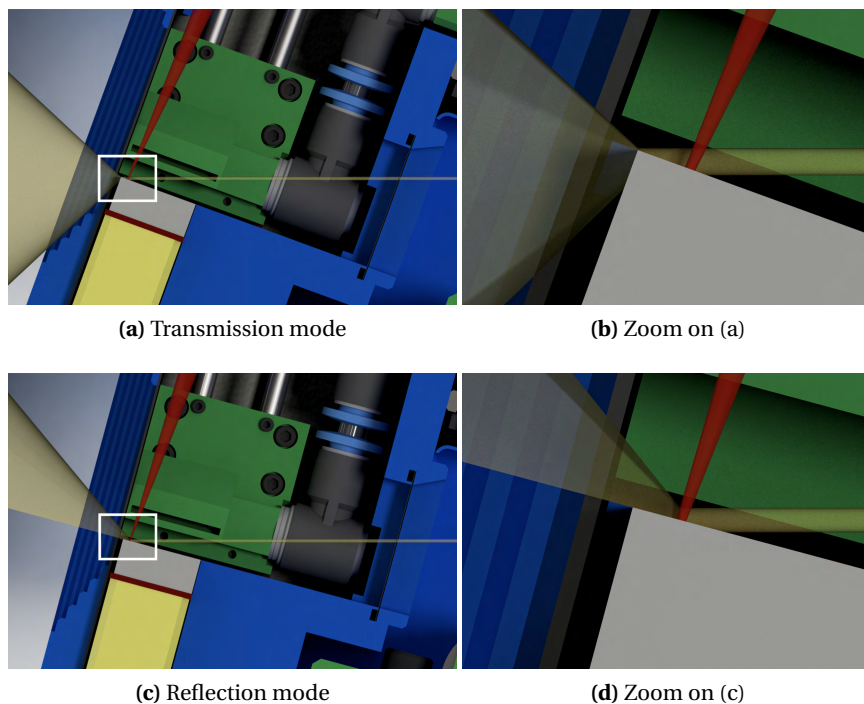
Figure 3.12 – 3D rendered cross section of the machine, illustrating the configuration for transmission (a,b) and reflection (c,d) mode. The X-ray beam (yellow) enters the printing chamber through the entrance window on the right side of the image. It then reaches the build plate (grey) where the laser beam (red) is scanning, and diffracts. The X-ray beam exits through the other window, on the left side.

Figure 3.13 show a 3D representation of an *operando* measurement in reflection mode. The X-ray beam (yellow) enters the machine at the back and diffracts on the build plate. The laser beam (red) enters the machine at the top of the chamber and scans the build plate to selectively fuse the powder particles together. The detector, in front of the machine, collects the 2D diffraction patterns with acquisition rates up to 22kHz acquisition rate. An illustrative video of the process is available at this link: https://youtu.be/qi42D3JiJN4.

To position correctly the X-ray beam on the sample, multiple diode scans are necessary. A diode is an X-ray detector that generates a voltage proportional to the flux of the X-ray beam. The diode is placed along the path of the direct beam, behind the MiniSLM device. Edges can be detected by moving the device relative to X-ray beam and monitoring voltage drops on the diode, indicative for the presence of material that lowers the transmission of the direct beam.
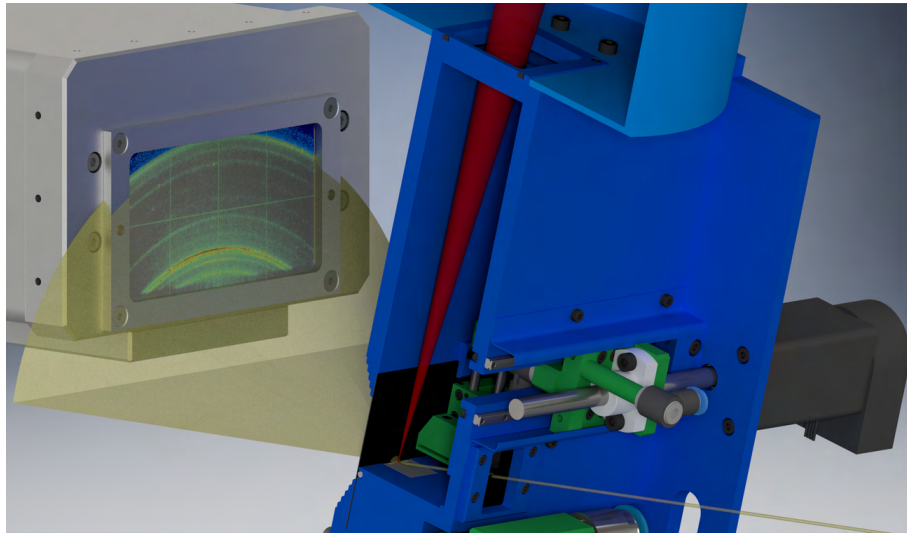
Figure 3.13 – Diffraction geometry during *operando* measurement

Figure 3.14a is a 3D rendering of the MiniSLM in diffraction position, and figure 3.14 a zoom on the X-ray entrance window. The glassy carbon windows have been made transparent in order to see what is happening inside the printing chamber. Once it is known that the X-ray beam is going through the window, a vertical scan is done to find the outer edge of the build plate, near the exit window (figure 3.14b - 1). Subsequently, the X-ray beam is positioned on the sample in order to cut the signal on the diode (as in figure 3.14b). An horizontal scan is performed to find the clearance gaps between the build plate and the frame of the machine (figure 3.14b - 2). This gap corresponds to the maximum of the voltage curve on the diode. Once the positions of build plate edge and the gaps are known, the X-ray beam can be positioned on the build plate for diffraction experiments.

(a) Tilted MiniSLM

(b) Zoom on the back window
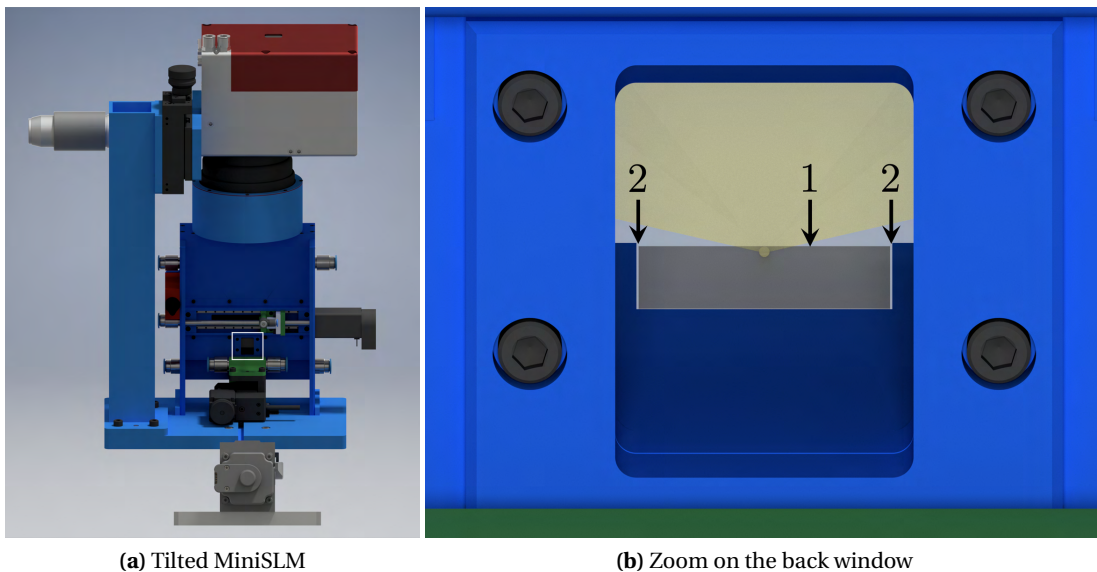
Figure 3.14 – View of the MiniSLM along the X-ray beam direction

3.3.2 MicroXAS beamline setup
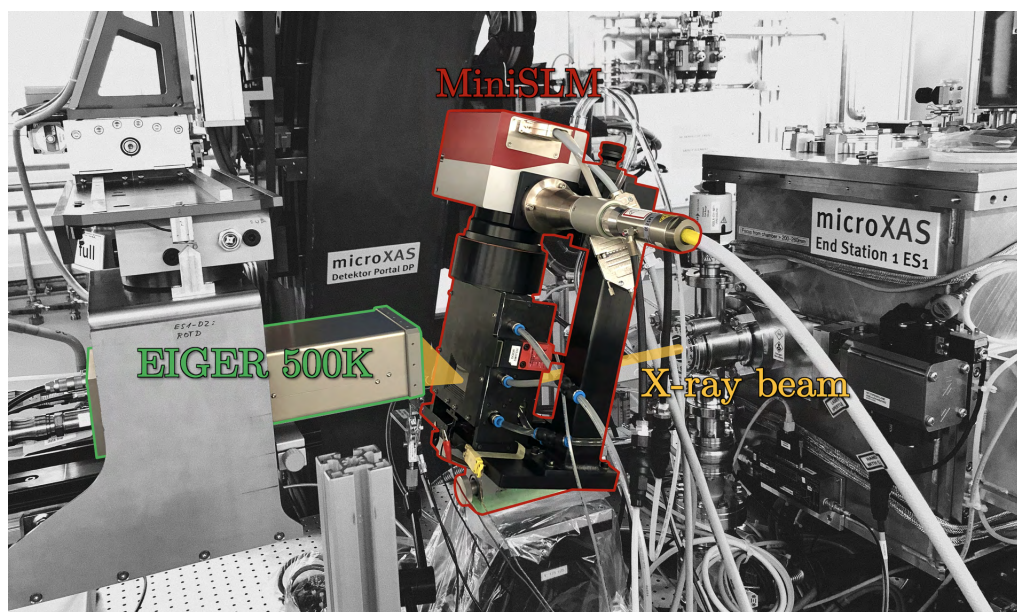
Figure 3.15 – MiniSLM machine mounted at the MicroXAS beamline

The MiniSLM was mounted at experimental station 2 on a heavy manipulator able to move the machine along the direction of the X-ray beam (Z-direction), vertical (Y-direction) and horizontal, perpendicular to the X-ray beam (X-direction). The X-ray detector was placed in front of the machine to capture the diffraction pattern, as illustrated in figure 3.15. The other components were placed on the experiment table, around the heavy manipulator. The rack containing the laser and the chiller was placed on the other side of the experiment station, highlighted in blue in figure 3.16.
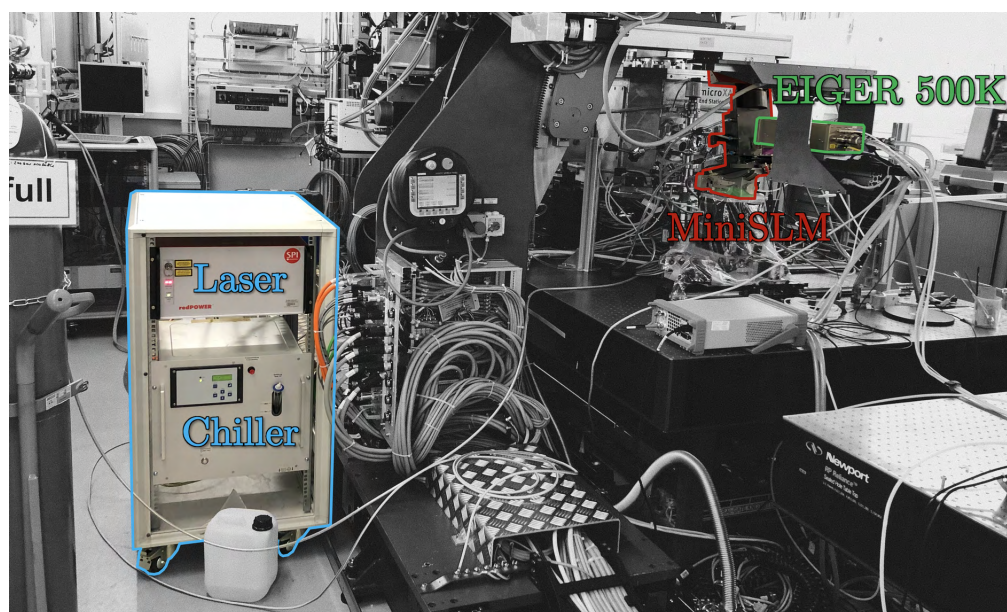
Figure 3.16 – Laser and chiller position at the MicroXAS beamline

The detector is a crucial component for *operando* measurements. During SLM processing the local microstructure changes very fast because of high laser scanning speeds (of the order of 1 m/s) and high heating/cooling rates (up to 10^6 K/s). In order to capture these phenomena a fast X-ray detector with sub-millisecond time resolution is crucial. This, in turn, requires an X-ray beam with high brilliance, in order to acquire diffraction spectra with sufficient statistics in each single frame. Furthermore, the background noise needs to be kept as low as possible. This can be achieved by X-ray detectors with energy threshold. X-ray detectors that work at very high frame rates usually have limited storage capacity. It is therefore important to properly synchronise the detector with the laser operation.

For the experiments reported in this work an in-house developed EIGER 500K detector [101] was used. It is an ultra-fast single photon counting hybrid detector with maximum storage capacity of 30'000 frames in 4-bit mode. The detection module has an area of approximately 8 x 4 cm^2 and contains 500'000 pixels, each with a size of 75 x 75 μm^2. The detector was operated at a frame rate of 20 kHz. The exposure time of a single frame was 45 μs. This detector is highlighted in green in figures 3.15 and 3.16.

3.3.3 MS beamline setup

The MiniSLM was mounted on an experiment table able to move in the XYZ directions of the beamline, the Z-positive direction being the outgoing direction of the X-ray beam, and the Y-positive direction being the vertical direction going up. The X-ray detector was placed in front of the machine to capture the diffraction pattern, as illustrated in figure 3.17. The other components were placed on the experiment table and around it. The detector used at the MS beamline is the same in-house developed EIGER 500K detector as reported in the previous section.
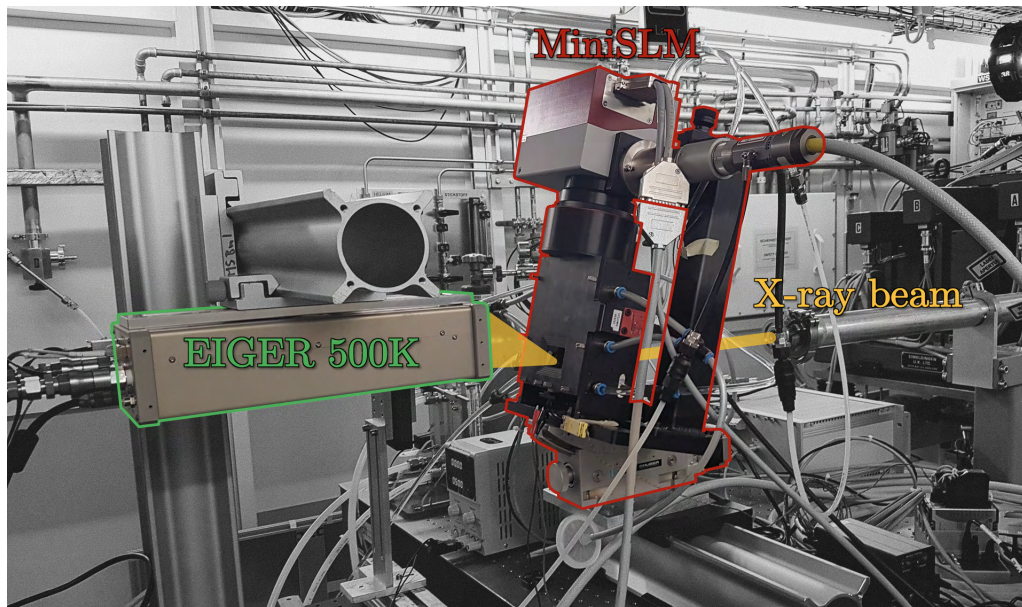
Figure 3.17 – MiniSLM machine mounted at the MS beamline

3.4   XRD principle and data analysis

3.4.1   XRD principle

This section is written based on the book of Cullity and Stock, *Elements of X-Ray Diffraction* [102]. The concept of the X-Ray Diffraction (XRD) will be explained here as an introduction for the X-ray data acquisition and analysis in the following parts. Firstly, the influence of path change on electromagnetic waves will be introduced, which is fundamental to understand the XRD phenomenon. Then the XRD geometry on a crystal lattice will be presented, and the Bragg law derived from it. Finally, synchrotron powder diffraction will be presented.

Influence of the path change on X-ray waves

X-rays are electromagnetic waves belonging to the high energy part of the light spectrum, after ultraviolet rays. Usually, X-rays used for diffraction have a wavelength within the range 0.5-2.5Å. The short wavelength is what allow X-rays to diffract when going through a crystal lattice.

The phenomenon of diffraction is essentially due to the way electromagnetic waves interact with each other. Let us consider an X-ray beam travelling from the left to the right direction, as in figure 3.18. Electromagnetic waves are polarised in both vertical and horizontal directions, perpendicular to their propagation direction. However, let us consider that waves are polarised only within the plane of the figure for the sake of simplicity.
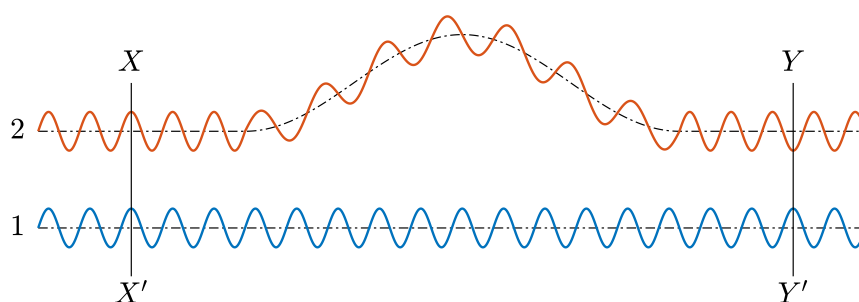
Figure 3.18 – Influence of path change on the phase of an electromagnetic wave

Two rays are compared in figure 3.18, the ray n°1 which propagates along a straight direction and the ray n°2 which experiences a path change. Before the change of path, the two rays are in phase as shown by the propagation front (XX'). However because the ray n°2 does not follow a linear trajectory, its phase changes compared to the ray n°1. If the path change is sufficient, the two rays become out of phase and their amplitudes oppose each other, as shown by the new propagation front (YY').

Diffraction geometry on a crystal lattice

Now let us consider a perfectly monochromatic X-ray beam of wavelength λ, composed of several parallel waves with a propagation from the left to right on figure 3.19. These waves are in phase, as shown by the propagation front (XX'), and interact with a crystal lattice at an incident angle θ, which is called the Bragg angle. The atoms are represented by black circles, and the atomic planes are separated by their inter-atomic

distance d. This distance d is of the same order of magnitude as the X-ray wavelength. The electromagnetic waves are scattered by the electron cloud around the atoms when reaching the atomic planes. Each atom subsequently becomes a point source of diffracted X-ray waves and the scattering phenomenon is happening in all directions. For the convenience of the illustration, only the waves with a scattering angle equal to the Bragg angle will be represented
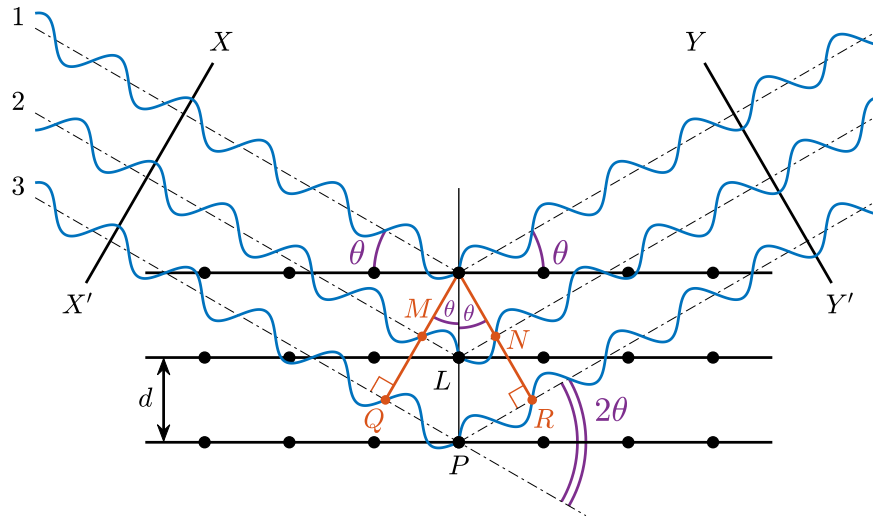
Figure 3.19 – X-ray diffraction geometry on a crystal lattice

Let's first consider the waves n°1 and n°2. The path difference between these two waves is equal to:

$$ML + LN = d\sin\theta + d\sin\theta = 2d\sin\theta \tag{3.1}$$

Similarly, the path difference between the waves n°1 and n°3 is equal to:

$$QP + PR = 2d\sin\theta + 2d\sin\theta = 4d\sin\theta \tag{3.2}$$

Now let us assume that the scattering phenomenon is happening for an infinity of waves. As a result, they must all be in phase after diffracting on the crystal lattice as shown by the second wave propagation front (YY') in order to exist. If this condition is not respected, for each diffracting wave there will always be at least another one out phase leading to an extinction of the signal as explained in the previous paragraph.

Going back to figure 3.19, this means that the path difference between two waves has to be a multiple integer of the wavelength. Thus equations 3.1 and 3.2 become:

$$k\lambda = 2d\sin\theta$$
$$k\lambda = 4d\sin\theta \tag{3.3}$$

Since k=1,2,3,... the two equations above are actually equal to each other, which allows to derive the Bragg law for diffraction:

$$n\lambda = 2d\sin\theta \tag{3.4}$$

Diffraction is only possible if the Bragg law is respected.

Synchrotron XRD principle

In synchrotron XRD when a single crystal is put inside the X-ray beam, diffraction occurs following the Bragg law (equation 3.4) as illustrated in figure 3.20a. All the atomic planes respecting the Bragg law are in diffraction condition and a spotty pattern can be visualised when an X-ray detector is place behind the sample. Such a diffraction pattern is called a Laue diffraction pattern. Each spot corresponds to a specific inter-atomic plane, and the angle between the direct X-ray beam and each diffracted beam is equal to 2θ as represented in the figure 3.19.

(a) Laue diffraction   **(b)** powder diffraction
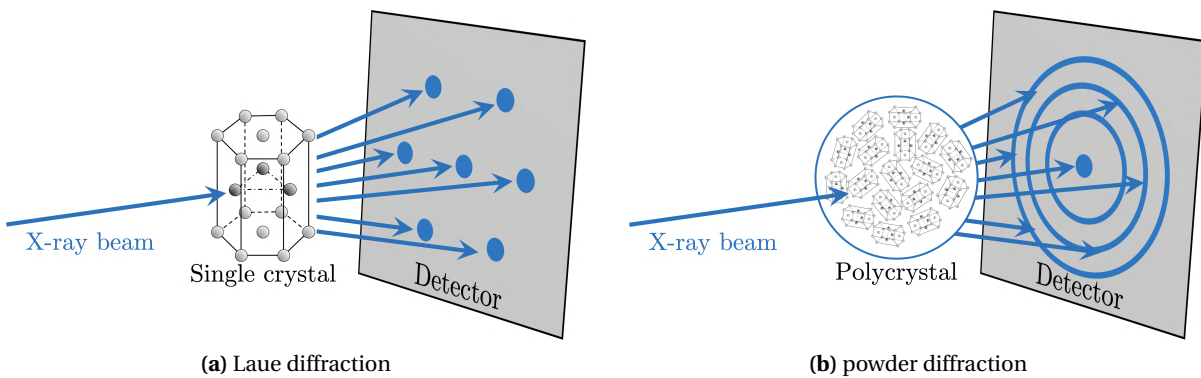
Figure 3.20 – X-ray diffraction geometry on a single crystal (Laue) and polycrystalline sample (powder).

When a polycrystalline sample is measured in the same way, it actually contains a multitude of single crystals oriented in different direction. Figure 3.20b illustrates what happens when a polycrystalline sample is studied with XRD. This time, rings are actually observed instead of spots. The fact that the crystals inside the sample are oriented differently rotates the Laue diffraction pattern around the direct beam for each crystal, resulting in rings for each inter-atomic plane family. Such a diffraction pattern is called a powder diffraction pattern. In the rest of this thesis, only powder diffraction experiments will be performed.

3.4.2 X-ray data acquisition
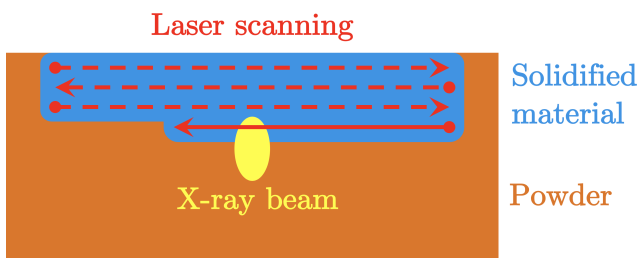
Figure 3.21 – Schematic of the experimental setup, the dashed lines represent the previous tracks scanned by the laser beam

Figure 3.21 sketches a top view of the experimental setup showing the combination of laser scanning and X-ray beam on the sample. The substrate, a commercially available Ti-6Al-4V alloy, is covered with a 30 layer of Ti-6Al-4V ELI (extra low interstitial, grade 23) gas atomised powder (orange). The laser beam (red) is scanning the sample along the horizontal direction using a conventional bi-directional strategy. The laser starts scanning at the top left corner, and the scanning vectors are separated by the desired hatch distance.

The powder melts upon arrival of the laser and solidifies into a dense material (blue) when the laser has passed. A gaussian X-ray beam is focused on the sample with an incidence angle, which results in the

projected and elongated illuminated area (yellow). This X-ray beam will capture the phase transformation of the material while the laser beam gets closer and then further away during scanning.

3.4.3 X-ray data analysis

During *operando* measurements, the collected images consist of 2D diffraction ring patterns. Each of these images was converted into a 1D diffraction pattern using the software Bubble [103]. This package is based on pyFAI, a well-established python library for fast powder integration [104]. Figure 3.22 shows an example of a 2D pattern and the resulting 1D pattern after azimuthal intergration.

(a) 2D XRD pattern on the EIGER 500K detector **(b)** 1D XRD pattern after azimuthal integration
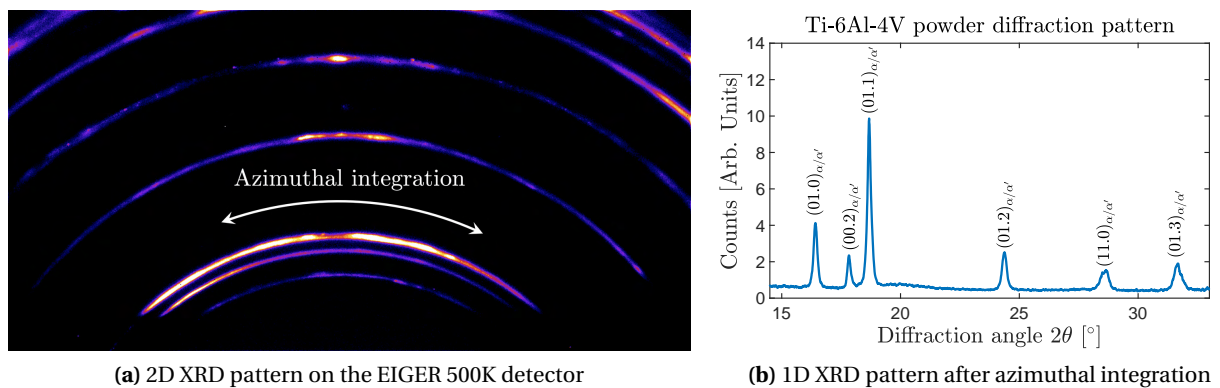
Figure 3.22 – Example of XRD pattern integration on the Ti-6Al-4V powder

Each of these 1D pattern is then stacked over time to reconstruct the phase evolution during an *operando* measurement. This is done using Matlab. Figure 3.23a shows a typical result after stacking of all the diffraction patterns on Matlab over the acquisition time. The X-axis corresponds to the 2θ diffraction angle, the Y-axis corresponds to the acquisition time and the outer axis to the peak intensity.

This sample corresponds to a bidirectional scanning of a 4x1 mm^2 area with a scanning vector length of 4 mm. The printing parameters for figure 3.23 are listed in table 3.3.

Table 3.3 – Printing parameters corresponding to figure 3.23

Laser power [W]	Scanning velocity [mm/s]	Hatch distance [μm]	Layer thickness [μm]
200	400	40	30

In the first part of the acquisition time, before 22 ms, the diffraction pattern corresponds to the α/α′ phases of the Ti-6Al-4V powder. The notation α/α′ will be used in this thesis as it is not possible to differentiate the two phases. At around t = 22 ms one can observe the first presence of the laser scanning the sample, with the appearance of the β phase after partial melting of the volume probed by the X-ray beam. When the laser beam has passed the X-ray probed volume, this β phase undergoes cooling which can be seen by the shift of the peak position toward higher angle value until it disappears. At this instant, the α/α′ phase reappears.
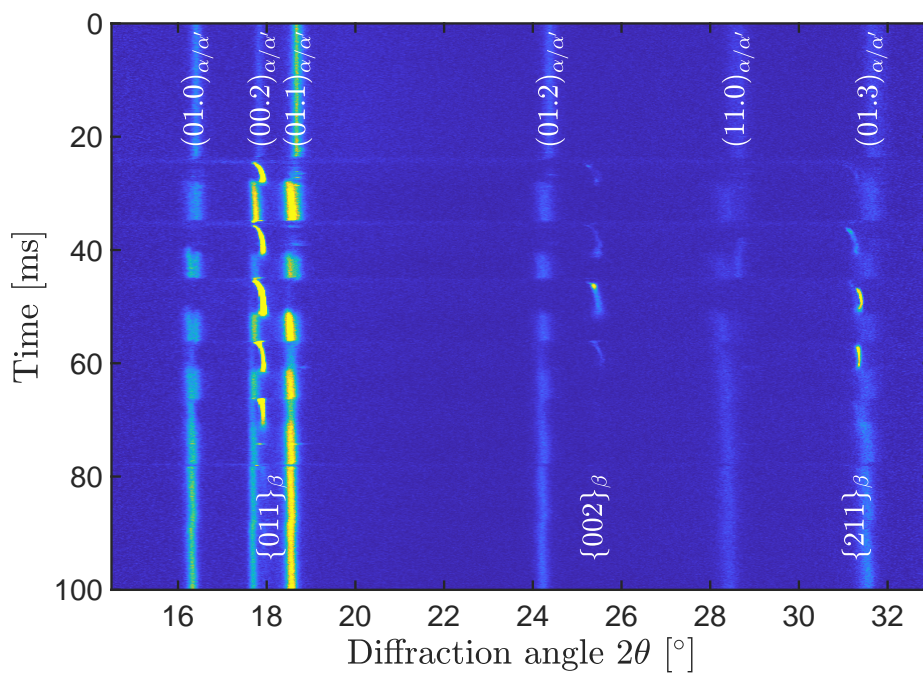
Figure 3.23 – Ti-6Al-4V phase evolution during *operando* XRD experiment

During this time, the laser keeps travelling. It takes 5 ms to the laser to travel to the edge, and turn around to print the next vector.
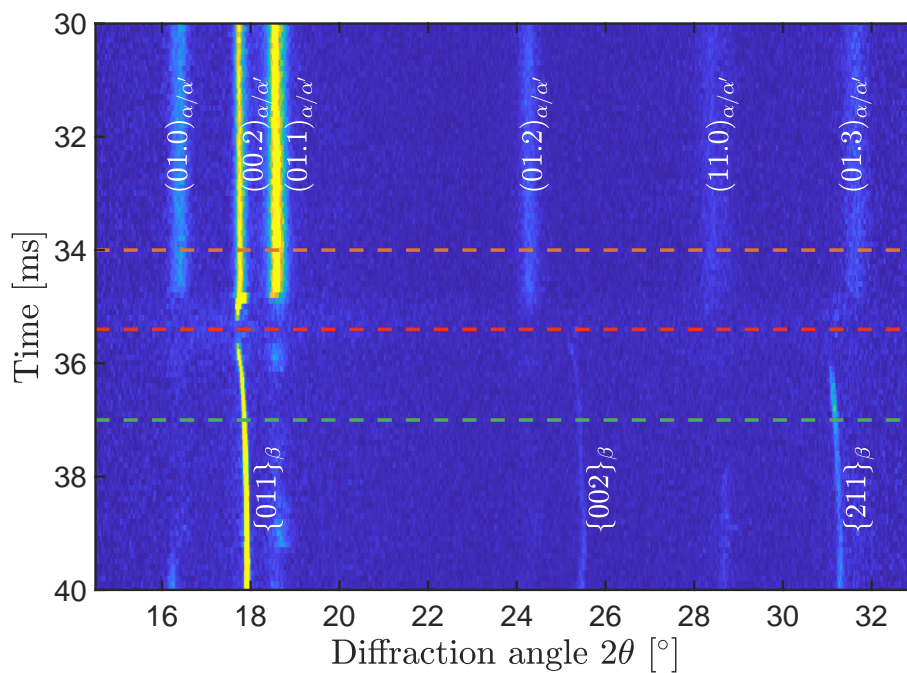
Figure 3.24 – Zoom between 30 ms and 40 on figure 3.23

The following scanning cycle is shown in detail in figure 3.24, which is a zoom of figure 3.23 between 30 ms and 40 ms. Figure 3.25 illustrates the situation in figure 3.24 step by step, with the corresponding colour code. For this cycle, the laser is overlapping with the area illuminated by the X-ray beam. One can observe the interaction of the melt pool with the probed volume with the disappearance of the the peak intensities, marked by the red dashed line. Then β will form from the melt, until it cools down and the α/α' form again. This cycling will be observed until the laser beam becomes too far from the X-ray probed area and its effect cannot be seen anymore.

(a) Position of the melt pool compare to the X-ray beam   **(b)** Corresponding XRD patterns obtained from figure 3.23b
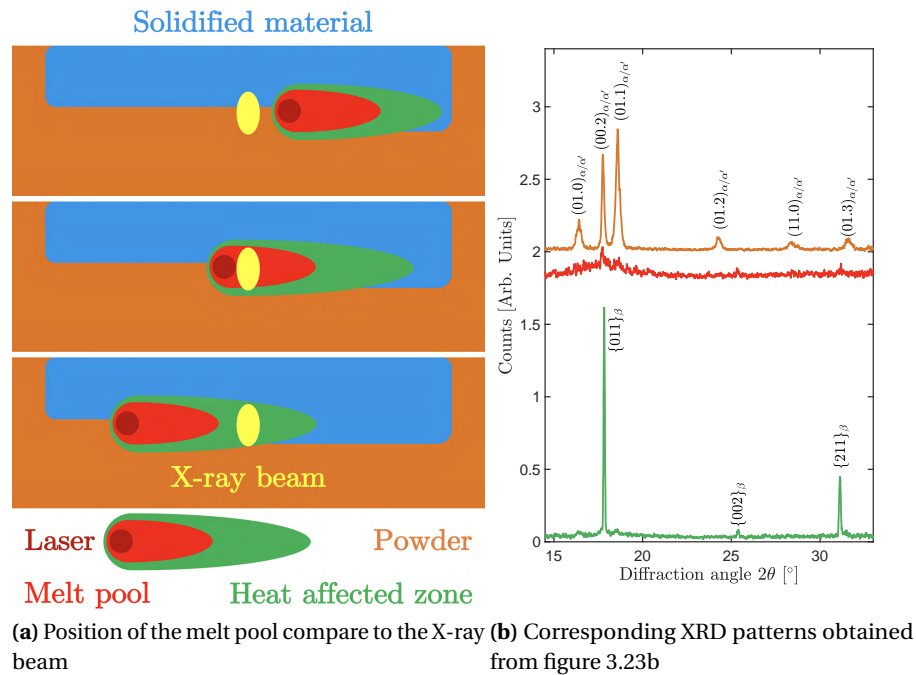
Figure 3.25 – Schematics of the melt pool crossing the X-ray beam, and corresponding XRD patterns extracted from figure 3.23b. The colour of the diffraction pattern corresponds to the phase interacting with the X-ray beam: α/α' in orange, β in green and liquid in red.

In principle, the diffraction peaks can be analysed by single peak fitting, which provides values for integrated intensity, peak position and width. However, because of texture formation, phase transformation or limited grain sample statistics, the intensity of the diffraction peaks is not always sufficient to perform reliable peak fitting. In that case, the first and second moment of the peaks are calculated, from which the centre of mass and variance are obtained as described in [105].

The equation of the centre of mass if given by:

$$< 2\theta > = \frac{\int 2\theta . \mathrm{I}(2\theta) d(2\theta)}{\int \mathrm{I}(2\theta) d(2\theta)} \tag{3.5}$$

with 2θ the diffraction angle and I(2θ) the peak intensity Following that, the variance can be determined with the following equation:

$$w(2\theta) = \frac{\int (2\theta - < 2\theta >^2) . \mathrm{I}(2\theta) d(2\theta)}{\int \mathrm{I}(2\theta) d(2\theta)} \tag{3.6}$$

Assuming that the diffraction peak has a Gaussian shape, the full-width at half-maximum (FWHM) of the peak can be determined as [106]:

$$\text{FWHM} = 2\sqrt{2\ln 2}\sigma \approx 2.355\sigma \tag{3.7}$$

with $\sigma = \sqrt{w(2\theta)}$ the standard deviation of the peak intensity distribution This value can then be used to determine the integrated intensity of the peak by summing the intensity values within a range corresponding to twice the FWHM value around the centre of mass of the peak. For a Gaussian distribution, this range corresponds to 98.15% of the total peak intensity.

To give a simple example for this method, the analysis has been done on a 1D XRD pattern of the α/α' phase shown in figure 3.25b. Figure 3.26 shows the diffraction pattern with the centre of mass of each peak representing the peak position, indicated by the red marker and the range corresponding to twice the FWHM indicated by the black markers.
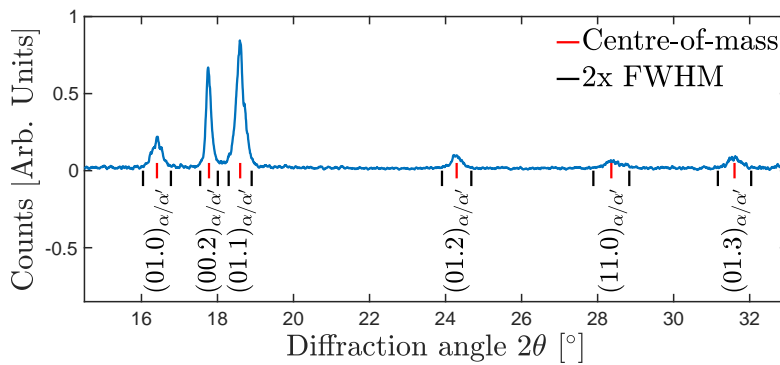
Figure 3.26 – Data analysis for a 1D XRD pattern

A Matlab routine was written to automatically perform such an analysis for selected diffraction peaks of all diffraction patterns corresponding to one exposure. During printing of one layer, typically 20'000 images are accumulated with a frame rate of 20kHz, corresponding to 1s exposure. The method of the centre of mass has the advantage to be able to analyse the data so quickly that it can be used during experiments at the beamline just after one *operando* XRD acquisition to adjust the measurement strategy for the next layer.

The data set presented in figure 3.23 was a good example to show the melt pool crossing the X-ray beam area, however it suffers from grain statistic issue, which means that not all the grains within the sample are in diffraction condition. As a result, no meaningful interpretation can be made on the results below since the data is not representative of the actual situation. For that reason, another set of data will be used to demonstrate the performances of the Matlab routine.

The new sample corresponds to a bidirectional scanning of an 8x2 mm^2 area with a scanning vector length of 8 mm. The printing parameters are listed in table 3.4.

Figure 3.27 shows an example of data analysis done on an XRD phase evolution pattern. The centre of mass is represented in red, and range correspond to twice the FWHM around the centre of mass in white over which the sum of the peak intensities is performed. Additionally, a sum over the background of the diffraction pattern is realised in order to analyse the diffuse scattering which is increasing during the laser scanning.

Table 3.4 – Sample parameters corresponding to figure 3.27

Laser power [W]	Scanning velocity [mm/s]	Hatch distance [μm]	Layer thickness [μm]
250	600	60	30

The diffuse scattering is due to a combination of thermal diffuse scattering and scattering from the melt pool. It is summed between 24.3° and 25.1° and between 27.3° and 34.2°, in the highlighted area.
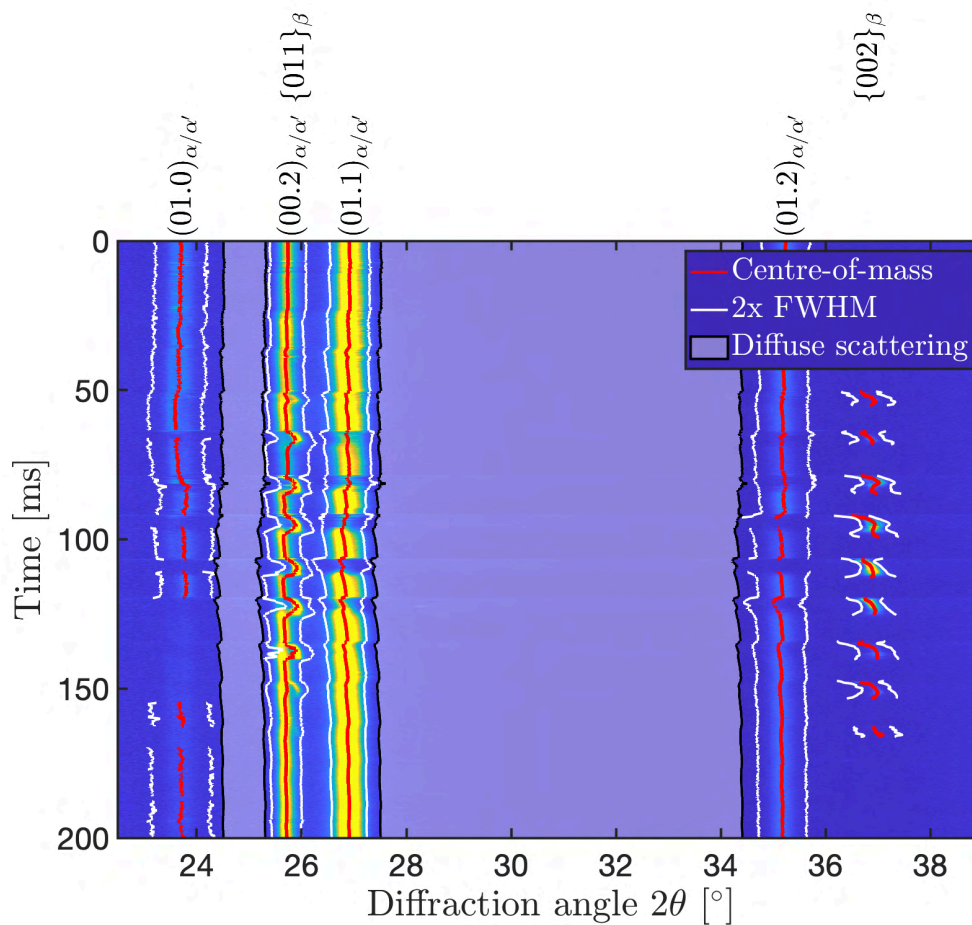
Figure 3.27 – Data analysis done over the XRD phase evolution presented in figure 3.23

The evolution of the integrated can be observed for selection of peaks to analyse the phase evolution during laser scanning. Figure 3.28 presents the integrated intensities of the $(01.1)_{\alpha/\alpha''}$ and $\{002\}_\beta$ reflections, and diffuse scattering from figure 3.27. The intensity of the diffuse scattering is strongly affected by thermal diffuse scattering and contributions from the liquid melt pool. The latter gives rise to a sharp increase in diffuse scattering that can be observed between the α phase disappearance and the β phase appearance.

53
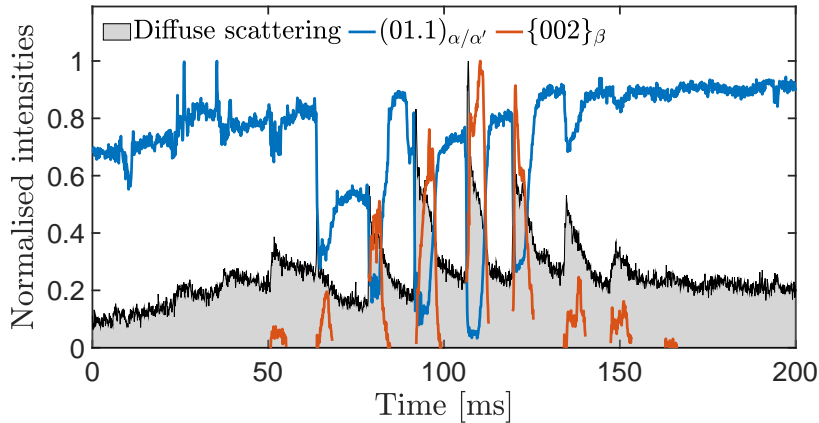
Figure 3.28 – Integrated intensities of the $(01.1)_{\alpha/\alpha''}$ and $\{002\}_\beta$ reflections, and diffuse scattering from figure 3.27

3.4.4 Temperature evolution from X-ray *operando* data

From the centre of mass data obtain in figure 3.27, it possible to compute the relative change of the peak position allows to calculate the elastic lattice strain ϵ of the crystal lattice as:

$$\epsilon = -cot\left(\frac{2\theta}{2}\right)\frac{2\theta - 2\theta_0}{2} \tag{3.8}$$

with 2θ the centre of mass of the peak and $2\theta_0$ a reference value here, taken at room temperature. Since the substrate is preheated to 340K before printing during experiments(measured with a thermocouple), the initial peak positions are slightly shifted from their room temperature values due to thermal expansion. The value of $2\theta_0$ in equation 3.8 was derived using the thermal expansion of Ti-6Al-4V (figure 3.11, below). The corresponding initial strain values at 340K corresponds then $\epsilon(t = 0) = 4.9 * 10^{-4}$.

Assuming that the lattice strain is mainly influenced by thermal effects, the average temperature T in the illuminated volume can be determined by:

$$T = \frac{\epsilon}{\alpha_L(T)} \tag{3.9}$$

with $\alpha_L(T)$ the temperature-dependent linear thermal expansion coefficient.

For Ti-6Al-4V, we did not find values for $\alpha_L(T)$ for the complete temperature range from room temperature up to the melting point obtained by one measurement technique. Therefore, the values obtained from two references were combined. Touloukian reports on $\alpha_L(T)$ for temperatures up to 1100K based on the fitting on several datasets available in the literature [107]. Li et al. measured the volume expansion coefficient for Ti-6Al-4V around the melting point using electrostatic levitation measurements [108]. Assuming that Ti-6Al-4V behaves isotropically, this change in volume can be linked to the linear thermal expansion since:

$$\frac{\Delta V}{V} = 3\frac{\Delta L}{L} = 3\alpha_L\Delta T \tag{3.10}$$

Figure 3.29 shows the resulting linear thermal expansion coefficient after combination of both references.
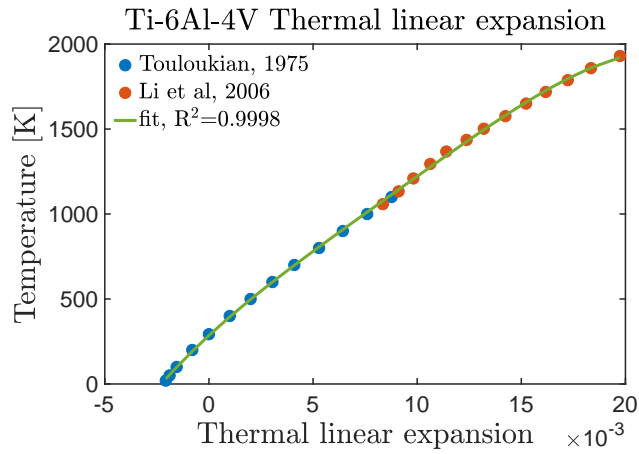
Figure 3.29 – Thermal linear expansion of Ti-6Al-4V as a function of temperature with data from [107, 108], fitted using a polynomial function

The equation of the polynomial curve obtained after fitting is:

$$T = -9.24 * 10^9 \left(\frac{\Delta L}{L}\right)^4 + 3.19 * 10^8 \left(\frac{\Delta L}{L}\right)^3 - 4.24 * 10^6 \left(\frac{\Delta L}{L}\right)^2 + 1.13 * 10^5 \frac{\Delta L}{L} + 285 \tag{3.11}$$

During the measurements reported in this work, the base plate was kept at a temperature of 340K. Therefore, the value of $2\theta_0$ in equation 3.8 was chosen such that the initial strain prior to printing $\epsilon(t=0)$ results in a temperature of 340K.
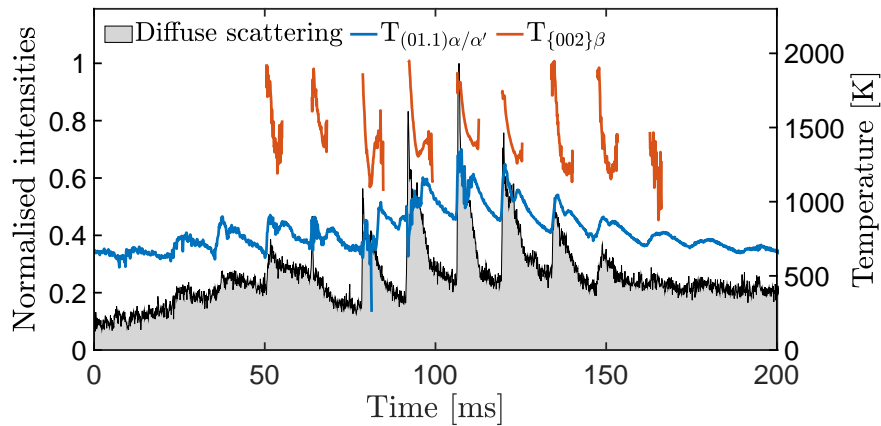
Figure 3.30 – Temperature profile derived from the $(01.1)_{\alpha/\alpha'}$ and $\{002\}_\beta$ centre of mass, and diffuse scattering in figure 3.27

Figure 3.30 shows the evolution of the temperature profile derived from the peak positions 2θ of the $(01.1)_{\alpha/\alpha'}$ and the $\{002\}_\beta$ reflections in figure 3.27, overlapped with the diffuse scattering. One can observe the sharp rise in the diffuse scattering matches well with the increase of temperature in the sample.

4 Results on Ti-6Al-4V

In this chapter, the best parameters for processing Ti-6Al-4V in the MiniSLM are presented for single track scanning. Then a porosity study was performed on 3D samples which yielded optimised printing parameters. Finally, *operando* experiments performed on the MiniSLM will be shown. The results of XRD experiments are given, which focus on the measurement configuration, the influence of the scanning vector length together with the temperature, and strain evolution in the sample. The influence of the X-ray beam size on the XRD measurements will also be shown. Lastly, images of the resulting microstructure will be displayed and related to the SLM process.

4.1   Ti-6Al-4V processing window

In SLM, many different parameter combinations can result in an acceptable laser melting result. The range of laser power (P) and scanning speed (v) chosen to produce well fabricated part or 3D structure are termed "processing window" in this thesis. The printing of different samples is the only way to determine the processing window of a material on the MiniSLM, and first trials are necessary to obtain samples of good quality for XRD experiments at the beamline. Determining the processing window for a given material starts by exploring previous literature, in order to narrow down the possibilities. Then samples are printed with a selection of parameter combinations aimed to discover which result in a high a low quality sample. Depending on the outcome, the processing window is defined. After many iterations, one should obtain samples of good density. Several parameters can directly influence the final quality of the printed part. Some of them are machine-dependent, and others can be fixed by the user. The one that are common to all the SLM systems are the laser power, scanning speed and strategy, hatch distance and layer thickness. The hatch distance is defined as being the space between two consecutive scanning vectors during laser scanning. Additionally, it is possible to adjust the laser spot diameter for the MiniSLM (figure 2.9).

Some authors refer to the energy density when discussing the processing window of an alloy during SLM [7, 13, 109]. The energy density is defined by:

$$E = \frac{P}{v * h * t} \tag{4.1}$$

where E is the energy density in J/mm^3, P is the laser power in units of W, v is the scanning speed in mm/s, t

the layer thickness in mm and h is the hatch distance in mm.

Since several different combinations of parameters can result in the same energy density value, it is not straight-forward to determine if they lie within the processing window. The approach taken here is to first fix the layer thickness at a value of 30 μm, according to the particle distribution of our Ti-6Al-4V powder [7, 109–113], and vary the laser power, scanning speed and hatch distance. An appropriate hatch distance, being the spacing between two consecutive scanning vector, is when the overlap is sufficient between the melted tracks to obtain a dense part. To determine this parameter, knowledge of the melt track width is necessary. However, it is necessary to first optimise the laser power and scanning speed by doing a single track study and working in the $P - v$ reference system [7, 8]. After selecting the parameters that give continuous and regular single tracks, the hatch distance can be determined. The terms "continuous" and "regular" are qualitative measures that will be detailed and presented below, along with photographs of single tracks as examples.

4.1.1 Single track scanning with 50 μm laser spot diameter

Based on the literature available [7, 31], several parameters combinations were selected with the laser power varying from 50W to 300W and the scanning speed from 100 mm/s to 1400mm/s. Since the build plate is only 12x12 mm^2, the tracks had to be printed in three different batches. Typical laser spot size being between 50 μm and 180 μm in commercial SLM systems [13], the MiniSLM laser spot size was initially chosen to be at 50 μm. The build plate material was made of commercialy available Ti-6Al-4V.

Table 4.1 – Parameter selection for the first batch of single tracks

Line	Power [W]	Speed [mm/s]	Line	Power [W]	Speed [mm/s]
1	50	400	2	50	600
3	50	800	4	50	1200
5	100	400	6	100	600
7	100	800	8	100	1200
9	125	400	10	125	600
11	125	800	12	125	1200
13	150	400	14	150	600
15	150	800	16	150	1200
17	175	400	18	175	600
19	175	800	20	175	1200
21	200	800	22	200	1200
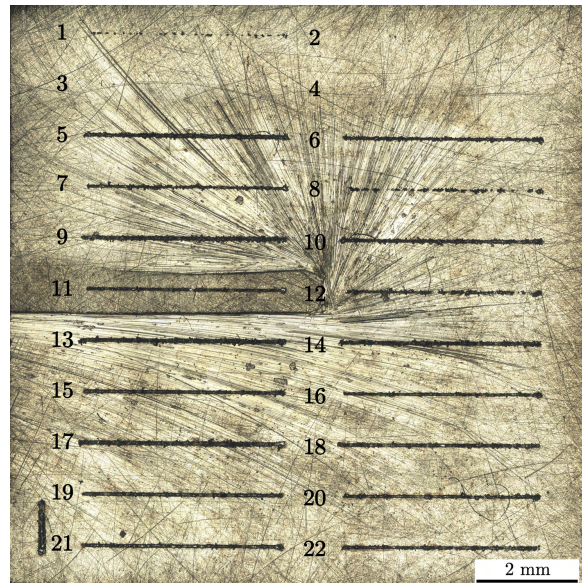
Figure 4.1 – First batch of printed single tracks.

Table 4.1 summarises the parameters used for the printing of the first batch of 22 tracks of 4 mm length. The laser power was selected between 50W and 200W, and the scanning speed between 400 mm/s and 1200 mm/s (figure 4.1). In order to cover a larger range or processing parameters, two other single track batches were made. The parameter selection for the second and third batches is presented in table 4.2. Figure 4.2 shows the results for the second batch (b) and the third batch (c) of single tracks.

Table 4.2 – Parameter selection of the second and third of single tracks

	(a) Second batch						(b) Third batch				
Line	Power [W]	Speed [mm/s]	Line	Power [W]	Speed [mm/s]	Line	Power [W]	Speed [mm/s]	Line	Power [W]	Speed [mm/s]
1	50	500	2	50	700	1	50	100	2	50	200
3	50	1000	4	50	1400	3	50	300	4	50	900
5	75	400	6	75	600	5	75	100	6	75	200
7	75	800	8	75	1200	7	75	300	8	75	900
9	100	500	10	100	700	9	100	100	10	100	200
11	100	1000	12	100	1400	11	100	300	12	100	900
13	125	500	14	125	700	13	125	100	14	125	200
15	125	1000	16	125	1400	15	125	300	16	125	900
17	150	500	18	150	700	17	150	100	18	150	200
19	150	1000	20	150	1400	19	150	300	20	150	900
21	175	500	22	175	700	21	175	100	22	175	200
23	175	1000	24	175	1400	23	175	300	24	175	900
25	200	500	26	200	700	25	200	400	26	200	600
27	200	1000	28	200	1400	27	200	900	28	200	1100
29	225	600	30	225	800	29	225	500	30	225	700
31	225	1000	32	225	1400	31	225	900	32	225	1200
33	250	600	34	250	800	33	250	500	34	250	700
35	250	1000	36	250	1400	35	250	900	36	250	1200
37	275	600	38	275	800	37	275	500	38	275	700
39	275	1000	40	275	1400	39	275	900	40	275	1200
41	300	1000	42	300	1400	41	300	800	42	300	1200
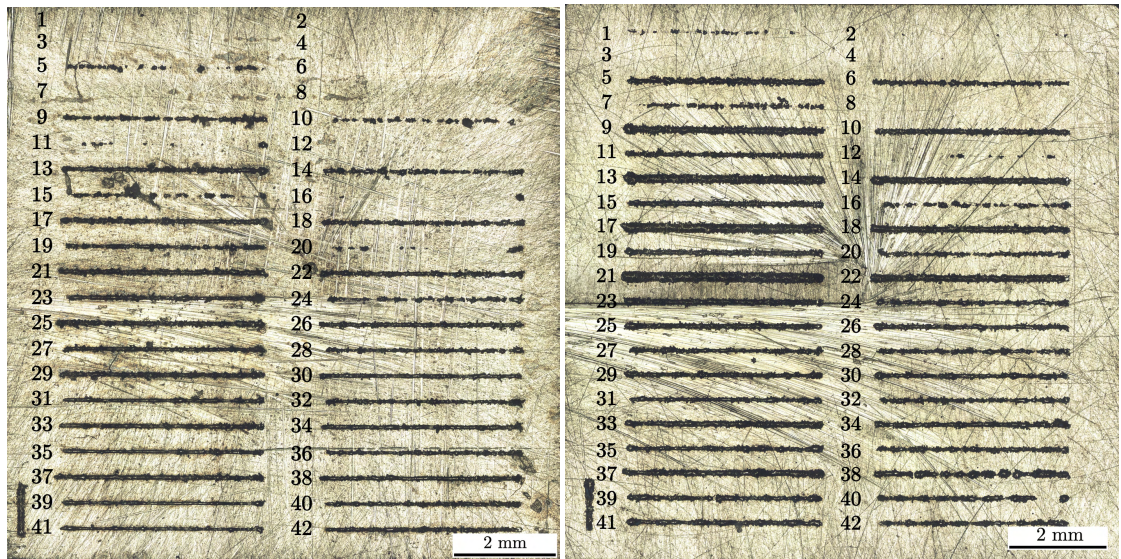
(a) Second batch

(b) Third batch

Figure 4.2 – Second and third batches of printed tracks

To visually inspect these tracks and assess their quality, the following criteria needed to be considered:

- Is the track continuous?
- Is the track regular?
- Does the track begin where the laser is turned on?
- Is the width of the track equal or larger than the laser spot diameter?

For each criterion, a value of 1 or 0 is attributed if the track respects it or not. A final score is given to each track with a maximum reachable quality factor of 4 points. Figure 4.3 illustrates example of different scenarios for the assessment of track quality. These tracks are reproduced from figure 4.1.

(a) Discontinous

(b) Regular/irregular
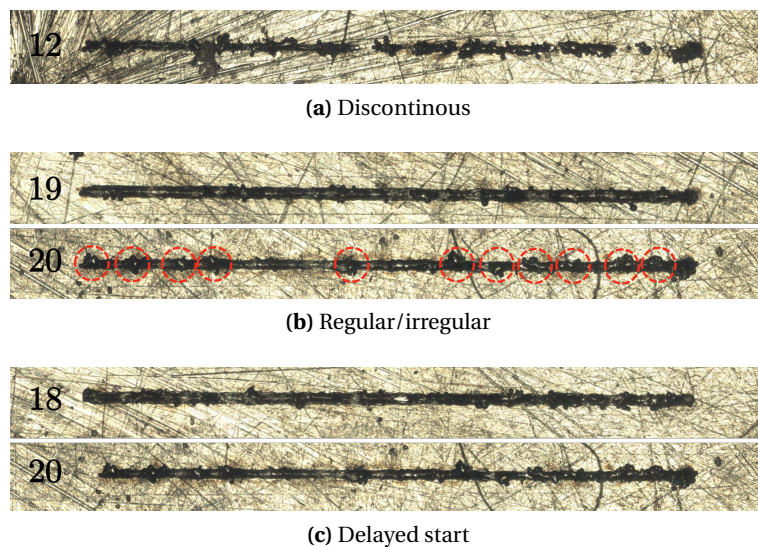
(c) Delayed start

Figure 4.3 – Example of discontinuous, regular and irregular tracks; and a delayed start (from figure 4.1)

For example, a track is considered continuous if there is no disruption along the melted area. Clearly, figure 4.3a shows track 12 is not continuous, and thus attributed the score of 0 for the continuity criterion. The regularity or irregularity was assessed by the number of balling events that occurred along the scanning length. Balling is the term used when a ball of molten material forms on the track because of the surface tension of the metal. It can happen when too much energy is transferred to the material creating a local coarsening of the melt pool until a ball appears (high laser power, low scanning speed). Balling can also happen when not enough energy is transmitted to the material and the melting of the powder is only partial, resulting with a discontinuous track (low laser power, high scanning speed) [114, 115]. Figure 4.3b illustrates the difference between what are considered a regular track (19) and an irregular track (20). A track is considered regular when few or small balling events are occurring along the melted track. On the contrary, a track is considered irregular when many large balling events are observed close to each other, as highlighted by the red circles on track 20, which has been been attributed a score of 0 for the regularity criterion.

A track can also have a delayed starting point. Figure 4.3c shows the difference between a track which starts where the laser is turned on (18) compared to a track that starts while the laser is already moving (20). In the second case, the track gets a score of 0 for the starting point criterion. This effect is observed when the scanning speed is high, which makes the absorbed laser energy too low to start the melting. Instead, the

beginning of the track is heated up until the temperature reaches the melting point. Finally, for the last criterion, the width of the track is compared with the laser diameter. If the width of the track is equal or larger to the laser spot diameter, the track gets a score of 1, which can be understood as enough energy is transmitted to the material.
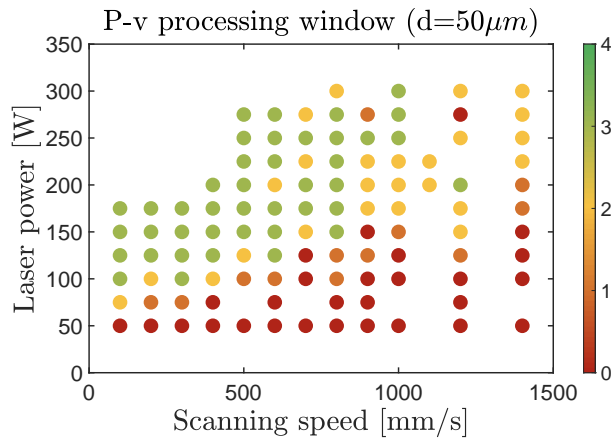
Figure 4.4 – $P - v$ diagram for a laser spot diameter of 50 μm. The colour bar represents the quality factor attributed to each track.

Figure 4.4 shows the $P - v$ processing window for this Ti-6Al-4V alloy with a laser spot diameter of 50 μm.The complete analysis can be found in tables B.1, B.2, B.3 in the appendices part. Two things can be observed in this diagram. First, good quality tracks can be found in the upper left side, while the bad tracks are located in the lower right corner. Second, there are no parameter combinations that obtains a score of 4 on the tracks made with the 50 μm laser spot diameter. This first result was helpful to determine a general trend toward selecting good parameters, however none was ideal to be considered part of the processing window. Based on these observations, two other batches were printed with laser spot diameters of 75 μm and 100 μm.

4.1.2 Single track scanning with 75 μm laser spot diameter

Table 4.3 – Parameter selection for the fourth batch of single tracks

Line	Power [W]	Speed [mm/s]	Line	Power [W]	Speed [mm/s]
1	125	200	2	125	400
3	125	600	4	125	800
5	150	200	6	150	400
7	150	600	8	150	800
9	175	200	10	175	400
11	175	600	12	175	800
13	200	200	14	200	400
15	200	600	16	200	800
17	225	200	18	225	400
19	225	600	20	225	800
21	250	200	22	250	400
23	250	600	24	250	800
25	275	200	26	275	400
27	275	600	28	275	800
29	300	200	30	300	400
31	300	600	32	300	800

The fourth batch of single tracks was made with a laser spot diameter of 75 μm. According to the $P - v$ diagram obtained in figure 4.4, the laser power was chosen between 125W and 300W and the scanning speed between 200 mm/s and 800 mm/s. A combination of 32 different parameter was selected, as shown in table 4.3.

The obtained tracks are presented in figure 4.5. They were observed and measure as done for the previous samples. The complete analysis can be found in table B.4 of the appendices part.

The corresponding $P - v$ graph is shown in figure 4.6. A clear separation of the data appeared, with a low quality factor for the high-speed regime. The tracks with a scanning speed of 400 mm/s or below seem to be promising and some attained a maximum of 4 for the quality factor.
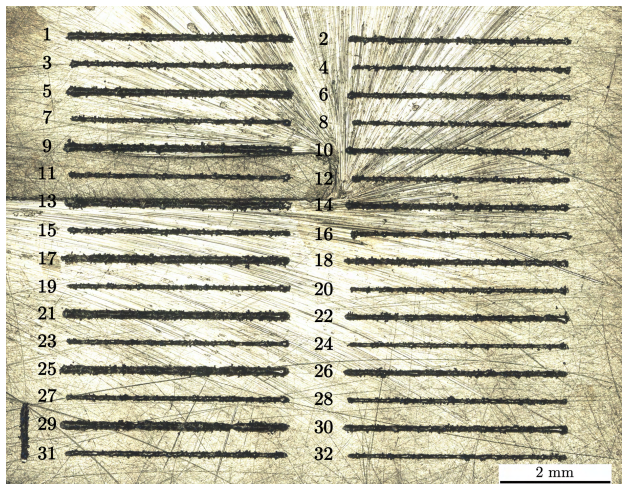
Figure 4.5 – Fourth batch of printed single tracks. The vertical line at the bottom left corner was made to know the sample orientation.
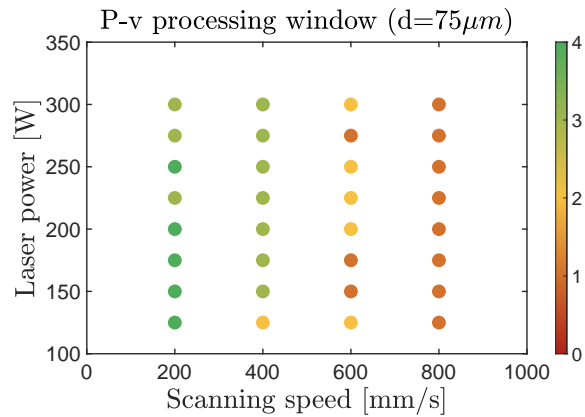
Figure 4.6 – $P-\nu$ diagram for a laser spot diameter of 75 µm. The colour bar represents the quality factor attributed to each track.

4.1.3   Single track scanning with 100 µm laser spot diameter

Finally, a fifth batch of tracks was made with a laser spot diameter of 100 µm. The same set of parameters displayed in table 4.3 was used for this sample preparation. The obtained tracks are presented in figure 4.7.

They were observed and measure as done for the previous samples. The complete quality assessment can be found in table B.5 in the appendices part. The corresponding $P-\nu$ graph is shown in figure 4.8. The parameter combinations in the upper portion of figure 4.8 have a good quality factor for a scanning speed of 400-600 mm/s. In this area, there is the highest density of a quality factors that score a value of 4. For this reason, it was decided that the laser spot diameter should remain at 100 µm for Ti-6Al-4V.
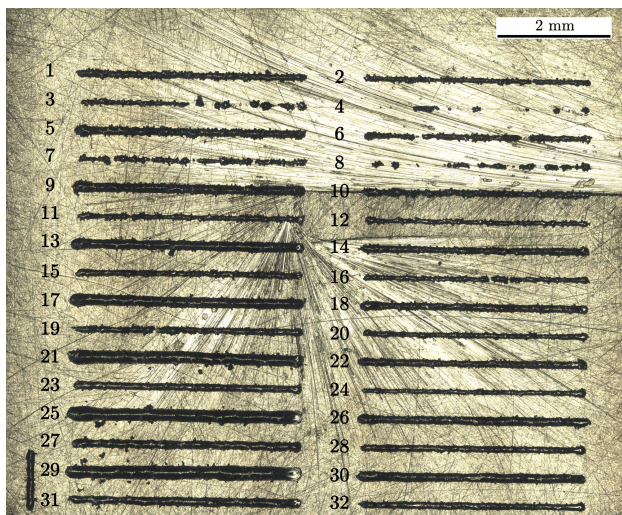
Figure 4.7 – Fifth batch of printed single tracks. The vertical line at the bottom left corner was made to know the sample orientation.
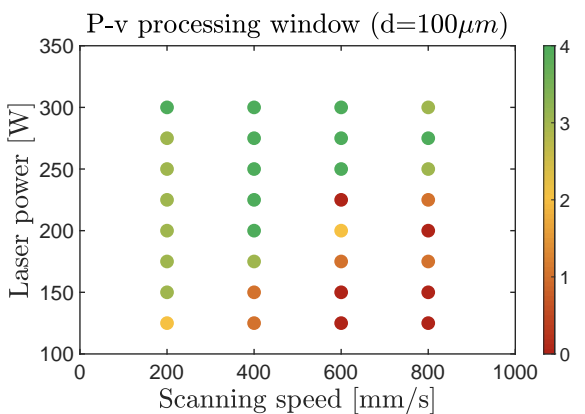
Figure 4.8 – $P-\nu$ diagram for a laser spot diameter of 100 µm. The colour bar represents the quality factor attributed to each track.

4.2 Sample porosity study

After optimising the $P - v$ processing window for Ti-6Al-4V, 3D samples were made in order to perform a density study. This section presents a first series of samples of which the density observations lead to the improvement of the recoating system. Then a second batch of sample was made to demonstrate the improvement in density.

4.2.1 First measurements

For this study, three scanning strategies were investigated to produce the most dense samples:

- Bidirectional: the laser beam raster scans each layer with the laser turning off at the end of each scanning vector (figure 4.9a)
- Bidirectional and 90° rotation: the laser beam raster scans one layer then scans the following layer with a scanning vector rotated 90° compared to the previous layer (figure 4.9b)
- Bidirectional crosshatch: the laser beam raster scans each layer twice, the second time being with the scanning vector rotated 90° compared to the first (figure 4.9c)

(a) Bidirectional

(b) Bidirectional and 90° rotation

(c) Bidirectional crosshatch
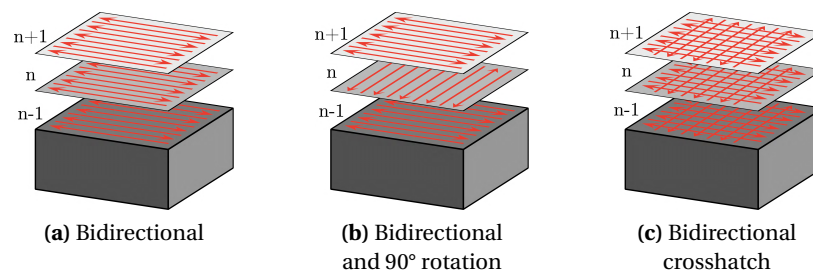
Figure 4.9 – Scanning strategies used for sample preparation

In total, 38 cubic samples with a volume of 4x4x4 mm^3 (figure 4.10a) were printed by selecting the laser power and scanning speeds within the optimised parameter range of figure 4.8. Details on the printing parameters are available in table B.6 in the appendices part. The sample density was measured using optical images of the cross-section along the build direction described in section 3.2. Figure 4.10b shows the results obtained after measurements.

(a) Printed cubic samples

(b) Optical density measurements
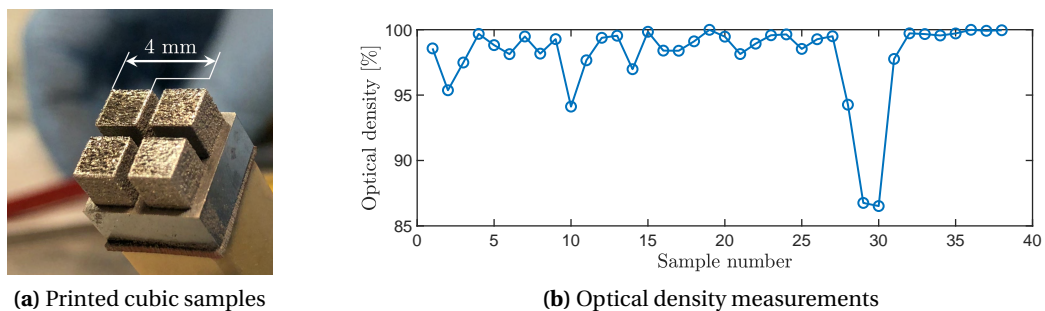
Figure 4.10 – Printed cubic samples and their optical density measurements

63

Figure 4.11a shows the obtained optical density results from figure 4.10b plotted against the sample energy density. The situation can be understood better by looking at samples 1 and 14 presented in figures 4.11b and c.

(a) Optical vs. Energy densities	**(b)** Sample 1	**(c)** Sample 14
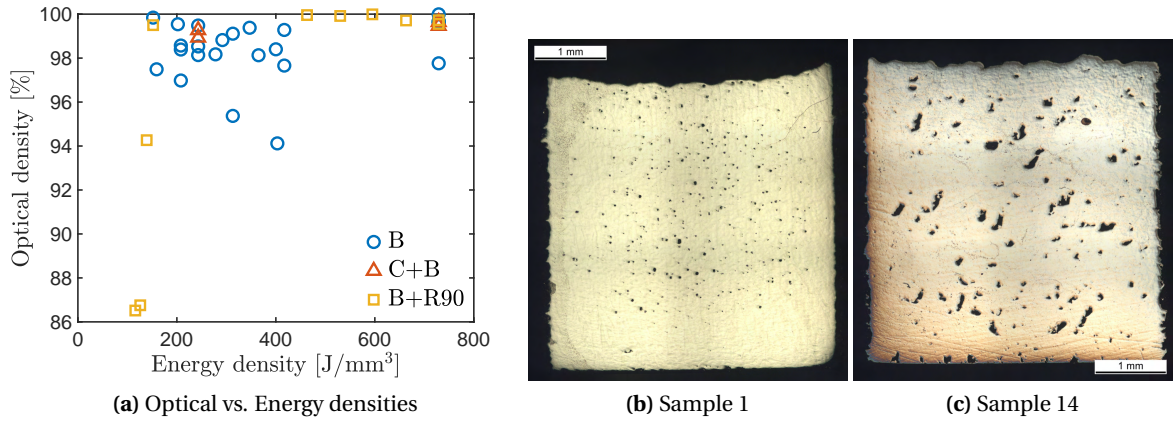
Figure 4.11 – (a) Optical vs. energy density (equation 4.1) for printing of the first batch from figure 4.10. B: Bidirectional scanning; C+B: Crosshatch + Bidirectional; B+R90: Bidirectional + 90° rotation; (b-c) selected samples 1 and 14

These samples were printed with the same parameters to investigate the process repeatability: a laser power of 150W, a scanning speed of 400 mm/s, a hatch distance of 60 µm, a layer thickness of 30 µm, and a bidirectional scanning strategy. However, sample 1 shows a density of 98.57% and sample 14 a density of 96.98%. Also, the cross-sections appear quite different as shown in figure 4.11b and c. With other words, the sample printing process is not reproducible. It has been reported that the compaction of the powder bed also plays a role in the final density of the printed sample in SLM processing [98]. After investigation of the powder deposition process, it turned out the recoater needed to be improved.

4.2.2 Sample printing with new recoater

(a) Printed cuboid samples	**(b)** Optical density measurements
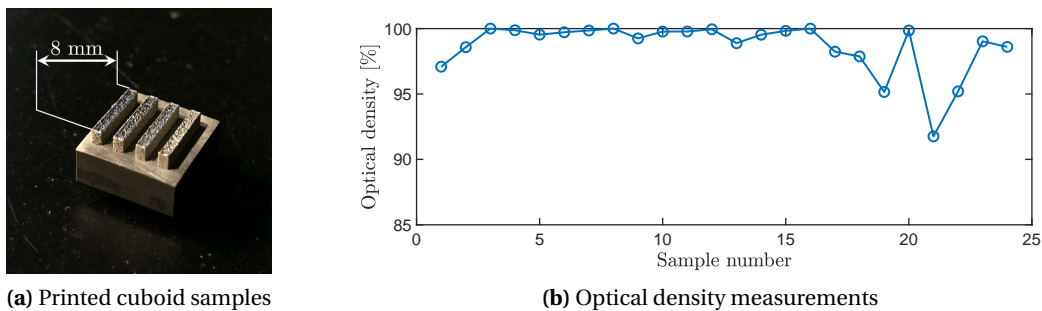
Figure 4.12 – Printed cuboid samples and their optical density measurements

A second set of 24 samples was printed with the new version of the recoater (see section 2.1.3). As before, the parameters were selected according to the processing window presented in figure 4.8. Details on the printing parameters are available in table B.7 in the appendices part. The samples have now a laser scanned

section of 8x1 mm^2, and a build height of 2 mm as shown in figure 4.12a. Such a dimension of the scanned area was selected to optimise printing with large scanning vector lengths, which will be used later in the *operando* measurements. To avoid additional variation in the printing parameters, the scanning strategy for all samples was selected as bidirectional with a 90° rotation between each layer (figure 4.9b).
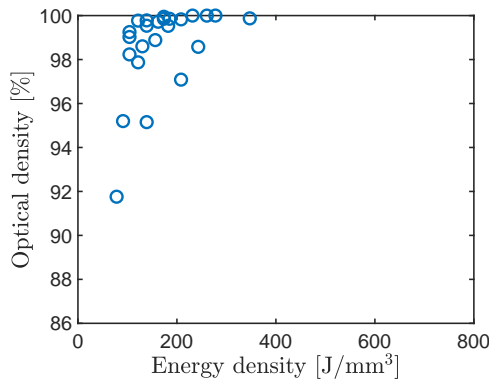
Figure 4.13 – Sample density compared to energy density (equation 4.1) for the printing of the second batch (figure 4.12).

The optical density of each sample was measured on a cross-section perpendicular to the building direction. This was obtained by polishing all the samples attached to the build plate at once (figure 4.12a). The results are displayed in figure 4.12b. This batch of samples shows higher density values than the one made with the old recoater (figure 4.10).

When comparing the obtained sample optical density against the sample energy density (equation 4.1) as shown by figure 4.13, the scattering of the data is similar to the results obtained previously in 4.11. However, the range of the observed optical density has largely reduced, with a minimum relative density increasing from 86% up to 92%.

4.3 *Operando* measurement for Ti-6Al-4V

4.3.1 Transmission vs. reflection mode

This experiment was realised at the MicroXAS beamline of PSI to compare the influence of the measurement configuration on the acquired XRD data. To perform the measurements in both transmission and reflection modes, the X-ray beam energy was chosen at 17.2 keV. This allows transmission trough the edge of the build plate as illustrated by figure 3.12b. The selected X-ray beam size was 30 x 12 μm^2 (horizontal x vertical) at Full-Width at Half-Maximum (FWHM). The scanned area for each layer was 4 x 1 mm^2 in a bi-directional fashion. During *operando* XRD, 8'000 diffraction patterns were acquired at a 20 kHz acquisition rate.

Table 4.4 – Sample parameter table

Laser power [W]	Scanning velocity [mm/s]	Hatch distance [μm]	Layer thickness [μm]
200	400	25	50

Table 4.4 shows the parameter set used for this measurement. A layer thickness of 50 μm was selected to compensate for the small hatch distance in the resulting energy density (equation 4.1). The machine was tilted at 20° for transmission measurement in order to go as deep as possible in the sample while minimising the attenuation length. This gives a projected X-ray beam size of 30 x 35 μm^2 at FWHM. For the reflection measurements, the machine was tilted at 15° in order to not cut the first diffraction peaks of the Ti-6Al-4V and the beam was placed at the centre of the scanned area, corresponding to 0.5 mm inside the sample from the edge. In reflection mode, the project X-ray beam size is 30 x 45 μm^2 at FWHM.
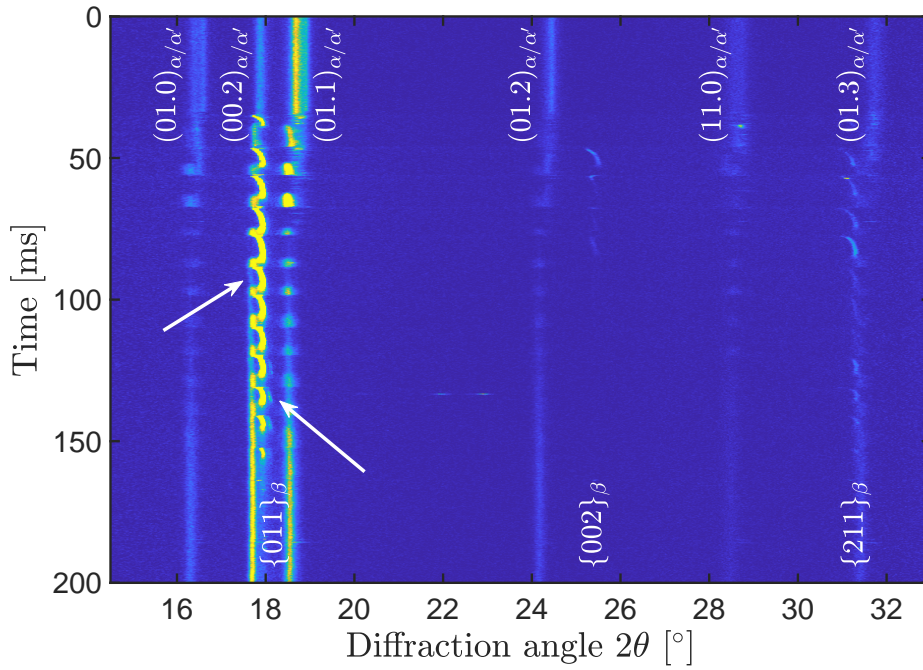
Figure 4.14 – XRD phase evolution in transmission mode
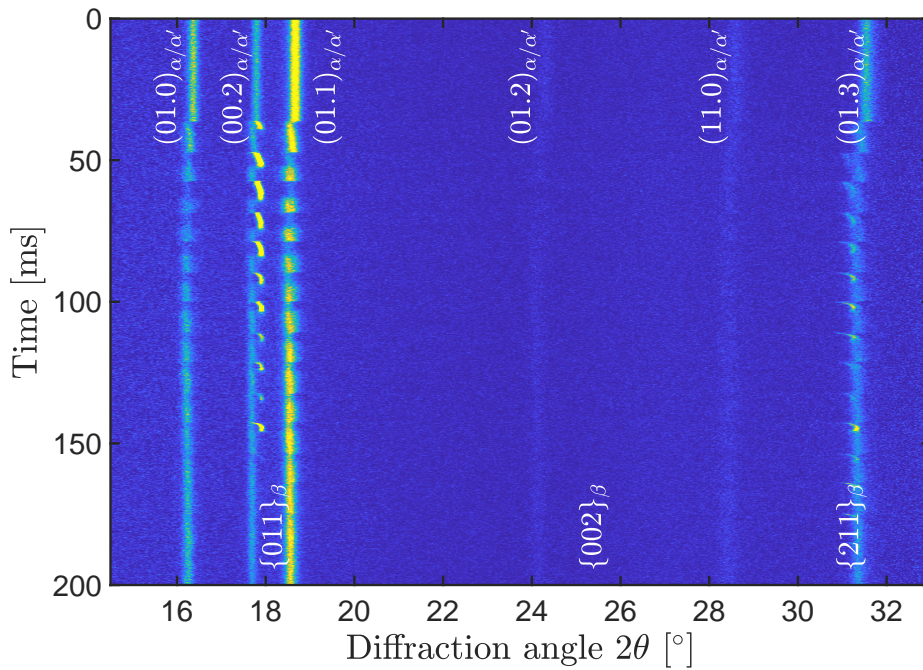
Figure 4.15 – XRD phase evolution in reflection mode

Figures 4.14 and 4.15 show the results obtained for both measurement configurations. They look very similar, with a clear cycling between the α and β phases. By observing the $(00.2)_{\alpha/\alpha'}$ and $\{011\}_\beta$ reflections in

transmission mode (figure 4.14), one can see that the α and β phases begin to coexist, starting before 100 ms as pointed out by the first arrow. Moreover, one can observe a doubling of the $\{011\}_\beta$ peak around t = 135 ms, as pointed out by the second arrow. This behaviour is not observed in reflection mode (figure 4.15).

This phenomenon can be explained by considering the diffraction geometry, and will be discussed later in this thesis. Because the overlap of information in the transmission mode makes the data interpretation difficult, only the reflection mode was used for the following experiments on Ti-6Al-4V.

4.3.2   Scanning vector influence

The results in the following sections have already been published in the journal Materials Today [116]. However, some differences can be found between the graphs in the publication and in this thesis. There are two main reasons for that:

- *The data analysis used for the publication used a fixed angular range to determine the centre of mass and integrated intensities. Since then, the data analysis process has been refined, as presented in section 3.4.3. Therefore, the intensities and derived temperature values might differ slightly in this work. These improvements are discussed later on, in section 6.4.*
- *The time axes have been shifted and the scanning line numbers changed to match the simulation work presented in the next chapter.*

Scanning vector length of 8 mm over an 8x2 mm^2 sample

The evolution of the diffraction patterns during printing with an 8 mm scanning vector length over a rectangular scanned area of 8x2 mm^2 was investigated at the MicroXAS beamline of PSI. The printing parameters used are listed in table 4.5. This set of parameters was chosen based on the previous parametric study to minimise pore formation (section 4.2). The reference sample for this work had a density of 99.96% determined by optical microscopy imaging (table B.7 in the appendices part).

Table 4.5 – Sample parameter table

Laser power [W]	Scanning velocity [mm/s]	Hatch distance [μm]	Layer thickness [μm]
250	600	60	30

During printing, 16'000 diffraction patterns were recorded with a time resolution of 50 μs (20 kHz frame rate). A 12 keV X-ray beam was used, with a size of 80 x 140 μm^2 (horizontal x vertical) at FWHM after projection on the sample at an incidence and of 15°. Figure 4.16 displays the diffraction intensity as a function of time and diffraction angle for the 3rd layer. The results for the other layers provide a similar image. The angular range includes the (01.0), (00.2), (01.1), and (01.2) reflections of the α/α' phase and the {011} and {002} reflections of the β phase. Here the laser starts scanning at t = 0 ms.

With a scanning speed of 600 mm/s, the laser takes 13.3 ms to print a single line. During printing of the
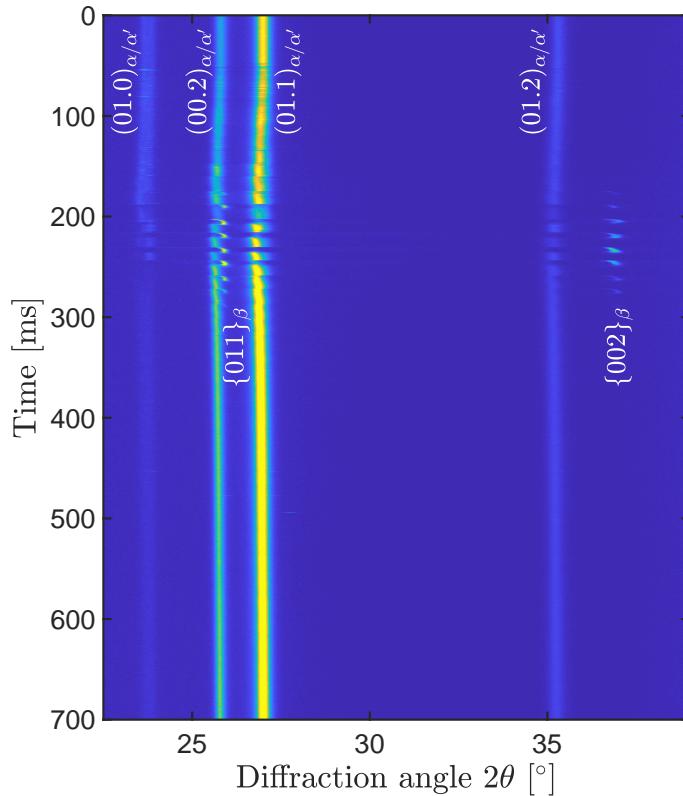
Figure 4.16 – XRD phase evolution in reflection mode for the 8x2 mm^2 sample

first 12 lines, the temperature in the surface region probed by the X-ray beam slowly increases, displayed by a slight angular shift of the diffraction peaks. When the laser beam approaches the position of the X-ray beam, the angular shifts become more pronounced, the intensities of the α/α' peaks start fluctuating and the β phase appears. Figure 4.17 shows a snapshot at t ≈ 190 ms, generated by FEM simulations, which corresponds to the moment the laser is printing the 14th line.
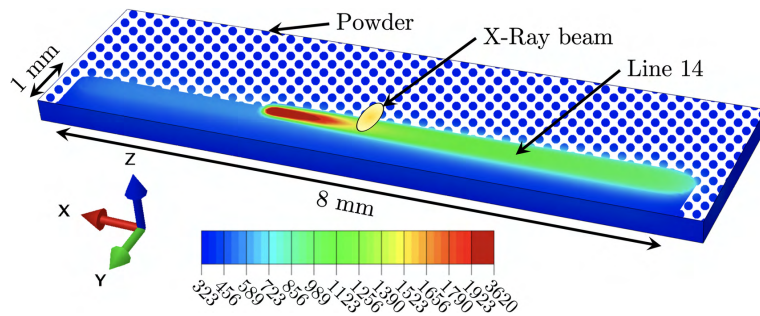
Figure 4.17 – Schematic representation of the relative position of laser, X-ray beam and HAZ at t ≈ 190 ms. (Temperature scale in degree Kelvin)

Figure 4.18a shows the integrated intensities of the the {002}$_β$ and the (01.1)$_{α/α'}$ reflections as a function of time, extracted from figure 4.16 between t = 0 ms and t = 500 ms. After the laser is switched on (t = 0 ms), the

intensity of the α peak starts fluctuating strongly from t ≈ 50 ms, which can be ascribed to moving powder and the presence of a plasma plume [117]. The β phase can be detected while printing lines 13 to 21. The gradual increase and decrease of the β phase with each line, and corresponding decrease in α phase can be understood considering the overlap between the melt pool with its surrounding Heat Affected Zone (HAZ) and probed X-ray volume, as is illustrated in figure 4.18b.
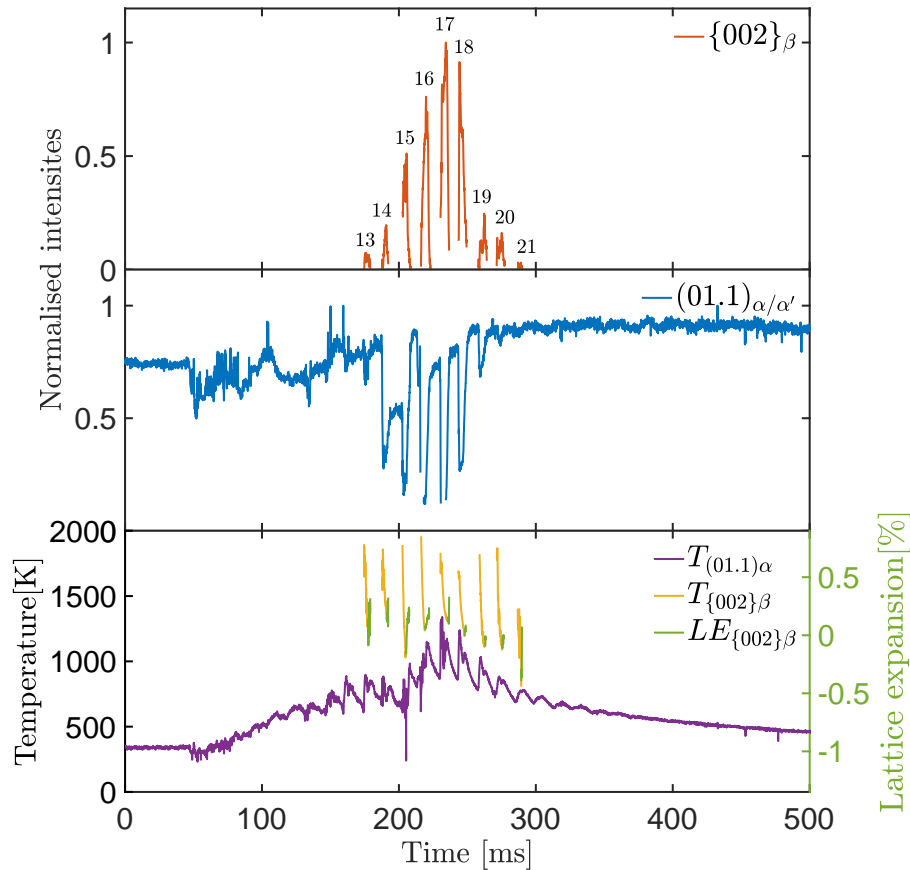
(a) Evolution of the integrated intensity of the $(01.1)_{\alpha/\alpha'}$ and $\{002\}_\beta$ reflections, and temperature profile derived from from the $(01.1)_{\alpha/\alpha'}$ and $\{002\}_\beta$ peak positions
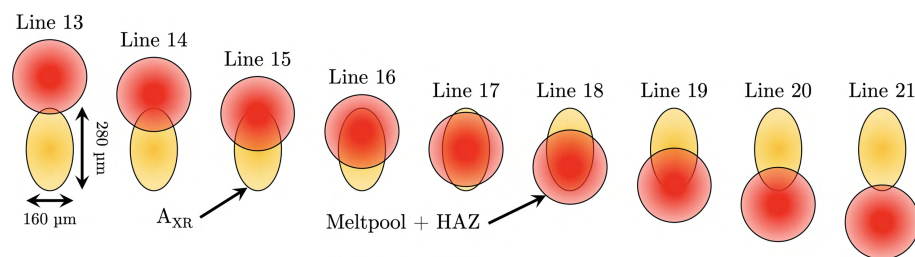
(b) Schematic representation of the relative position of the laser line scan (red) and X-ray beam (yellow) when the laser is at the same X position as the X-ray beam (see figure 4.17)

Figure 4.18 – Integrated intensities from the $(01.1)_{\alpha/\alpha'}$ and $\{002\}_\beta$ reflections, temperature profile and relative position of the laser line scan (red) and X-ray beam (yellow)

Here, we consider the HAZ as the region where the temperature rises above the β transus. We define the total X-ray probed surface region (A_{XR}) as twice the FWHM of the X-ray beam profile. In cycle 13, the centre of

the laser beam is approximately 240 µm away from the centre of A_{XR}, which is well beyond the expected size of the melt pool. Nevertheless, the heat flow in the powder is high enough to partially induce the α to β transition in the probed powder volume. During cycle 17, the laser and X-ray beam experience the largest overlap. Here, the highest intensity of β is measured while the α diffraction peaks vanish completely. Between 190 ms and 260 ms, the intensity of the α/α' phase decreases rapidly each time the laser passes A_{XR}. This allows a very precise determination of the time needed for the laser to print multiple lines and the settling time the laser needs between two consecutive lines. For the setup used in this work the scanning head has a settling time of 0.63 ± 0.05 ms, which was found to be independent of scanning speed or dimensions of the printed structure.

Thermal expansion and contraction change the lattice spacing between crystallographic planes during heating and cooling, and thus the position of α/α' and β diffraction peaks. Additionally, internal stresses and variations in chemical composition can have an effect on the lattice spacing. In first approximation, we assume that the decrease in lattice spacing of the β phase is solely due to thermal contraction during initial cooling from the melt. The temperature evolution shown in figure 4.18a is then calculated from the lattice spacing using the thermal expansion curve in section 3.4.4. Upon further cooling, the lattice spacing of the β phase suddenly increases, which coincides with the β → α/α' transition. This is indicated by the green curve in figure 4.18a. In this regime it is not possible to reliably separate the contributions of thermal, chemical and stress effects and therefore no cooling rates can be reported.

As shown in figure 4.18a, the average temperature of the α/α' phase in A_{XR} increases very shortly after the laser is switched on. The fluctuations correspond with the laser approaching and travelling away from A_{XR}. These fluctuations are not only visible during the cycles where transformation to β is observed, but also earlier and later on. During the three sequential scanning lines after the laser passed A_{XR}, the average temperature of the α/α' phase reaches respectively 1220K, 1030K and 880K. During these cycles, A_{XR} still partially transforms to β, reaching temperatures above 1600K, resulting in a strong temperature gradient in the probed surface region.

Scanning vector length of 2 mm over a 2x2 mm^2 sample

The above experiments demonstrated the evolution of the phases during the scanning of an 8 mm line, which is long enough to allow the β to be fully transformed back into α/α' before the laser hits back A_{XR}. The experiment in this section investigates what happens when the length of the line scan is decreased to dimensions used during various scanning strategies such as chessboard or island scanning. The evolution of the diffraction patterns during printing with a 2 mm scanning vector length over a rectangular scanned area of 2x2 mm^2 was followed at the MicroXAS beamline. The printing parameters used for the printing are listed in table 4.5 and are the same as than the ones used for the 8x2 mm^2 sample.

During printing,16'000 diffraction patterns were recorded with a time resolution of 50 µs (20 kHz frame rate). A 12 keV X-ray beam was used, with a size of 80 x 140 µm^2 (horizontal x vertical) at FWHM after projection on the sample at an incidence and of 15°. Figure 4.19 displays the diffraction intensity as a function of time and diffraction angle for the 2nd layer. The results for the other layers provide a similar image. The angular range includes the (01.0), (00.2), (01.1), and (01.2) reflections of the α/α' phase and the {011} and {002} reflections of the β phase. Here the laser starts scanning at t = 0 ms.
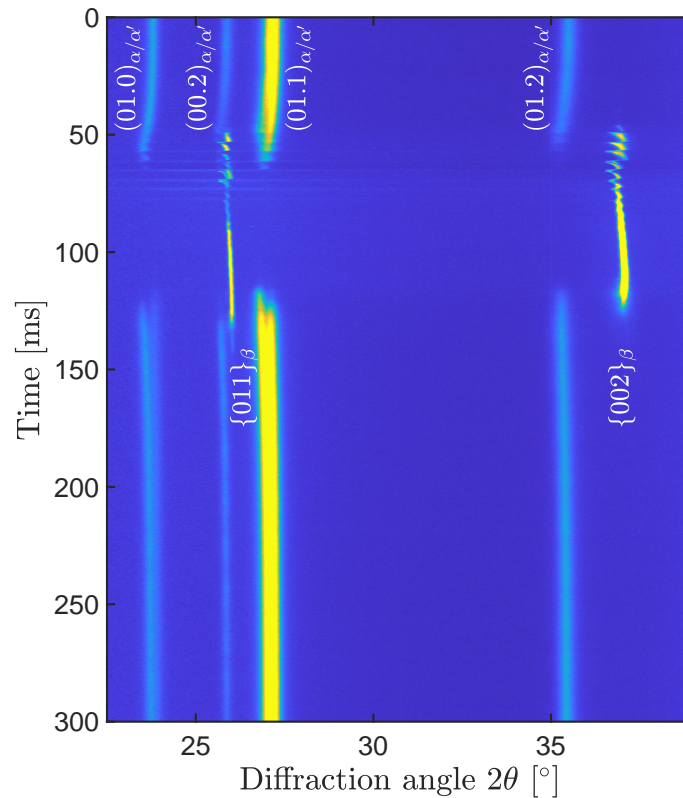
Figure 4.19 – XRD phase evolution in reflection mode for the 2x2 mm^2 sample

With a scanning speed of 600 mm/s, the laser takes 3.3 ms to print a single line of 2 mm length. This explains why the temperature in A_{XR} increases sooner in figure 4.19 compared to figure 4.16, as shown by the angular shift of the diffraction peaks at t $\approx$ 40 ms. When the laser beam approaches the position of the X-ray beam, the angular shifts become more pronounced, the intensities of the α/α' peaks start fluctuating and the β phase appears. However instead of observing a cycling between the α/α' and β phases as shown in figure 4.16, here the β persists during most of the laser scanning time which ends at t $\approx$ 130 ms.

Figure 4.20a shows the integrated intensities of the $(01.1)_{α/α'}$ and the $\{002\}_β$ reflections; the average temperature in A_{XR} as well as the lattice expansion reflecting the building up of residual stress as a function of time, extracted from figure 4.19. Between the scanning line 13 and 16, the α/α' and β phases co-exist, the average temperature in the α/α' phase rises up to about 1300K and strong temperature fluctuations are be observed for β between the β transus and 1900K.

For the 2x2 mm^2 sample, the β phase can be detected while printing lines 13 until the end of the laser scanning whereas it was only present between line 13 and 21 for the 8x2 mm^2 sample. To understand the origin of this behaviour, figure 4.20b illustrates three different instances on figure 4.20a with schematic representations of the relative position of X-ray beam and the melt pool with its HAZ (red and green) on snapshots from FEM simulations.
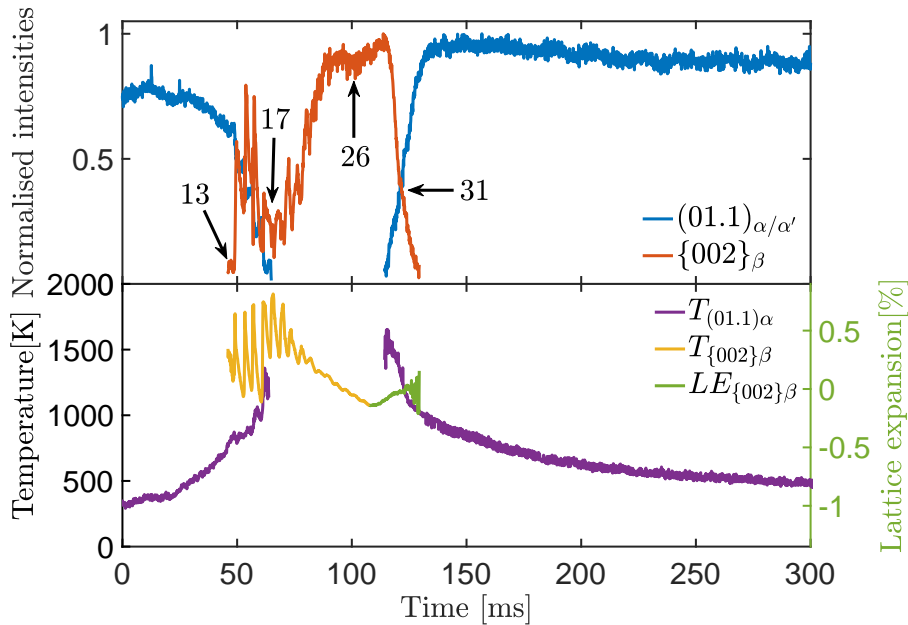
(a) Evolution of the integrated intensity of the $(01.1)_{\alpha/\alpha'}$ and $\{002\}_\beta$ reflections, and temperature profile derived from from the $(01.1)_{\alpha/\alpha'}$ and $\{002\}_\beta$ peak positions during printing of a 2x2 mm² layer
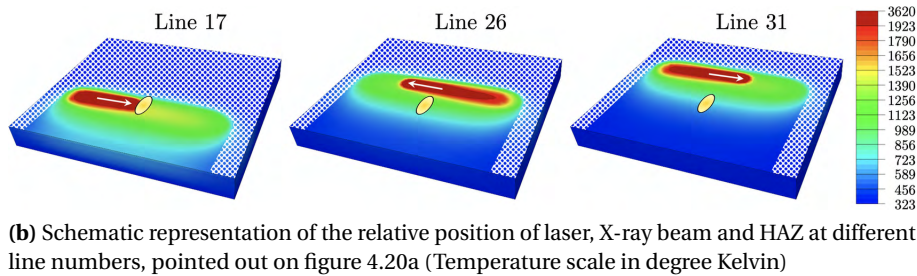
(b) Schematic representation of the relative position of laser, X-ray beam and HAZ at different line numbers, pointed out on figure 4.20a (Temperature scale in degree Kelvin)

Figure 4.20 – Integrated intensities from the $(01.1)_{\alpha/\alpha'}$ and $\{002\}_\beta$ reflections and schematics of the laser position compared to the X-ray beam

Because of the much shorter scanning length, the local heat input on the 2x2 mm² sample is much larger than in the 8x2 mm² sample. This is can be seen by the size of the green volume that moves along the 2x2 mm² sample surface in figure 4.20b.

4.3.3 Residual strain after SLM processing

Figure 4.21a and b shows the lattice strain evolution over time for the (01.0), (00.2), (01.1) and (01.2) α/α' reflections in the 2x2 mm² and 8x2 mm² samples, respectively. Assuming that the powder is strain-free, the increase in strain during heating reflects the thermal expansion, which is why the curves for the different reflections fall (mostly) on top of each other. During cooling after solidification of the β phase, residual stresses are expected to form due to the high thermal gradients present in the material [75].

In the 2x2 mm² sample (figure 4.21a), the α/α' phase reappears at t ≈ 130 ms. While cooling down to

(a) Strain evolution in the 2x2 mm^2 sample

(b) Strain evolution in the 8x2 mm^2 sample
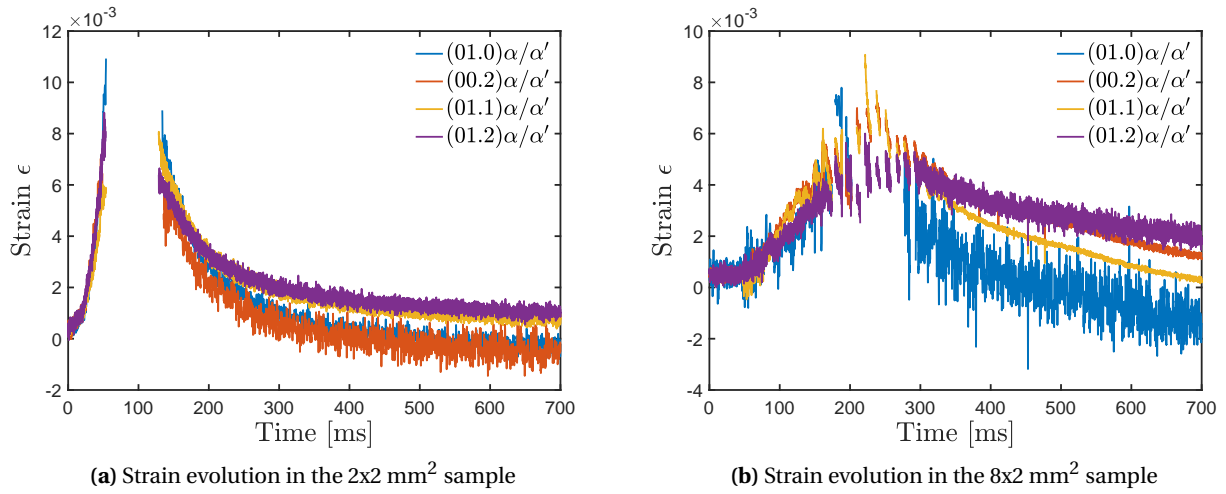
Figure 4.21 – Strain evolution of the α/α′ phase in the 2x2 mm^2 (a) and 8x2 mm^2 (b) samples during laser scanning computed from equation 3.8 for different crystallographic planes. The initial strain increase is attributed to the lattice expansion during heating, and the decrease to the lattice contraction during cooling. The gap in (a) comes from the fact that the α/α′ phase is completely transformed into β at t ≈ 50 ms and transforms back at t ≈ 130 ms.

approximately 340K, the lattice strain decreases, but with rates that depend on the lattice reflection. The difference in lattice strain between the (01.0)/(00.2) planes and the (01.1)/(01.2) amounts 4×10^{-4}, suggesting the presence of minor residual strains. Figure 4.21b shows a stronger divergence of the strain for the different reflections during cooling down of the 8x2 mm^2. Even though the data is more scattered, the difference in lattice strain between (01.2) and (01.0) reaches 3.2×10^{-3}. Calculating residual stress from these results is not possible solely based on these data, and is beyond the scope of this thesis. Besides, due to the elastic-plastic anisotropy of bulk Ti-6Al-4V, one needs also to take into account the difference in texture and α/α′ needle morphology, as shown in section 4.4.1.

4.3.4 Temperature profile of the β phase in the 8x2 mm^2 sample

In the section 4.3.2, the temperature profile was calculated for the $\{002\}_\beta$ reflection of the 3$^{\text{rd}}$ layer of an 8x2 mm^2 sample. In this section, a close attention is paid to the accuracy of the temperature measurement, since the β phase peak position fluctuates a lot during SLM processing of the larger sample.

Figure 4.22 shows the results for different layers of the same 8x2 mm^2 sample when the β phase appears and disappears during laser scanning. The laser spot overlaps with A_{XR} for the β event at line 17, determined by the maximum intensity of the β phase. The centre of mass has been calculated for all these patterns and overlapped on the peak intensity. The fact that not all the same lines are visible for the different scanning lines is due to limited grain statistics.

The temperature curves for each layer are calculated and presented in figure 4.23. The β events 21 from layer 3 and 13 from layer 9 were not included since the data is not meaningful. To compare the absolute temperature profile of each event within one layer, the beginning of the cooling has been set when the laser

(a) Layer 3   **(b)** Layer 5   **(c)** Layer 7   **(d)** Layer 9
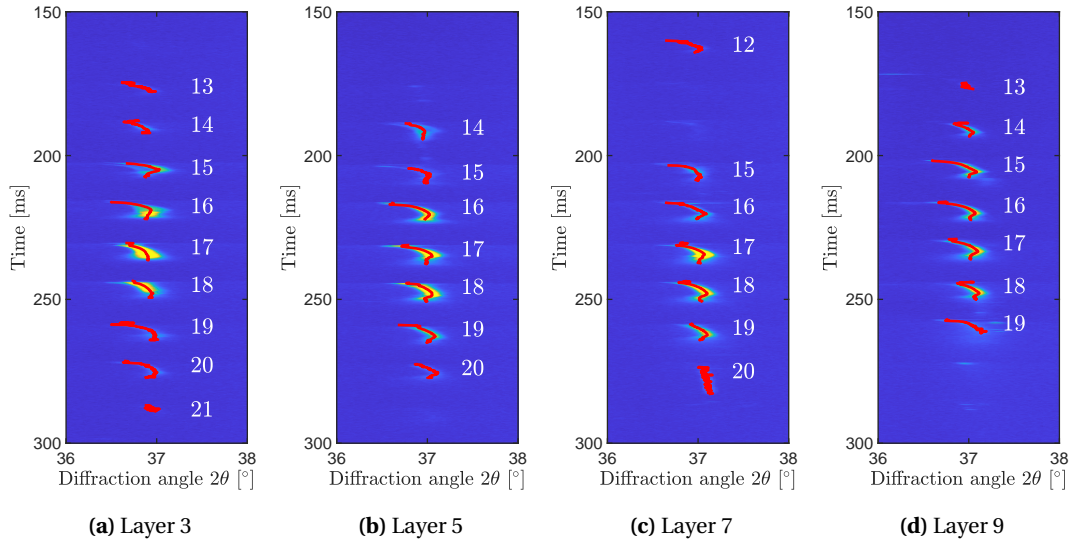
Figure 4.22 – Zoom on the $\{002\}_\beta$ diffraction peak during *operando* measurement for layers 3, 5, 7and 9 of the 8x2 mm^2 sample. The position of the centre of mass is highlighted in red.

(a) 8x2 mm^2 sample - layer 3   **(b)** 8x2 mm^2 sample - layer 5

(c) 8x2 mm^2 sample - layer 7   **(d)** 8x2 mm^2 sample - layer 9
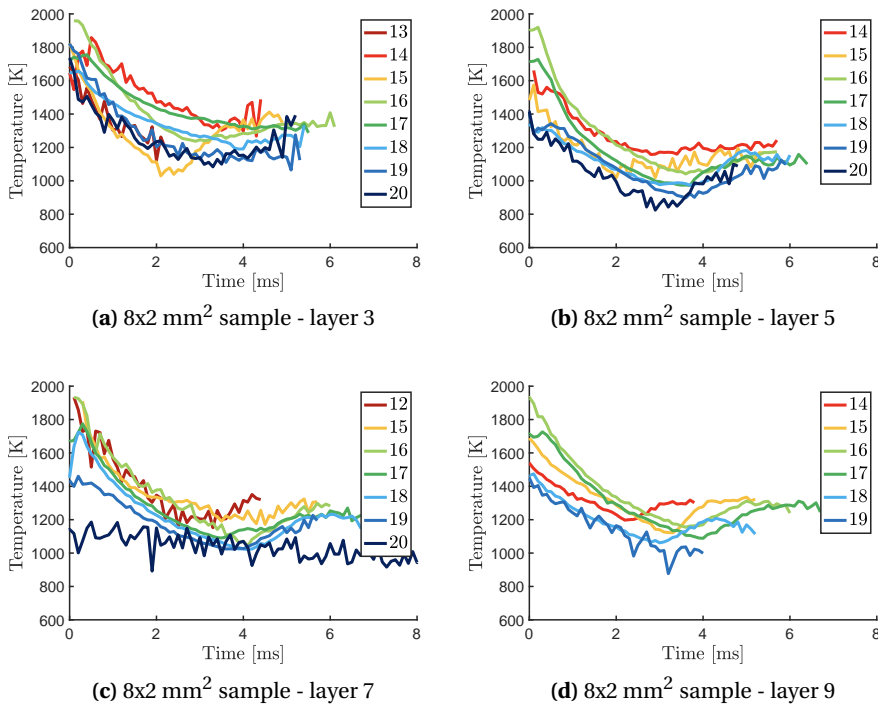
Figure 4.23 – Temperature curve for each beta event of figure 4.22, starting at the maximum of the diffuse scattering for each event.

beam is closest or overlapping with A_{XR}, so that all the curves are starting with the same time reference. The starting temperature of each line should increase while the laser approaches A_{XR} during bi-directional

scanning, and reaches the maximum value around line 17 when the laser and X-ray beams overlap. As the laser moves away, the temperature decreases. The slopes are comparable for all the measurements at a given temperature, which is expected since the cooling rates should only beare proportional to the temperature. In all the plots presented in figure 4.23, the maximum temperature is reached for line 16 which starts around 1900 K, close to the melting point of Ti-6Al-4V.

The starting temperature of each curve in figure 4.23 has been artificially shifted to 0K to visualise the cooling rates, and presented in figure 4.24. What is expected is that the lines 16, 17 and 18 would have the highest cooling rates because they correspond to partial or full melting of the material (see figure 4.18b). Consequently, the lines before 16 and after 18 should have lower cooling rates, since A_{XR} is mostly probing the powder or solid material at this time.

(a) 8x2 mm^2 sample - layer 3

(b) 8x2 mm^2 sample - layer 5

(c) 8x2 mm^2 sample - layer 7

(d) 8x2 mm^2 sample - layer 9
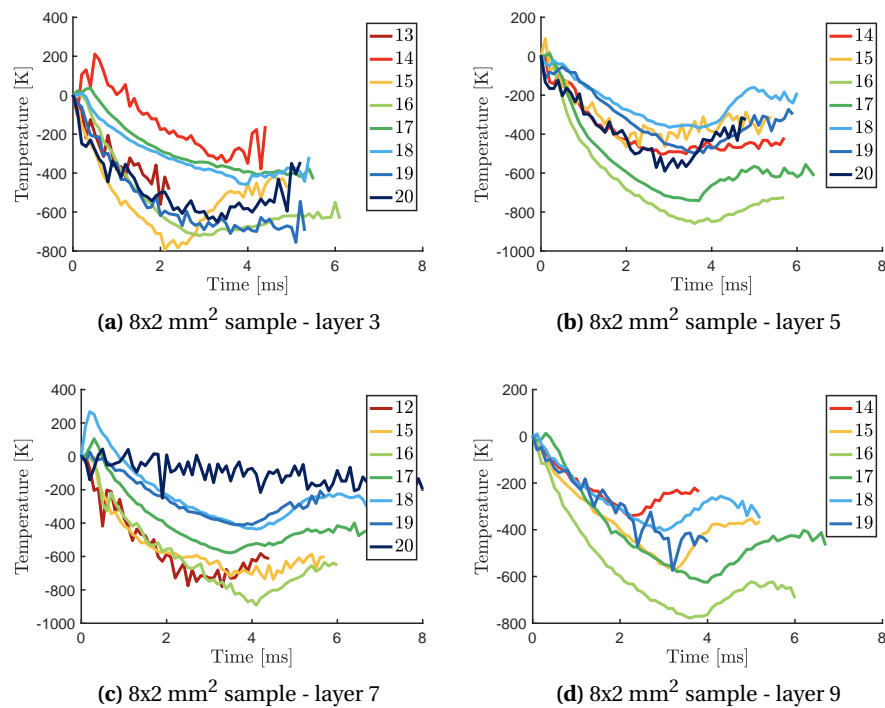
Figure 4.24 – Temperature curve for each beta event of figure 4.22, starting at the maximum of the diffuse scattering for each event.

Figures 4.24b and d display this trend. i.e. the cooling rates are increasing and decreasing with the line number as expected, with a maximum value around -4×10^5 K/s for line 16. However the same observation cannot be made for figures 4.24a and c.

Figures 4.25a and b show a zoomed-in view of layer 3 at the beginning of lines 16 and 17, respectively. When looking at the overlapping between the centre of mass (red) and the peak intensity for line 16, the peak diffraction angle gradually increases from t ≈ 216 ms. This provides a good estimation of the temperature evolution in A_{XR}. However for line 17, the situation is a bit more complex. Between t = 230.7 ms and t = 231.1 ms, the centre of mass follows the contribution from a grain which is at a temperature lower than expected. At t = 231.1 ms, a second contribution joins the peak intensity, as shown in figure 4.25c.

(a) Line 16   **(b)** Line 17   **(c)** Intensity evolution of line 17
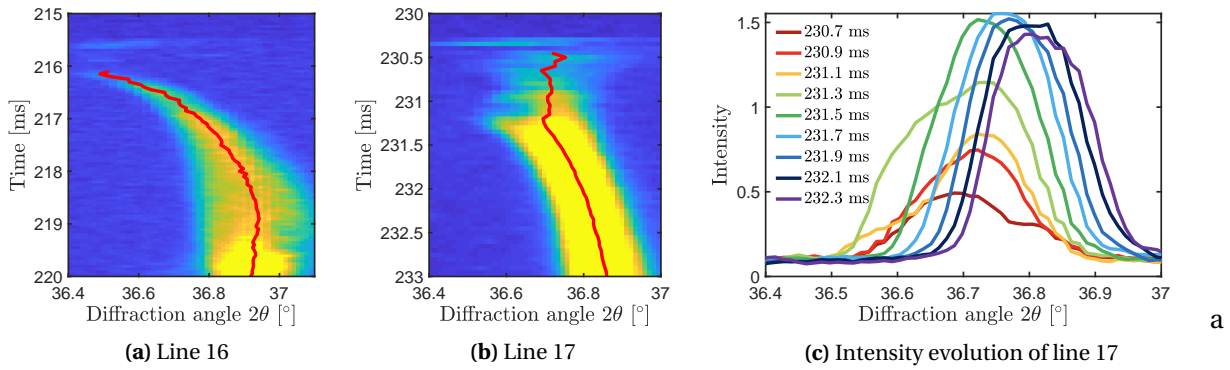
Figure 4.25 – Centre of mass (red) for lines 16 and 17 taken from layer 3, and evolution of the peak intensity for line 17 (figure 4.22)

This behaviour is not isolated, since figure 4.26 shows the same situation from line 17 in layer 7 (figure 4.22c). At t = 230.7 ms, the centre of mass follows a β peak at higher angle value and thus at lower temperature. At t = 231.1 ms, a second contribution at higher temperature suddenly appears. A t = 231.5 ms the two contributions have merged together into one peak while the probed area is cooling down. Because of the presence of this first contribution before t = 231 ms, the centre of mass is not following the high temperature peak starting below 36.6° which does not represent the bulk behaviour. However, once the two contributions have merged, the centre of mass follows well the intensity of the resulting peak.

(a) Line 17   **(b)** Intensity evolution of line 17
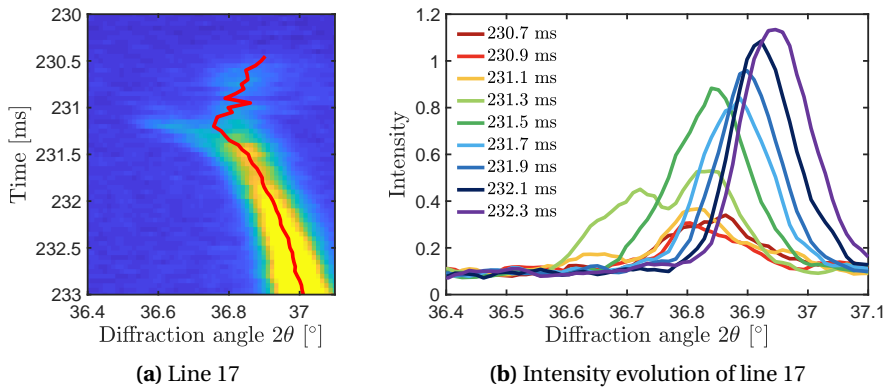
Figure 4.26 – Centre of mass and evolution of the intensity in line 17 for layer 7 (figure 4.22c)

In both cases, the higher angular position of the first contribution to the β peak shape comes from a diffracting grain at a lower temperature. The lower angular position of the second contribution shows that the temperature from the grain diffracting is higher. For that to happen, these two grains must be located at different positions. Figure 4.27 illustrates the situation when the melt pool is crossing A_{XR}, e.g. for line 17. The laser spot diameter, melt pool and heat affected zone widths are represented up to scale compared to the X-ray beam area (see figure 4.18b and table B.5). The lengths displayed here are only for illustration purposes. The X-ray beam position is fixed and the laser scanning from the left to the right side of the page.

When the laser reaches A_{XR}, the material included within the HAZ of the melt pool heats up and the phase

(a) First contribution appearance   **(b)** Second contribution appearance
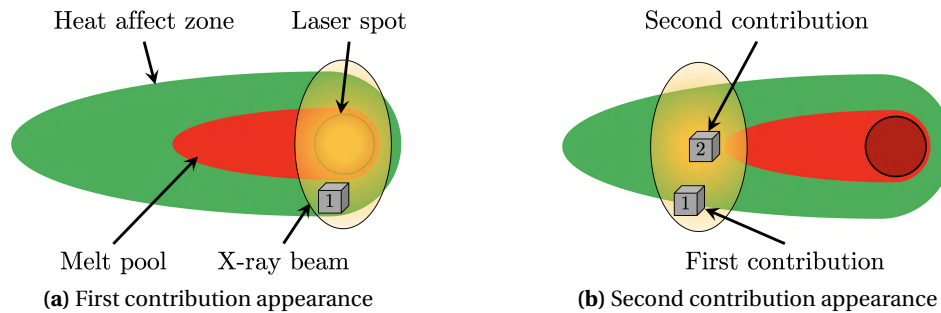
Figure 4.27 – Illustration of the different grain contributions to the XRD pattern during overlap of the laser beam with A_{XR}. The laser scanning direction goes from the left to the right.

transformation $\alpha \rightarrow \beta$ occurs without reaching the melting point. This is illustrated by grain 1 in figure 4.27a. While this first grain heats up, the laser keeps travelling across the X-ray beam until the tail of the melt pool starts to solidify into the β phase (grain 2 in figure 4.27b). In this scenario, grain 1 transforms earlier to the β phase, compared to grain 2. On the other hand, grain 2 starts from a higher temperature. This explains the observations made in figure 4.25b: first, a low temperature contribution becomes visible, followed by a high temperature contribution. After the melt pool exits the X-ray beam, the temperature of the region within A_{XR} becomes more homogeneous, explaining the nicer peak shape obtained at the end.

This situation was illustrated for line 17, but remains valid for any line where both the melt pool and heat affected zone are present in A_{XR} during laser scanning. This also explains why temperature profiles and cooling rates presented in figures 4.25 and 4.26 are skewed compared to what is expected. The initial temperatures might not be accurate, however when the cooling starts (which corresponds to the merging of the peaks), the estimated values become more reliable.

The fact that contributions from different locations are intervening in determining peak position during the formation of the β phase makes the analysis difficult. Affected peaks have a bad shape due to poor grain statistics, and it is not possible to perform standard fitting procedures for the whole experiment to separate grain contributions. The centre of mass, which is a weighted average, provides the best possible estimate for the peak position of single peaks. However, one clearly has to pay attention when multiple contributions are present. Here it is required to look carefully at the intensity distribution to know when the temperature profile represent accurately the situation.

4.3.5 Footprints from the different beamlines

Influence of two different X-ray beam spot size on the data acquired from the printing of a 2x2 mm^2 sample

The synchrotron beamline characteristics have an important influence on the X-ray diffraction footprints of the microstructural evolution during printing. This is illustrated by comparing the results from *operando* experiments performed at MicroXAS and MS, two hard X-ray beamlines located at the Swiss Light Source (SLS). The main difference between these two beamlines is the X-ray beam size. At the MS beamline, the X-ray beam was focused down to a size of 130 x 60 μm^2 (horizontal x vertical) at FWHM, which corresponds

to an illuminated area A_{XR} = 130 x 230 μm^2 on the sample surface region at an incidence angle of 15°. The MicroXAS beamline exhibits additional focusing optics (KB mirrors) close to the sample position. This was used to focus down the X-ray beam to 80 x 35 μm^2 (horizontal x vertical) at FWHM, resulting in A_{XR} = 80 x 140 μm^2 at an incidence angle of 15°.

The processing parameters used for the experiments are the same as those used in the previous sections, and are listed in table 4.5. At each beamline, samples with an area of 2x2 mm^2 were printed. The X-ray beam was positioned in the middle of the printed area. The laser scanning started at the outer edge and covered the complete scanned area in a bi-directional fashion. As the hatch distance was smaller than the vertical dimension of A_{XR}, the laser beam passed multiple times through the area illuminated by the X-ray beam.
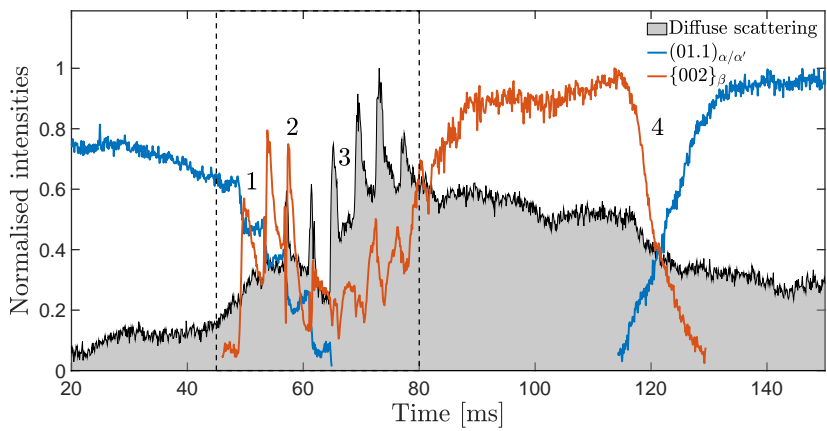
(a) Integrated intensities of a 2x2 mm^2 sample at MicroXAS
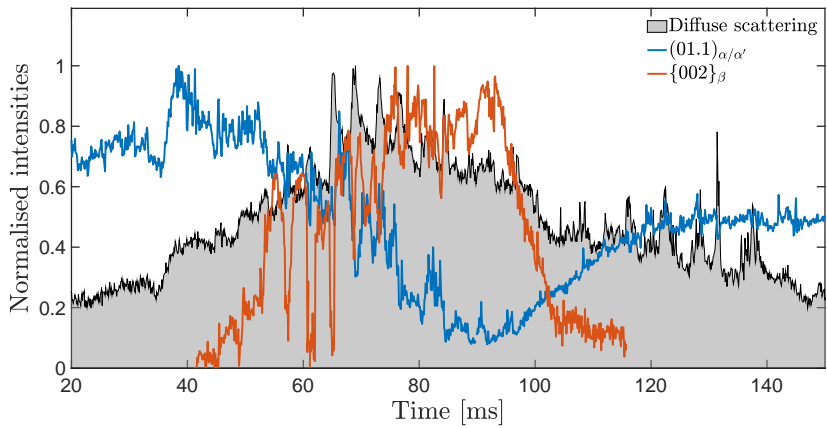
(b) Integrated intensities of a 2x2 mm^2 sample at MS

Figure 4.28 – Comparison of the integrated intensities obtained at the MicroXAS and MS beamlines on a 2x2 mm^2 sample printed with the parameters listed in table 4.5. The integrated intensities of the $(01.1)_{\alpha/\alpha'}$ (blue) and the $\{002\}_{\beta}$ (red) reflections are shown here, together with the diffuse scattering (grey).

Figures 4.28a and b display the evolution of the integrated intensities of the $(01.1)_{\alpha/\alpha'}$ and the $\{002\}_{\beta}$ reflections (respectively blue and red curves) together with the intensity of the diffuse scattering (grey background) as a function of time while printing a single layer of the 2x2 mm^2 sample, measured at the MicroXAS and MS

beamlines, respectively. Note that the intensity of each phase is normalised to its maximum.

The results from the MS beamline are qualitatively similar to the ones obtained at MicroXAS. There are, however, a few key differences that are related to the significantly larger size of A_{XR}. First, the signals at MS are noisier, even though the intensity of the incoming X-ray beam is comparable to the one of MicroXAS. This may be related to the spatter created during printing. The X-ray beam area at MS is about three times larger compared to MicroXAS, resulting in significantly higher chance for interaction with spatter. Furthermore, the observed fluctuations of the intensities may be affected by moving powder caused by denudation and entrainment effects. Second, the α/α' phase never disappears at MS because there is always a part of A_{XR} where the temperature is below the β-transus temperature. Finally, the intensity of the diffuse scattering signal from the melt pool is less pronounced. The major advantage of using a larger X-ray beam lies in a better grain sampling statistics of the solid phase.

Note that strong variations in intensity of the β phase are observed, especially in the first lines when the α/α' phase starts disappearing, which probably can be assigned to the fact that only limited number of grains are in diffraction conditions. For instance, after an initial increase in the overall intensity, the β phase exhibits an unexpected minimum intensity between t = 60 ms and t = 80 ms. In contrast, at MS the overall shape of the intensity of the β phase exhibits a more gradual increase (figure 4.28).

(a) Zoom on figure 4.28a between 45 ms and 80 ms

(b) Schematic representation
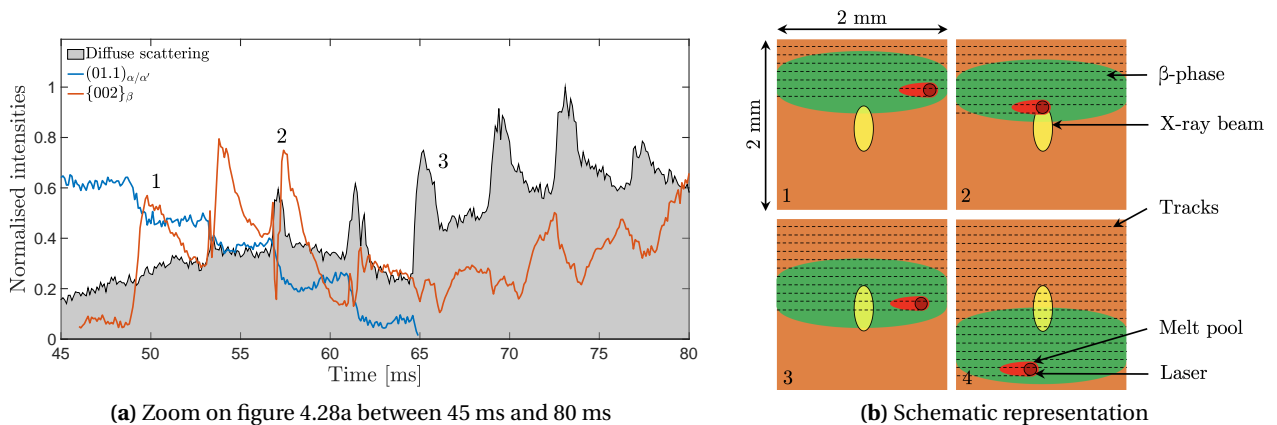
Figure 4.29 – Details on the intensities evolution in figure 4.28a and schematic representation of the relative position of laser, X-ray beam and HAZ at different instants, pointed out on figures 4.28a and 4.29a. The dashed lines represent the previously printed tracks.

To obtain a maximum of information on the interaction of laser and material, the size of the X-ray spot should be similar as that of the laser spot. Figure 4.29a shows a zoom of figure 4.28 between 45 ms and 80 ms. Figure 4.29b displays a schematic that shows at particular times (numbered in figure 4.28a and 4.29a) the relative position of the laser, X-ray beam, melt pool and the region that exhibits the β-phase. This schematic is inspired by the results from finite element simulations, as shown in figure 4.20b.

The printing starts at t = 0 ms, where the laser beam is far away from A_{XR} and only the α/α' phase is visible. Between t = 47 ms and t = 66 ms, the α/α' phase gradually disappears in a step-like manner. Here, part of A_{XR} is transformed to the β phase, as shown schematically in figure 4.29b for the position 1. At t = 58 ms, the diffuse scattering exhibits a short increase in intensity. This is the signature of the melt pool that passes partly

through A_{XR} (see also position 2 in figure 4.29b). At t = 66ms, the α/α' phase has completely disappeared. During the next transition, the melt pool passes through the centre of A_{XR} (position 3). The melt pool passes 6 times through A_{XR}, as witnessed by the 6 spikes in the diffuse scattering. The last passage occurs at t = 78 ms. Beyond this point, the laser beam does not overlap anymore with A_{XR}. The temperature in A_{XR} decreases, but remains above the β-transus temperature for another 40 ms. At t = 120 ms the β phase gradually transforms into the α/α' phase. At t = 135 ms, printing has finished, after which the temperature in A_{XR} keeps on decreasing and the little remaining β phase transforms further into α/α'. Finally, the microstructure exhibits no β phase anymore.

Influence of a very small X-ray beam size

The results in transmission mode presented in section 4.3.1 were acquired with an X-ray beam size of 30 x 12 μm^2 (horizontal x vertical) at FWHM under an incidence angle of 20°, which results in a 30 x 35 μm^2 projected spot size. An interesting observation can be made on the result of figure 4.14 by zooming on the $(01.1)_{\alpha/\alpha'}$ and $\{011\}_\beta$ reflections between 54 ms and 69 ms. Figure 4.30 shows the evolution of these peaks with their integrated intensities normalised over their respective maximum. The evolution of the diffuse scattering (DS) is shown in grey, which correspond to the sum of all the intensities in the background between 16.7° and 17.5° and between 19.2° and 23.8° in figure 4.14 normalised over its maximum.

(a) Diffraction data   **(b)** Integrated intensities
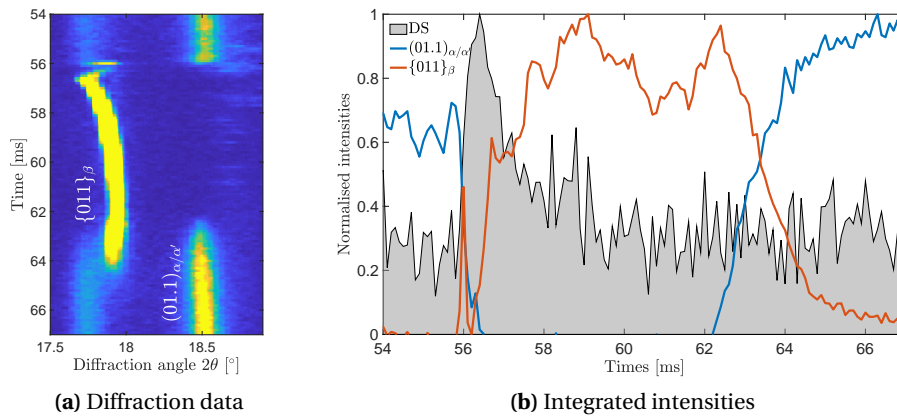
Figure 4.30 – Zoom on figure 4.14a showing the $(01.1)_{\alpha/\alpha'}$ and $\{011\}_\beta$ reflections and their integrated intensities between between 50 ms and 70 ms.

At t = 56 ms the laser beam gets closer to the X-ray probed area, the intensity of the α/α' phase decreases very fast and a short (0.2 ms) β signal is visible. Upon further heating no diffraction peaks are visible, indicative for a complete melting. While the diffuse scattering intensity decreases, the β peak intensity increases. Simultaneously, the peak position of the β phase shifts towards higher angle values which is an indication of the cooling of the material. The β phase exists until the temperature gets sufficiently low for the α phase to appear again. The present of the β phase at t ≈ 56 ms in figure 4.30a can be observed thanks to the small size of the X-ray beam compared to the laser beam. Note that after t = 62 ms, the $\{011\}_\beta$ peak is moving towards lower angle values while the α/α' phase starts to form. This shift towards lower angle values has been observed in the previous sections and is attribute to strain generation within the material.

4.4 Influence of the scanning vector length on the final microstructure

4.4.1 *Operando* XRD samples

The experiments presented in section 4.3.2 demonstrated that the evolution of the phases during the scanning of an 8 mm line was different than when a 2 mm scanning vector length is used. In the first case, the scanning time of a single track is long enough to allow the β phase to be fully transformed back into α/α′ before the laser hits back the probed volume A_{XR}. This does not happen for a 2 mm scanning vector length. In this section, the influence of the scanning vector length on the final microstructure is investigated, when decreased to dimensions used during strategies such as chessboard or island scanning.

Table 4.6 – Sample parameter table

Laser power [W]	Scanning velocity [mm/s]	Hatch distance [μm]	Layer thickness [μm]
250	600	60	30
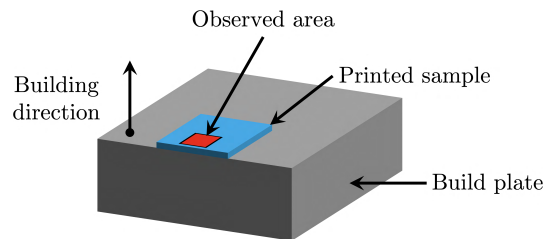
Figure 4.31 – Illustration of the observed area

Three samples with different size were printed with the parameters listed in table 4.6, similarly as in section 4.3.2. The samples dimensions are 2x2 mm^2, 4x4 mm^2 and 6x6 mm^2 with a total build height corresponding to 5 layers. Their respective XRD data are given in figures 4.31(a)-(c). The texture and grain size of the printed samples was investigated by Electron Back Scatter Diffraction (EBSD) using a field emission gun scanning electron microscope (FEG SEM) Zeiss ULTRA 55 equipped with an EDAX Hikari Camera operated at 25 kV in high current mode with a 120 μm aperture.

The samples were mechanically polished on the top surface perpendicular to the building direction using 3 μm diamond suspension and up to 0.04 μm colloidal silica to obtain a smooth surface for EBSD. Only very little material was removed, in order to observe the microstructures and texture for the last layer. Low and high-resolution mapping was performed with step sizes of 1 μm and 0.1 μm, respectively as shown in figure 4.31. The software package ARPGE [118] was used to reconstruct the β phase from the EBSD data. Post processing of the EBSD data and map reconstruction was done with the EDAX OIM Analysis 7.3 software package. Inverse Pole Figure (IPF) maps were cleaned up using grain dilation method to remove bad indexing points. The resulting observations are shown in figure 4.32.

As expected, thee different temperature history has an effect on the resulting α/α′ microstructure. Figure 4.32 (d)-(f) show EBSD pictures of the second last layer. The microstructure consists of blocks (outlined by dashed lines) that have the same size as the prior β grains, shown in figure 4.32(g)-(i). Such a block pattern was also observed in [9] and [111]. However, the size of the blocks was related to the hatch spacing while in our case, the size is related to scanned area and duration of the material staying above the β transus, which is largest in the 2x2 mm^2 sample. High resolution EBSD presented in figure 4.32(j)-(l) show a hierarchical α′ martensitic structure formed in a basket weave pattern. At least 4 size variations of α′ can be seen. The primary α′ needles have a width of 2-3 μm while for the last generation it can be as thin as 50 nm. The average width of the α′ needles decreases as the print cross-section increases. These results will be discussed in a later chapter.

(a) XRD pattern - 2x2 mm^2 sample

(b) XRD pattern - 4x4 mm^2 sample

(c) XRD pattern - 6x6 mm^2 sample

(d) α/α′ IPF map - 2x2 mm^2 sample

(e) α/α′ IPF map - 4x4 mm^2 sample

(f) α/α′ IPF map - 6x6 mm^2 sample

(g) Prior-β grains - 2x2 mm^2 sample

(h) Prior-β grains - 4x4 mm^2 sample

(i) Prior-β grains - 6x6 mm^2 sample

(j) α′needles - 2x2 mm^2 sample

(k) α′ needles - 4x4 mm^2 sample

(l) α′ needles - 6x6 mm^2 sample
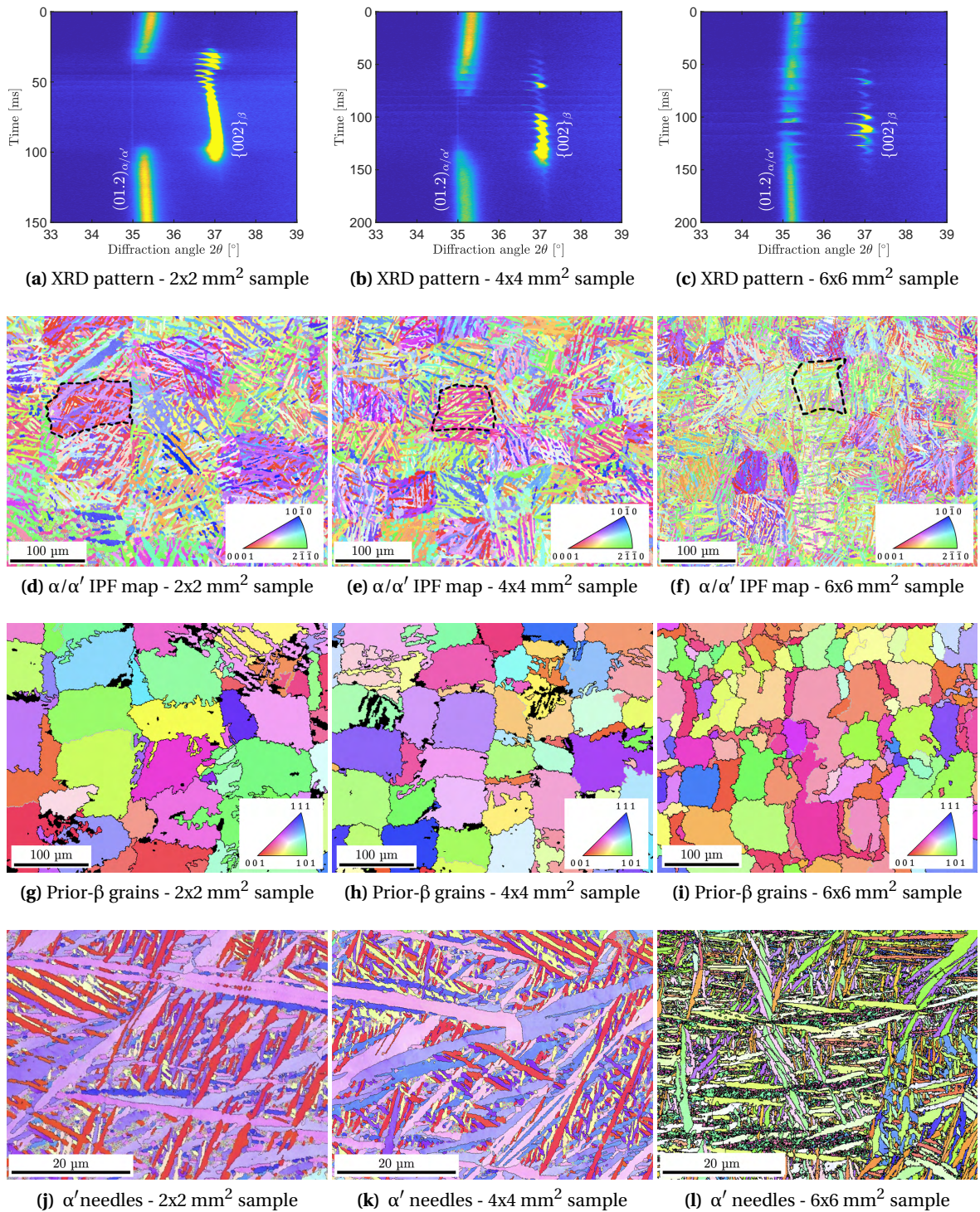
Figure 4.32 – Influence of scanning strategy on the resulting microstructure. (a)-(c) Evolution of the intensities of the (01.2)$_{α/α′}$ and {002}$_β$ reflections while printing; (d)-(f) IPF maps of the building planes; (g)-(i) IPF maps of the reconstructed prior-β grains; (j)-(l) High-resolution IPF maps showing basket weave microstructures with variants of α′ martensitic laths from the highlighted regions in (d)-(f). For figures (d)-(l), the orientation of the IPF is given normal to the observation plane, e.g. parallel to the building direction.

4.4.2 Columnar growth in larger samples

In the previous section, the samples investigated had a build height of 5 layers for *operando* XRD measurements, each one of them being 30 μm thick, this corresponds to a sample height of 150 μm. It is known that Ti-6Al-4V exhibits a columnar growth along the build direction due to the directional thermal gradients during SLM processing [6, 68]. Additional measurements were performed on the frontal plane of the 2x2 mm^2 sample presented in figure 4.32 as illustrated in figure 4.33a to observe the grain growth along the build direction.

(a) Frontal plane of the short sample

(b) EBSD mapping of the tall sample
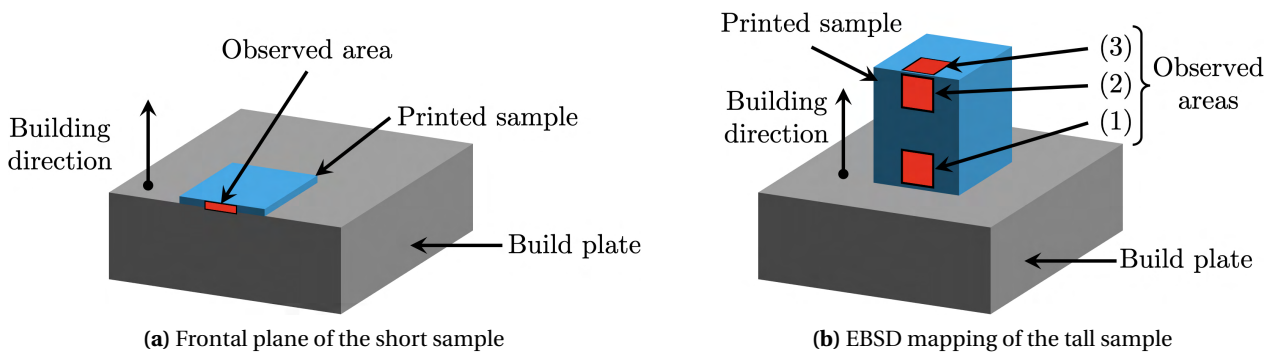
Figure 4.33 – Illustration of the observed areas

Figure 4.34a reveals the α/α′ microstructure along the build direction, and figure 4.34b shows the corresponding reconstructed prior-β grains. Since this measurement has been done close to the build plate, no columnar growth is observed yet.

(a) α/α′ IPF map

(b) Prior-β grains
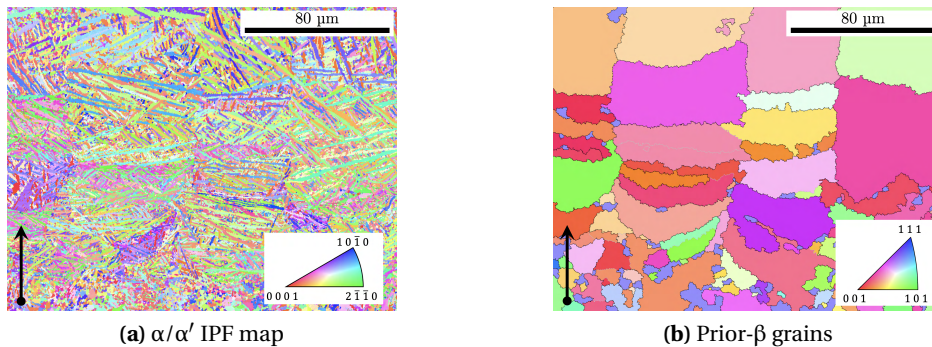
Figure 4.34 – Frontal plane observation for the 2x2 mm^2 sample. The black arrow indicates the building direction. (Courtesy of Dr. Cynthia S.T. Chang)

As a result, taller samples were printed, with a total build height of 1 mm to study the effect of the scanning strategy on the columnar growth. The printed cross sections were chosen as 1x1 mm^2, 2x2 mm^2 and 6x6 mm^2 so that all samples can fit on a single build plate. Similarly as before, an EBSD mapping of these samples was done at the top surface, but also along the build height. Figure 4.33b illustrates the three observed areas, as indicated by the different numbers. A first map was taken on the frontal plane, close to the build plate (1), a second one also on the frontal plane but close to the top surface (2), and finally a third one on the top surface close to the frontal plane (3).

Figure 4.35 present the EBSD maps arranged according to the measurement location, as presented in figure 4.33b. As expected, the measurements reveal the α/α′ microstructure of the samples.

(a) α/α′ IPF map - 1x1 mm^2 **(b)** α/α′ IPF map - 2x2 mm^2 **(c)** α/α′ IPF map - 6x6 mm^2
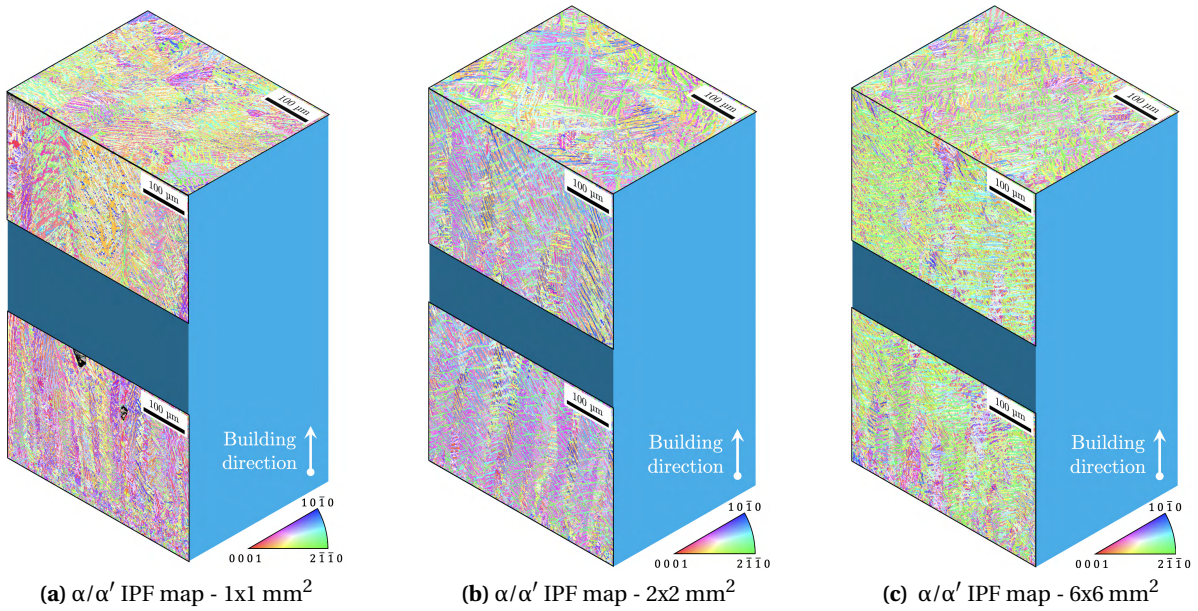
Figure 4.35 – IPF maps of the building and front planes for the sample height of 1 mm (courtesy of Dr. Cynthia S.T. Chang)

In order to observe to columnar growth along the build height, figure 4.36 presents the evolution of the prior-β grains reconstructed from figure 4.35 for the 1x1 mm^2 (a), 2x2 mm^2 (b) and the 6x6 mm^2 (c) samples.

(a) Prior-β grains - 1x1 mm^2 **(b)** Prior-β grains - 2x2 mm^2 **(c)** Prior-β grains - 6x6 mm^2
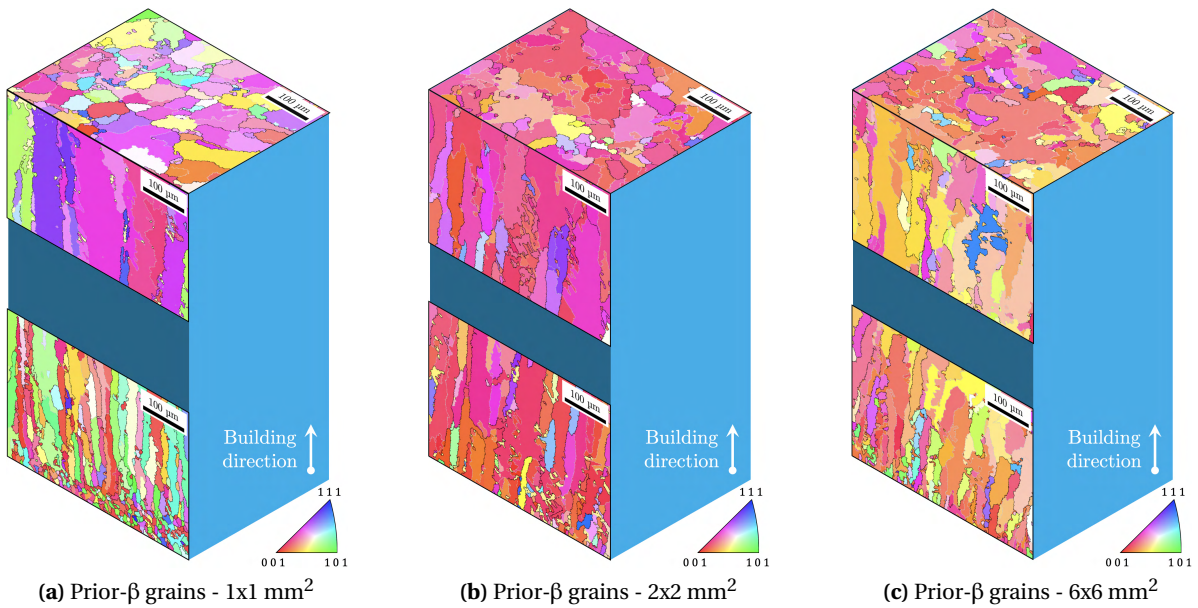
Figure 4.36 – IPF maps of the reconstructed prior-β grains from figure 4.35 (courtesy of Dr. Cynthia S.T. Chang)

When looking at the columnar growth at the bottom of the sample (close to the build plate) on the frontal plane in figure 4.36, one can observe smaller prior-β grain here compared to figure 4.34b due to a finer starting microstructure for the build plate. When looking at the the columnar growth on the upper part of the sample, there is a clear size effect that is visible between the 1x1 mm^2 (a) and the 6x6 mm^2 (c) samples. The prior-β grain growth is enhanced by the shorted scanning vector length in the 1x1 mm^2, as expected from the results in the previous section. The same observation can be made when comparing the 1x1 mm^2 (a) and the 2x2 mm^2 samples. However, this difference is less pronounced when comparing the 2x2 mm^2 and the 6x6 mm^2 samples. This is due to a variant selection mechanism happening during the columnar growth: certain crystallographic orientations have a more favourable growing mechanisms than other ones, explaining why certain grains becomes larger while other are disappearing [119].

5 Simulations

Because the manufacturing parameters optimisation on commercial SLM machines is a repetitive process, the role of simulations has become more and more important to help predicting the material behaviour during printing. These models must undergo validation to be trusted. The MiniSLM allows to record the temperature evolution in the sample, which can be use as a validation criteria for the models. An in-depth presentation of the methods used to build the simulations is given in this chapter. The simulation outputs will be then compared to the temperature results from the previous chapter.

5.1 Methods

5.1.1 FEM modelling methodology

Simulations were performed using the Finite Element Analysis (FEA) software Abaqus/CAE [120]. Figures 5.1a and b present the model geometries used to simulate the 8x2 mm^2 and 2x2 mm^2 experimental samples, respectively. The simulated geometries are composed of a build plate with a coarse mesh and the printed sample with a finer mesh, as shown in figure 5.1c.

During *operando* experiments, a sample is printed with 5 layers, each of them being 30 μm thick, giving a total sample height of 150 μm. The sample in the simulation has dimensions of 8.4 x 2.2 x 0.15 mm^3 for the 8x2mm^2, and 2.4 x 2.2 x 0.15 mm^3 for the 2x2 mm^2. It is divided into two subsections along the Z-direction: the first 30 μm correspond to the layer of freshly deposited powder with a 60 x 60 x 30 μm^3 mesh size (orange); below, a 120 μm representing the already printed layers, simulated with a mesh size of 60 x 60 x 60 μm^3 (blue).

To reduce computation time, the size of the build plate that was simulated was restricted, the further environment was mimicked with boundary conditions. The build plate in the simulations has dimensions of 9.4 x 2.7 x 1 mm^3 and 2.4 x 2.7 x 1mm^3 for the 8x2mm^2 and 2x2mm^2, respectively. The material properties of the build plate are defined as bulk Ti-6Al-4V. The mesh size follows a gradient-like pattern with element dimensions going from 120 μm near the sample to 300μm on the outer side. A DC3D8 (3D 8-node linear) element type was used to mesh all the parts. A fixed-temperature boundary condition of 340K is applied on the bottom, back and sides of the build plate section. This temperature value was selected in correlation with a thermocouple measurement performed experimentally on the substrate.

(a) Simulation geometry for the 8x2 mm² sample and corresponding coordinate system

(b) Simulation geometry for the 2x2 mm² sample

(c) Zoom on (a) and (b)
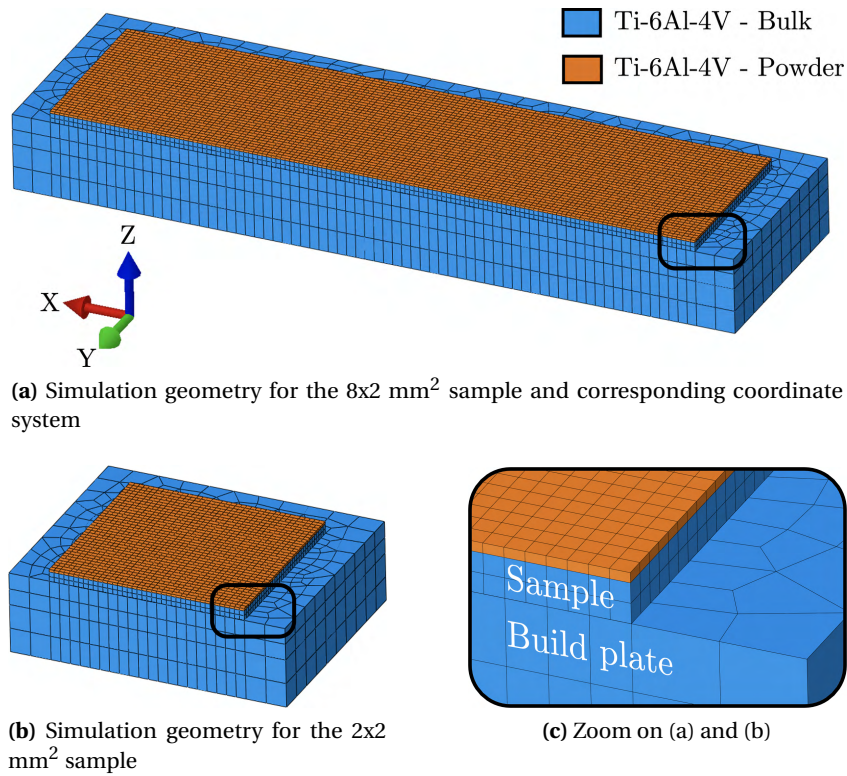
Figure 5.1 – Simulation geometry for the 8x2 mm² and 2x2 mm² samples, corresponding coordinate system and zoom on the simulation geometry showing the sample and build plate

In Abaqus, the problem was modelled as an uncoupled heat transfer analysis in two stages. The first stage consists of a transient analysis of the laser scanning. An automatic time step increment was selected with a range between 10^{-8}s and 10^{-5}s, with an initial time step of 10^{-6}s. The total accumulated simulation time was 130.16 ms for the 2x2 mm² sample and 460.12 ms for the 8x2 mm² sample. The second stage consists of a transient analysis of the sample cooling after the laser scanning is completed and the laser is switched off. Here, the automatic time step increment was selected in the range between 10^{8}s and 10^{-4}s, with an initial time step of 10^{-6}s. The total accumulated simulation time was 1s for both samples. The equation solver was set to use a direct method, with a quasi-Newton solution technique. The extrapolation of the previous states at the start of each increment was set to use a parabolic function.

The laser scanning was modelled using the DFLUX subroutine, with a scanning direction along the X-axis. In our previous work [116, 121], we showed that a constant time offset was present between the temperature peaks during laser scanning. This is related to the settling time of the scanning head, needed for the mirrors to change position from the end of one scanning track to the beginning of the following one. During this period, the laser is turned off. The experimentally measured settling time was 0.63 ms for bi-directional scanning and was considered in our laser scanning subroutine.

Heat losses were taken into account by applying a surface film condition with the FILM subroutine to all exposed surfaces, i.e. the top and front of the sample and build plate assembly. Finally, material transformation from powder to bulk Ti-6Al-4V upon laser melting and solidification was allowed by using the USDFLD subroutine. More details are given in the following section.

5.1.2 Material properties

The thermophysical properties for the bulk Ti-6Al-4V are taken from the book of Mills [122]. We consider here the density ρ, thermal conductivity k and the specific heat capacity C_p as presented in figure 5.2.

(a) Density of the bulk and powder

(b) Thermal conductivity of the bulk and powder

(c) Specific heat capacity of the bulk
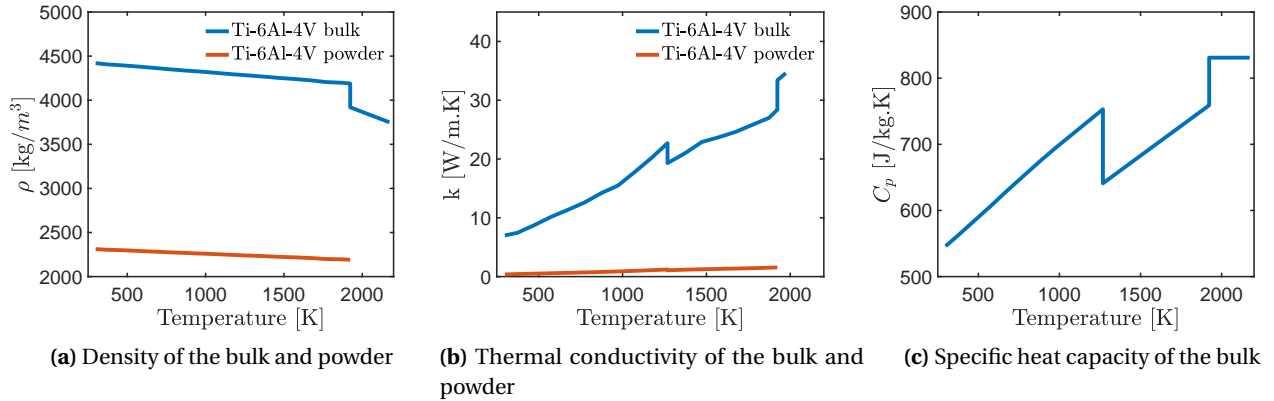
Figure 5.2 – Ti-6Al-4V thermophysical properties used in Abaqus. The data for the bulk is taken from Mills [122].

We consider the powder distribution as simple cubic, with a packing coefficient of 0.523 [98, 123]. The powder density in figure 5.2 is obtained by multiplying the bulk density before the melting point by the packing coefficient. The thermal conductivity of the powder is obtained following the equation of Sih and Barlow [124]:

$$
\frac{k}{k_g} = \left(1 - \sqrt{1-\varphi}\right)\left(1 + \frac{\varphi k}{k_g}\right)
$$
$$
+ \sqrt{1-\varphi}\left\{(1-\phi)\left[\frac{2}{1-\frac{Bk_g}{k_s}}\left(\frac{B}{\left(1-\frac{Bk_g}{k_s}\right)^2}\left(1-\frac{k_g}{k_s}\right)\ln\frac{k_s}{Bk_g} - \frac{B+1}{2} - \frac{B-1}{1-\frac{Bk_g}{k_s}}\right) + \frac{k_R}{k_g}\right] + \frac{\phi k_{contact}}{k_g}\right\} \quad (5.1)
$$

with k the thermal conductivity of the powder bed, k_g the thermal conductivity of the gas [125], k_s the thermal conductivity of the solid (figure 5.2b), φ the porosity of the powder bed, k_R the thermal conductivity of the powder owing to radiation [124], ɸ the surface contact between particle (here we chose ɸ=0.05 [126]) and B the deformation parameter of the particle (we assume B=1 for spherical particles). Since ɸ>0.01, we have $k_{contact} \approx k_s$ [124]. The values obtained after calculation (figure 5.2b) are of the same order of magnitude as used in [127].

To simulate the transformation from powder to solid after laser melting, the USDFLD subroutine is used in Abaqus. The red curves for density (ρ) and thermal conductivity (k) in figure 5.2 a and b describe the powder properties at the beginning of the simulation. When the laser scans and the temperature locally exceeds the melting point locally, the material transforms and follows the bulk properties described by blue curves. The specific heat capacity (C_p) pictured in figure 5.2c is used for both the bulk state or powder state. The latent heat of fusion and vaporisation are given in table 5.1. The complete code for the USDFLD subroutine is available in section C.2 of the appendices part.

Table 5.1 – Latent heat of Ti-6Al-4V [36, 122]

Latent heat of fusion			2.86×10^5 J/kg
Solidus	1877.15 K	Liquidus	1923.15 K
Latent heat of vaporisation			9.83×10^6 J/kg
Liquidus	3563.15 K	Vaporisation	3663.15 K

5.1.3 Heat losses

The heat losses q_{loss} are modelled with the FILM subroutine in Abaqus. The complete code for the FILM subroutine is available in section C.2 of the appendix part. The heat losses can be introduced through a film coefficient h [128] with:

$$q_{loss} = h \times (T - T_0) \tag{5.2}$$

with T the local surface temperature and T_0 is the sink temperature, both in Kelvin (room temperature, 298.15 K).

The idea here is to establish a film coefficient that which combines convection losses (h_c) and radiation losses (h_r). In the case of convection losses, the equation is:

$$q_{conv} = h_c \times (T - T_0) \tag{5.3}$$

The heat losses by convection are directly proportional to the value of h_c. In the case of radiation losses, the heat transfer is represented by the equation:

$$q_{rad} = \varepsilon \sigma (T^4 - T_0^4) \tag{5.4}$$

With ε the emissivity of the material and σ the Stefan-Boltzmann constant. Equation 5.4 can be rewritten:

$$q_{rad} = \varepsilon \sigma (T^2 + T_0^2)(T^2 - T_0^2) = \varepsilon \sigma (T^2 + T_0^2)(T - T_0)(T + T_0) \tag{5.5}$$

By introducing $h_r = \varepsilon \sigma (T^2 + T_0^2)(T + T_0)$ the radiation heat transfer coefficient, the equation 5.5 becomes:

$$q_{rad} = h_r \times (T - T_0) \tag{5.6}$$

Then by combining equations 5.2, 5.3 and 5.6, one can write:

$$q_{loss} = q_{conv} + q_{rad} = h_c \times (T - T_0) + h_r \times (T - T_0) = (h_c + h_r) \times (T - T_0) = h \times (T - T_0) \tag{5.7}$$

The film coefficient, which now combines convection and radiation losses, can now be written as:

$$h = h_c + h_r = h_c + \varepsilon \sigma (T^2 + T_0^2)(T + T_0) \tag{5.8}$$

The emissivity of the material is temperature-dependent. The emissivity values were extracted from the measurements done by Yang et al. [129] and fitted as shown in figure 5.3. The equation obtained after fitting

is:

$$\varepsilon = \begin{cases} \varepsilon(T) \; if \; \varepsilon(T) < 1 \\ 1 \; if \; \varepsilon(T) > 1 \end{cases}$$

$$with \; \varepsilon(T) = 0.231 + 3.06 \times 10^{-4} \exp\left[-7.55 \times 10^{-3} \left(4.19 \times (T - 273.15)\right)\right]$$

(5.9)
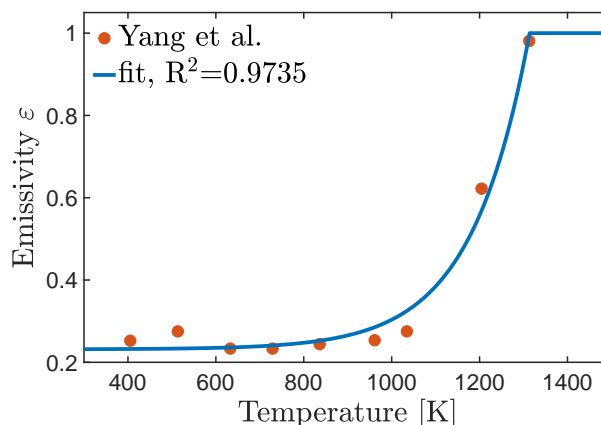
Figure 5.3 – Emissivity curve for Ti-6Al-4V. The red markers are the experimental values taken from Yang et al. [129]. The blue curve is obtained after fitting the data using equation 5.9.

5.1.4 Laser heat source models

Different laser heat source models were selected to compare the simulation outputs and experimental data obtained by X-ray diffraction. Table 5.2 gives an overview of the parameters of the different models. The complete code for the different DFLUX subroutines is available in section C.2 of the appendix part.

Model 1: Simple ellipsoid model (M1)

The first laser source model was taken from Zhang et al. [36] and consists of an ellipsoidal heat flux derived from the double ellipsoid model of Goldak [130]. The volumetric heat source equation is the following:

$$Q(x, y, z, t) = \frac{2\eta P}{abc\pi\sqrt{\pi}} \exp\left[-\left(\frac{(x + vt)^2}{a^2} + \frac{y^2}{b^2} + \frac{z^2}{c^2}\right)\right]$$

(5.10)

with η the absorptivity of the material, P the laser power; a, b and c the ellipsoid semi-axis, and v the scanning speed. Here $a = e \times r$, $b = \frac{r}{e}$ and $c = d$ with e the melt pool eccentricity, r the laser radius, and d the penetration depth of the laser. In the simulation, we do not consider any eccentricity, so $e = 1$. The laser power was set at P = 250W and the radius at $r = 50\mu$m. As reported by Zhang [36], the laser penetration was chosen to be within the powder layer, $d = 30\mu$m, and the laser absorption was set at $\eta = 55\%$.

In model M1 of Zhang at al. both radiation and convection losses are considered, with a heat transfer coefficient of 18 W/m^2.K [36] for convection losses. We will consider a heat transfer coefficient h_c=20 W/m^2.K to match the following models.

Model 2: Double ellipsoid model (M2)

The second laser source is the one used by Mirkoohi et al. [77]. Four different heat source models are compared in the paper of Mirkoohi. The semi-ellipsoid model from Goldak [130] was retained because it predicted the melt pool geometry over a wide range of process parameters. The heat source equation is the following:

$$Q(x, y, z, t) = \begin{cases} \frac{6\sqrt{3}f_f \eta P}{a_f bc\pi\sqrt{\pi}} \exp\left[-3\left(\frac{(x+vt)^2}{a_f^2} + \frac{y^2}{b^2} + \frac{z^2}{c^2}\right)\right] \; for \; x > vt \\ \frac{6\sqrt{3}f_r \eta P}{a_r bc\pi\sqrt{\pi}} \exp\left[-3\left(\frac{(x+vt)^2}{a_r^2} + \frac{y^2}{b^2} + \frac{z^2}{c^2}\right)\right] \; for \; x < vt \end{cases} \tag{5.11}$$

with η the absorptivity of the material, P the laser power; a_f, a_r, b and c the ellipsoid semi-axis, and v the scanning speed. Here a_f is the ellipsoid semi-axis in front of the laser, and a_r in rear of the laser. Moreover, two additional coefficients - f_f and f_r - are introduced as the fraction of heat deposited in the front and rear of the heat source, where $f_f + f_r = 2$. For the sake of continuity on $x = 0$, we apply the constraint:

$$\frac{f_f}{a_f} = \frac{f_r}{a_r} \tag{5.12}$$

In the same fashion as the model of Zhang, the laser penetration was chosen to be within the powder layer, $d = 30\mu m$, and the laser absorption was set at $\eta = 55\%$. The laser power was set at P = 250W and the radius at $r = 50\mu m$. We chose $a_f = r$ and $b = r$ and $c = d$. A 3-dimensional representation of the model is given in figure 5.4.
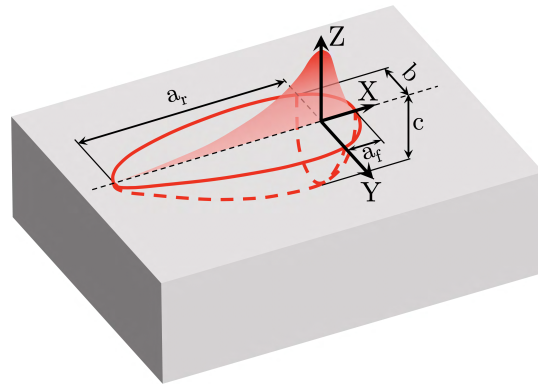
Figure 5.4 – Graphic representation of Goldak's double ellipsoid model

In model M2, both radiation and convection losses are considered, with a heat transfer coefficient of h_c=20 W/m^2.K for the convection losses [77].

Models 3 and 4: Cylindrical heat source with parabolic penetration depth (M3, M4)

The third and fourth models are taken from Ali et al. [78]. The heat source expression is defined as a cylindrical heat source with a parabolic decay for the penetration in the material. The equation is the following:

$$Q(r, z) = I_r \times I_z \; with \begin{cases} I_r = 2.2032\eta\frac{P}{\pi r_0^2} \; for \, r < r_0 \\ I_z = -15z^2 + 4z + 2 \; for \; 0 > z > -250\mu m \end{cases} \tag{5.13}$$

With I_r the radial intensity of the laser, I_z the intensity penetration depth, η the absorptivity of the material, P the laser power and r_0 the laser spot radius. The laser power was set at P = 250W and the radius at $r_0 = 50\mu m$, and the absorptivity was set at η = 60%, as suggested by Ali.

Additionally, an enhanced thermal conductivity is considered to account for the Marangoni convection inside the melt pool [6]. The thermal conductivity for M3 and M4 is equal to:

$$k^*(T) = \lambda \times k(T) \ with \ \lambda = \begin{cases} 1 \ if \ T < T_{melt} \\ 4 \ if \ T > T_{melt} \end{cases} \tag{5.14}$$

With k the thermal conductivity in figure 5.2, and λ the isotropic enhancement coefficient.

In the model M3, only the convection losses are considered, with a heat transfer coefficient consider of h_c=20W/m^2.K; and the radiation losses are ignored [78]. In the model M4, radiation losses are added to M3.

Table 5.2 – Simulation summary

Parameters	M1 (Zhang et al. [36])	M2 (Mirkoohi et al. [77])	M3 (Ali et al. [78])	M4 (Ali et al. [78])
Laser heat flux	Ellipsoid	Double ellipsoid	Cylindrical + Parabolic	Cylindrical + Parabolic
Absorption (η)	55%	55%	60%	60%
Convection losses (h_c)	20 W/m^2.K	20 W/m^2.K	20 W/m^2.K	20 W/m^2.K
Radiation losses (h_r)	Accounted	Accounted	Ignored	Accounted
Material properties	Mills [122]	Mills [122]	Mills [122] Enhanced k	Mills [122] Enhanced k

5.2 FEM simulation and experimental results

The simulation results presented in this section are compared to the experimental temperature profiles extracted from figures 4.19 and 4.16 in section 4.3.2, which were measured with an X-ray beam spot size of 80x140 μm^2 FWHM. Because the α/α′ diffraction pattern is an overlap of two different series of peaks coming from the α and α′ phases (see figure 3.7), a slight peak doubling is observed in some of the reflections we measured. The $(01.2)_{\alpha/\alpha'}$ reflection was chosen since it does not show any strong peak doubling, which could influence the temperature result. The $\{002\}_\beta$ reflection was selected as the only stand-alone β peak on the diffraction pattern.

The temperature profiles were extracted by taking a weighted average of the nodal temperature of 42 nodes at the centre of the sample, where the X-ray beam is positioned (figure 4.17). These nodes represent a volume corresponding to the probed X-ray volume with an area of 120 x 360 μm^2 and a depth of 30 μm, the mesh height of the powder layer (accounting for the X-ray penetration in the material). They are separated into two groups of 21 nodes each positioned on top of each other. In the (X,Y) plane the spacing among the nodes is 60 μm. In the Z-direction, they are separated by 30 μm. To calculate the average nodal temperature in the simulations, the nodes positioned on top of each other (Z-direction) are first averaged. A weighting function corresponding to the X-ray beam intensity distribution is then applied to these 21 nodes. Figure 5.5a shows the resulting group of 21 nodes superimposed to the multivariate Gaussian intensity distribution, figure 5.5b shows a top view in the (X,Y) plane.

Since the experimental temperature profile does not include the temperature of the molten phase, only the

(a) 3D X-ray beam projected on the sample surface

(b) Top view of (a)
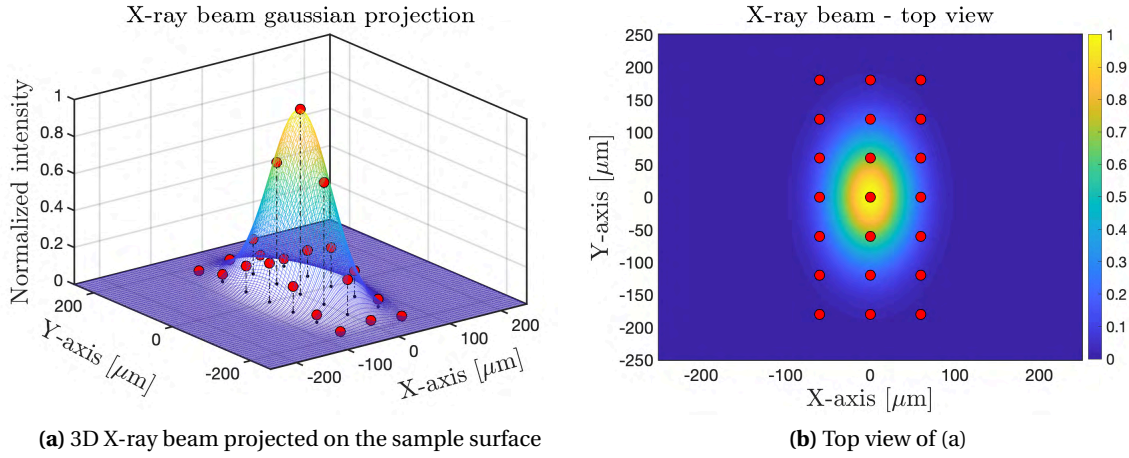
Figure 5.5 – 3-dimensional representation of the X-ray Gaussian intensity distribution with an 80x140 μm^2 FWHM. The red markers present the position of the nodes used to calculate the average temperature in the simulation. The vertical dashed lines represent the projection of the markers onto the (X,Y) plane.

nodes that having a temperature below 1923.15 K, for which the material is solid, are considered for the weighted averaging. The resulting temperature follows the equation:

$$\bar{T} = \sum_i \frac{m_i T_i}{m_i} \; with \; m_i = \begin{cases} m_i \; if \; T < T_{melt} \\ 0 \; if \; T > T_{melt} \end{cases} \tag{5.15}$$

With $\bar{T}$ the weighted average temperature, T_i the nodal temperature, m_i the weighting coefficient from the X-ray intensity profile (figure 5.5) and T_{melt} the melting point of Ti-6Al-4V.

5.2.1 2x2 mm^2 sample

Figure 5.6a-d provides for the 4 models the simulated temperature evolution as a function of time (dashed) as well as the evolution of the molten volume percentage (filled curve) for the cycles close to the time when the laser crosses the probed surface region A_{XR} . Because only the nodes outside of the molten volume are used to calculate the weighted average, as shown in equation 5.15, the size of the molten volume influences the shape of the temperature evolution. This causes a change in slope during heating, as is clearly visible for model M1 (figure 5.6) which has the highest molten volume percentage. Figures 5.6e-f show the melt pool dimensions at t ≈ 65 ms for the four models with a view from the top and the middle cross-section along the X-axis. The black lines show the mesh size (60 μm in X-Y plane, 60/30 μm in Z-direction for solid/powder respectively). The red dots show the position of the nodes used for the calculation of the average temperature.

Figure 5.7a compares the simulated temperature profile for the four models (dashed lines) with the experimental results for the (01.2)$_{\alpha/\alpha'}$ and the {002}$_\beta$ reflections. The laser scanning starts at t = 0 ms and finishes at t ≈ 130 ms, which is indicated by the black arrow. The experimental temperature evolution in the probed volume exhibits three regimes: (1) heating-up of the α/α' phase until the first signal from the β phase is observed at t ≈ 48 ms; (2) cycling within the β phase while the laser is scanning, the highest temperature is reached when the laser overlaps with A_{XR} at t≈ 65 ms; (3) cooling down after the laser is sufficiently far away

(a) 2x2 mm^2 sample - Model M1

(b) 2x2 mm^2 sample - Model M2

(c) 2x2 mm^2 sample - Model M3

(d) 2x2 mm^2 sample - Model M4

(e) Melt pools for models M1 at t≈65 ms

(f) Melt pools for models M2 at t≈65 ms

(g) Melt pools for models M3 at t≈65 ms

(h) Melt pools for models M4 at t≈65 ms
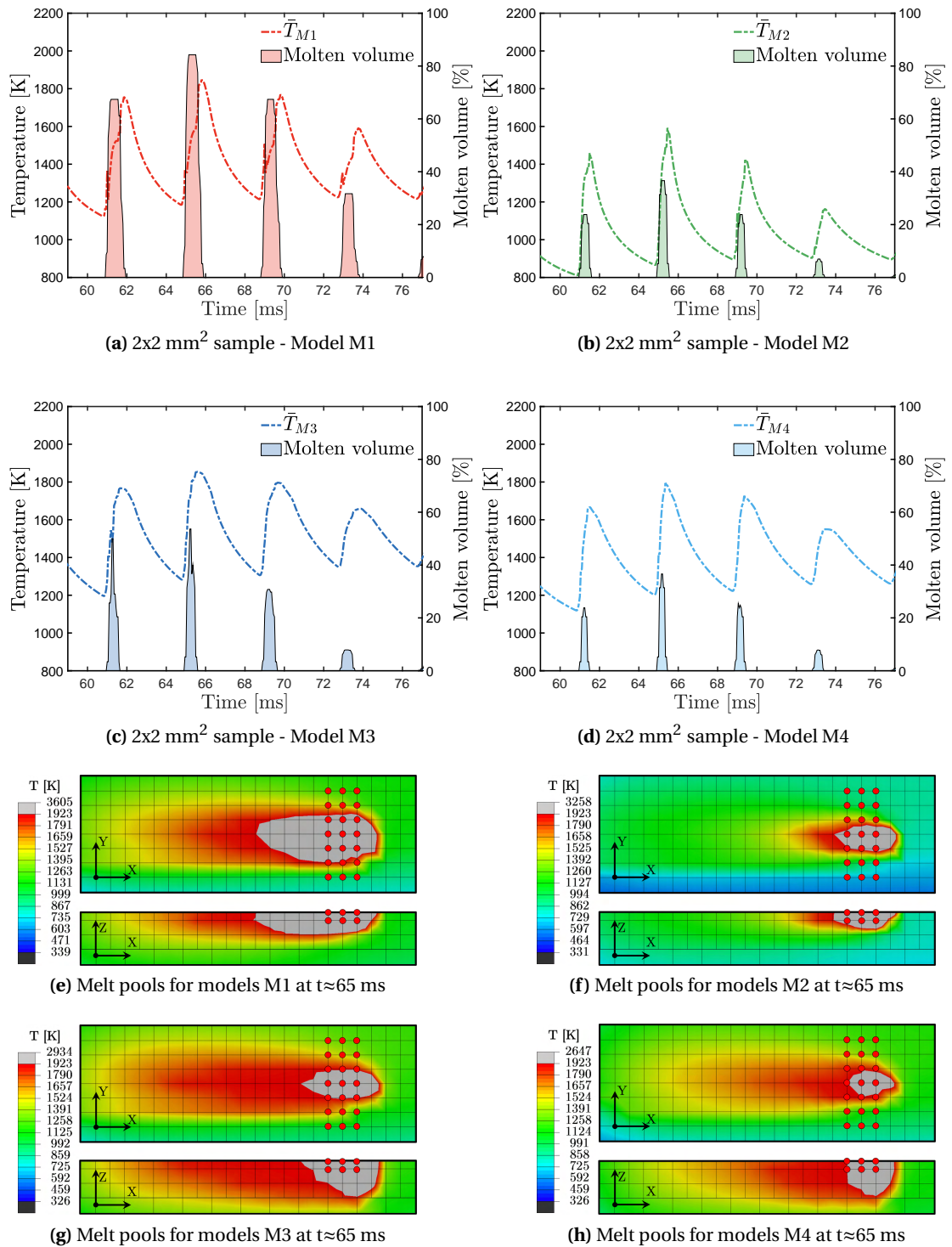
Figure 5.6 – Average temperature and molten volume interaction with A$_{XR}$ for: a) M1; b) M2; c) M3 and d) M4; e)-h) Top view and cross-section of the simulated melt pools for models M1 to M4 at t≈65 ms, when the laser beam overlaps with A$_{XR}$.

from A_{XR}, i.e. from t ≥ 76 ms on, during which the β phase disappears and the α/α′ phase is formed. All 3 regimes are also observed in the simulated curves (without phase information). All models have difficulties in predicting the temperatures measured during heating-up in the first regime. Figure 5.7b zooms into the second regime around the cycle for which the maximum temperature is obtained, corresponding to the time when the laser spot overlaps with A_{XR} (t ≈ 65ms).

(a) 2x2 mm^2 sample - Experiment vs. Simulation

(b) Zoom on (a)
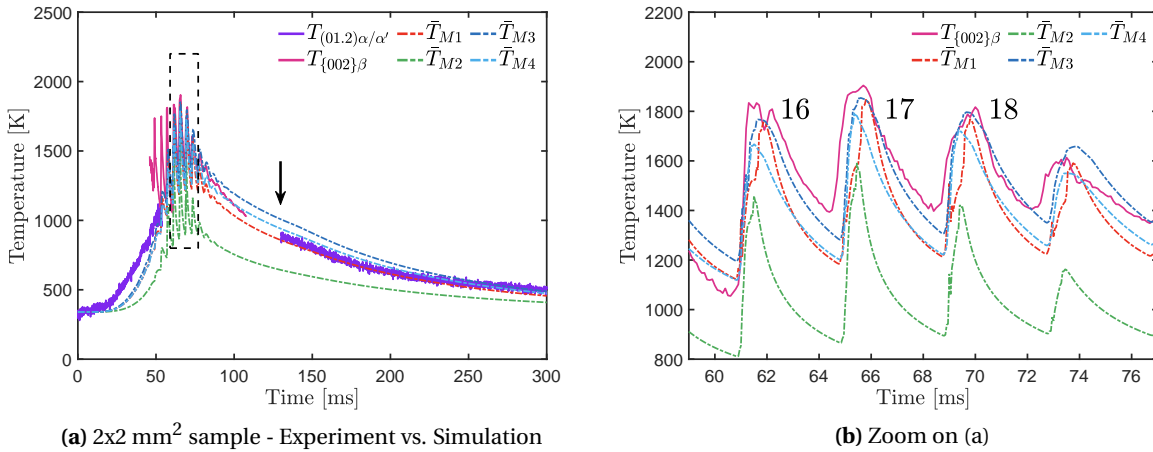
Figure 5.7 – Experimental temperature profile of the $(01.2)_{\alpha/\alpha'}$ and 002_β reflections from figure 4.19 in purple and pink, respectively, with superimposed the simulated results for models M1 to M4 superimposed in dashed lines. The black arrow indicates the end of the laser scanning. A top view and cross-section of the simulated melt pools for models M1 to M4 at t≈65 ms is presented below, when the laser beam overlaps with A_{XR}.

The model M1 (figure 5.7a and b, red) seems to predict quite well many aspects of the experimental temperature profile of the laser scanning for the 2x2 mm^2 sample. When the laser and X-ray coincidence is maximal, the simulated profile tends to underestimate only slightly the experimental data (figure 5.7b). The temperature rise in this cycle is a bit delayed which can be attributed to the larger width of the melt pool (figure 5.6e), leaving fewer remaining nodes for the calculation of the average nodal temperature. After completing a 2x2 mm^2 layer, the cooling down matches the experimental curve well.

The model M2 (figure 5.7a and b, green) underestimates the temperature profile during the coincidence cycle (t ≈ 65 ms) by 400K on average. Furthermore, the overall heating and cooling curves of the α/α′ phase (figure 5.7a) are lower compared to the other models. The melt pool size (figure 5.6f) is rather small, it has a length of approximately 250 μm (X-direction), a width of around 100 μm (Y-direction), and a depth of around 70 μm (Z-direction).

The model M3 (dark blue) matches well the temperature curve in the high-temperature β regime (figure 5.7b). It also predicts much better the initial heating-up during the deposition of the first lines (figure 5.7a). In the cooling part of the temperature curve (figure 5.7a, after t ≈ 80ms), the model tends to overestimate the experimental α/α′ temperature by almost 200K, which can be ascribed to the fact that radiation losses are not included [78]. The melt pool (figure 5.6g) has an interesting profile; it goes quite deep compared to the models M1 and M2. It has a length of around 330 μm (X-direction), a width of around 120 μm (Y-direction) and a depth of around 150 μm (Z-direction). This very deep melt pool is likely due to a combination of the

enhanced thermal conductivity and the parabolic penetration depth. The heat penetration goes down to 250 µm compared to a penetration depth restricted to the first layer in the case of M1 and M2. This results in a consequently larger heated volume, as seen by the spread of the red area in the tail of the melt pool (figure 5.7e).

The model M4 (cyan), which adds radiation loss to M3, reduces the maximal temperature that is reached and brings down the temperature profile in the high-temperature β regime (figure 5.7b) as well as during the cooling part after printing a complete layer. The heating part of the temperature when the laser approaches A_{XR} remains the same. By comparing figure 5.6g and h, one can see that the width and depth of the melt pool are comparable between M3 and M4. In M4, a width of 110 µm is obtained in the Y-direction and a depth of 140 µm in the Z-direction. In other words, adding radiation loss reduces the length of the melt pool to 130 µm.

5.2.2   8x2 mm^2 sample

The 8x2 mm^2 model contains around 4 times more elements than the 2x2 mm^2 model, so the computation time is much longer. For that reason, we chose to simulate the 8x2 mm^2 sample for only the models M1 and M4.

Figure 5.8a and b show the comparison between the simulated (dashed lines) and experimental temperature evolutions obtained from the X-ray data (figure 4.16). The laser scanning starts at t = 0 ms and finishes at t ≈ 460 ms, as indicated by the black arrow. Figure 5.8b zooms in around t ≈ 232ms, the time when the laser spots overlaps with A_{XR}. Figure 5.8c and d show the melt pool dimensions at t ≈ 232ms for the two models M1 and M4 with a view from the top and a middle cross-section along the X-axis.

Due to the larger scan vector used in the 8x2 mm^2 sample, the phase transformation from α/α′ to β occurs during each line scan. The simulated temperature is averaged over the nodes and provides no phase-specific information. Similar as for the 2x2 mm^2 sample, three regimes can be recognised in the temperature evolution: (1) heating during the first line scan, the X-ray probed volume remaining in the α/α′ phase (figure 5.8a, until t ≈ 180ms); (2) cycles close to the scan line overlapping with A_{XR} (here the experimental curve shows the β and α/α′ phases) including the line with the maximum temperature (figure 5.8b, at t ≈ 230ms); and (3) cooling after the last signal coming from the β-phase has disappeared (figure 5.8a, from t ≈ 290ms).

The simulated melt pool dimensions are smaller in the 8x2 mm^2 sample when compared with the 2x2 mm^2 sample. This can be explained by the larger scanning vector, reducing overall heat accumulation in A_{XR}, and the larger sample representing a stronger heat sink. As a result, the thermal gradient around the melt pool is higher and the melt pool becomes smaller. The melt pool of M1 (figure 5.8c) has an elongated profile along the X-direction with a length of 450 µm. It is still shallow in the Z-direction, with a depth of 80 µm. The width is similar to the 2x2 mm^2 sample with 200 µm along the Y-direction. For the model M4 (figure 5.8d), the obtained melt pool is very small, it has a length of 140 µm along the X-direction, a width of 70 µm along the Y-direction and a depth of 110 µm in the Z-direction.

During laser scanning of the first lines, before A_{XR} is reached, the two models predict well the increase in temperature of the α/α′ phase. (figure 5.8a). The predicted temperatures of the β phase at t ≈ 230ms, when the laser coincides with A_{XR}, are close to the experimental one. The predicted cooling curve does however

(a) 8x2 mm^2 sample - Experiment vs. Simulation

(b) Zoom on (a)

(c) Melt pools for models M1 at t≈232 ms

(d) Melt pools for models M4 at t≈232 ms
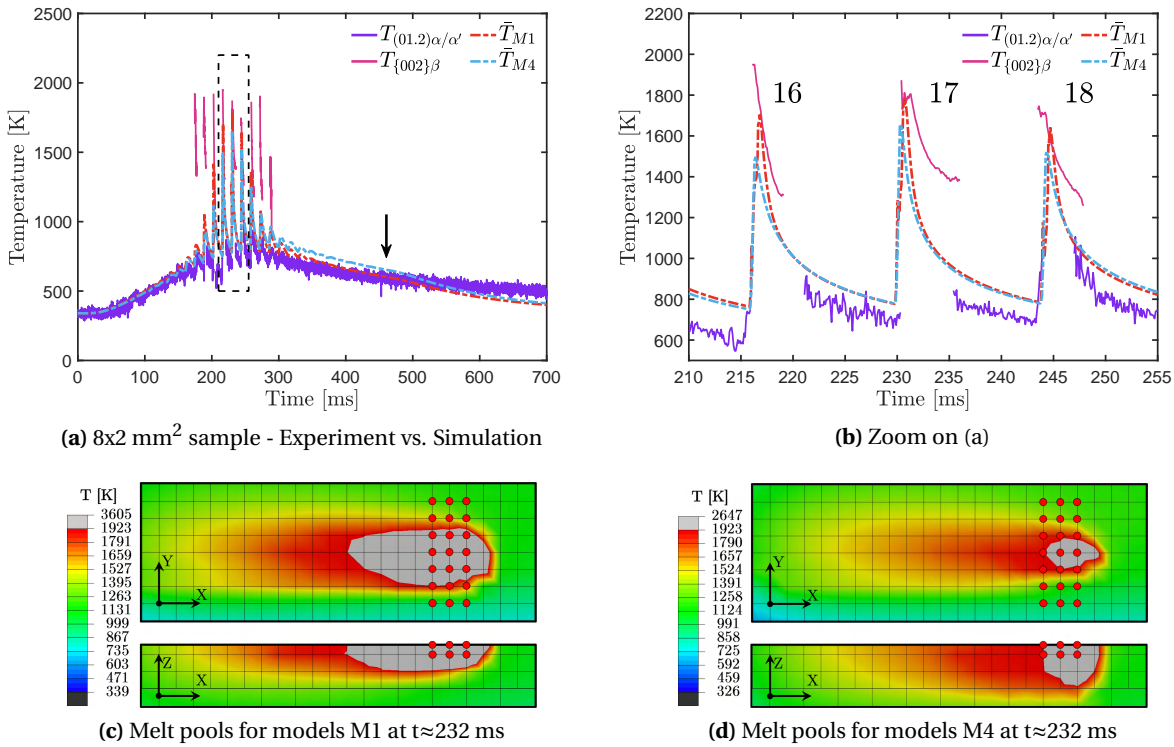
Figure 5.8 – Experimental temperature profile from figure 4.16 together with the temperature profile of the $(01.2)_{\alpha/\alpha'}$ and 002_β reflections in purple and pink, respectively, with superimposed the simulated results for models M1 and M4 superimposed in dashed lines. The black arrow indicates the end of the laser scanning. A top view and cross-section of the simulated melt pools for models M1 and M4 at t≈232 ms is presented below, when the laser beam overlaps with A_{XR}.

not follow the experimental cooling from the β and the α/α′ phase. Here, one has to take into account that the transformation is not homogeneous over the experimentally probed volume and that the temperatures are derived from the individual diffraction peaks, whereas the simulation does not provide information on phase composition. During cooling of the α/α′ phase (t > 290ms), M4 predicts slightly higher temperatures than experimentally measured. At t ≈ 460ms, when the laser is switched off, the simulated curves show a small change in the slope and the X-ray probed volume starts cooling faster.

5.2.3 Melt pool depth and width and optical microscope images of cross-section

It has been shown in literature that one can study the melt pool bead profile by doing single line printing on an unused substrate, and reveal the microstructure by chemical etching [131]. Single lines of 8 mm and 2 mm lengths were printed on a Ti-6Al-4V substrate after the deposition of a 30 μm thick power layer. The printing parameters used are the same as the one listed in table 4.5 in section 4.3.2. Figure 5.9 shows the obtained samples.

A cross-section was made in center of the sample, indicated by the white dashed line. Both faces were mechanically polished and etched with Kroll's reagent. Figure 5.10 show the results of the left- and right-hand
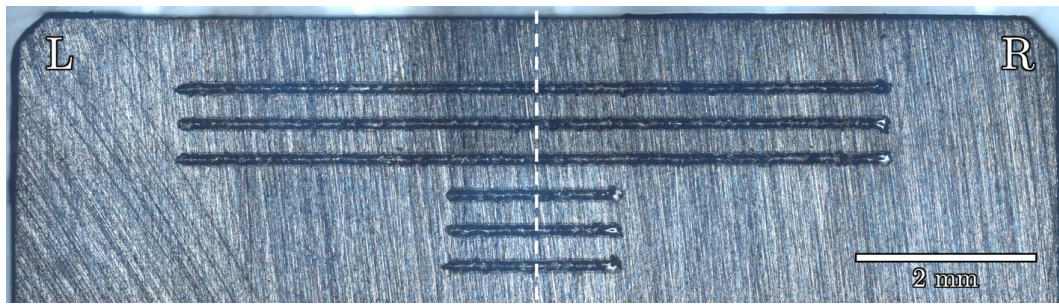
Figure 5.9 – Single tracks of 8 mm and 2 mm long made in Ti-6Al-4V

sides respectively, after etching.
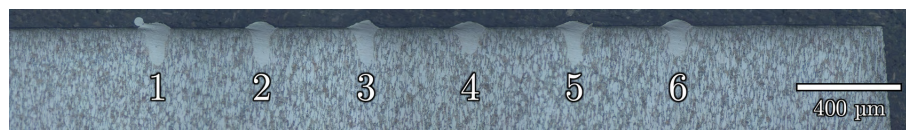
(a) Cross-section from the left hand side of figure 5.9 (L)

(b) Cross-section from the right hand side of figure 5.9 (R)

Figure 5.10 – Cross-sections of a single track. The contrast between the light α/α' phase of the weld bead and the darker $\alpha + \beta$ microstructure allows to determine the size of the melt pool

This way, it is easy to distinguish the α/α' microstructure of the weld bead in light grey, which can be attributed to the melt pool, from the darker $\alpha + \beta$ microstructure of the Ti-6Al-4V substrate [131]. Since no major difference was observed between the 8 mm long track and the 2 mm one, a number was assigned to each bead (figure 5.10) and the width and depth of each of them was measured. The results are listed in table 5.3 .

Table 5.3 – Dimension of the weld beads measured from figure 5.10

Bead number	1	2	3	4	5	6	7	8	9	10	11	12	Mean	Standard deviation
Width [µm]	119	109	121	130	120	113	123	119	115	120	114	109	118	6
Depth [µm]	160	166	163	122	165	134	126	145	158	148	163	150	150	15
Aspect ratio	1.34	1.52	1.35	0.94	1.38	1.18	1.02	1.22	1.38	1.23	1.43	1.38	1.28	0.17

6 Discussions

This chapter focuses on discussing the results obtained on Ti-6Al-4V through experimentation and simulations. First, the topic of the parameter transferability from the literature to the MiniSLM is reviewed. Then the influence of the measurement configuration and the detector speed on the XRD phase evolution during measurements is detailed. This is followed by a presentation of the data analysis improvement on Matlab. Afterwards, the phase evolution of the material is compared to the resulting microstructure. The question of the appropriate choice of the X-ray beam size will be answered. Finally, the comparison between the simulated and experimental results is inspected more closely.

6.1 Machine parameters transferability

In SLM processing, finding the good parameter combination to produce fully dense samples on a given machine is a tedious procedure. Various parameter combinations are reported in literature for Ti-6Al-4V, with laser power varying from 50W to 300W and scanning speeds from 100 mm/s to 1400 mm/s [7, 31]. Depending on the reference, the hatch distance is also often reported together with the laser power and scanning speed.

(a) P − v window from Song et al. [72]

(b) P − v window from Gong et al. [7]
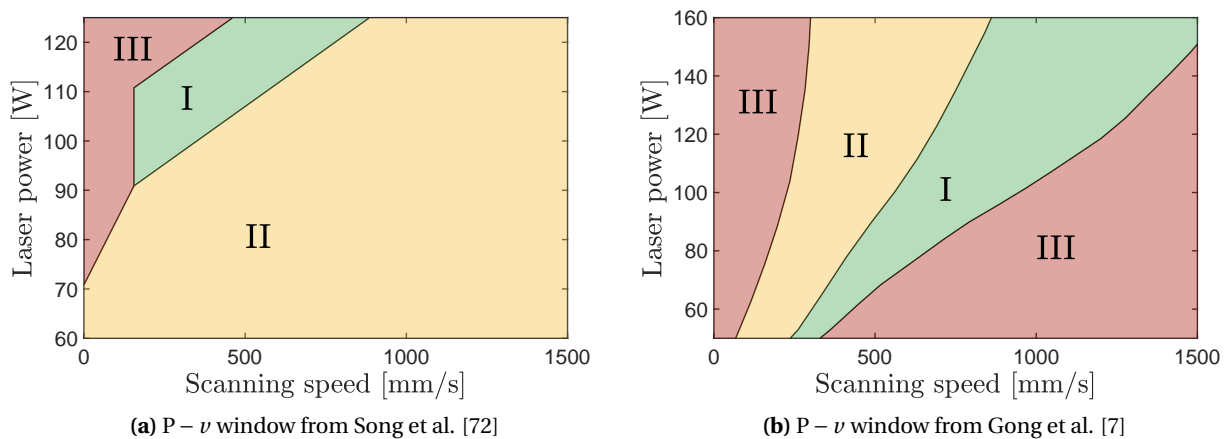
Figure 6.1 – Processing windows based on the laser power (P) and scanning speed (v) combinations, obtained from the literature for Ti-6Al-4V

Three different laser spot diameters (50 μm, 75 μm and 100 μm) were tested in section 4.1 over a large range of parameter combinations. Here, the results obtained in section 4.1 are compared with the literature to assess the machine parameter transferability of the MiniSLM. Song et al. reported a parameter study based on the printing of single tracks with a laser power varying from 60W to 125W and a scanning speed between 100 mm/s to 1600 mm/s [72]. The resulting $P - v$ processing map is presented in figure 6.1a. Gong et al. also reported similar results based on a sample porosity study. The laser power varied between 50W and 160W, and the scanning speed reached up to 1600 mm/s [7], as shown in figure 6.1b.
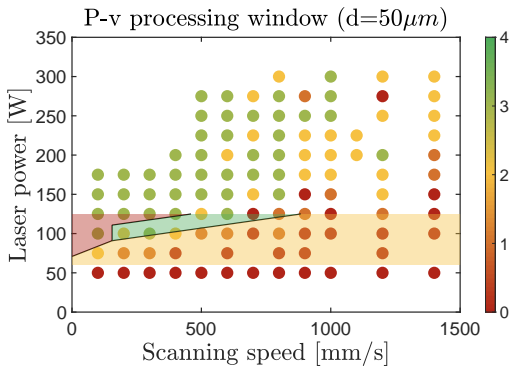
(a) Figures 4.4 with results from Song et al. [72]
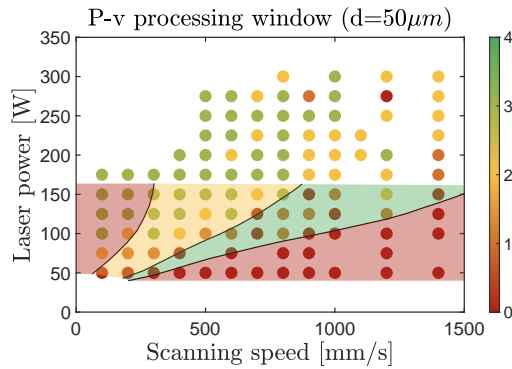
(b) Figures 4.4 with results from Gong et al. [7]
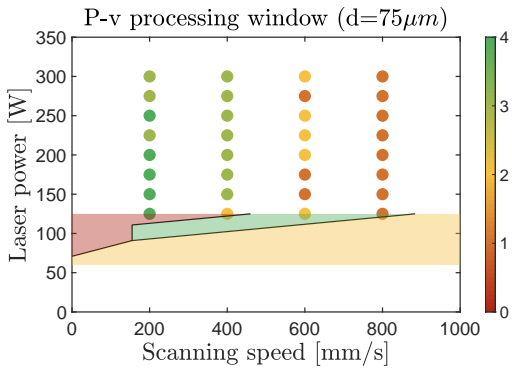
(c) Figures 4.6 with results from Song et al. [72]
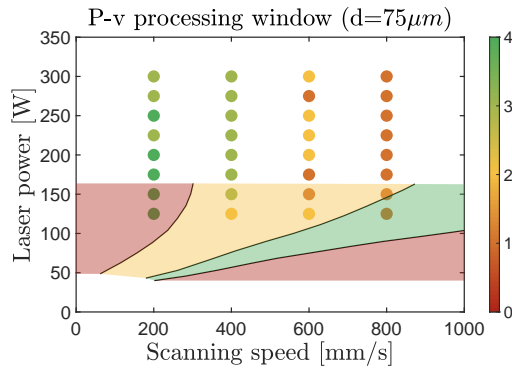
(d) Figures 4.8 with results from Gong et al. [7]
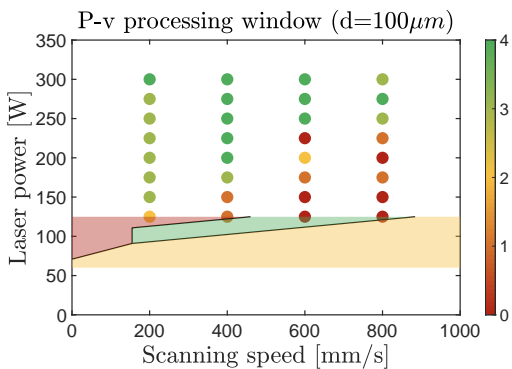
(e) Figures 4.8 with results from Song et al. [72]
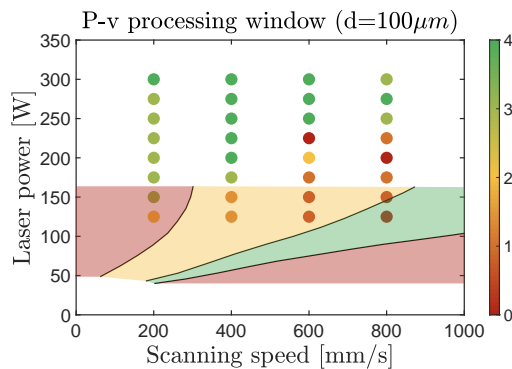
(f) Figures 4.4 with results from Gong et al. [7]

Figure 6.2 – MiniSLM $P - v$ processing windows taken from figures 4.4, 4.6 and 4.8 determined in section 4.1, overlapped with the processing windows reported in the literature (figure 6.1).

Figure 6.1 present three distinct zones:

- Zone I: This is a good processing area, where samples are dense and single tracks continuous and of good quality.
- Zone II: Partial melting occurs in this area, which leads to defect in the sample
- Zone III: Samples cannot be made properly, either because of balling or cracking phenomena

The results from literature have been superimposed onto the obtained processing windows of Ti-6Al-4V on the MiniSLM in section 4.1. Figure 6.2 shows the overlap between figure 6.1 and figures 4.4, 4.6 and 4.8. Even though the laser power range between the data from literature and the experimental measurements differs, one can make conclusions by extrapolating the curves of the different zone.

The good processing window of the MiniSLM for Ti-6Al-4V is represented by the green circles. These values lie outside of the zone I reported by Song et al, as presented by figures 6.2a, c and e. The optimum parameter combinations for Ti-6Al-4V on the MiniSLM have lower scanning speed values compared to what is expected from the literature, which corresponds here to the zone III. The same observation can be made when observing figures 6.2b, d and f where the results compared to the processing window reported by [7]. The optimum results of the MiniSLM lies within zones II and III, and not in zone I.

To summarise, these results are quite contradictory. Of course, the accuracy of such maps is primarily based on the judgement of the person doing the measurement and sample observation. However, if sample parameters were truly transferable to the MiniSLM, a small overlap should happen between the samples produced in this work and other literature sources. The present discussion shows that this is not the case, and therefore it is important to test the material *ex situ* and proceed to sample observation and quality assessment before jumping directly to *operando* XRD measurements with the MiniSLM.

6.2 Influence of the measurement configuration on the XRD pattern

The MiniSLM was designed to work both in reflection and transmission modes, as presented in section 3.3.1. A first series of experiments realised at the MicroXAS beamline revealed some intriguing differences for two samples processed with the same parameters but different measurement configuration. The two XRD patterns displaying these results are introduced in section 4.3.1. Figure 6.3 shows a zoom on figures 4.14 and 4.15 between t = 70 ms and t = 160 ms, and an angular range between 17° and 19.5° around the $(00.2)_{\alpha/\alpha'}$, $(01.1)_{\alpha/\alpha'}$ and $\{011\}_\beta$ reflections.

Between t = 70 ms and t ≈ 90 ms, one can observe the expected cycling between the α/α' and β phases. From t ≈ 90 ms, the intensity of the α/α' phase starts to increase while the β phase exists, as shown by the first arrow in figure 6.3a. This is expected since a part of the β grains probed by the X-ray beam slowly transforms back into α/α' because the laser is moving away. However, a second β peak is observed from t ≈ 120 ms in transmission mode in figure 6.3a shown by the second arrow. This second peak is at an angular position that does not correspond to the $\{011\}_\beta$ reflection, and is not present in the measurements done in reflection mode in figure 6.3b.

Figure 6.4 illustrates the situation with two schematics. In the transmission mode (a), the X-ray beam is going

(a) Result in transmission mode, coming from figure 4.14

(b) Result in reflection mode, coming from figure 4.15
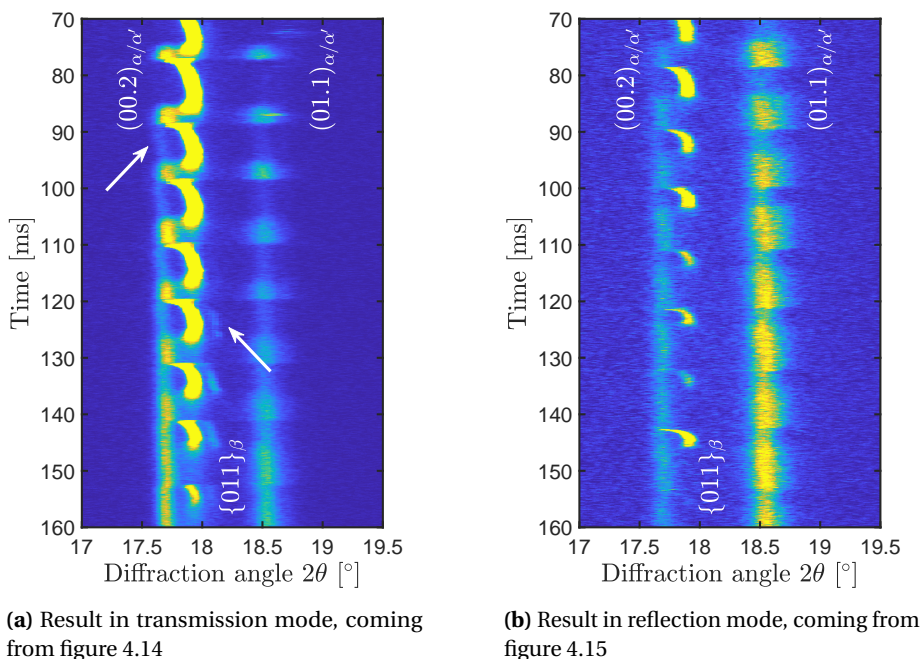
Figure 6.3 – Comparison of the XRD phase evolution in transmission and reflection modes, taken from figures 4.14 and 4.15

through the sample, and the diffracted signal can come from any location along the X-ray beam path in the sample. In the reflection mode (b), the information is more localised and comes only from a volume defined by the penetration depth of the X-ray beam, highlighted in yellow. Consequently, the transmission mode is recording information coming from different depth in the sample, while the reflection mode configuration is only probing the surface region.

(a) Transmission mode
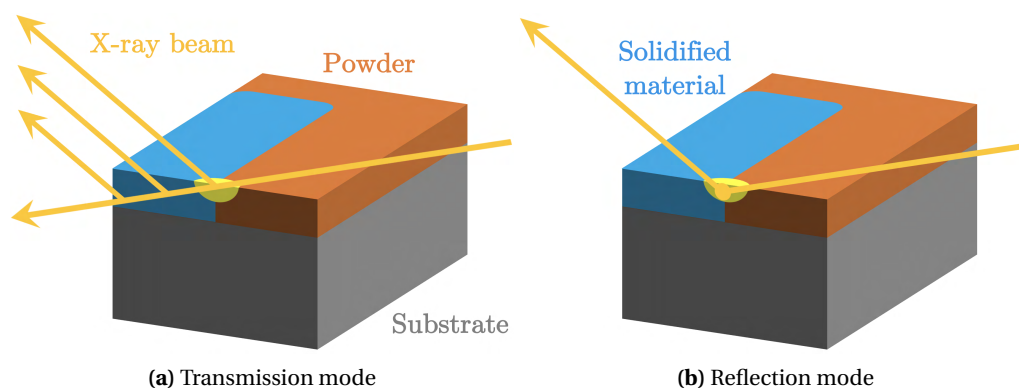
(b) Reflection mode

Figure 6.4 – Diffraction geometries in transmission and reflection mode corresponding to the situation in figure 6.3.

The fact that the recorded β phase in transmission mode comes from different depths shift the position of the signal reaching the detector, as shown by the parallel arrows in figure 6.4a. This is why an overlap of the

information is observed in figure 6.3a.

A possibility to overcome this issue would be to use the Energy-Dispersive X-Ray Diffraction (EDXRD) technique which can provide information on the depth of the signal depending of the energy of the X-ray radiation [132, 133]. However, to perform such an experiment, a specific energy sensitive X-ray detector is needed. Unfortunately, there are no detector of this type capable of reaching the high speed acquisition of the EIGER 500K used in this work. For that reason, all the measurements done on Ti-6Al-4V have been performed in reflection mode, to avoid any additional constraint for the data analysis.

6.3 Importance of the X-ray detector

Since the CCMX-Challenge AM[3] receives the support of the Swiss watch and precious metals industry, gold based alloys are of interest for the project. The material used in this work is a gold-copper-silver based alloy composed of 75wt% Au, 20.5wt% Cu and 4.5wt% Ag. This alloy is referred to as red gold due to its colour, or 5N according to the standard colours adopted for watch cases [134]. Because gold is a heavy element, very high X-ray energies are needed to perform XRD experiments, higher than what is available at PSI. For that reason, the MiniSLM setup was transported to the Petra III-P07 beamline of the Desy synchrotron in Hamburg, where XRD measurements could be done at 79.6 keV with an X-ray beam size of 140 x 140 μm^2 at FWHM. More details are presented in the appendix A.
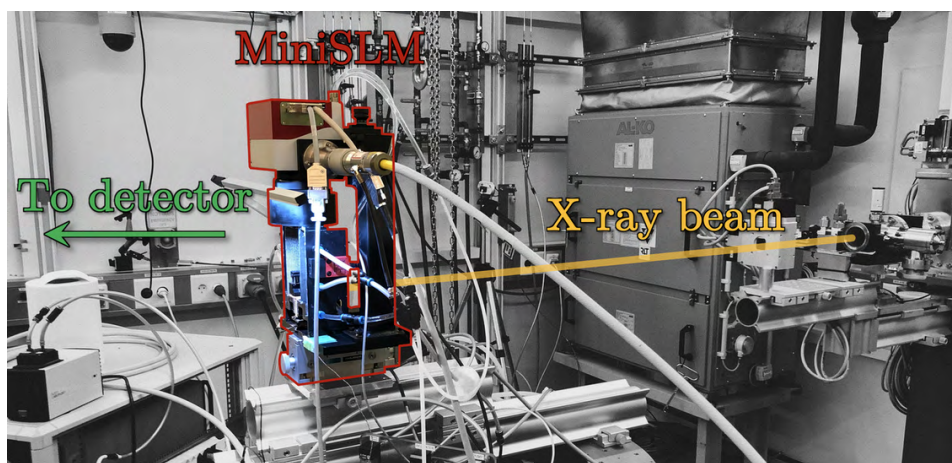
Figure 6.5 – MiniSLM mounted at the Petra III-P07 beamline

Figure 6.5 shows the MiniSLM installed at the P07 beamline. For an X-ray beam energy of 79.6 keV, the Bragg angle of some peaks is less than 5° (equation 3.4). To use the MiniSLM in reflection mode in that situation would mean to to tilt machine to a very low angle value to avoid shielding the diffracted signal, which would results in a very large projected X-ray beam and a low penetration depth of the probed surface region. To avoid that, the MiniSLM had to be used in the transmission mode configuration. Since the diffracted angles are small, the detector was positioned at 1.4m of the machine to collect XRD patterns, as in [135].

The ultra-fast EIGER 500K detector used for the results obtained on Ti-6Al-4V could not be employed in this experiment, because its silicon-based module is not compatible with the high X-ray energies of the Petra III-P07 beamline. Instead, a Pilatus3 X CdTe 2M detector was used to acquire the XRD patterns at its

maximum acquisition rate of 250Hz. At this frequency, an XRD pattern is captured every 4 ms. To put things in perspective, this is 80 times slower than the 20kHz of the EIGER 500K, capturing an XRD pattern every 50 µs.

Table 6.1 – Sample parameter table

Laser power [W]	Scanning velocity [mm/s]	Hatch distance [µm]	Layer thickness [µm]	Laser spot diameter [µm]
390	200	150	40	80
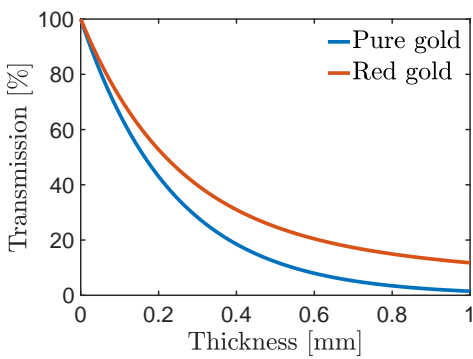
Figure 6.6 – Gold and red gold thickness vs. transmission curve at 80 keV from [136]

Two type of samples were printed during this experiment: a 2x2 mm^2 sample and a 6x6 mm^2 sample. The printing parameter used for this experiment are summarised in table 6.1. Since the experiment is performed in transmission mode, the X-ray beam had to be positioned very close to the sample edge to keep a transmission between 30% and 40 % (figure 6.6).

Figure 6.7 shows the resulting phase evolution of the 5N alloy for the 2x2 mm^2 sample (a) and the 6x6 mm^2 sample (b). Red gold does not exhibit any phase transformation during laser melting, which explains that the same peaks are visible during the whole scanning process. The beginning of the laser scanning is represented by the while arrow at t ≈ 20 ms. Since X-ray beam is close to the edge, the beginning the laser scanning is visible from the first printed line.

(a) XRD phase evolution for the 2x2 mm^2 sample

(b) XRD phase evolution for the 6x6 mm^2 sample
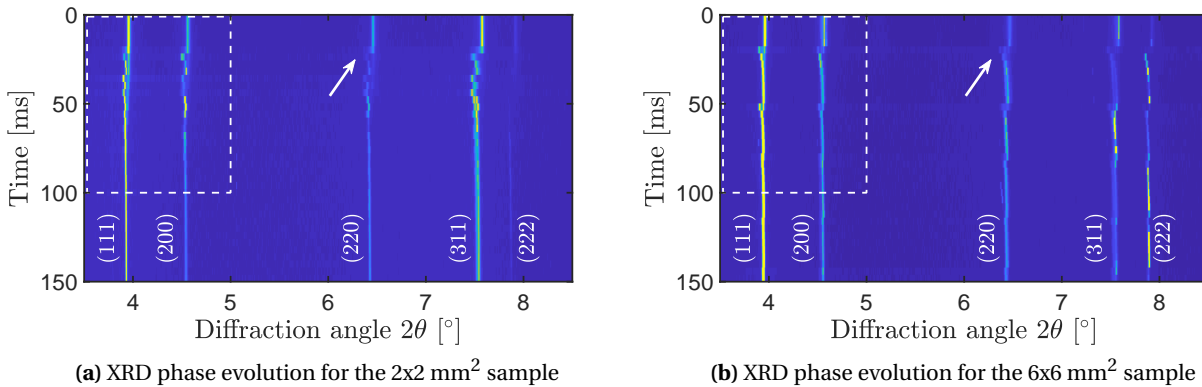
Figure 6.7 – Phase evolution of the 5N alloy during XRD experiment. The beginning of the laser scanning event is indicated by the white arrow and has been set arbitrarily to t ≈ 20 ms for visualisation purposes.

Figure 6.8 presents a zoom on the highlighted regions in figure 6.7 to follow the (111) and (200) reflections. At a scanning speed of 200 mm/s, it takes 10 ms for the laser to travel 2 mm, and 30 ms to travel 6 mm. This means that in figure 6.8a, a peak position shift towards lower angular values should be observed every 10 ms,

starting from 20 ms for the 2x2 mm^2 sample. However, because of the slow acquisition rate of the detector, this is not resolved properly in the phase evolution of the 5N alloy. Using the same reasoning, a peak position shift should be observed every 30 ms in figure 6.8b for the 6x6 mm^2 sample. This repetition rate is longer than for the 2x2 mm^2 sample, and the peak position shift is better resolved here with a frame rate of 4 ms. Unfortunately, the quality of this data is not good enough to perform analysis procedures presented in

(a) 2x2 mm^2 sample - zoom in figure 6.7a

(b) 6x6 mm^2 sample - zoom in figure 6.7b
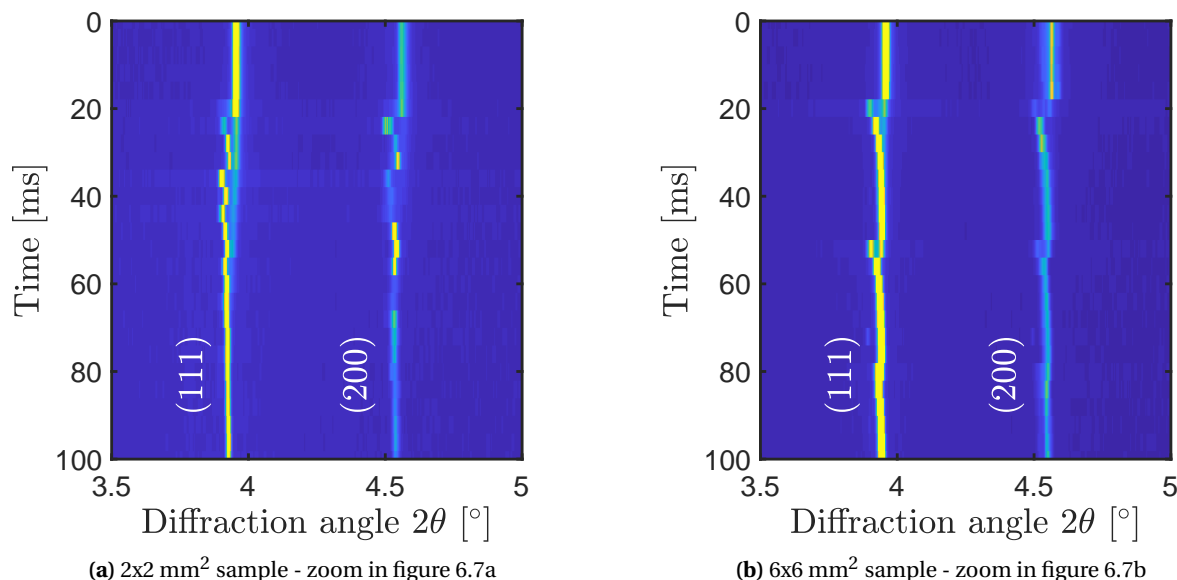
Figure 6.8 – Phase evolution of the 5N alloy during XRD experiment. Zoom in the highlighted regions of figure 6.7

chapter 4 on Ti-6Al-4V. Nevertheless, these results highlight the importance of having a fast detector to track the evolution of the XRD signal. Without the EIGER 500K developed at PSI, it would not have been possible to obtain high-quality data and perform *operando* XRD experiments on Ti-6Al-4V.

Note that now EIGER CdTe detector with high acquisition rate detector are available, with a frame rate of up to 2kHz [137].

6.4 Data analysis improvements

The data acquired with the MiniSLM during *operando* measurements needs special attention for interpretation. A standard peak fitting procedure cannot be employed because of the poor peak shape related to limited grain statistics during high-speed acquisition at 20 kHz. Therefore, the centre of mass method is used to determine the evolution of the peak position. In the results published in the journal Materials Today [116], a first approach was used with a fixed angular range to determine the centre of mass variation over time for the phase evolution data sets.

After the publication of the first results, deeper analysis were performed to have a better understanding of the situation. However some discrepancies were observed after processing the data. It turned out that the results were strongly dependent on the person performing the analysis if the background intensity is not cut out properly.

Therefore, a more refined method was needed to guarantee that the centre of mass measurement is accurate and repeatable. After investigation, it appeared that keeping the angular integration range fixed to determine the centre of mass was the source of the problem, since all the intensities included within the defined range will be accounted for the weighted average, including the background. If one does not know how to select the range properly, then the calculated values will not follow properly the experimental peak. To solve this, a dynamic range was implemented though a Matlab routine, offering more robustness to the analysis procedure.

(a) Fixed range integration for the centre of mass

(b) Dynamic range integration for the centre of mass
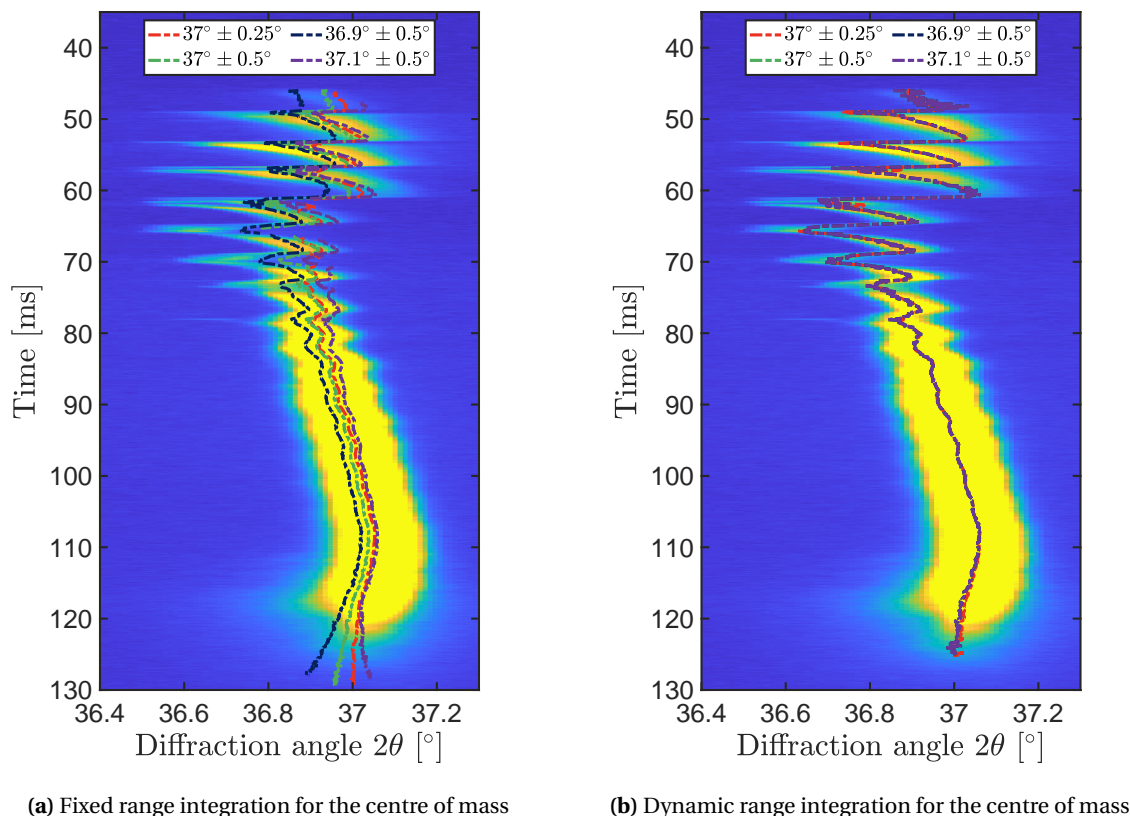
Figure 6.9 – Example of the old (a, fixed range) and new (b, dynamic range) analysis methods performed on the $\{002\}_\beta$ peak from the 2x2 mm^2 sample presented in figure 4.19, with contribution of the background

Figure 6.9 shows an example of the analysis performed with the old and new methods. The fixed range analysis is presented in figure 6.9a, with different centre of mass curves determined by the ranges presented in the legend. For example, "37°±0.5°" means that the centre of mass is centred around 37° and calculated between 36.5° and 37.5° for each diffraction pattern. The measurement was performed without cutting out the background to illustrate the influence of its low intensity on the centre of mass calculation (see equation 3.5).

By comparing the red and green curves, it appears that the integration range has an effect on the location of the centre of mass. This is easily understandable, as the contribution of the background increases with the integration range. Subsequently, comparing the green, dark blue and purple curves reveals that the centre of the integration range considerably shifts the centre of mass value. This can also be understood as varying the

background contribution in the weighting average. It is clear that the way the background of the diffraction is accounted has a strong influence on the calculation.

Figure 6.9b shows the new method with a dynamic range where a Matlab routine finds automatically the local maximum of the peak and centre the integration range around it, making it symmetrical around the peak position. As a result, the calculated centre of mass is less dependent on the initial range values. These parameters now act as a starting point, indicating to the Matlab routine where to begin, and the rest is done automatically. This proves to be a more appropriate calculation method, since all the curves overlap and follow well the peak intensity (in yellow).

6.5 *Operando* phase evolution for Ti-6Al-4V during SLM processing

6.5.1 Kinetics of phase transformation

Case of a long scanning vector

Figure 6.10a highlights the evolution of the integrated intensities, diffuse scattering, temperature and lattice expansion of both phases during the cycle 17 of the printing of the 8x2 mm^2 sample presented in section 4.3.2. This cycle is when the laser beam is coincident with A$_{XR}$. The same colour scheme as in figure 4.18a was employed. The diffuse scattering was obtained by summing the background intensity in figure 4.16 between 24° and 25.2° and between 27.5° and 34.6°. Figure 6.10b shows three snapshots of the relative position of the melt pool, HAZ and X-ray beam, obtained from FEM simulations to illustrate the situation.
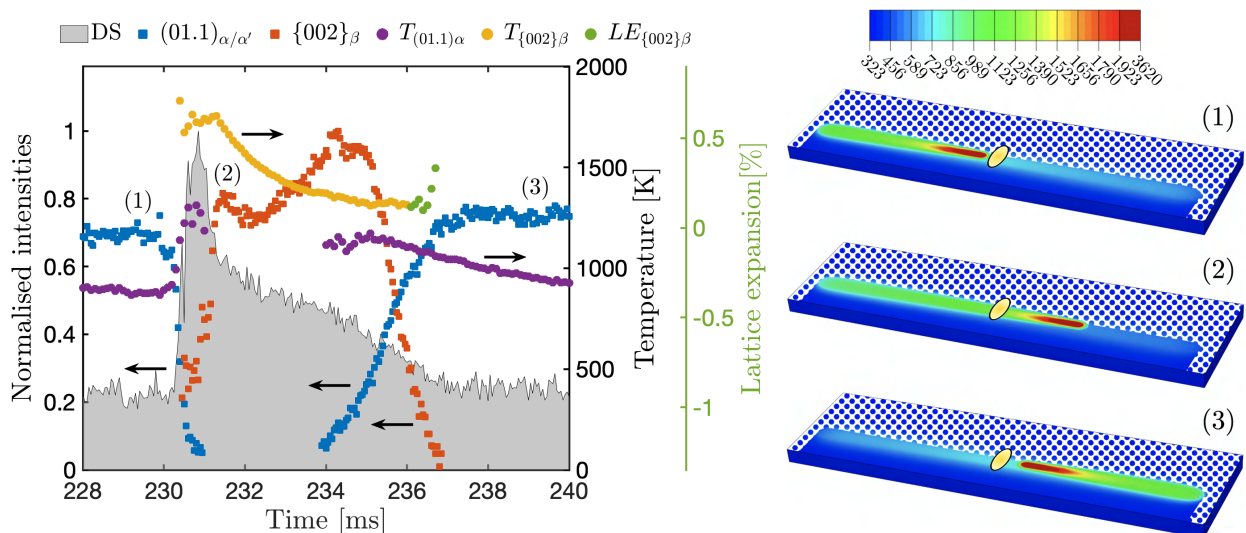
(a) Evolution of the integrated intensities, diffuse scattering and temperature   **(b)** Schematics of the laser position relative to A$_{XR}$ (Temperature scale in Kelvin)

Figure 6.10 – X-ray diffraction results during printing of line 17 from figure 4.18 representing: a) the evolution of integrated intensities of the $(01.1)_{\alpha/\alpha'}$ and $\{002\}_\beta$ as well as the diffuse scattering (DS) from figure 4.16 and the corresponding temperature and lattice expansion in the α/α' and β phases; b) schematics of the laser position relative to A$_{XR}$ with the number corresponding to (a).

Just before the laser approaches A_{XR}, only the α/α' phase is present with an average temperature of 880K. At t = 230 ms the intensity of α/α' peaks drop sharply and the first signs of the β phase are seen at t = 230.5 ms. This transition is followed by a raise in the average temperature of α/α' phase, followed by the β phase. At t = 231 ms, the average temperature of β phase has reached 1800K, which is close to the theoretical melting temperature of Ti-6Al-4V (1923.15K). At the same time, the diffuse scattering displays a sharp increase and decrease, signature of the amorphous scattering from melt pool crossing A_{XR}. The intensity of the β phase increases rapidly during 0.8 ms, a time interval during which the laser travels 0.5 mm. The relative position between laser and A_{XR} is shown in figure 6.10b-(2). In other words, the laser has passed well beyond A_{XR} before the maximum is reached.

During the next 3.5 ms, the average temperature of the β phase decreases fast, with an initial cooling rate of -2.7×10^5 K/s. The diffuse scattering intensity decreases similarly as the temperature, highlighting the reduction of thermal agitation within the sample. When the β transus is reached, the β phase intensity starts dropping and the α/α' phase reappears. A tensile residual stress is formed in the $\{002\}_\beta$ planes, as reflected by the green curve. During 9 ms, α/α' cools down reaching an average temperature of 930K. During this time, the laser has travelled 5.4 mm and has approached A_{XR} again, (schematically presented in the figure 6.10b-(3). The total duration that A_{XR} is fully in the β phase while printing this line amounts to 2 ms. This rapid $\alpha/\alpha' \leftrightarrow \beta$ phase transformation scheme is experienced several time by A_{XR} during the laser scanning as shown in figure 4.18.

Case of a short scanning vector

The situation is different for the 2x2 mm^2 sample presented in section 4.3.2. Figure 6.11 displays the evolution of the integrated intensities, diffuse scattering, temperature and lattice expansion of both α/α' and β phases during laser scanning. The same colour scheme as in figure 4.20a was employed. The diffuse scattering was obtained by summing the background intensity in figure 4.19 between 24° and 25.2° and between 27.5° and 34.6°. The laser is turned on a t = 0 ms.

During the scanning of the 2x2 mm^2 sample, the α/α' phase disappears in a step like manner between 50 ms and 65 ms, revealing that the laser beam and thus the melt pool is intersecting a larger section of A_{XR} at each hatch increment. The temperature of the α/α' phase increases until the complete disappearance of its intensity. While the α/α' phase disappears, the first sign of the β phase is visible at $t \approx 46$ ms and persists until the end of the printing process at $t \approx 130$ ms. With A_{XR} at the centre of the printed area, the laser and X-ray beams overlap at $t \approx 66$ ms as shown by the sharp rise in the diffuse scattering and highest temperature value in figure 6.11.

The temperature of the β phase experiences sharp fluctuations between 50 ms and 78 ms, together with the diffuse scattering, highlighting the interaction between the amorphous melt pool and A_{XR}. During this time, the intensity of the β phase also exhibits steep variations in its profile, with an overall drop between 58 ms and 90 ms. This strange behaviour in the intensity is most likely due do to a grain statistic issue, meaning that most of the β grains are not diffracting on the detector module anymore. This is not observed when a larger X-ray beam is used, as shown by the results from the MS beamline in figure 4.28b. This phenomenon disappears after 90 ms when the laser is getting further away from A_{XR} as shown by the diffuse scattering peak disappearance, and the β intensity signal is at its maximum until the end of the laser scanning.
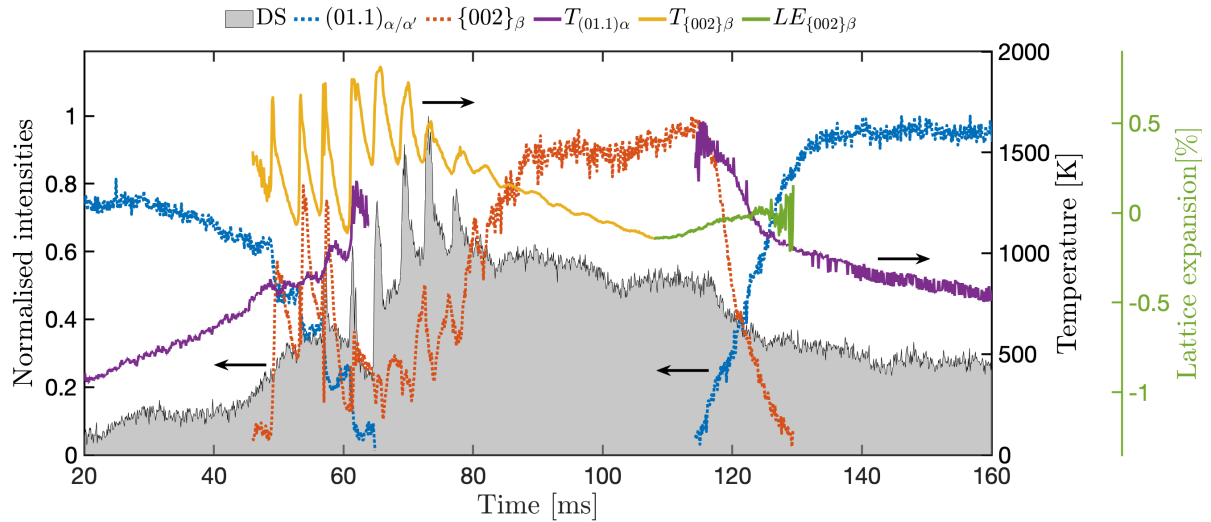
Figure 6.11 – X-ray diffraction results during printing a 2x2 mm^2 sample from figure 4.20 representing the evolution of integrated intensities of the $(01.1)_{\alpha/\alpha'}$ and $\{002\}_\beta$ as well as the diffuse scattering (DS) from figure 4.19 and the corresponding temperature and lattice expansion in the α/α' and β phases

From t $\approx$ 90ms until 130 ms, the β phase experiences an average cooling rate of -1.1×10^4K/s, which is more than an order of magnitude lower than what was obtained for the 8 mm scanning vector length at the end of the β phase cycle. At the same time, the diffuse scattering decreases slowly as in the previous paragraph, revealing the reduction of thermal agitation within A_{XR}. Between 110 ms and 130 ms the β phase disappears and the α/α' phase reappears progressively. Simultaneously, a tensile strain is observed in the $(01.1)_{\alpha/\alpha'}$ and $\{002\}_\beta$ planes. The total time that the β phase is continuously present in the sample reaches 84 ms for the 2x2 mm^2 scanned area.

6.5.2 Impact on the microstructure

The microstructures of samples manufactured during *operando* XRD experiments were presented in section 4.4.1. Three samples were shown in figure 4.32: a 2x2 mm^2, a 4x4 mm^2 and a 6x6 mm^2. Figure 6.12 shows the XRD phase evolution and α/α' microstructure of the 6x6 mm^2 and 2x2 mm^2 samples.

The cycling in the 6x6 mm^2 sample displayed in figure 6.12a is comparable to what is happening in the 8x2 mm^2 sample with a rapid $\alpha/\alpha' \leftrightarrow \beta$ phase transformation. The resulting microstructure is presented in figures 6.12b and c, showing an acicular α' structure. The α' needles exhibit various sizes in figure 6.12c. Coarse primary α' needles are visible with a length of 10-20 µm and a width of less than a micron. Secondary α' laths with a length of few microns are present between these coarse primary α' needles. Substructures going down to tertiary and quadratic α' laths can be observed, following this reasoning. This kind of structure is typical from the α' martensitic phase [9].

Figure 6.12d shows the XRD phase evolution for the 2x2 mm^2 sample. As described earlier, the amount of time the material stays at high temperature in the β phase is much longer for a short scanning vector. Because the local heat input is higher, the cooling rates are one order of magnitude lower before the β phase

disappears. Such a behaviour is affecting the microstructure as shown in figure 6.12e and f. Thanks to the lower cooling rates, the final primary α' needles are much coarser than for the 6x6 mm^2 sample (see figure 6.12c), with a length of more than 50 µm and a width of few microns.

(a) XRD pattern - 6x6 mm^2 sample   **(b)** α/α' IPF map - 6x6 mm^2 sample   **(c)** α' needles - 6x6 mm^2 sample

(d) XRD pattern - 2x2 mm^2 sample   **(e)** α/α' IPF map - 2x2 mm^2 sample   **(f)** α' needles - 2x2 mm^2 sample
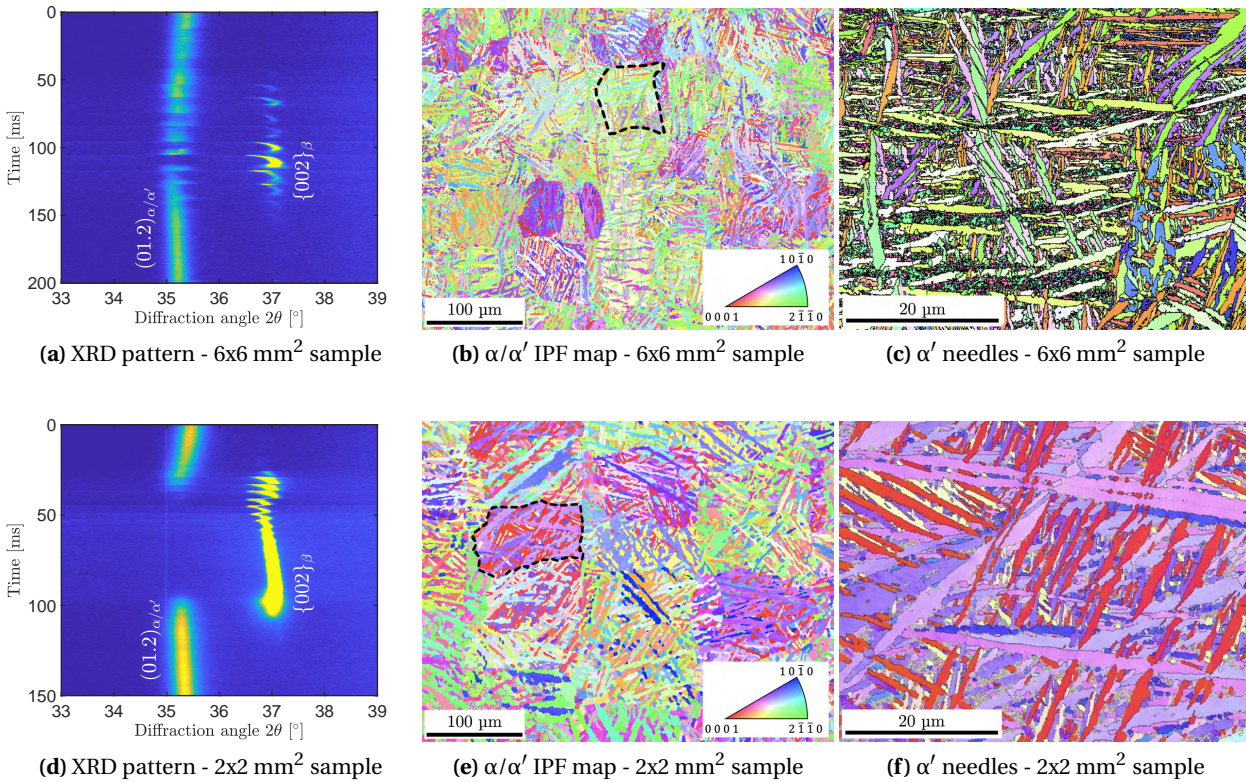
Figure 6.12 – Influence of scanning strategy on the resulting microstructure. (a,d) Evolution of the intensities of the $(01.2)_{\alpha/\alpha'}$ and $\{002\}_\beta$ reflections while printing; (b,e) IPF maps of the building planes; (c,f) High-resolution IPF maps showing basket weave microstructures with variants of α' martensitic laths from the highlighted regions in (b) and (e). (Taken from figure 4.32)

The reconstructed prior-β presented in figure 6.13 also reveal the thermal history of the samples. The 6x6 mm^2 sample which had rapid $\alpha \leftrightarrow \beta$ shows prior-β grain size of 60 µm or less, while the 2x2 mm^2 sample displays larger prior-β grain size, with some bigger than 100 µm. Since the the 2x2 mm^2 sample stays for a longer time in the β regime, the prior-β grains have more time to grow than for the larger sample. When the temperature goes below the β transus and the martensitic transformation starts, the α' needles are growing within the β grains. Thanks to the slower cooling rates following the growth of the β grains in the 2x2 mm^2 sample, the α' laths are larger compared to the 6x6 mm^2 sample.

Apart from the processing parameters such as laser power, hatch distance and scanning speed; the scanning strategy plays an important role in the final microstructure after printing. Numerous scanning strategies exist, such as raster, helix, island or inter-layer stagger scanning. Often the length of the scanning vectors is reduced in order to lower residual stresses, although some contradictory results exist in literature regarding its effect [138, 139].

Here, it was shown that the length of the scanning vector significantly influences the thermal history at a

given point in the printed structure. This is crucial for materials that experience phase transformations during solidification, and particularly important when printing parts with hollow channels or open lattice structures [110, 140]. For such parts, varying the scanning vector lengths is unavoidable, which may lead to components with spatially heterogeneous mechanical properties.

(a) Prior-β grains - 6x6 mm^2 sample

(b) Prior-β grains - 2x2 mm^2 sample
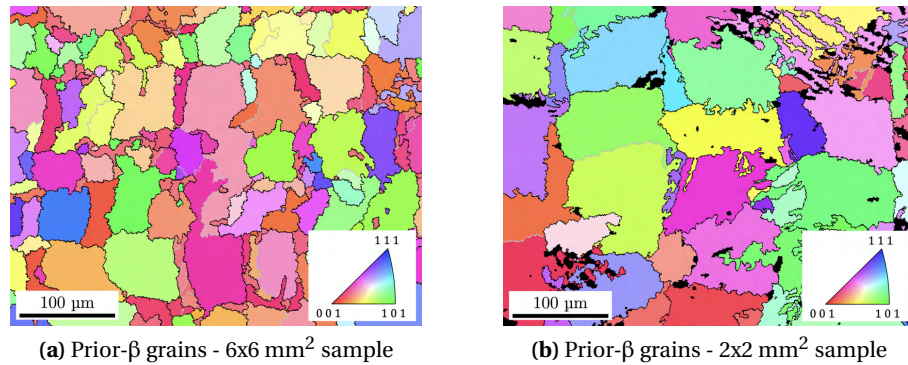
Figure 6.13 – IPF maps of the reconstructed prior β grains of figures 6.12b and e

In general, a refined grain structure is desirable for good mechanical properties. However, because of the shorter scanning length imposed by dimensional constraints when printing porous structure, fewer grains might be present within the solidified sections, which might be detrimental for the overall mechanical behaviour of the final part. For that reason, it might be of interest to adapt the scanning strategy to avoid this situation.

6.6 Influence of the X-ray spot size

Different X-ray beam sizes were used during *operando* measurements, the results were presented in section 4.3.5. Three X-ray beam sizes were used, which were, after projection on the sample:

- A small beam with dimensions of 30 x 35 µm^2 at FWHM
- A medium beam with dimensions of 80 x 140 µm^2 at FWHM
- A large beam with dimensions of 130 x 230 µm^2 at FWHM

Figure 6.14 shows the comparison between these three X-ray beam sizes, with dimensions are up to scale. The X-ray beam is composed of two sections: the Full-Width at Half-Maximum (FWHM), where 76% of the intensity is present (in orange) and the tail of the beam where the intensity is low but can still contribute to the diffraction pattern (in blue). The laser spot diameter is 100 µm and the the melt pool width (vertical) is 120 µm in agreement with the measurements presented in table B.5. The HAZ is considered as the volume where the β phase is formed. The width (vertical) is equal to 480 µm, corresponding to the representation in figure 4.18b. The length (horizontal) is here qualitative and only for illustration purposes. The surrounding of the HAZ is considered as α/α′ phase. The scanning direction is from the left to the right side of the page.

The results obtained with a small beam are shown in figure 4.30. The phase intensity evolution clearly depicts the laser beam crossing A$_{XR}$: while the α/α′ phase disappear, the β phase is observed shortly, corresponding to the front of the HAZ. Then, the diffuse scattering signal increase and decreases over 1 ms, signature of the

melt pool amorphous region. Finally, the β phase intensity reappears, corresponding to the tail of the HAZ, until it transforms back into α/α′. As a result, a small X-ray beam size compared to the melt pool gives a very local and detailed information on the phase transformations happening in the material. However, the main drawback of this method is that it is difficult to efficiently gather data. It took a lot of trial, and probably some luck before obtaining the results displayed in figure 4.30. Since the A_{XR} is quite small, not a lot of grains are sampled within the material, which makes the probability to have some in diffraction condition reaching the detector module low. Since beamline measurement time is expensive, using this X-ray beam size is not the most appropriate strategy. Moreover, the hatch distance must be quite small to capture the laser scanning event properly. For the results reported in figure 4.30, the hatch distance use was 25 µm. For larger hatch distances, A_{XR} might fall in between two tracks which then does not capture well the overlapping event.

(a) Beam of 30 x 35 µm^2 at FWHM   **(b)** Beam of 80 x 140 µm^2 at FWHM   **(c)** beam of 130 x 230 µm^2 at FWHM
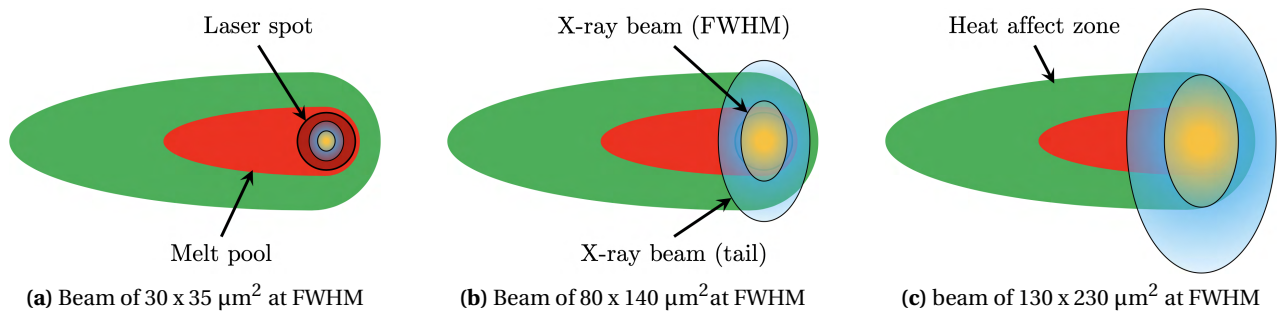
Figure 6.14 – Comparison between laser spot diameter, melt pool and HAZ with different X-ray beam sizes. Here the laser spot diameter is 100 µm and the width of the melt pool is taken as 120 µm, corresponding to the data presented in table B.5. The X-ray beam indicated are up to scale.

The results collected with a large X-ray beam are shown in figure 4.28b. Using a larger beam improves the grain statistic issue: since a broader surface region is probed, more grains are sampled and thus the probability to have some in diffraction condition reaching the detector module increased. This is nicely observed in the signal of the β phase which increases and decreases, without too much fluctuations. However, this method has the disadvantage to probe locations outside of the region of interest (melt pool and HAZ), as represented in figure 6.14c. This makes the interpretation more difficult as the information from the α/α′ phase never completely disappears. Moreover, since the X-ray beam is larger, it is more likely to observe perturbation on the XRD patterns, particles flying around inside the chamber.

The results with a medium X-ray beam size shows the best compromise as it samples enough grains to have relatively good measurement statistics without going out of the region of interest. For Ti-6Al-4V, this size corresponds to a vertical projected FWHM dimension of the same order of magnitude as the melt pool width.

To summarise, optimised dimensions for A_{XR}, after projection on the sample, should be comparable to the melt pool width to avoid collecting unnecessary information, which makes data analysis more difficult. However the grain size of the material must also be taken into account, as it will influence the amount of sampled grains. If this quantity is too low, the diffracted intensities will not be good enough to record properly the laser scanning process.

6.7 Experiments vs. simulations

6.7.1 Melt pool dimensions

The flat part of the temperature profile derived from the β peak position is an evidence of the melt pool crossing A_{XR} (detailed in section 4.3.4). This is in particularly visible in figure 5.7b for the 2x2 mm^2 sample at t ≈ 65 ms, but also in figure 5.8b for the 8x2 mm^2 sample at t ≈ 230 ms. This plateau lasts 0.9 ms in both the 2x2 mm^2 and 8x2 mm^2 samples and can be correlated with a length of the melt pool of 540 μm passing A_{XR} at a scanning speed of 600 mm/s.

The melt pool dimensions obtained in the simulations are summarised in figure 6.15 for the 2x2 mm^2 (a) and the 8x2 mm^2 sample (b). The experimental values including the standard deviation are also provided. The melt pool width and depth are taken from table 5.3. To obtain the experimental value of the length of the melt pool, the flat part of the temperature profile derived from the X-ray data in figures 5.7b and 5.8b are used. The error bar is derived from the detector time resolution, ±50 μs, resulting in an uncertainty of ±30 μm for the melt pool length. According to the results for the 2x2 mm^2 sample, M1 predicts the length of

(a) 2x2 mm^2 sample - melt pool sizes

(b) 8x2 mm^2 sample - melt pool sizes
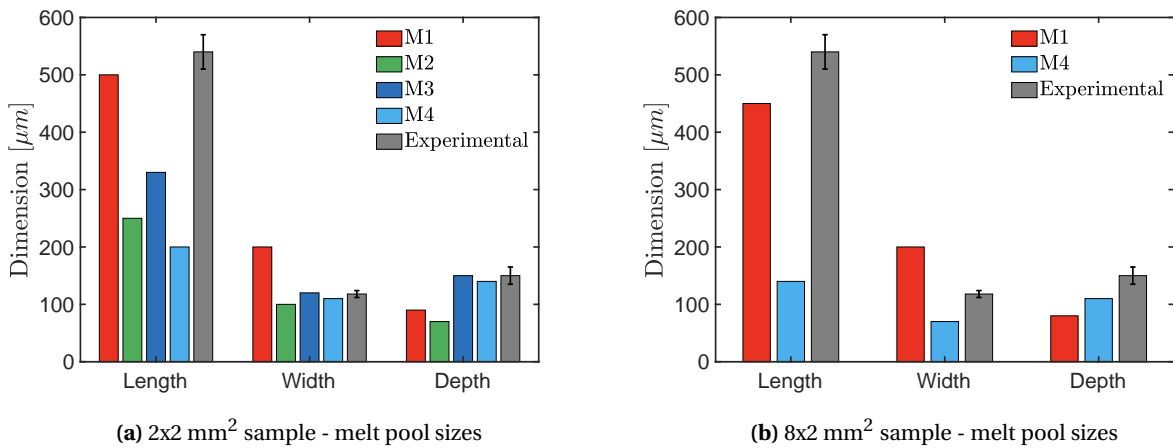
Figure 6.15 – Melt pool sizes comparison for the 2x2 mm^2 sample (a) and the 8x2 mm^2 sample (b) with the experimental results.

the melt pool at best. However, the model overestimates the width and depth of the melt pool. Model M2 tends to underestimate all three dimensions. Models M3 and M4 are underestimating the length but are quite accurate regarding the width and depth.

The difference between M1 and M2 can be explained by the steeper gradient in the laser energy distribution of M2. By looking at equation 5.10, the exponential decay constant is equal to -1 at $r=r_0$. Which means:

$$Q(r_0) = \frac{1}{e} \times Q(0) \approx 0.37 \times Q(0) \tag{6.1}$$

with $Q(r_0)$ the heat flux at the laser radius and $Q(0)$ the heat flux at the centre of the laser beam. In other words, the heat flux at the laser radius is still 37% of the heat flux at the centre of the laser beam, explaining the large spread of the melt pool. The volumetric heat source equation 5.11 for M2 has an exponential decay

constant equal to -3 at r=r$_0$. Which means:

$$Q(r_0) = \frac{1}{e^3} \times Q(0) \approx 0.05 \times Q(0) \tag{6.2}$$

The heat flux at the laser radius is only 5% of the heat flux at the centre of the laser beam and the energy distribution is, therefore, more concentrated around the centre of the laser beam, resulting in smaller melt pool dimensions. The introduction of deeper heat penetration in model M3 and M4 provides good predictions of the depth of the melt pool. The enhanced isotropic thermal conductivity is probably responsible for the better prediction of the width, it can however not predict the melt pool length accurately. Note that taking into account the radiation losses in M4 increases the underestimation of the melt pool length. However, it has little influence on the predicted width and depth. The influence of the scan vector on the simulation predictions seems to be more important in M4 compared to M1. The predicted melt pool length in M1 is 10% less in the 8x2 sample compared to the 2x2 sample, but the width and the depth are hardly affected. For the model M4, all the dimensions are considerably more reduced when a larger scanning vector is used: 30% for the melt pool length, 36% for the width, and 21% for the depth.

It is important to remember that the experimental values for the width and depth of the melt pool are derived from a single line scan (see section 5.2.3). Because of the influence of the scanning vector length (a smaller length result in a higher surrounding temperature), the experimental values in the 2x2 mm^2 sample might be slightly higher than those reported. The material surrounding the melt pool has a lower temperature in the 8x2 mm^2 sample, as confirmed in the temperature curve and melt pool images (figure 5.8), resulting in higher thermal gradients.

6.7.2 Temperature evolution in the X-ray probed surface region

When the laser approaches

(a) 2x2 mm^2 sample - heating rates

(b) 8x2 mm^2 sample - heating rates
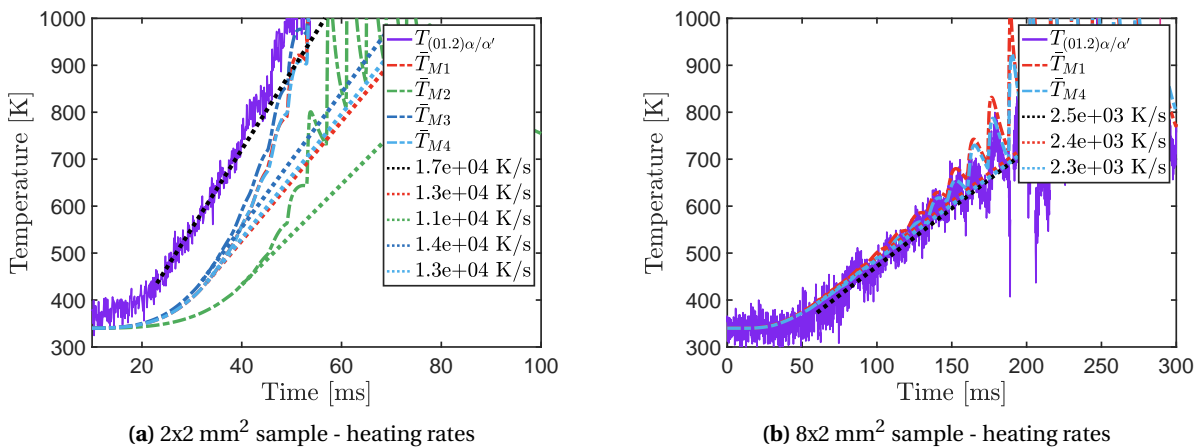
Figure 6.16 – Experimental and predicted temperature evolution in A$_{XR}$ when the laser approaches (a) for the 2x2mm sample, (b) for the 8x2mm sample. For the 2x2 sample, the predicted heating rates are shown when the temperature reaches 440K.

Figure 6.16 zooms in on the temperature evolution in the X-ray probed surface region before the local

temperature high enough to reach the β transus: (a) in the 2x2 mm^2 and (b) in the 8x2 mm^2 sample. The experimental temperature raises linearly between 400 and 850K in both samples: the rate amounts 1.7×10^4K/s in the small sample and 2.5×10^3K/s in the large sample. In the large sample, the temperatures predicted by M1 and M4 are in good agreement with the experiment. In the small sample, the predicted temperatures are lagging for all models. Around 440K, the heating rates are comparable with the experimental one, their values are shown in the captions of figure 6.16. When the laser approaches further A$_{XR}$ and the temperature rises, the heating rates are increasing and the simulated temperature catches up with the experimental one.

Cooling rates during laser scanning across A$_{XR}$

The complex evolution of the diffracted {002}$_β$ intensity in cycle 17 presented in section 4.3.4 demonstrates that the calculation of the β cooling rates should be done while visually inspecting the evolution of the diffraction pattern. Using an average over the cycles closest to maximum overlap is recommended.
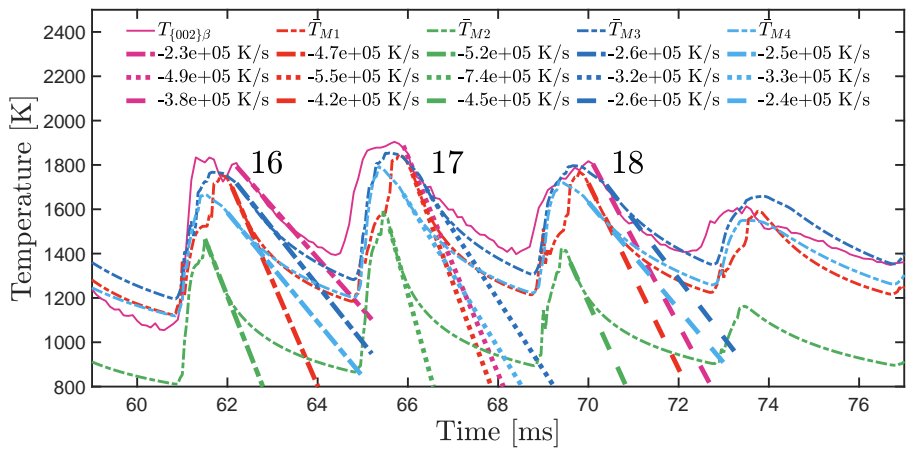
(a) 2x2 mm^2 sample - cooling rates in the β phase
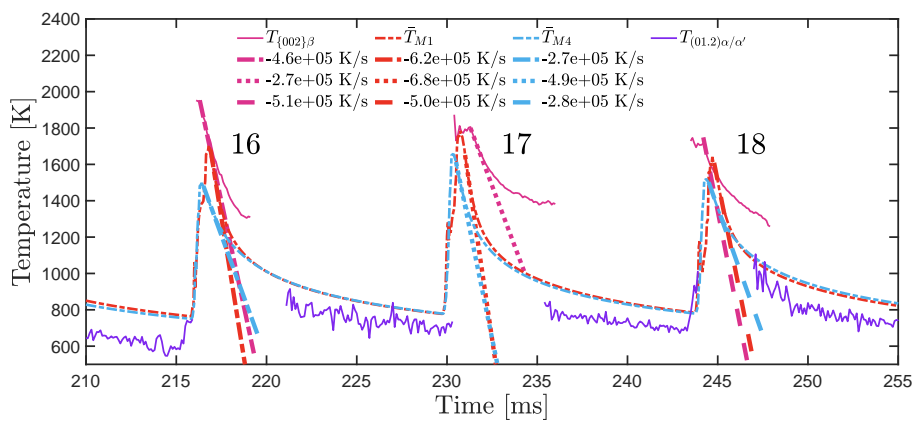
(b) 8x2 mm^2 sample - cooling rates in the β phase

Figure 6.17 – Cooling rates measurements for the the cycles 16, 17 and 18 from figures 5.7b and 5.8b

To obtain an average cooling rate, the three cycles around the maximum temperature in figures 5.7b and 5.8b have been taken into account both experimentally as in the simulated models.

Figure 6.17 shows the cooling rates measurements for both 2x2 mm^2 and 8x2 mm^2 samples. The results are summarised in table 6.2, and the average cooling rate calculated for each model.

<p align="center">Table 6.2 – Average cooling rate in the β phase</p>

	Experimental	M1	M2	M3	M4
Cooling rates from 2x2 mm^2 sample (10^5K/s)					
Cycle 1	-2.3	-4.7	-5.2	-2.6	-2.5
Cycle 2	-4.9	-5.5	-7.4	-3.2	-3.3
Cycle 3	-3.8	-4.2	-4.5	-2.6	-2.4
Average	-3.7	-4.8	-5.7	-2.8	-2.7
Cooling rates from 8x2 mm^2 sample (10^5K/s)					
Cycle 1	-4.6	-6.2	N/A	N/A	-2.7
Cycle 2	-2.7	-6.8	N/A	N/A	-4.9
Cycle 3	-5.1	-5	N/A	N/A	-2.8
Average	-4.1	-6	N/A	N/A	-3.5

The average experimental cooling rate of the β phase in the 2x2 mm^2 sample is -3.7×10^5K/s . The cooling rates as well as the shape of the cooling curve are rather well predicted by model M3 and M4 as shown in figure 5.7b. These models include an enhanced laser penetration depth and enhanced thermal conductivity. The maximum temperature of the β phase predicted by M3 is close to the experimental value (1900K) and is 100K lower for M4. The predicted temperature before the laser comes back is 100K lower in M3 compared to the experiment and 170K lower in M4. These differences can be explained by the radiation loss that is taken into account in M4. Models M1 and M2 overestimate the cooling rate. M1 predicts a similar maximal β temperature as M3, whereas M2 predicts only a maximum value close to 1600K.

The experimental cooling curve for the 8x2 mm^2 sample, has two parts: the first part represents the cooling of the β phase, the second the cooling of the α/α′ phase (figure 5.8). As shown in section 4.3.2, upon the transformation of parts of the X-ray probed surface region from β to α/α′, the β phase exhibit residual stress. Therefore the last part of the experimental β cooling curve is not solely driven by thermal contraction. The predicted cooling curves lie in between the experimental α/α′ and β cooling curve (figure 5.8b). The experimentally measured average cooling rate of the β phase (-4.1×10^5K/s) is of the same order of magnitude as the one measured in the 2x2 mm^2 sample. The trends predicted by M1 and M4 are similar as in the 2x2 mm^2 sample: M1 predicts a comparable maximum temperature but a too high cooling rate, the maximal temperature predicted by M4 is lower, but the average cooling rates are not so far from the experimental ones. Both models overestimate the temperature of the α/α′ phase by around 100K.

Cooling rates after laser scanning

Figure 6.18 shows the cooling curves after the laser is scanning the last lines (therefore far away from A$_{XR}$) and after the laser is switched off (a) for the 2x2 mm^2 and (b) the 8x2 mm^2 samples. In both samples, the

X-ray probed surface region remains in the α/α' phase. The cooling rates (shown by dotted curves, values given in caption) are calculated for the moment the laser is switched off. This is at t = 140 ms in the 2x2 mm^2 sample and t = 500ms in the 8x2 mm^2 sample.

When the laser is switched off, the temperature of the α/α' phase predicted by M1 agrees well with the experimental measures for both types of samples. In the 2x2 mm^2 sample this temperature corresponds to 880K, whereas it is 600K in the 8x2 mm^2 sample. The model M3 predicts too high temperatures in the 2x2 mm^2 sample, adding the radiation loss (M4) reduces this temperature but the values are still higher than experimentally measured (also for the 8x2 mm^2 sample). The predicted temperature of M3 is 200K below that of M1.

(a) 2x2 mm^2 sample - cooling rates in the α/α' phase   **(b)** 8x2 mm^2 sample - cooling rates in the α/α' phase
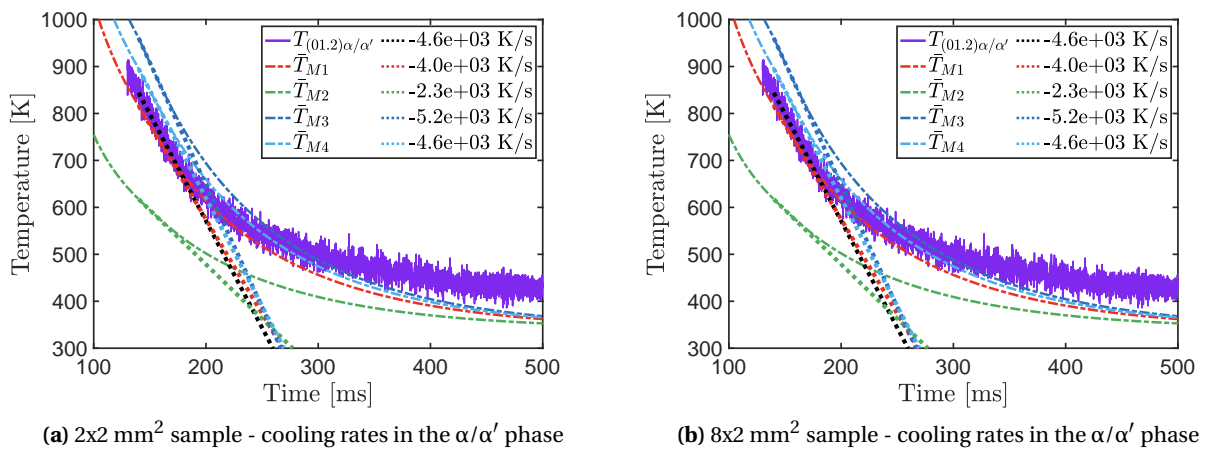
Figure 6.18 – Temperature evolution in the α/α' phase and cooling rates at the moment the laser is switched off : (a) the 2x2 mm^2, laser switched off at t $\approx$ 140 ms; (b) 8x2mm sample, laser switched off at t $\approx$ 500 ms

The experimental cooling rates at the moment the laser is switched off is a factor of 10 lower in the 8x2 mm^2 sample (-4.6×10^2K/s) compared to the 2x2 m^2 sample (-4.6×10^3K/s) because of the higher accumulated temperature and the fact that the heat losses are directly proportional to the temperature (section 5.1.3). It is however interesting to look at the shape of the cooling curves predicted by M1 and M4 in both samples. When temperatures are still high (above $\pm$ 550K) the predictions for 2x2 mm^2 sample (except M3) follow well the shape of the experimental curve, but once below 550K the predicted values get much lower. Remarkably, the temperature predicted by all models is very similar i.e. $\approx$340K (the temperature of the substrate) whereas the experimental values suggest 100K higher. A similar trend is observed in the 8x2 sample, where below 550K, the computational samples cool down much faster than the experimental ones.

When comparing experimental and predicted cooling curves, one has however to keep in mind that the experimental temperature is derived assuming that the change in lattice parameter is solely due to thermal expansion/contraction. Measurements reveal however important anisotropy in the lattice strain among the different reflections measured (figure 6.19). In the above analysis, temperatures were derived considering the X-ray diffraction peak $(01.2)_{\alpha/\alpha'}$. Compared to the initial lattice distance measured at 340K, these lattice planes get into tension after cooling, whereas others go into compression, such as, for instance, the $(01.0)\alpha/\alpha'$ in the 8x2 mm^2 sample.

(a) 2x2 mm^2 sample - cooling in the α/α′ phase

(b) 8x2 mm^2 sample - cooling in the α/α′ phase
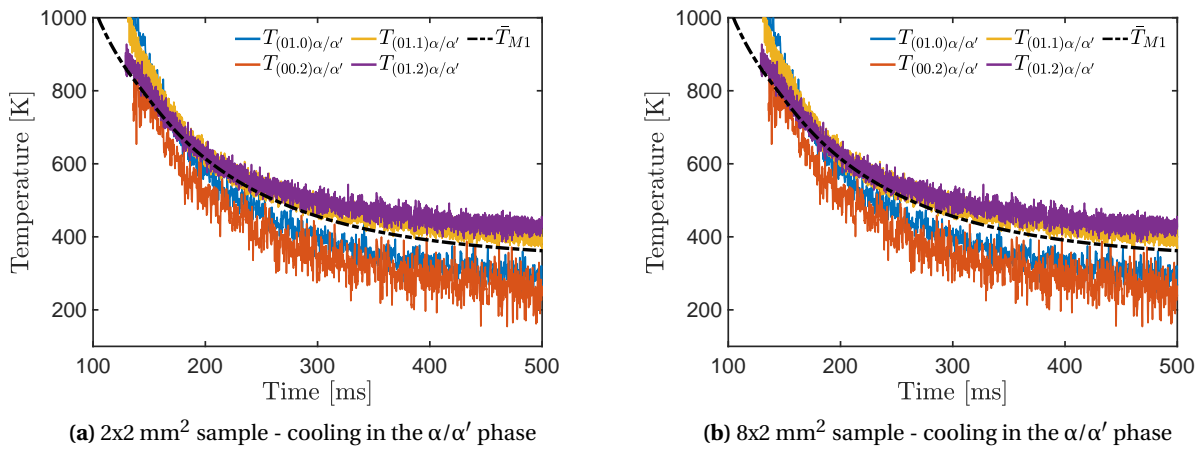
Figure 6.19 – Temperature profiles in the α/α′ phase calculated from the different reflections (figure 4.21) (a) for the 2x2 mm^2 , (b) for the 8x2 mm^2 sample. For comparison, the temperatures predicted by model M1 are added.

Figure 6.19 shows the simulated and experimental temperature profile calculated from the different α/α′ diffraction peaks (a) for the 2x2 mm^2 sample, (b) for the 8x2 mm^2 samples. Deriving the temperature from different reflections can give variations of up to 500K in the large sample, less in the smaller sample. Deriving the correct values requires detailed knowledge of the elastic-plastic anisotropy as well as taking into account the difference in texture of the samples [116].

In summary, the models M1 and M4 catch quite well the immediate cooling rates of the β phase after the laser has passed A$_{XR}$ as well as the shape of the cooling curves. The predicted values of maximum β temperature are good for M1 and M3, but adding radiation loss to M3 reduces these temperatures again. Differences in cooling behaviour of the α/α′ phase after the laser has travelled far away from the X-ray probed area or after the laser is switched off, suggests the importance of the introduction of elastic/plastic anisotropy in the models. To address the sluggish heating transfer to the α/α′ phase in the 2x2 mm^2 (not present in the 8x2 mm^2 sample) we explore the influence of the mesh size and anisotropic enhanced thermal conductivity.

6.7.3   The role of enhanced thermal conductivity and mesh size

In M4 an isotropic thermal conductivity coefficient was used above the melting point (equation 5.14) in order to mimic Marangoni effects. The value λ=4 was chosen to obtain a melt pool shape that matches the width and depth of a single track [78]. Previously, it has been demonstrated that heat gradients could be modified by introducing an anisotropic enhancement coefficient, influencing the temperature profile within the sample [141].

To investigate the influence of anisotropic versus isotropic enhanced thermal conductivity, a 1x1 mm^2 sample was simulated using M4 with different values of the enhancement parameters in the three principal directions. The temperature profiles were extracted with the same X-ray beam weighted averaging technique. The overall temperature evolution is shown in figure 6.20a, details are provided in the zoom-in around

the cycle where the laser crosses A_{XR} (figure 6.20b). The curves are labelled $\bar{T}_{M4(XYZ)}$; X, Y and Z being the value of the enhancement coefficient in the X, Y, and Z directions respectively. The curve labelled $\bar{T}_{M4(444)}$ corresponds to the reference sample with an isotropic coefficient of 4 as used in the original M4 simulation (equation 5.14). Furthermore, to explore the role of mesh size, a 1x1 mm² sample was simulated with an isotropic enhancement coefficient of 4 and a finer meshing element size of 30 x 30 x 30 µm². The curve is labelled $\bar{T}_{M4(fine)}$.

(a) 1x1 mm² sample - temperature profile   **(b)** Zoom on (a)
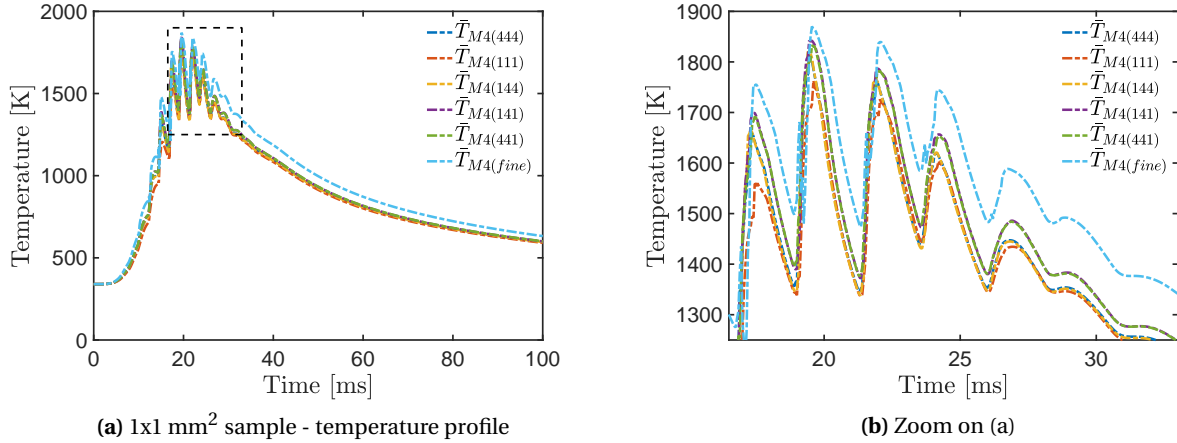
Figure 6.20 – Overall temperature profile for the different simulated models; b) Detailed profiles zoomed in the highlighted area in (a) around the instant when the laser cross A_{XR} (t ≈ 20 ms)

Changing the enhancement parameter in all three directions ($\bar{T}_{M4(111)}$ vs $\bar{T}_{M4(444)}$) or only in the (Y,Z) directions ($\bar{T}_{M4(111)}$ vs $\bar{T}_{M4(144)}$) has little impact on the temperature profile in the high-temperature regime. Increasing the enhancement coefficient in the Y direction ($\bar{T}_{M4(111)}$ vs $\bar{T}_{M4(141)}$), or the (X,Y) directions ($\bar{T}_{M4(111)}$ vs $\bar{T}_{M4(441)}$) slightly increases the temperature profile by about 40K on average. Reducing the mesh size has however a bigger influence on the temperature profile (curve $\bar{T}_{M4(fine)}$). This is evident when comparing $\bar{T}_{M4(444)}$ with $\bar{T}_{M4(fine)}$, where the mesh size in the (XY) plane was reduced from 60 µm to 30 µm. The temperature profile of the smaller meshed sample shifts up by about 100K on average.

To verify the influence of the mesh size with our experimental data, a 2x2 mm² sample was simulated with the model M4 and the fine mesh – M4(fine). Figure 6.21a compares the experimental data, pink for the β phase and purple for the α/α′ phase. The predictions for model M4 are shown in light blue, for the model M4 with refined mesh in orange. The laser scanning starts at t = 0 ms, and the black arrow shows when the laser beam is switched off. The laser crosses A_{XR} at t ≈ 65 ms. Figure 6.21c shows the predicted melt pool dimensions for M4(fine). Figure 6.21d shows the temperature evolution and the molten volume during 4 cycles evolution around t ≈ 65 ms. The refinement of the mesh in the (X,Y) plane improves the heat flow in these directions. As a result, the melt pool width and length increase (see figure 5.6h), the depth stays the same. The overall temperature profiles shift to higher values by 50K and are now closer to the experimental data. During the initial heating, the simulated curve remains however lagging. In other words, refining the mesh diminishes the difference between experimental and predicted values because the heat can travel better to A_{XR}. However, some differences remain, pointing to the role of material parameters used in the simulations. The size of the melt pool has slightly increased in the width, now measuring around 150 µm,

and in the length with 270 μm. The depth remains the same, at 150 μm.
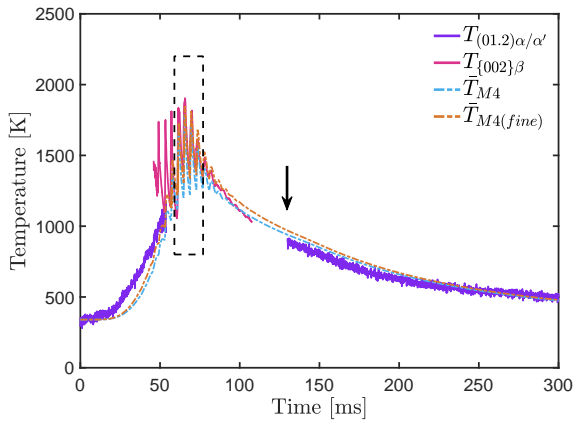
(a) 2x2 mm^2 sample - temperature profile
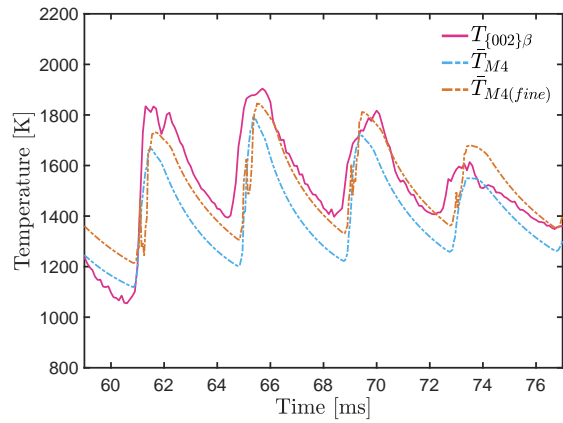
(b) Zoom on (a)
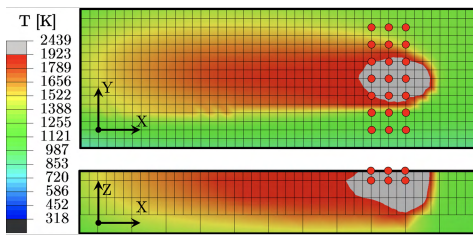
(c) Melt pool size
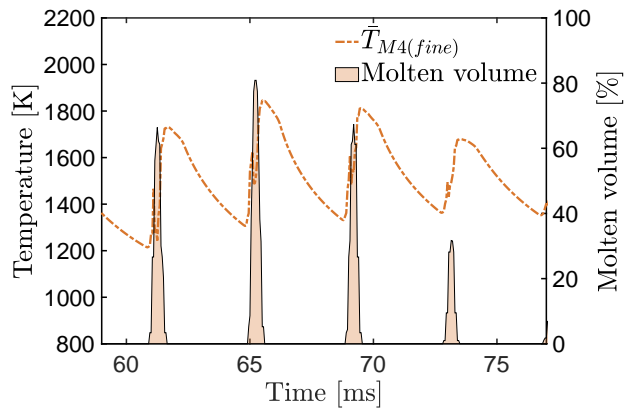
(d) Average temperature and molten volume interaction with A_{XR}

Figure 6.21 – Experimental temperature evolution derived from the $(01.2)_{\alpha/\alpha'}$ and $\{002\}_\beta$ reflections in purple and pink, respectively, and simulated results for model M4 and M4(fine) in dashed lines. A top view and cross-section of the simulated melt pools for model M4(fine) at t ≈ 65 ms are presented, with molten volume interaction.

7 Conclusion

A new machine for *operando* XRD experiments

The MiniSLM is a novel miniaturised device dedicated to the SLM processing of metallic powders, compatible with XRD measurements techniques. It has been successfully developed and tested at PSI and is now part of its infrastructure as an end-user station. In recent years, several similar devices have been developed at other synchrotron light sources. However the MiniSLM setup presented at PSI is one of a kind. It is the only device existing capable of using complex scanning strategies over a 3D powder bed while recording *operando* the influence of multiple scanning vectors on the microstructure evolution via XRD experiments.

Its design includes all the different components from commercial SLM systems. New layers can be deposited thanks to the recoating system together with a high precision displacement stage for the build plate. A 500W fibre laser coupled to a high precision scanning unit can selectively melt the metallic powder. A preheating option is available to heat up the build plate. And an inert gas circuit allows to create a protective atmosphere to prevent oxidation of the material during the printing process. Its custom-made software gives flexibility to the user to create simple or complex geometries, and synchronise both the laser scanning and the X-ray detector triggers for XRD measurements.

Before performing *operando* XRD experiments, it is important to proceed to trials with the desired material in order to determine its processing windows on the MiniSLM, since the optimum scanning parameters can differ from what is reported in the literature. Once found, it is possible to produce highly dense parts. Moreover, it is critical to consider which X-ray beam size is the most adapted to the material of the study and the objectives of the experiments. A larger beam will result in better grain statistic but will also capture less pertinent information and external perturbations. A smaller beam will provide a more accurate and detailed picture of the experiment, at the expense of the quality of the signal since less grains in the material will be probed by the X-ray beam. Therefore, a compromise has to be found.

This MiniSLM is designed to be used in either reflection or transmission modes during XRD experiments. The XRD patterns acquired in transmission mode are the result of a convolution of information coming from different depths in the material, which makes the data analysis challenging. The reflection mode only probes the surface region of the sample, which eases the data interpretation process since the information comes only from a limited volume. This measurement configuration has been used as the preferred method to

acquired XRD in this dissertation.

A method developed for rapid analysis

Because of the character of the data acquired, a specific procedure has been developed to analyse the large quantity of diffraction pattern collected during the XRD measurements. Up to 20'000 diffraction patterns can be acquired for a single *operando* acquisition. For that reason, it is critical to optimise the analysis routine to extract information from the diffraction patterns in a rapid and efficient manner. The method of the centre of mass proves to be suitable for that purpose, allowing to analyse the data between two XRD measurement during beamline experiments. By doing a weighting average of the diffraction peak intensity, a good estimation of the peak position can be found without relying on a more complex fitting procedure. Once the peak position is found, it is possible to convert it into strain and then temperature values, giving an estimate of the temperature evolution within the X-ray illuminated region. Moreover, the peak intensities can also be measured by integrating over a certain range around the peak position. Finally, a Matlab routine has been developed and refined such that the output of the program does not depend on the user performing the data analysis.

Results on Ti-6Al-4V

The phase transformation of a Ti-6Al-4V alloy has been followed during laser scanning. It has been demonstrated that the scanning vector length has an influence on the duration of the β phase existence at high temperatures. A long scanning vector generates a cycling between the α/α′ and the β phases within the X-ray probed area, which leads to a finer microstructure. A short scanning vector accumulates the heat locally due to the rapid back and forth of the laser over the scanned area. Therefore, the β phase persists much longer, allowing the prior-β grains to grow larger than when when a long scanning vector is used. Consequently, the final α′-martensitic lathes size increases.

Depending on the size of the structure built, the final mechanical properties of the printed part can be affected. For thin wall structures or porous structures, it would be detrimental to have only few large grains within the wall thickness. For that reason, attention should be paid when using different scanning strategies, like the chessboard scanning pattern.

By following the peak position change over time in the XRD pattern, it is possible to derive the strain evolution within the X-ray probed area during laser scanning. Afterwards, it can be converted into a temperature, owing that a correct thermal expansion coefficient is used. This gives an immediate estimation of the cooling rates, which vary between 10^3 K/s and 10^6 K/s for Ti-6Al-4V. Following reflections coming from different crystallographic planes may lead to a significant difference in the final strain value after laser scanning, which is a proof of the residual stresses buildup in the sample due to SLM processing.

The obtained temperature curves can be used to help for the validation of FEM based analysis. The MiniSLM offers the possibility of a direct measurement of the sample temperature, which can then be used as a reference to confirm the accuracy of FEM calculations. Obtaining accurate temperature values is a critical aspect of simulation predictions, since the calculations of residual stresses and phase field evolution are based on the thermal gradients within the sample.

Outlook

The MiniSLM has been tested on Ti-6Al-4V to investigate diverse aspects of the material evolution under SLM processing conditions thanks to ultra-fast XRD experiments. It opens a new door for alloy development and computational modelling by offering a real-time tracking of the material evolution during laser scanning.

Only a handful of already existing alloys are compatible with the SLM technique due to its extreme manufacturing conditions with very high heating and cooling rates. This can be understood as most of the alloys existing today were not made for laser powder bed-based processing. Therefore, the design new kind of alloys dedicated for SLM appears as a necessity, as it was done for other conventional manufacturing techniques.

The strength of the MiniSLM lies in its capability to track the apparition order of different phases in the material during *operando* XRD experiments. Designing new alloys is a delicate task. Their behaviour can be anticipated by phase field modelling, but these are just predictions. The MiniSLM is able to give a direct insight into the microstructure evolution under SLM processing, which can greatly cut the dedicated research time.

Towards a second generation

Because of time constraints in the machine development, the design of the MiniSLM was made such that the device is simple enough to be manufactured, assembled an operational within the second year of the project. After experimenting a lot, it appears that some flaws still need to be addressed, which is the case for any prototype developed for research purposes.

The gravity based recoating system is not well suited for powder with low flowability, which hinders the correct deposition of a new layer. For that reason, a double piston based system might be a good alternative, with one piston moving upward to feed the powder and a second one with the build plate moving downward. The new layer is then deposited by a scrapper moving above both pistons. Moreover, the preheating system is not powerful enough in the actual version of the machine, and a larger resistor is needed. This means that the entire build plate and its support should be redesigned.

The scanning unit mirrors have a coating for both infrared a green wavelength. A green laser could be adapted on the machine to study the effect of the change of wavelength on the metallic powder. Most of the metals have quite a high reflectivity under infrared wavelength, however when switching to a green laser source, the reflectivity decreases which is beneficial since the printing process may become more stable. The choice of a green laser as a source for the MiniSLM was left open, in case a one would become available. However, interchanging laser means that the lens and laser entrance window of the printing chamber have to be exchanged, since the current ones are only for infrared wavelength. A change of lens also involve an offsetting of the whole scanning head according to the new laser beam path.

Finally, only the reflection mode configuration was considered in this thesis. If an energy sensitive X-ray detector with ultra fast acquisition is developed in the future, it could be possible to perform EDXRD with the MiniSLM in transmission mode configuration. This technique would add a depth resolution on the measurements, which could help to resolve what is happening under the surface of the sample for the layers which experience a partial remelting process or subsequent heating cycles.

Appendices Part II

A Bronze (CuSn8) and red gold (5N)

Precious metals are materials of interest for the AM[3] project. A prime candidate is an 18-carat red gold alloy (75wt% Au-20.5wt% Cu-4.5wt% Ag or 51.1at% Au-43.3at% Cu-5.6at% Ag) that we will refer to as 5N according to the standard colours adopted for watch cases [134]. There are very few studies on SLM processing for gold alloys. It has been shown that it is possible to reduce the amount of porosity by surface treatment or addition of alloying element inside Au-Cu-Ag powder [142] and that it would have an impact on the grain size and hardness of the material [59]. However, no studies were conducted on the investigation of microstructure evolution during SLM processing and how it relates to the mechanical properties.
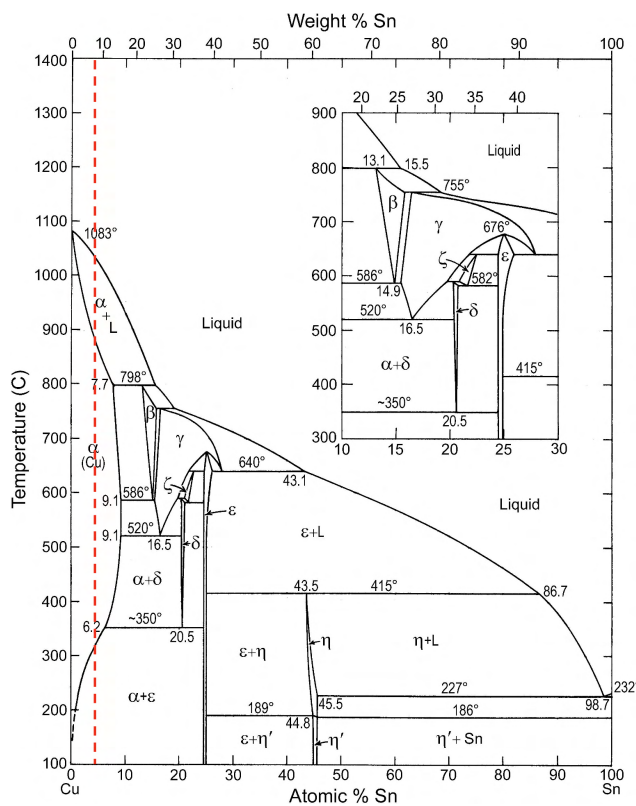
Figure A.1 – Cu-Sn phase diagram. Image from [143].

Before starting to study directly the 5N alloy, a bronze alloy has been selected as a cheaper alternative to optimise the printing parameters on the machine. The alloy studied first here is CuSn8 (wt%), which is supposed to behave similarly as the 5N under SLM processing condition. This alloy is used to determine the processing window ($P - \nu$) on the MiniSLM.

A.1   CuSn8

A.1.1   Material

CuSn8 is a copper-based alloy containing 92 wt% of copper (Cu) and 8 wt% of tin (Sn). Based on its phase diagram (figure A.7) it is composed of two phase: a dominant Cu-α phase which is Face-Centred Cubic (FCC) with a lattice spacing a = 3.61443 Å; and an ε phase which is orthorhombic, and has the chemical composition is Cu_3Sn with the lattice spacings a = 5.529 Å, b = 47.75 Å and c = 4.323 Å [143].

A.1.2 Reflectivity

It is possible to determine the reflectivity of a metal under a normal incidence using the Fresnel equation:

$$R = \frac{(n-1)^2 + k^2}{(n+1)^2 + k^2} \tag{A.1}$$

with R the reflectivity under normal incidence, n the real part and k the imaginary part of the metal complex refractive index [144].

Such complex refractive coefficients have been measured and are available in the literature [145]. Based on these values, it is possible to plot the reflectivity of copper and tin over the illumination wavelength. Figure A.2 shows the reflectivity of copper and tin until a wavelength of 1200 nm. The fibre laser used in the MiniSLM is an infrared laser with a wavelength of 1070 nm, and is represented on the figure by the purple vertical line. By looking at the curves in figure A.2, the reflectivity of Cu is at 96% and the one of Sn is at 82%. The reflectivity of metals cannot be added linearly, but for a mixture of different elements, the refractive index follows the equation:

$$3\left(\frac{n^2 - 1}{n^2 + 2}\right) = \sum_j N_j \alpha_j \tag{A.2}$$

with n the refractive index of the mixture, N_j the number of atoms of each component per unit volume and α_j the polarisability of each component [146].

The polarisabilities of Cu and Sn are not directly available. However a quantitative observation can be made here. CuSn8 is composed by 92 wt% of Cu and 8 wt% of Sn, which corresponds to 96 at% of Cu and 4 at% of Sn. One can observe that the total refractive of a mixture is proportional to the number of atoms present in the unit volume, thus the atomic percentage. It is clear that Cu is dominant compared to Sn, as a result the reflectivity of CuSn8 will be certainly above 90%. This alloy will then reflect an important part of the laser energy, and only a small fraction will be absorbed by the material.

Figure A.2 – Reflectivity curves for Cu and Sn. The gap in the Sn curve is due to the lack of data from the literature. The purple line represents the laser wavelength of the MiniSLM

A.1.3 Powder characterisation

The CuSn8 powder was provided by Heraeus. Table A.1 shows the chemical composition and other powder properties given by the manufacturer. This powder is gas atomised with a particle size distribution of 15-45 μm, within the typical range for SLM processing. Before using this powder to make samples, characterisation was performed to assess if the material is compliant to the information communicated by the manufacturer. SEM imaging and particle distribution measurement were done to look at the particle shape and their size

range. EDS investigation were also realised to inspect chemical composition in the powder, and possible elemental segregation.

Table A.1 – CuSn8 powder data from Heraeus

Chemical Composition		Important measurement parameters	
Element	Concentration [wt%]	Angle of repose [°]	26.2
Copper (Cu)	balance	Powder density [g/cm^3]	5.03
Tin (Sn)	8	Average angle of spatula [°]	29.3
		Fluidity index	71

SEM images

To investigate the powder characteristics, a field emission gun scanning electron microscope (FEG SEM) Zeiss NVision-40 was used on a sample of powder deposited on a conductive carbon tape. Figure A.3 shows an SEM image of the powder (a) with a zoom on few particles (b). These images reveal that the powder particle is not as spherical as expected, with agglomerates on the particles, which might impact the flowability of the powder [14].

(a) CuSn8 powder particles   **(b)** Zoom 5x
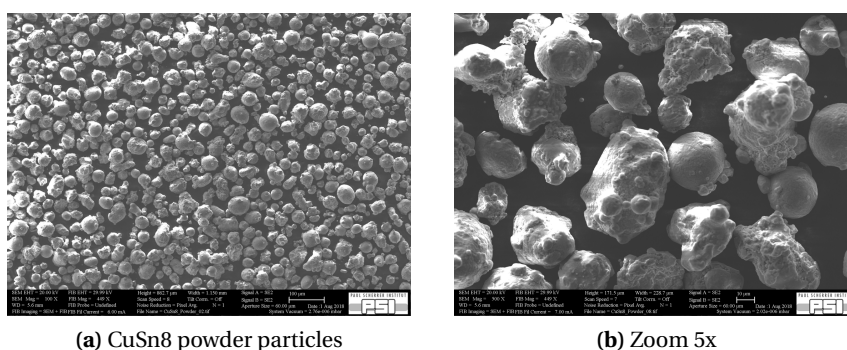
Figure A.3 – SEM imaging of the CuSn8 powder

Particle size distribution

$D_{10}=16.5\mu m$
$D_{50}=26.6\mu m$
$D_{90}=44.5\mu m$
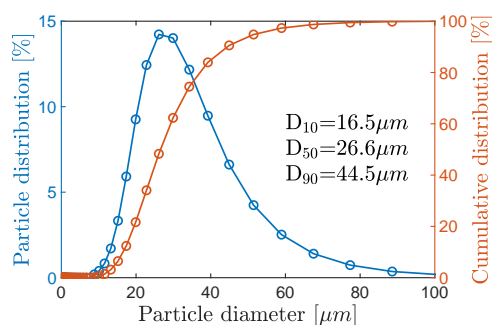
Figure A.4 – CuSn8 particle size diameter

The particle range communicated by Heraeus is 15-45 µm. To confirm that, the particle size distribution was measured by a laser diffraction particle size analyser Partica LA-950 V2 system (Horiba, Tokyo, Japan). Figure A.4 shows the particle distribution on the left vertical axis and the cumulative distribution on the right axis. From this distribution, the D_{10}, D_{50} and D_{90} were measured to determine the size repartition in this CuSn8 powder. The D_{10}, D_{50} and D_{90} are at 16.5 µm, 26.5 µm and 44.5 µm respectively. The particle size distribution of this powder corresponds well to the range provided by the manufacturer, and is comparable to the one obtain for the Ti-6Al-4V.

EDS measurements
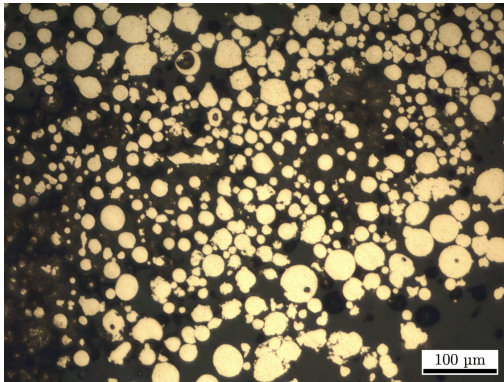
Figure A.5 – CuSn8 powder particle cross sections

To investigate the powder chemical composition, an EDS analysis system from Oxford Instruments was used. A sample of powder was embedded and polished to obtain cross sections of the powder particles. Figure A.5 shows the embedded particles after polishing under an optical microscope. Some particles present apparent pores created during the gas atomisation process.

An EDS mapping was performed on the cross section of one particle, as shown in figure A.6. The chemical content is correct inside the CuSn8 bronze particle matches with the values announced by the manufacturer (table A.1). Inside the particle, one can differentiate the eutectic copper-tin phase which has high tin content (figure A.6b, bright phase) and the dendritic α-Cu phase with low tin content (figure A.6b, dark phase) [147].
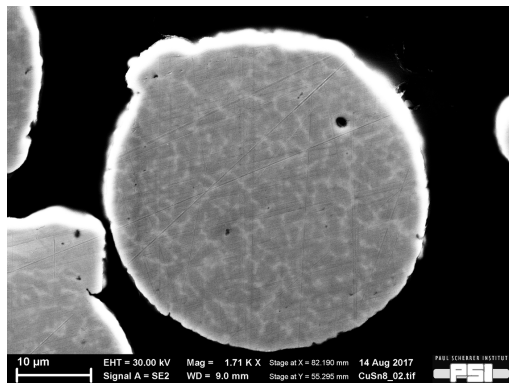
(a) Powder particle cross section
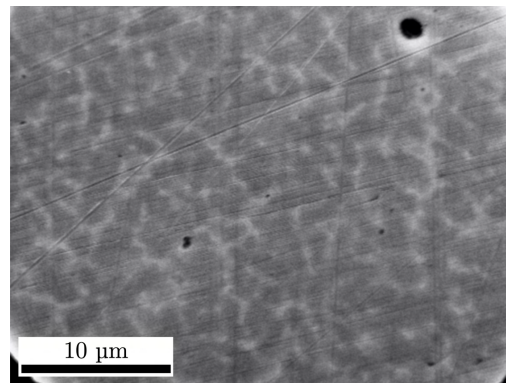
(b) Region of interest for EDS mapping
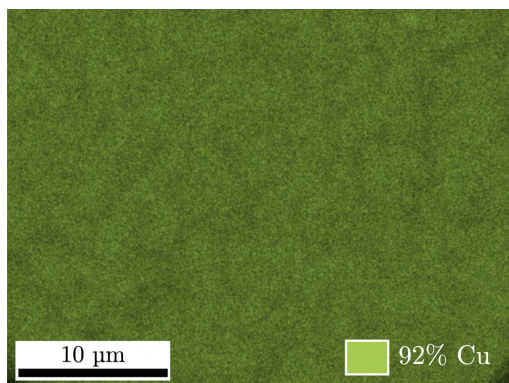
(c) Cu content
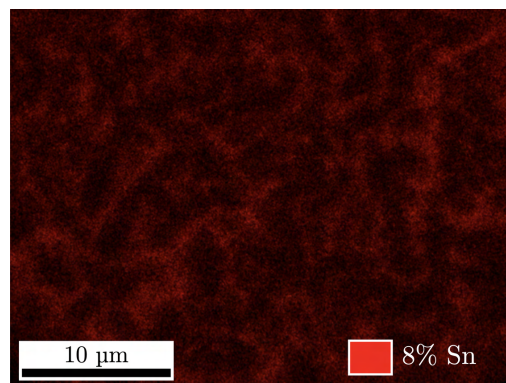
(d) Sn content

Figure A.6 – EDS mapping of one CuSn8 particle cross section

A.2 Red Gold - 5N

A.2.1 Material

The atomic composition of 5N is 51.1at% Au-43.3at% Cu-5.6at% Ag, which is close to the equiatomic AuCu alloy. It is known from literature that this alloy undergoes an order-disordered transformation [148, 149] that can lead to misfits strains between the ordered precipitates and the disordered matrix. This behaviour may affect the part during SLM printing by inducing warping and must be considered.
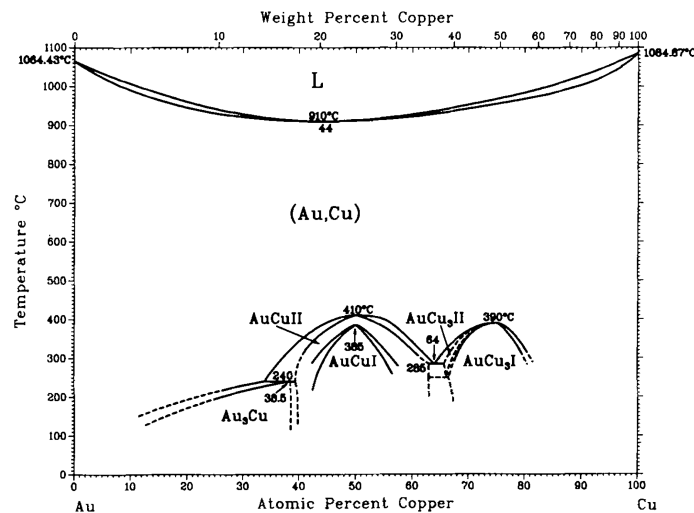
Figure A.7 – Au-Cu phase diagram. Image from [150].

The structural transformation of the Au-Cu (figure A.7) system was described by Hirabayashi et al. [148] and Syutkina et al. [151]:

- Above 410°C, AuCu has a disordered FCC structure with a lattice parameter a = 3.88 Å (figure A.8a). When cooling down, it undergoes ordering transformation and forms two different lattice structures.
- AuCuII (figure A.8c), between 410°C and 380°C which is orthorhombic (a = 3.96 Å, b=10a, c = 3.67 Å) and where gold and copper atoms exchange (002) planes along b direction every fifth cells (antiphase boundaries) [151].
- AuCuI (figure A.8b), below 380°C which has a Face-Centred Tetragonal (FCT) structure (a = 3.96 Å, c = 3.67 Å) made of alternated (002) planes of only gold or only copper atoms. The ordered AuCuI has preferential growth direction along {110} [148].

When the disordered AuCu FCC phase transforms into the ordered AuCuI FCT phase, a considerable amount of strain is introduced inside the material because of coherent AuCuI precipitates with a different c/a ratio (c/a=0.92) [148, 151]. It has been first reported by Kurnakow et al. [152] and then later by Arunachalam et al. [153] that the quenched α-AuCu alloy (which correspond to the disordered phase) has a soft and ductile behavior. On the contrary the alloy becomes hard and brittle when ordered into AuCuI after annealing. This behaviour is important for SLM processing since the material experiences a series a different cooling rates, from the top layer where the material is rapidly quenched from the liquid phase to the underlying layer where the alloy experiences a subsequent reheating cyclces.

(a) Disordered α-AuCu FCC phase

(b) Ordered AuCuI FCT phase

(c) Unit cell of the AuCuII superstructure
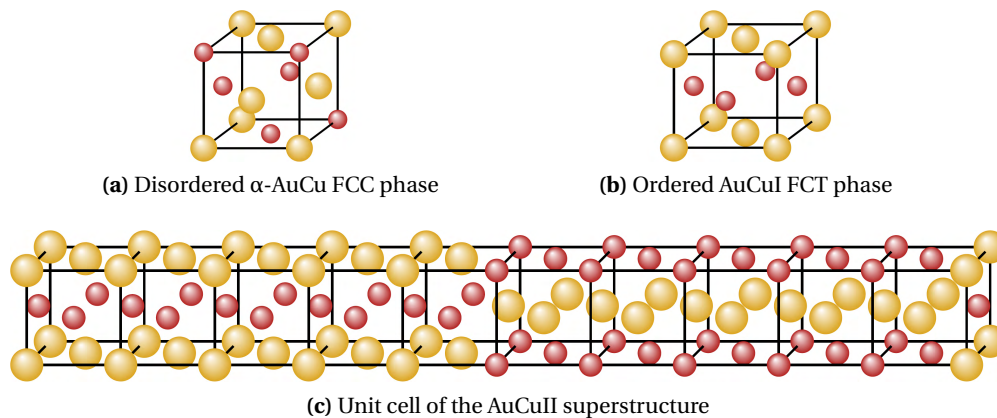
Figure A.8 – Crystallographic faces of the Au-Cu system. Images taken from [154].

Until now, research on how cooling rate affects the order-disorder transformation and the microstructure has not been performed. There are few publications about SLM of gold but focused on the external aspect of the material and how to improve density and surface quality. Processing parameters of pure gold (24 ct) during SLM have been reported by Khan et al. to obtain dense parts [14, 155]. However, the minimum porosity level reached was around 10%, which is not suitable for watch and jewelry industries.

Alloying of 3N powder (75wt% Au, 12.5 wt% Cu, 12.5wt% Ag) [134] with Fe and Ge has been reported by Klotz et al. [59, 142] to improve part density and surface finish by reducing thermal conductivity and reflectivity. Alloying with Ge or Fe changes reduces the electrical conductivity of the 3N alloy. According to the Wiedmann-Franz and Hagen-Rubens laws, a decrease in electrical conductivity respectively reduces the thermal conductivity and reflectivity of the alloy [142].

A maximum density of 99.8% was reached after addition of Ge in the powder [142]. Grain size variation was also observed after alloying [59]. Fe has a tendency to increase the grain size whereas Ge produces grain refinement. This behavior will affect the ductility of the part during SLM. Another strategy to improve the density and surface finish of the SLM parts is laser re-melting of the layer. This has been reported on 5N by Zito et al. [156], who managed to reduce the apparent porosity level to 0.01%.

A.2.2 Reflectivity

The reflectivity of the 5N alloy was calculated in the same way as in section A.1.2, using equation A.1 and the refractive coefficients available in [145]. The resulting curves for the different elements are presented in figure A.9.

At the wavelength of the MinSLM laser, the reflectivity of Cu is at 96% and the one of Au and Ag are at 98%. In the same way as CuSn8, this alloy will reflect an important part of the laser energy, and only a small fraction will be absorbed by the material. One can thus assume that they will behave the same under infrared laser illumination.
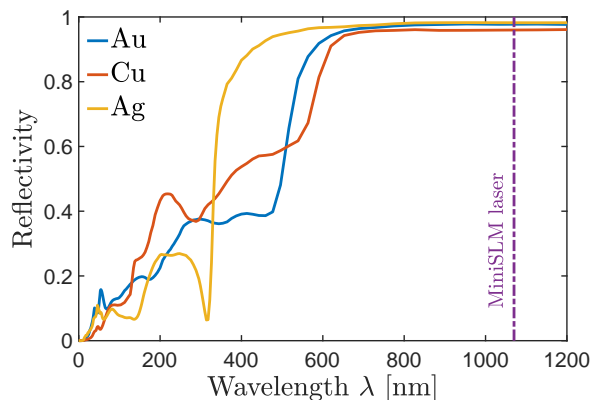
Figure A.9 – Reflectivity curves for Au, Cu and Sn. The purple line represents the laser wavelength of the MiniSLM

A.2.3 Powder characterisation

The 5N powder was also provided by Heraeus, the same company supplying the CuSn8 powder. Table A.2 shows the chemical composition and the particle size distribution given by the manufacturer. This powder is gas atomised with a particle size distribution of 15-45 µm.

Table A.2 – 5N powder data from Heraeus

Chemical Composition		Particle size distribution	
Element	Concentration [wt%]	Particle range	diameter [µm]
Gold (Au)	75.1	D_{10}	13.77
Cupper (Cu)	20.4	D_{50}	25.61
Silver (Ag)	4.5	D_{90}	40.84

SEM images

(a) CuSn8 powder particles

(b) Zoom 5x
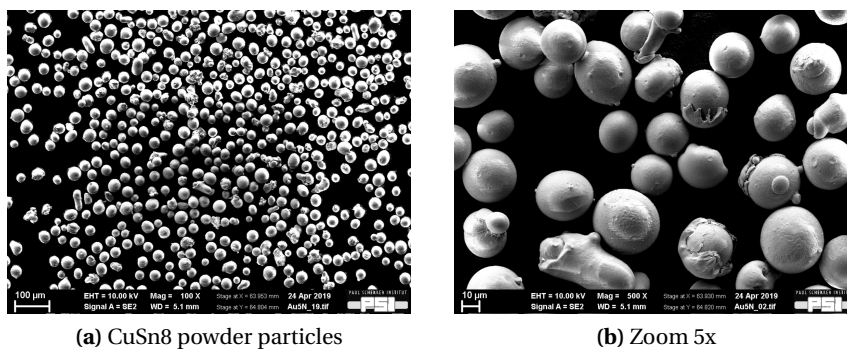
Figure A.10 – SEM imaging of the 5N powder

A sample of powder deposited on a conductive carbon tape was observed by SEM imaging. Figure A.10 shows an SEM image of the powder (a) with a zoom on few particles (b). It has a spherical shape, characteristic from

135

the gas atomisation process.

Particle size distribution

The particle range communicated by Herareus is 15-45 µm. Figure A.11 shows the particle distribution on the left vertical axis and the cumulative distribution on the right axis, measured by the company. Because of time constraints, it was not possible to measure the particle size distribution at PSI.
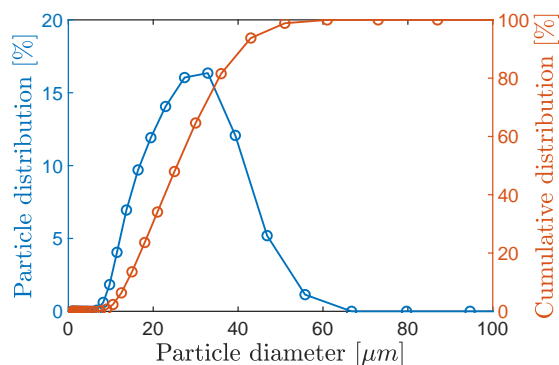
Figure A.11 – 5N powder particle size diameter measured by Heraeus

EDS measurements

To investigate the powder chemical composition, an EDS analysis system from Oxford Instruments was used. A sample of powder was embedded and polished to obtain cross sections of the powder particles. Figure A.12 shows the embedded particles after polishing under an optical microscope. Some particles present apparent pores created during the gas atomisation process.
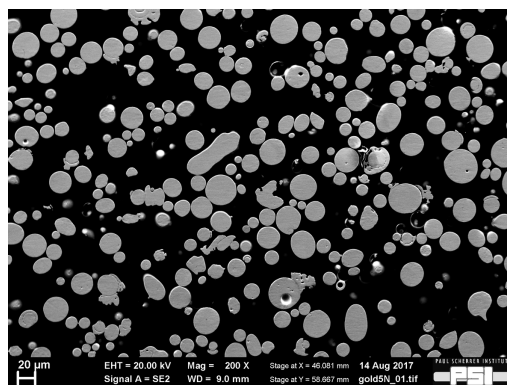
Figure A.12 – CuSn8 powder particle cross sections

An EDS mapping was performed on the cross section of one particle, as shown in figure A.13. The red gold particles have a homogeneous repartition of chemical elements but the composition is different from the one announced by Heraeus (see table A.2). The gold concentration is close to 75.1%, but copper is under 20.4% and silver is higher than 4.5%. This variation in the measured chemical composition for the red gold may be

due to the presence of the embedding resin during the EDS mapping. The chemical content is correct inside the CuSn8 bronze particle, (figure A.6) which comfort the previous statement because no resin is present in the mapping area.

(a) Powder particle cross section

(b) Region of interest for EDS mapping

(c) Cu content

(d) Sn content
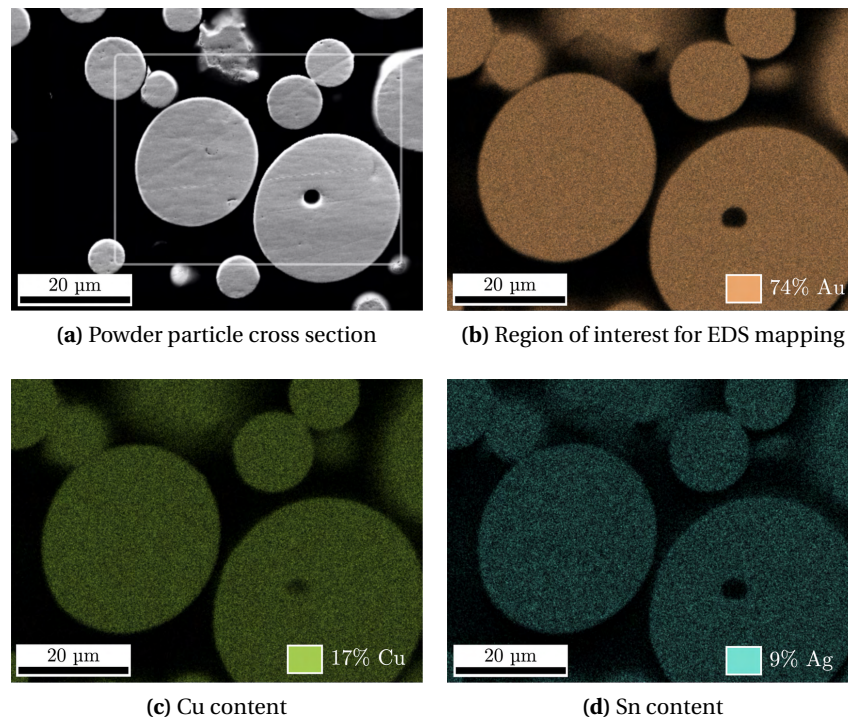
Figure A.13 – EDS mapping of few 5N particle cross section in the area highlighted in (a)

A.3 CuSn8 processing window

A.3.1 Laser scanning with a 100 μm laser spot diameter

In order to determine the printing parameters of this CuSn8 alloy, the same approach was taken as for the Ti-6Al-4V in section 4.1. This particular chemical composition has not been reported in the literature for SLM processing. However, the printing parameters of similar copper based alloy are available. The printing of pure copper has been reported with very high power and scanning speed with up to 1kW and 4000 mm/s, respectively [60, 61]. CuSn10 was printed with a laser power of 271W and a scanning speed of 210 mm/s in [157]. Another study reports the SLM processing of CuSn4 with a laser power between 50W and 195W, and a scanning speed between 50 mm/s and 1950 mm/s [158].

Here a power variation between 200W and 350W was chosen, with a step of 25W; and a scanning speed between 150 mm/s and 400 mm/s with a step of 50 mm/s. The resulting parameter combinations are listed in table A.4. A first set of 42 lines of 4 mm length were printed with a laser spot diameter of 100 μm, and is presented in figure A.14. The layer thickness was 40 μm. The build plate used in all CuSn8 printed sample are made from commercially available CuSn8 alloy.

Table A.3 – Parameter selection for the single track scanning for CuSn8

Line	Power [W]	Speed [mm/s]	Line	Power [W]	Speed [mm/s]	Line	Power [W]	Speed [mm/s]
1	200	150	15	200	250	29	200	350
2	225	150	16	225	250	30	225	350
3	250	150	17	250	250	31	250	350
4	275	150	18	275	250	32	275	350
5	300	150	19	300	250	33	300	350
6	325	150	20	325	250	34	325	350
7	350	150	21	350	250	35	350	350
8	200	200	22	200	300	36	200	400
9	225	200	23	225	300	37	225	400
10	250	200	24	250	300	38	250	400
11	275	200	25	275	300	39	275	400
12	300	200	26	300	300	40	300	400
13	325	200	27	325	300	41	325	400
14	350	200	28	350	300	42	350	400
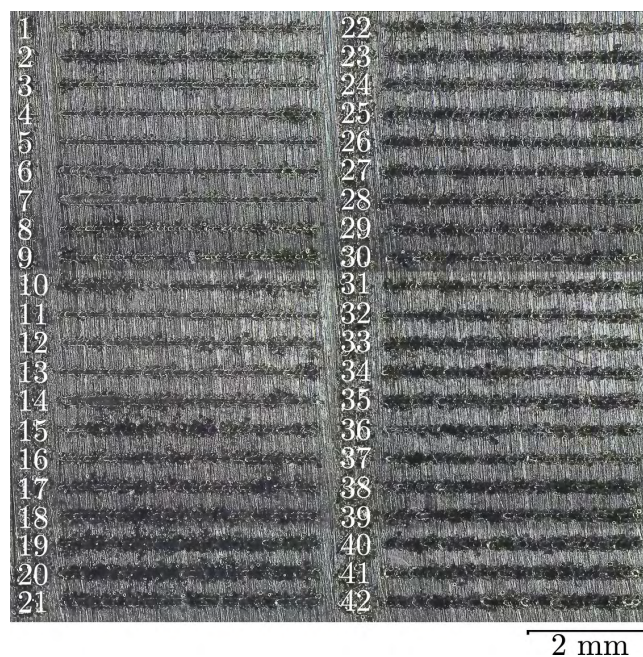
Figure A.14 – CuSn8 single tracks printed with a 100 µm laser spot diameter

By looking at figure A.14, what is striking is the high number of dark or black lines. Basically all the single tracks from line n°15 until line n°42 are blackened by some sort of deposit generated during printing. This is most likely soot that is generated by printing instabilities and adhere to the surface after laser scanning [159]. The printing process was performed under inert atmosphere with an oxygen content of less than 0.2% measured at the oxygen sensor, so it is unlikely that this is the cause. Nevertheless, some tracks still seem to be acceptable. The lines 3, 4, 5, 11, 12, 13 and 28 were selected for the printing of 4x4x0.4 mm^3 samples. The hatch was selected as being 70% of the line width, and the scanning strategy used was bi-directional scanning with a 90° rotation between each layer. The results for lines 3, 4, 5 and 11 is presented in figure A.15.

(a) Samples from lines 3, 4, 5, 11   **(b)** Zoom on sample "Line 3*
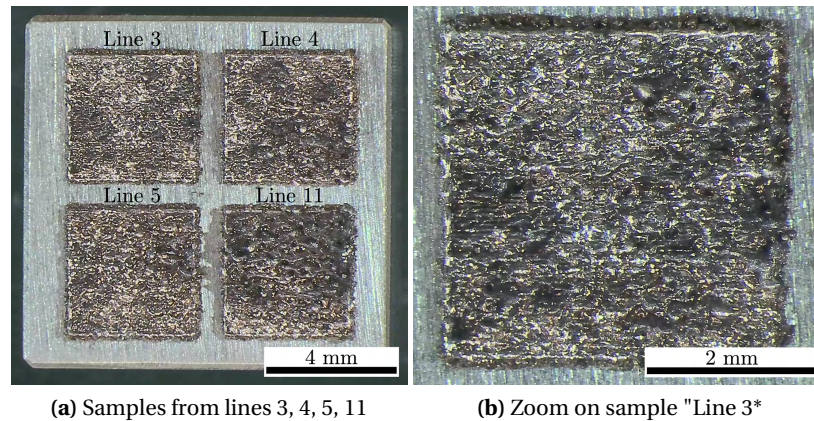
Figure A.15 – Cusn8 square printed sample with selected parameters from table A.4

The surface quality of these samples turned out to be very bad. Figure A.15b shows a zoom on the sample where the parameters of line 3 were used. The surface is highly irregular, and full of open pores. The previous layers are visible, which indicates that strong instabilities are occurring during the SLM processing of this CuSn8 alloy. For such short samples (0.4 mm height), it is simple to correlate the top surface quality to the sample density, which is very low. A similar result was obtained for the samples printed with the parameters from lines 12, 13 and 28.

A.3.2 Laser scanning with a 50 μm laser spot diameter

Since copper based alloys have a high reflectivity for infrared wavelength ($\approx$ 98%), one possibility for the printing to be unsuccessful with a 100 μm laser spot diameter is that the surface energy density is too low to maintain stable processing conditions. The surface energy density can be defined by:

$$E_S = \frac{P}{\pi r^2} \tag{A.3}$$

with P the laser power and r the laser spot radius.

In order to increase the surface energy density, the laser spot diameter has been decreased to 50 μm, which means that the surface energy density has become 4 times higher. The same parameters presented in table A.4 were used to print single tracks with a laser spot diameter of 50 μm. The results are presented in figure A.16. The layer thickness was 40 μm. The results are not better than the one obtained in figure A.14. Samples were nevertheless manufactured to verify if the is an improvement when printing 3D structures. The parameters from lines 1, 3, 8 and 10 are presented in figure A.17. The hatch was selected as being 70% of the line width and the scanning strategy used was bi-directional scanning with a 90° rotation between each layer. The number on the bottom right corner of each sample corresponds to the line number used in table A.4. The surface quality is still very bad but there is a slight improvement on the soot deposition on the top of the sample by comparing with figure A.15. It remains that the processing instabilities during printing are still present with the new laser spot diameter.
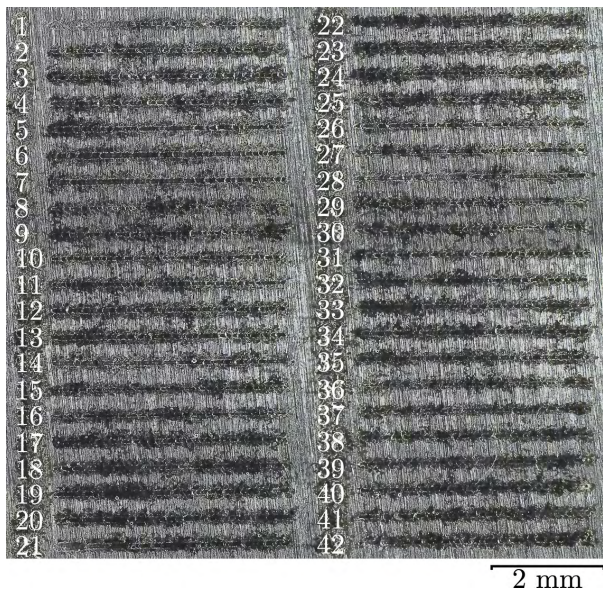
Figure A.16 – CuSn8 single tracks printed with a 50 μm laser spot diameter
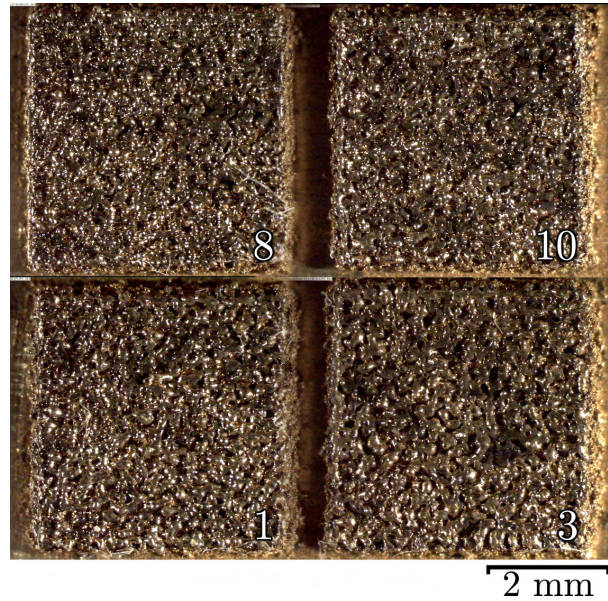
Figure A.17 – Cusn8 square printed sample with selected parameters from table A.4

A.3.3 Single layer study

To understand better what is happening, it is necessary to take a step back in the layer deposition process and observe how the first layer looks after printing. Several printing parameter combination were explored with laser power between 200W and 400W, and scanning speeds between 100 mm/s and 800 mm/s. The hatch distance was kept constant at 100 μm for all the sample, the layer thickness was at 40 μm and the laser spot diameter at 50 μm. The scanned area was chosen as 4x1 mm^2 on a CuSn8 substrate.
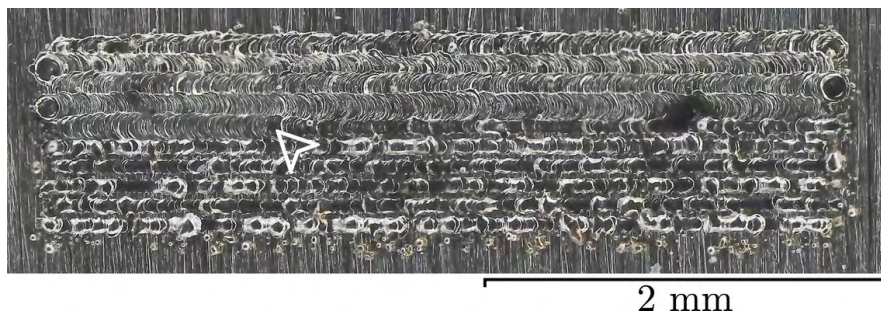
Figure A.18 – Single layer for a laser power of 300W and a scanning speed of 250 mm/s. The laser scanning starts on the top left corner. The white arrow represents the transition from stable to unstable regime.

Figure A.18 shows the result for the sample printed with a laser power of 300W and a scanning speed of 250 mm/s. The laser starts on the top left corner of the rectangle and scans the layer in a bi-directional fashion. The first four lines printed seem to be of good quality, with nice melted tracks and no soot deposition. However at the 5th line, there is a transition from this stable regime to an unstable regime as represented by the white arrow on figure A.18. The melt tracks become strongly irregulars, and soot deposition is observed on the sample.

This phenomenon can be explain by looking at the different heat loss mechanisms that are intervening during laser scanning. Figure A.19 shows the phenomena happening during laser scanning in a cross section of the melted track along the scanning direction. The laser beam (dark red) reaches the sample surface and is partially reflected by the alloy, which is the first kind of loss that will be qualified as "reflection losses". What is absorbed by the material contributes to the formation of the melt pool (red). The sample experiences then two type of heat losses. The first one are the convection and radiation losses (green) happening on the surface of the sample, where the heat is extracted form the sample by gas convection above the sample and radiation of the alloy, respectively. The second one are conduction losses, where the heat travels through the sample. In order to maintain a stable melt pool, the energy absorbed from the laser beam by the material must balance all the losses mechanism happening simultaneously.
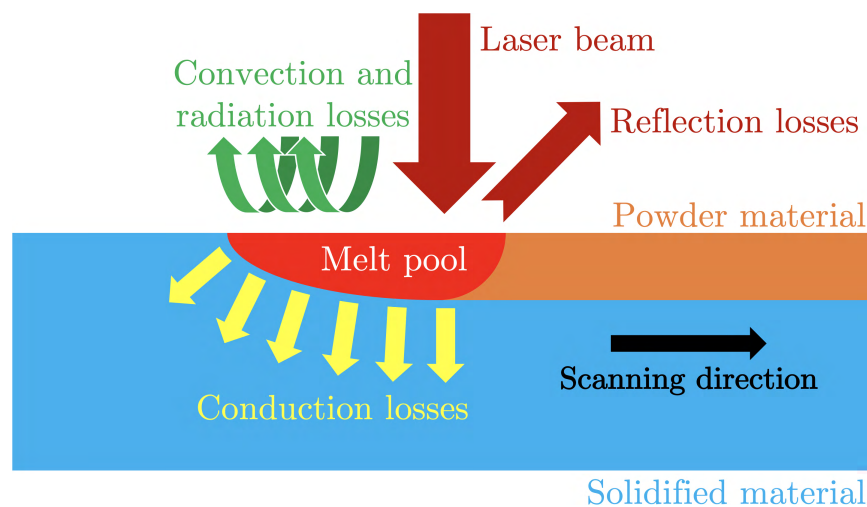
Figure A.19 – Heat losses present during laser scanning

The first important point to consider here is the reflectivity of the CuSn8. As presented in section A.1, the reflectivity of this alloy is above 90%, which means that actually a limited amount of the laser energy is absorbed by the material. Additionally, it has been observed that the reflectivity of metals drops by a coefficient between 20% to 50% after reaching the liquid state. In the case of laser melting of CuSn8, this means that the alloy is quite difficult to melt with an infrared laser and a high power is therefore required. However it experiences a strong energy input after reaching the melting point, which is a first factor of instability.

Secondly, it is well known that copper is an excellent thermal conductor, that's why it is widely used as heat sink material. CuSn8 has a thermal conductivity of 62 W/m.K at room temperature [160]. Moreover, the thermal conductivity tends to increase with the temperature thanks to thermal agitation within the material. All that put together makes the conduction losses quite important for this experiment since substrates of CuSn8 are also used to avoid material contamination.

Looking again at figure A.18, the possible explanation behind what happened is that the melt pool is quite stable since the laser energy input balances the heat losses within the material. But at the 5th line, thus equilibrium is disrupted by either a reduction in the energy input due to some soot shielding the laser beam, or an increase of the heat losses because of the temperature going up in the sample.

Table A.4 – Parameter selection for the single layer scanning for CuSn8

Layer	Power [W]	Speed [mm/s]	Energy density [J/mm³]	Layer	Power [W]	Speed [mm/s]	Energy density [J/mm³]
1	250	200	313	2	250	250	250
3	250	300	208	4	250	350	179
5	300	350	214	6	300	400	188
7	300	450	167	8	300	500	150
9	400	500	200	10	600	250	146
11	400	700	143	12	800	250	125
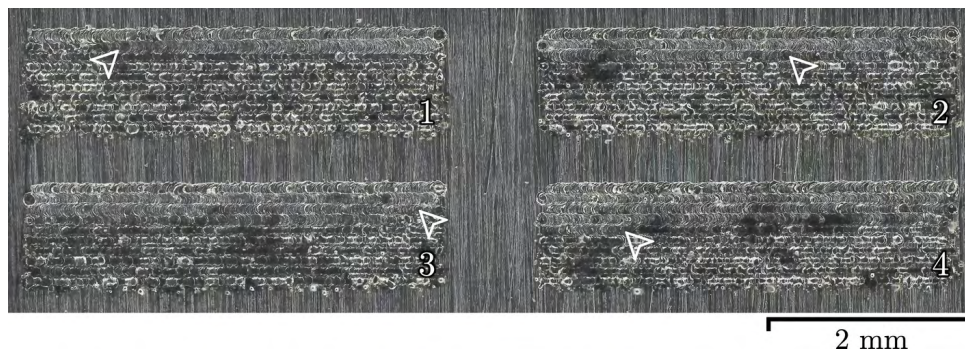
Figure A.20 – Selected layer 1 to 4, with printing parameters indicated in table A.4. The location of the disruption is indicated by the white arrow.

It is possible to track the evolution of this disruption point by looking at single layers printed with different parameter combinations. Table A.4 presents a selection of some parameters in the explored range with the calculated energy density. The first four layers are shown in figure A.20. They were printed at a constant power of 250W and a scanning speed going from 200 mm/s for layer 1 to 350 mm/s for layer 4. One can observe that increasing the scanning speed delay the moment at which the disruption appears.
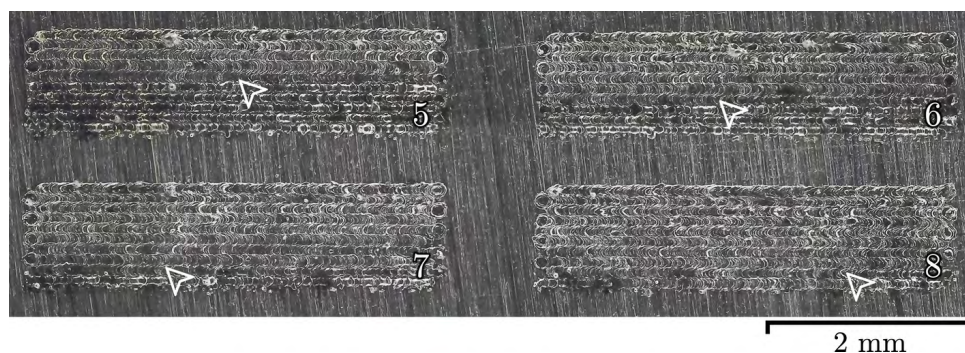
Figure A.21 – Selected layer 5 to 8, with printing parameters indicated in table A.4. The location of the disruption is indicated by the white arrow.

Figure A.21 shows the layers 5 to 8. They were printed at a constant power of 300W and a scanning speed going from 350 mm/s for layer 5 to 500 mm/s for layer 8. By comparing layers 4 and 5, one can see that the manifestation of the disruption is slightly delayed with the increase in power. Similarly as before, by

comparing layers 5 to 8, one can observe that the scanning speed extends again the number of lines of good quality. By looking at layer 8, the printing of this layer is almost completely done without defect, which suggests that the power and scanning speed should be increased again.
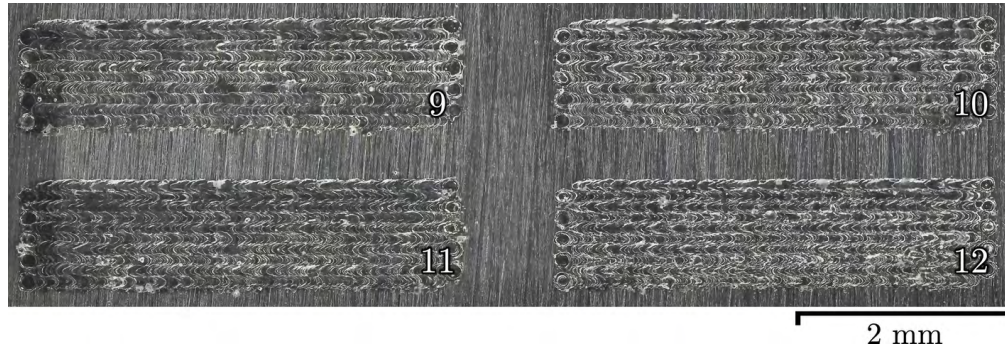
Figure A.22 – Selected layer 9 to 12, with printing parameters indicated in table A.4. The location of the disruption is indicated by the white arrow.

Figure A.22 shows the layers 9 to 12. For this batch of printed layers, the power was increased to 400W and the speed chosen was going from 500 mm/s to 800 mm/s. No disruption was observed in the tracks, which was highly encouraging. However, when trying to print larger areas, e.g. 4x4 mm^2, the instabilities appeared again the in the tracks. Unfortunately, because of time constraints, this study was not pushed further. As result, no processing window has been determined for the CuSn8 allow on the MiniSLM.

A.4   Measurements at the Petra II-P07 beamline

An experiment was performed on the 5N red gold alloy at the Petra III-P07 beamline of the Desy synchrotron in Hamburg. This experiment is introduced in section 6.3 in the discussion chapter. Because of the difficulties to process the CuSn8 properly, a processing window could not be determine for this alloy. Therefore, the parameters used were communicated by the LMTM research group at EPFL, also involved in the CCMX-Challenge AM[3]. These parameters are presented in table A.5, below.

Table A.5 – Sample parameter table

Laser power [W]	Scanning velocity [mm/s]	Hatch distance [µm]	Layer thickness [µm]	Laser spot diameter [µm]
390	200	150	40	80
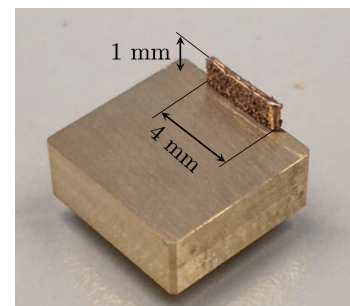
Figure A.23 – Thin wall sample

In this section, additional results obtained during the XRD measurments are presented. A thin vertical wall consisting of the stacking of several single tracks was built. Figure A.23 shows the printed sample. The track length was 4 mm, and the total build height was 1 mm, using parameters in table A.5. The thickness of the wall reached around 170 µm, which made it possible perform XRD in transmission and scanning the sample

with the X-ray beam (similarly as the work presented in [135]).

The X-ray beam energy was set at 79.6 keV and the beam size was 140 x 140 μm^2. The detector used was a Pilatus3 X CdTe 2M. The wall was scanned horizontally and vertically with step sizes of 100 μm, allowing to map the sample. The goal of this experiment is to observe if ordering is happening in the 5N alloy after SLM processing. It is possible to detect the ordering phenomena in the material thanks to the presence of super-lattice reflections [135].

(a) XRD pattern of the 5N alloy   **(b)** Multiple scattering phenomenon
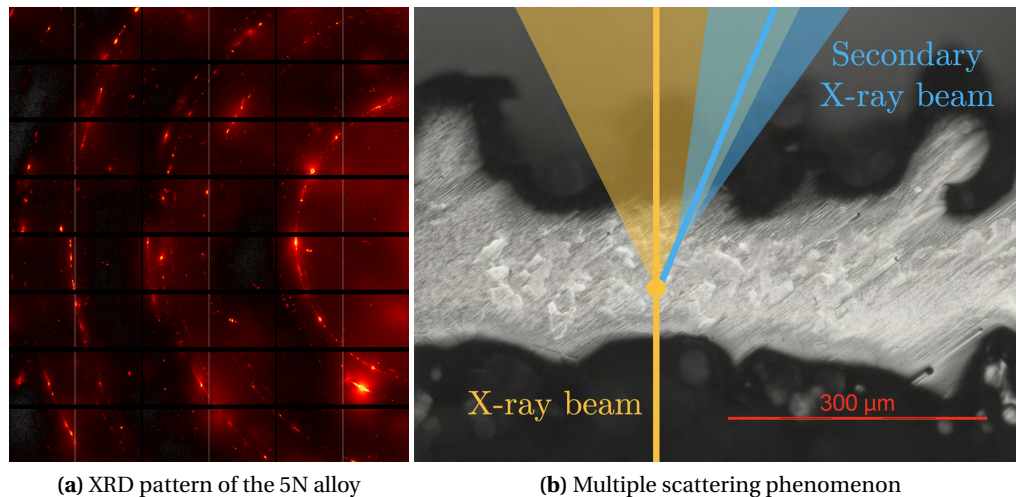
Figure A.24 – Multiple scattering phenomenon happening during the XRD measurement of the thin wall sample

Figure A.24a shows a 2D XRD pattern on the detector during the mapping process. One can observe that the diffraction rings are very spotty. This reveals that the grain size in the sample is quite large compared to the X-ray beam. Additionally, extra spots which do not belong to the diffraction rings are present on this pattern. This phenomena is due to multiple scattering happening within the sample.

Figure A.24b shows a polished cross-section of the wall sample perpendicular to the build direction viewed from the top, revealing the large grain size in the red gold alloy. The incoming X-ray beam is shown in orange and comes from the bottom of the image. Diffraction occurs while it goes through the sample. The diffraction cone is represented in light orange around the X-ray beam. Because the grain size is large, the diffracted signal generates this spotty pattern presented in figure A.24a. Since the wall is thick enough, one of the spots can behave as a secondary X-ray source. Multiple scattering can occur, creating a second diffraction pattern overlapping with the first one. This is shown by the secondary X-ray beam in blue in figure A.24b.

Figure A.25a shows the 1D XRD pattern after integration of figure A.24 in blue. The different lattice reflections have been indexed with the subscript "o" for the ordered phase and "d" for the disordered phase. Figure A.25b presents a zoom in the highlighted region of figure A.25a, revealing the super-lattice reflections of the ordered phase.

All the non indexed peaks in figure A.25 are coming from the multiple scattering effect. These peaks are random and can appear at different angular position depending on the X-ray beam location on the thin

(a) 1D XRD pattern of figure A.24

(b) Zoom on (a)
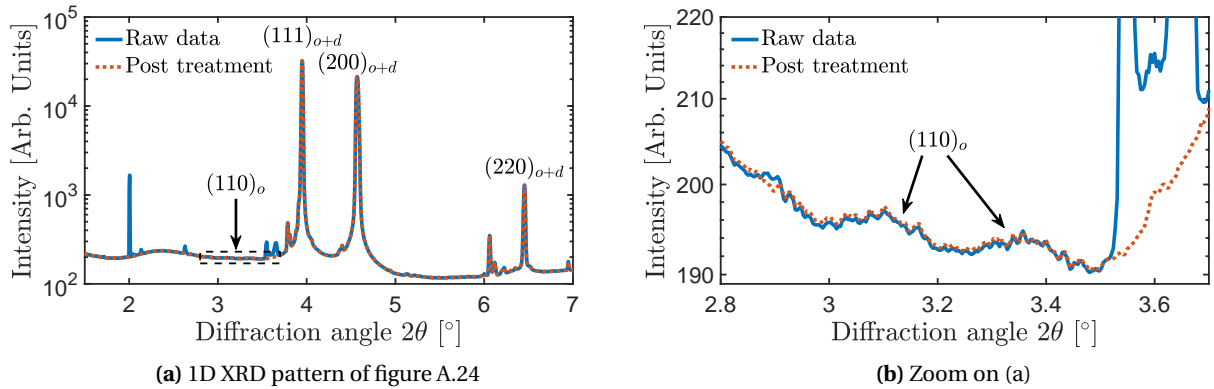
Figure A.25 – Raw XRD pattern from figure A.24. The different peaks have been indexed. All the non-indexed peaks are resulting from the multiple scattering phenomenon.

wall. Since the intensities of the super-lattice reflections are low, this can make the analysis difficult. For that reason, a post-processing of the 2D XRD pattern (like figure A.24) has been done on the software Fiji [100] to remove the outliers in this region. The resulting post-processed pattern is shown in red in figure A.25.

(a) Wall mapping following the $(110)_o$ reflection

(b) Wall mapping following the $(111)_{o+d}$ reflection

(c) Wall mapping following the $(200)_{o+d}$ reflection

(d) Wall mapping following the $(220)_{o+d}$ reflection
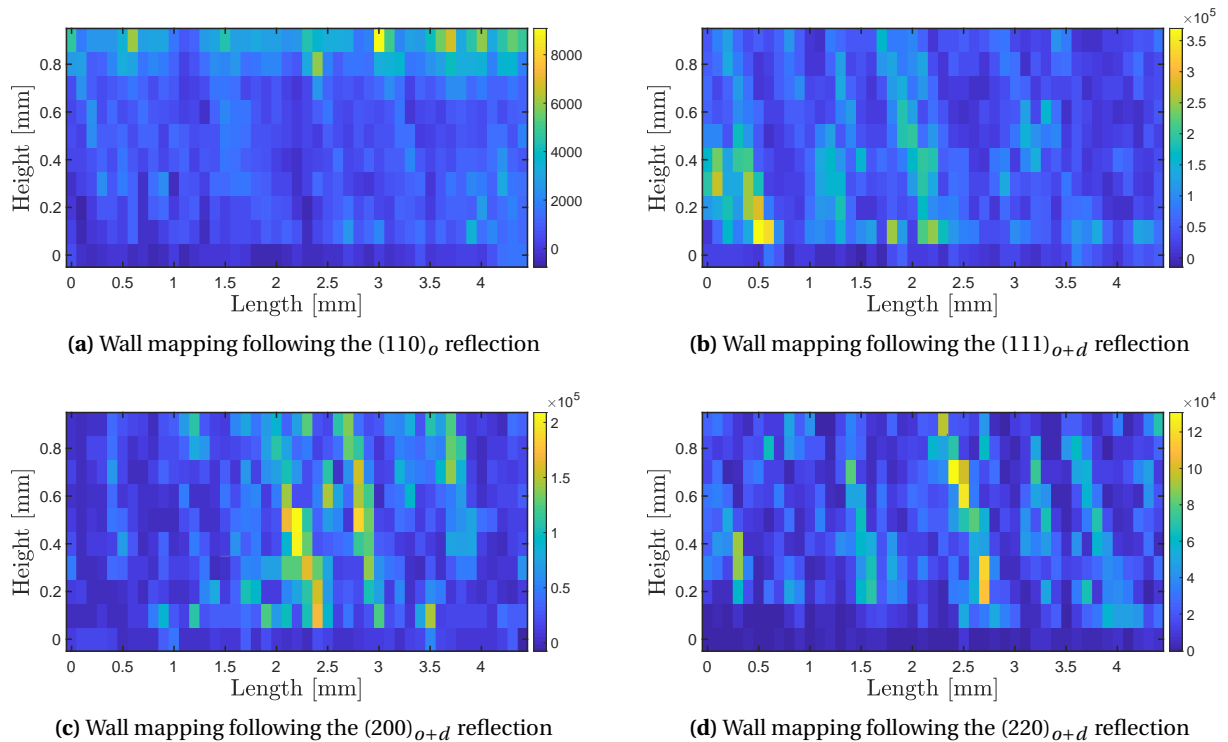
Figure A.26 – Mapping of the wall sample after scanning with the X-ray beam, following the $(110)_o$ (a), $(111)_{o+d}$ (b), $(200)_{o+d}$ (c) and $(220)_{o+d}$ (d) reflections. The intensity is indicated by the colour bars.

The intensities of the $(110)_o$, $(111)_{o+d}$, $(200)_{o+d}$ and $(220)_{o+d}$ reflections have been followed during the scanning of the thin wall sample and are presented in figure A.26. Because of the large grain size of the

(a) $(110)_o$ reflection

(b) $(111)_{o+d}$ reflection

(c) $(200)_{o+d}$ reflection

(d) $(220)_{o+d}$ reflection
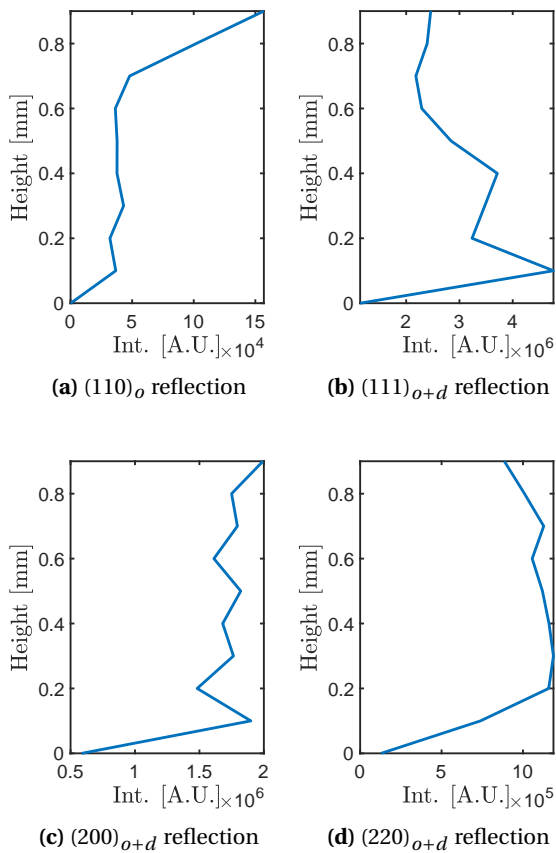
Figure A.27 – Intensity sum over the sample length from figure A.26

sample and the large step size used for scanning, it is difficult to draw a conclusion based on the results presented here. There is a clear grain statistic issue. This can be overcome by summing the intensities over the length of the thin wall.

Figure A.27 presents the intensity evolution of the $(110)_o$, $(111)_{o+d}$, $(200)_{o+d}$ and $(220)_{o+d}$ reflections over the sample height, after summing over the length. The super-lattice reflection intensity from the $(110)_o$ is clearly higher at the top of the sample, showing that the ordering phenomenon occurs for the last printed layers. On the contrary, the intensity of the $(111)_{o+d}$ increases with the sample depth. The intensities of the $(200)_{o+d}$ and $(220)_{o+d}$ reflections are quite flat after doing the summing (figures A.27c and d).

The fact that ordering occurs for the last printed layers might be related to the influence of the quenched-in excess vacancies reported in [135]. Since the ordering phenomenon induces strain in the material as reported in section A.2.1, this may lead to change in the dimension of the printed part by warping.

B Experimental data

B.1 Ti-6Al-4V processing window quality assessment

B.1.1 Single track scanning with 50 μm laser spot diameter

Table B.1 – Parameter selection of the first batch of single tracks printing

Line	Power [W]	Speed [mm/s]	Width [μm]	Continuity	Regularity	Beginning	Width>d$_{las}$	Total
1	50	400	22	0	0	0	0	0
2	50	600	0	0	0	0	0	0
3	50	800	0	0	0	0	0	0
4	50	1200	0	0	0	0	0	0
5	100	400	80	1	0	0	1	2
6	100	600	55	0	0	0	1	1
7	100	800	55	0	0	0	1	1
8	100	1200	43	0	0	0	0	0
9	125	400	83	1	0	1	1	3
10	125	600	67	1	0	1	1	3
11	125	800	60	0	0	0	1	1
12	125	1200	53	0	0	0	1	1
13	150	400	82	1	0	1	1	3
14	150	600	71	1	0	1	1	3
15	150	800	73	1	1	0	1	3
16	150	1200	55	1	0	0	1	2
17	175	400	90	1	0	1	1	3
18	175	600	71	1	0	1	1	3
19	175	800	68	1	1	0	1	3
20	175	1200	59	1	0	0	1	2
21	200	800	75	1	0	1	1	3
22	200	1200	60	1	0	1	1	3

Table B.2 – Parameter selection of the second batch of single tracks printing

Line	Power [W]	Speed [mm/s]	Width [μm]	Continuity	Regularity	Beginning	Width>d$_{las}$	Total
1	50	500	0	0	0	0	0	0
2	50	700	0	0	0	0	0	0
3	50	1000	0	0	0	0	0	0
4	50	1400	0	0	0	0	0	0
5	75	400	0	0	0	0	0	0
6	75	600	0	0	0	0	0	0
7	75	800	0	0	0	0	0	0
8	75	1200	0	0	0	0	0	0
9	100	500	66	0	0	0	1	1
10	100	700	41	0	0	0	0	0
11	100	1000	0	0	0	0	0	0
12	100	1400	0	0	0	0	0	0
13	125	500	66	0	0	1	1	2
14	125	700	39	0	0	0	0	0
15	125	1000	36	0	0	0	0	0
16	125	1400	0	0	0	0	0	0
17	150	500	67	1	0	1	1	3
18	150	700	46	1	0	1	0	2
19	150	1000	51	0	0	0	1	1
20	150	1400	0	0	0	0	0	0
21	175	500	84	1	0	1	1	3
22	175	700	58	1	0	1	1	3
23	175	1000	62	1	0	0	1	2
24	175	1400	51	0	0	0	1	1
25	200	500	76	1	0	1	1	3
26	200	700	70	1	0	1	1	3
27	200	1000	67	1	0	0	1	2
28	200	1400	54	0	0	0	1	1
29	225	600	78	1	0	1	1	3
30	225	800	62	1	0	1	1	3
31	225	1000	63	1	0	0	1	2
32	225	1400	61	1	0	0	1	2
33	250	600	79	1	0	1	1	3
34	250	800	65	1	0	1	1	3
35	250	1000	55	1	1	0	1	3
36	250	1400	51	1	0	0	1	2
37	275	600	74	1	0	1	1	3
38	275	800	66	1	0	1	1	3
39	275	1000	56	1	1	0	1	3
40	275	1400	59	1	0	0	1	2
41	300	1000	58	1	1	0	1	3
42	300	1400	69	1	0	0	1	2

Table B.3 – Parameter selection of the third batch of single tracks printing

Line	Power [W]	Speed [mm/s]	Width [μm]	Continuity	Regularity	Beginning	Width>d$_{las}$	Total
1	50	100	17	0	0	0	0	0
2	50	200	0	0	0	0	0	0
3	50	300	0	0	0	0	0	0
4	50	900	0	0	0	0	0	0
5	75	100	81	1	0	0	1	2
6	75	200	51	0	0	0	1	1
7	75	300	64	0	0	0	1	1
8	75	900	0	0	0	0	0	0
9	100	100	110	1	0	1	1	3
10	100	200	96	1	0	0	1	2
11	100	300	69	1	0	1	1	3
12	100	900	0	0	0	0	0	0
13	125	100	156	1	0	1	1	3
14	125	200	111	1	0	1	1	3
15	125	300	89	1	0	1	1	3
16	125	900	52	0	0	0	1	1
17	150	100	172	1	0	1	1	3
18	150	200	122	1	0	1	1	3
19	150	300	103	1	0	1	1	3
20	150	900	36	0	0	0	0	0
21	175	100	203	1	0	1	1	3
22	175	200	106	1	0	1	1	3
23	175	300	105	1	0	1	1	3
24	175	900	59	1	0	0	1	2
25	200	400	92	1	0	1	1	3
26	200	600	80	1	0	0	1	2
27	200	900	62	1	0	0	1	2
28	200	1100	63	1	0	0	1	2
29	225	500	73	1	0	1	1	3
30	225	700	77	1	0	0	1	2
31	225	900	57	1	0	0	1	2
32	225	1100	52	1	0	0	1	2
33	250	500	113	1	0	1	1	3
34	250	700	82	1	0	1	1	3
35	250	900	71	1	0	1	1	3
36	250	1200	58	1	0	0	1	2
37	275	500	118	1	0	1	1	3
38	275	700	87	0	0	1	1	2
39	275	900	80	0	0	0	1	1
40	275	1200	46	0	0	0	0	0
41	300	800	81	1	0	0	1	2
42	300	1200	51	1	0	0	1	2

B.1.2   Single track scanning with 75 μm laser spot diameter

Table B.4 – Parameter selection of single tracks printing

Line	Power [W]	Speed [mm/s]	Width [μm]	Continuity	Regularity	Beginning	Width>d_{las}	Total
1	125	200	111	1	1	1	1	4
2	125	400	73	1	0	1	0	2
3	125	600	77	1	0	0	1	2
4	125	800	40	1	0	0	0	1
5	150	200	119	1	1	1	1	4
6	150	400	66	1	1	1	0	3
7	150	600	69	1	0	0	0	1
8	150	800	43	1	0	0	0	1
9	175	200	97	1	1	1	1	4
10	175	400	81	1	0	1	1	3
11	175	600	55	1	0	0	0	1
12	175	800	51	1	0	0	0	1
13	200	200	121	1	1	1	1	4
14	200	400	76	1	0	1	1	3
15	200	600	76	1	0	0	1	2
16	200	800	58	1	0	0	0	1
17	225	200	106	1	0	1	1	3
18	225	400	82	1	0	1	1	3
19	225	600	76	1	0	0	1	2
20	225	800	64	1	0	0	0	1
21	250	200	144	1	1	1	1	4
22	250	400	83	1	0	1	1	3
23	250	600	75	1	1	0	0	2
24	250	800	63	1	0	0	0	1
25	275	200	141	1	0	1	1	3
26	275	400	83	1	0	1	1	3
27	275	600	73	1	0	0	0	1
28	275	800	66	1	0	0	0	1
29	300	200	136	1	0	1	1	3
30	300	400	87	1	0	1	1	3
31	300	600	77	1	0	0	1	2
32	300	800	58	1	0	0	0	1

B.1.3 Single track scanning with 100 μm laser spot diameter

Table B.5 – Parameter selection of single tracks printing

Line	Power [W]	Speed [mm/s]	Width [μm]	Continuity	Regularity	Beginning	Width>d_{las}	Total
1	125	200	96	1	0	1	0	2
2	125	400	73	0	0	1	0	1
3	125	600	57	0	0	0	0	0
4	125	800	0	0	0	0	0	0
5	150	200	107	1	0	1	1	3
6	150	400	59	0	0	1	0	1
7	150	600	73	0	0	0	0	0
8	150	800	0	0	0	0	0	0
9	175	200	151	1	0	1	1	3
10	175	400	92	1	1	1	0	3
11	175	600	77	1	0	0	0	1
12	175	800	54	1	0	0	0	1
13	200	200	148	1	0	1	1	3
14	200	400	118	1	1	1	1	4
15	200	600	68	1	1	0	0	2
16	200	800	72	0	0	0	0	0
17	225	200	180	1	0	1	1	3
18	225	400	106	1	1	1	1	4
19	225	600	90	0	0	0	0	0
20	225	800	72	1	0	0	0	1
21	250	200	216	1	0	1	1	3
22	250	400	121	1	1	1	1	4
23	250	600	114	1	1	1	1	4
24	250	800	68	1	1	1	0	3
25	275	200	211	1	0	1	1	3
26	275	400	123	1	1	1	1	4
27	275	600	140	1	1	1	1	4
28	275	800	105	1	1	1	1	4
29	300	200	234	1	1	1	1	4
30	300	400	153	1	1	1	1	4
31	300	600	105	1	1	1	1	4
32	300	800	96	1	1	1	0	3

B.2   Ti-6Al-4V porosity measurements

B.2.1   Sample parameters and measured densities

Table B.6 – Parameter selection and density measurements

Sample	Scanning strategy	Laser power [W]	Scanning velocity [mm/s]	Hatch distance [μm]	Layer thickness [μm]	Energy density [J/mm^3]	Density Optical ImageJ
1	B	150	400	60	30	208	98.57%
2	B	150	400	40	30	313	95.37%
3	B	200	700	60	30	159	97.49%
4	B	175	200	40	30	729	99.68%
5	B	175	400	50	30	292	98.82%
6	B	175	400	40	30	365	98.13%
7	B	175	400	60	30	243	99.48%
8	B	200	400	60	30	278	98.17%
9	B	200	400	40	30	417	99.28%
10	B	150	310	40	30	403	94.12%
11	B	100	200	40	30	417	97.66%
12	B	250	400	60	30	347	99.38%
13	B	200	550	60	30	202	99.54%
14	B	150	400	60	30	208	96.98%
15	B	150	550	60	30	152	99.84%
16	B	200	400	25	50	400	98.40%
17	B	250	400	60	50	208	98.39%
18	B	250	400	40	50	313	99.11%
19	B	175	200	40	30	729	99.99%
20	C+B	175	200	40	30	729	99.47%
21	B	175	400	60	30	243	98.14%
22	C+B	175	400	60	30	243	98.93%
23	B	175	200	40	30	729	99.57%
24	C+B	175	200	40	30	729	99.64%
25	B	175	400	60	30	243	98.53%
26	C+B	175	400	60	30	243	99.27%
27	B+R90	150	550	60	30	152	99.50%
28	B+R90	150	600	60	30	139	94.27%
29	B+R90	125	550	60	30	126	86.76%
30	B+R90	125	600	60	30	116	85.52%
31	B	175	200	40	30	729	97.76%
32	B+R90	175	200	40	30	729	99.72%
33	B	175	200	40	30	729	99.66%
34	B+R90	175	200	40	30	729	99.56%
35	B+R90	175	220	40	30	663	99.71%
36	B+R90	175	245	40	30	595	99.99%
37	B+R90	175	275	40	30	530	99.92%
38	B+R90	175	315	40	30	463	99.96%

Note: B-Bidirectional; C-Crosshatch; R90-Rotation 90°

Table B.7 – Parameter selection and density measurements for the second batch

Sample	Scanning strategy	Laser power [W]	Scanning velocity [mm/s]	Hatch distance [μm]	Layer thickness [μm]	Energy density [J/mm^3]	Density Optical ImageJ
1	B + R90	150	400	60	30	208	97.09%
2	B + R90	175	400	60	30	243	98.58%
3	B + R90	200	400	60	30	278	100.00%
4	B + R90	250	400	60	30	347	99.87%
5	B + R90	150	600	60	30	139	99.54%
6	B + R90	175	600	60	30	162	99.72%
7	B + R90	200	600	60	30	185	99.86%
8	B + R90	250	600	60	30	231	100.00%
9	B + R90	150	800	60	30	104	99.25%
10	B + R90	175	800	60	30	122	99.77%
11	B + R90	200	800	60	30	139	99.78%
12	B + R90	250	800	60	30	174	99.95%
13	B + R90	150	400	80	30	156	98.89%
14	B + R90	175	400	80	30	182	99.53%
15	B + R90	200	400	80	30	208	99.81%
16	B + R90	250	400	80	30	260	100.00%
17	B + R90	150	600	80	30	104	98.23%
18	B + R90	175	600	80	30	122	97.87%
19	B + R90	200	600	80	30	139	95.15%
20	B + R90	250	600	80	30	174	99.86%
21	B + R90	150	800	80	30	78	91.76%
22	B + R90	175	800	80	30	91	95.20%
23	B + R90	200	800	80	30	104	99.03%
24	B + R90	250	800	80	30	130	98.60%

C Coding

C.1 Porosity measurement in Fiji

C.1.1 List of commands

- Convert the cropped section into a grey scale image: this can be achieved in Fiji by selecting *Image>Type>8-bit* in the menu bar.
- Apply a threshold to separate the image into black and white pixels: the command in Fiji is *Image>Adjust>Threshold*. The method with the optimum result to isolate the pores is the "Minimum" method. However, some samples need manual adjustment to have an accurate estimation of the density.
- Determine the porosity of the sample with the black and white pixel ratio: first, the area fraction option must be activated under *Analyze>Set Measurements* in the menu bar. Once activated, the ratio can be made by selecting *Analyze>Measure*.

C.1.2 Macro for batch processing

To process multiple sample, a macro was written in Java script and is presented below.

```
//Porosity measurement script by Samy Hocine
//V1.0

//Select input and output folder
input_folder=getDirectory("Select the input directory");
output_folder=getDirectory("Select the output directory");

//Get the file list inside the input folder
file_list=getFileList(input_folder);
n=lengthOf(file_list);

//Measuring porosity and save results
```

```
setBatchMode(true);
for (i=0; i<n; i++) {
open(input_folder+file_list[i]);
run("8-bit");
setAutoThreshold("Minimum dark");
run("Convert to Mask");
run("Set Measurements...", "area area_fraction redirect=None decimal=3");
run("Measure");
file_name=substring(file_list[i], 0, lastIndexOf(file_list[i], "."));
saveAs("Results", output_folder+i+"_"+file_name+".csv");
close();
}
setBatchMode(false);
```

C.2 Subroutines used for Abaqus simulation

C.2.1 USDFLD subroutine to model the material state change

```
      SUBROUTINE USDFLD(FIELD,STATEV,PNEWDT,DIRECT,T,CELENT,
     1 TIME,DTIME,CMNAME,ORNAME,NFIELD,NSTATV,NOEL,NPT,LAYER,
     2 KSPT,KSTEP,KINC,NDI,NSHR,COORD,JMAC,JMATYP,MATLAYO,LACCFLA)
C
      INCLUDE 'ABA_PARAM.INC'
C
      CHARACTER*80 CMNAME,ORNAME
      CHARACTER*3 FLGRAY(15)
      DIMENSION FIELD(NFIELD),STATEV(NSTATV),DIRECT(3,3),
     1 T(3,3),TIME(2)
      DIMENSION ARRAY(15),JARRAY(15),JMAC(*),JMATYP(*),COORD(*)
C
C     Subroutine to change material properties
C
      DOUBLE PRECISION T_NODE,T_MAX,T_MAX_OLD
C
      PARAMETER (T_MELT=1923.15D0) !Melting point of Ti64 [K]
C
      T_MAX_OLD=STATEV(1)
C
      CALL GETVRM('TEMP',ARRAY,JARRAY,FLGRAY,JRCD,JMAC,JMATYP,
     1 MATLAYO,LACCFLA)
      T_NODE=ARRAY(1)
C
C     Update field variable
C
      T_MAX=MAX(T_NODE,T_MAX_OLD)
      STATEV(1)=T_MAX
C
      IF (T_MAX .GE. T_MELT) THEN
      FIELD(1)=1.D0
      ELSE
      FIELD(1)=0.D0
      ENDIF
C
      RETURN
      END
```

C.2.2 FILM subroutine to model the convection and radiation losses

```fortran
      SUBROUTINE FILM(H,SINK,TEMP,KSTEP,KINC,TIME,NOEL,NPT,
     1 COORDS,JLTYP,FIELD,NFIELD,SNAME,NODE,AREA)
C
      INCLUDE 'ABA_PARAM.INC'
C
      DIMENSION H(2),TIME(2),COORDS(3),FIELD(NFIELD)
      CHARACTER*80 SNAME
      DOUBLE PRECISION e0,hR,dhR
C
C     Stefan Boltzmann constant, heat transfer coeffecient
      PARAMETER (sigma=5.67D-8,hC=20.D-3)
C
C     Sink temperature [K]
      SINK=298.15D0
C
C     Emissivity [K]
      e0=0.2316D0+0.3066D-3*EXP(-7.552D-3*(4.196D0-(TEMP-273.15D0)))
C
C     Radiatiation losses coefficient [mW/mm^2.K]
      hR=sigma*e0*(TEMP**2+SINK**2)*(TEMP+SINK)*1.D-3
C
C     Rate of change of the film coefficient (dhR/dT)
      dhR=sigma*e0*((TEMP+SINK)**2+2*TEMP**2)*1.D-3
C
      H(1)=hC+hR       !Film coefficient [mW/mm^2.K]
      H(2)=dhR         !Rate of change of the film coefficient
C
      RETURN
      END
```

C.2.3 DFLUX subroutine to model the laser scanning heat flux

Model 1: Simple ellipsoid model (M1)

```fortran
      SUBROUTINE DFLUX(FLUX,SOL,KSTEP,KINC,TIME,NOEL,NPT,COORDS,
     1 JLTYP,TEMP,PRESS,SNAME)
C
      INCLUDE 'ABA_PARAM.INC'
C
      DIMENSION FLUX(2),TIME(2),COORDS(3)
      CHARACTER*80 SNAME
```

```
      DOUBLE PRECISION X0,Y0,Z0,X,Y,Z,OLD_TIME
      INTEGER n
C
C     Laser power [mW], Laser absorption 0<A<1, Laser beam radius [mm],
C     Penetration depth [mm]
      PARAMETER (P=2.5D5,A=0.55D0,R0=50.D-3,D0=30.D-3)
C     Laser beam velocity [mm/s],  Hatching distance [mm], Settling time [s], Pi value
      PARAMETER (V=600.D0,H0=60.D-3,ST=0.63D-3,PI=3.1415926D0)
C     Ellipsoid parameters
      PARAMETER (A0=R0,B0=R0,C0=D0)
C     Length of the scanning vector [mm], Scanning time length for one vector [s],
C     Volume heat flux of the laser beam [mW/mm^3]
      PARAMETER (XL=2.D0,TL=XL/V,Q=2.D0*A*P/(A0*B0*C0*(PI**1.5)))
C
      SAVE n, OLD_TIME
C
C     Laser scanning code
C
      X0=0.D0    !Starting coordinates of the laser beam
      Y0=0.D0
      Z0=0.D0
C
      X=COORDS(1)
      Y=COORDS(2)
      Z=COORDS(3)
C
C     Update of the laser path
C
      IF (TIME(1) .LE. TL+(ST/2)) THEN
      n=0
      ELSE IF (TIME(1) .GT. (n+1)*(TL+ST)-(ST/2)) THEN
      n=n+1
      ENDIF
C
      IF (MOD(n,2) .EQ. 0) THEN
C
      IF ((TIME(1) .LE. n*(TL+ST)) .OR.
     1(TIME(1) .GT. n*(TL+ST)+TL)) THEN
C
      FLUX(1)=0.D0
C
      ELSE
C
```

```
      X0=X0+V*(TIME(1)-n*(TL+ST))
      Y0=Y0-n*H0
C
      FLUX(1)=Q*EXP(-((X-X0)**2/A0**2+(Y-Y0)**2/B0**2+(Z-Z0)**2/C0**2))
C
      ENDIF
C
      ELSE
C
      IF ((TIME(1) .LE. n*(TL+ST)) .OR.
     1(TIME(1) .GT. n*(TL+ST)+TL)) THEN
C
      FLUX(1)=0.D0
C
      ELSE
C
      X0=XL-V*(TIME(1)-n*(TL+ST))
      Y0=Y0-n*H0
C
      FLUX(1)=Q*EXP(-((X-X0)**2/A0**2+(Y-Y0)**2/B0**2+(Z-Z0)**2/C0**2))
C
      ENDIF
C
      ENDIF
C
      OLD_TIME=TIME(1)
C
      RETURN
      END
```

Model 2: Double ellipsoid model (M2)

```
      SUBROUTINE DFLUX(FLUX,SOL,KSTEP,KINC,TIME,NOEL,NPT,COORDS,
     1 JLTYP,TEMP,PRESS,SNAME)
C
      INCLUDE 'ABA_PARAM.INC'
C
      DIMENSION FLUX(2),TIME(2),COORDS(3)
      CHARACTER*80 SNAME
      DOUBLE PRECISION X0,Y0,Z0,X,Y,Z,OLD_TIME
      INTEGER n
C
C     Laser power [mW], Laser absorption 0<A<1, Laser beam radius [mm],
```

```
C       Penetration depth [mm]
        PARAMETER (P=2.5D5,A=0.55D0,R0=50.D-3,D0=30.D-3)
C       Laser beam velocity [mm/s],  Hatching distance [mm], Settling time [s], Pi value
        PARAMETER (V=600.D0,H0=60.D-3,ST=0.63D-3,PI=3.1415926D0)
C       Ellipsoid parameters, Ff/Af=Fr/Ar for continuity at X=X0
        PARAMETER (Ff=0.6D0,Fr=2.D0-Ff,Af=R0,Ar=Fr*Af/Ff,B0=R0,C0=D0)
C       Length of the scanning vector [mm], Scanning time length for one vector [s]
        PARAMETER (XL=2.D0,TL=XL/V)
C       Volume heat flux in front of the laser beam [mW/mm^3]
        PARAMETER (Qf=6.D0*(3.D0**0.5)*Ff*A*P/(Af*B0*C0*PI**1.5))
C       Volume heat flux in rear of the laser beam [mW/mm^3]
        PARAMETER (Qr=6.D0*(3.D0**0.5)*Fr*A*P/(Ar*B0*C0*PI**1.5))
C
        SAVE n, OLD_TIME
C
C       Laser scanning code
C
        X0=0.D0     !Starting coordinates of the laser beam
        Y0=0.D0
        Z0=0.D0
C
        X=COORDS(1)
        Y=COORDS(2)
        Z=COORDS(3)
C
C       Update of the laser path
C
        IF (TIME(1) .LE. TL+(ST/2)) THEN
        n=0
        ELSE IF (TIME(1) .GT. (n+1)*(TL+ST)-(ST/2)) THEN
        n=n+1
        ENDIF
C
        IF (MOD(n,2) .EQ. 0) THEN
C
        IF ((TIME(1) .LE. n*(TL+ST)) .OR.
       1(TIME(1) .GT. n*(TL+ST)+TL)) THEN
C
        FLUX(1)=0.D0
C
        ELSE
C
        X0=X0+V*(TIME(1)-n*(TL+ST))
```

```
      Y0=Y0-n*H0
C
      IF(X .GE. X0) THEN
      FLUX(1)=Qf*EXP(-3.0D0*((X-X0)**2/Af**2+(Y-Y0)**2/B0**2
     1+(Z-Z0)**2/C0**2))
      ELSE
      FLUX(1)=Qr*EXP(-3.0D0*((X-X0)**2/Ar**2+(Y-Y0)**2/B0**2
     1+(Z-Z0)**2/C0**2))
      ENDIF
C
      ENDIF
C
      ELSE
C
      IF ((TIME(1) .LE. n*(TL+ST)) .OR.
     1(TIME(1) .GT. n*(TL+ST)+TL)) THEN
C
      FLUX(1)=0.D0
C
      ELSE
C
      X0=XL-V*(TIME(1)-n*(TL+ST))
      Y0=Y0-n*H0
C
      IF(X .LE. X0) THEN
      FLUX(1)=Qf*EXP(-3.0D0*((X-X0)**2/Af**2+(Y-Y0)**2/B0**2
     1+(Z-Z0)**2/C0**2))
      ELSE
      FLUX(1)=Qr*EXP(-3.0D0*((X-X0)**2/Ar**2+(Y-Y0)**2/B0**2
     1+(Z-Z0)**2/C0**2))
      ENDIF
C
      ENDIF
C
      ENDIF
C
      OLD_TIME=TIME(1)
C
      RETURN
      END
```

Models 3 and 4: Cylindrical heat source with parabolic penetration depth (M3, M4)

```fortran
      SUBROUTINE DFLUX(FLUX,SOL,KSTEP,KINC,TIME,NOEL,NPT,COORDS,
     1 JLTYP,TEMP,PRESS,SNAME)
C
      INCLUDE 'ABA_PARAM.INC'
C
      DIMENSION FLUX(2),TIME(2),COORDS(3)
      CHARACTER*80 SNAME
      DOUBLE PRECISION X0,Y0,Z0,X,Y,Z,R,OLD_TIME
      INTEGER n
C
C     Laser power [mW], Laser absorption 0<A<1, Laser beam radius [mm],
C     Penetration depth [mm]
      PARAMETER (P=2.5D5,A=0.6D0,R0=50.D-3,D0=30.D-3)
C     Laser beam velocity [mm/s],  Hatching distance [mm], Settling time [s], Pi value
      PARAMETER (V=600.D0,H0=60.D-3,ST=0.63D-3,PI=3.1415926D0)
C     Length of the scanning vector [mm], Scanning time length for one vector [s],
C     Volume heat flux of the laser beam [mW/mm^3]
      PARAMETER (XL=2.D0,TL=XL/V,Q=2.55D0*0.864D0*A*P/(PI*(R0**2)))
C
      SAVE n, OLD_TIME
C
C     Laser scanning code
C
      X0=0.D0     !Starting coordinates of the laser beam
      Y0=0.D0
      Z0=0.D0
C
      X=COORDS(1)
      Y=COORDS(2)
      Z=COORDS(3)
C
C     Update of the laser path
C
      IF (TIME(1) .LE. TL+(ST/2)) THEN
      n=0
      ELSE IF (TIME(1) .GT. (n+1)*(TL+ST)-(ST/2)) THEN
      n=n+1
      ENDIF
C
      IF (MOD(n,2) .EQ. 0) THEN
C
```

```
       IF ((TIME(1) .LE. n*(TL+ST)) .OR.
      1(TIME(1) .GT. n*(TL+ST)+TL)) THEN
C
       FLUX(1)=0.D0
C
       ELSE
C
       X0=X0+V*(TIME(1)-n*(TL+ST))
       Y0=Y0-n*H0
       R=SQRT((X-X0)**2+(Y-Y0)**2)
C
       IF (R .LE. R0) THEN
       FLUX(1)=Q*(-15*(Z)**2+4.D0*(Z)+2.D0)
       ELSE
       FLUX(1)=0.D0
       ENDIF
C
       ENDIF
C
       ELSE
C
       IF ((TIME(1) .LE. n*(TL+ST)) .OR.
      1(TIME(1) .GT. n*(TL+ST)+TL)) THEN
C
       FLUX(1)=0.D0
C
       ELSE
C
       X0=XL-V*(TIME(1)-n*(TL+ST))
       Y0=Y0-n*H0
       R=SQRT((X-X0)**2+(Y-Y0)**2)
C
       IF (R .LE. R0) THEN
       FLUX(1)=Q*(-15*(Z)**2+4.D0*(Z)+2.D0)
       ELSE
       FLUX(1)=0.D0
       ENDIF
C
C      IF (TIME(1) .NE. OLD_TIME) THEN
C      WRITE(7,*) 'LINE',n+1,'X:',X0,'Y:',Y0,'TIME:',TIME(1)
C      ENDIF
C
       ENDIF
```

```
C
      ENDIF
C
      OLD_TIME=TIME(1)
C
      RETURN
      END
```

Bibliography

[1] Additive manufacturing 2013. URL https://www.rolandberger.com/en/Publications/pub_additive_manufacturing_2013.html.

[2] Ian Gibson, David Rosen, and Brent Stucker. *Additive Manufacturing Technologies.* Springer New York, New York, NY, 2015. ISBN 978-1-4939-2112-6 978-1-4939-2113-3. doi: 10.1007/978-1-4939-2113-3.

[3] GE launch $1.4 billion takeover bid for SLM Solutions and Arcam AB - 3D Printing Industry, August 2017. URL https://3dprintingindustry.com/news/ge-launch-1-4-billion-takeover-bid-slm-solutions-arcam-ab-95311/.

[4] David Appleyard. Powering up on powder technology. *Metal Powder Report*, 70(6):285–289, November 2015. ISSN 00260657. doi: 10.1016/j.mprp.2015.08.075.

[5] M Simonelli, Y Y Tse, and C Tuck. Microstructure of Ti-6Al-4V produced by selective laser melting. *Journal of Physics: Conference Series*, 371:012084, July 2012. ISSN 1742-6596. doi: 10.1088/1742-6596/371/1/012084.

[6] Lore Thijs, Frederik Verhaeghe, Tom Craeghs, Jan Van Humbeeck, and Jean-Pierre Kruth. A study of the microstructural evolution during selective laser melting of Ti–6Al–4V. *Acta Materialia*, 58(9):3303–3312, May 2010. ISSN 1359-6454. doi: 10.1016/j.actamat.2010.02.004.

[7] Haijun Gong, Khalid Rafi, Hengfeng Gu, Thomas Starr, and Brent Stucker. Analysis of defect generation in Ti–6Al–4V parts made using powder bed fusion additive manufacturing processes. *Additive Manufacturing*, 1-4:87–98, October 2014. ISSN 2214-8604. doi: 10.1016/j.addma.2014.08.002.

[8] John J. Lewandowski and Mohsen Seifi. Metal Additive Manufacturing: A Review of Mechanical Properties. *Annual Review of Materials Research*, 46(1):151–186, July 2016. ISSN 1531-7331. doi: 10.1146/annurev-matsci-070115-032024.

[9] Jingjing Yang, Hanchen Yu, Jie Yin, Ming Gao, Zemin Wang, and Xiaoyan Zeng. Formation and control of martensite in Ti-6Al-4V alloy produced by selective laser melting. *Materials & Design*, 108:308–318, October 2016. ISSN 02641275. doi: 10.1016/j.matdes.2016.06.117.

[10] C. Kenel, D. Grolimund, X. Li, E. Panepucci, V. A. Samson, D. Ferreira Sanchez, F. Marone, and C. Leinenbach. In situ investigation of phase transformations in Ti-6Al-4V under additive manufacturing conditions combining laser melting and high-speed micro-X-ray diffraction. *Scientific Reports*, 7(1), December 2017. ISSN 2045-2322. doi: 10.1038/s41598-017-16760-0.

Bibliography

[11] J. W. Elmer, T. A. Palmer, S. S. Babu, and E. D. Specht. In situ observations of lattice expansion and transformation rates of α and β phases in Ti–6Al–4V. *Materials Science and Engineering: A*, 391(1): 104–113, January 2005. ISSN 0921-5093. doi: 10.1016/j.msea.2004.08.084.

[12] Gerald F Marshall. *Handbook of Optical and Laser Scanning*. 2004.

[13] Dirk Herzog, Vanessa Seyda, Eric Wycisk, and Claus Emmelmann. Additive manufacturing of metals. *Acta Materialia*, 117:371–392, September 2016. ISSN 13596454. doi: 10.1016/j.actamat.2016.07.019.

[14] Mushtaq Khan and Phill Dickens. Selective Laser Melting (SLM) of pure gold. *Gold Bulletin*, 43(2): 114–121, 2010. URL http://www.springerlink.com/index/U227737759273R53.pdf.

[15] B. Ferrar, L. Mullen, E. Jones, R. Stamp, and C. J. Sutcliffe. Gas flow effects on selective laser melting (SLM) manufacturing performance. *Journal of Materials Processing Technology*, 212(2):355–364, February 2012. ISSN 0924-0136. doi: 10.1016/j.jmatprotec.2011.09.020.

[16] Holly D. Carlton, Abdel Haboub, Gilbert F. Gallegos, Dilworth Y. Parkinson, and Alastair A. MacDowell. Damage evolution and failure mechanisms in additively manufactured stainless steel. *Materials Science and Engineering: A*, 651:406–414, January 2016. ISSN 09215093. doi: 10.1016/j.msea.2015.10.073.

[17] Alexander Ladewig, Georg Schlick, Maximilian Fisser, Volker Schulze, and Uwe Glatzel. Influence of the shielding gas flow on the removal of process by-products in the selective laser melting process. *Additive Manufacturing*, 10:1–9, April 2016. ISSN 2214-8604. doi: 10.1016/j.addma.2016.01.004.

[18] W. J. Sames, F. A. List, S. Pannala, R. R. Dehoff, and S. S. Babu. The metallurgy and processing science of metal additive manufacturing. *International Materials Reviews*, 61(5):315–360, July 2016. ISSN 0950-6608, 1743-2804. doi: 10.1080/09506608.2015.1116649.

[19] Shichun Li, Genyu Chen, Seiji Katayama, and Yi Zhang. Relationship between spatter formation and dynamic molten pool during high-power deep-penetration laser welding. *Applied Surface Science*, 303: 481–488, June 2014. ISSN 0169-4332. doi: 10.1016/j.apsusc.2014.03.030.

[20] K. A. Mumtaz and N. Hopkinson. Selective Laser Melting of thin wall parts using pulse shaping. *Journal of Materials Processing Technology*, 210(2):279–287, January 2010. ISSN 0924-0136. doi: 10.1016/j.jmatprotec.2009.09.011.

[21] I. Yadroitsev, L. Thivillon, Ph. Bertrand, and I. Smurov. Strategy of manufacturing components with designed internal structure by selective laser melting of metallic powder. *Applied Surface Science*, 254 (4):980–983, December 2007. ISSN 0169-4332. doi: 10.1016/j.apsusc.2007.08.046.

[22] Jamasp Jhabvala, Eric Boillat, Thibaud Antignac, and Rémy Glardon. On the effect of scanning strategies in the selective laser melting process. *Virtual and Physical Prototyping*, 5(2):99–109, June 2010. ISSN 1745-2759. doi: 10.1080/17452751003688368.

[23] Amanda S. Wu, Donald W. Brown, Mukul Kumar, Gilbert F. Gallegos, and Wayne E. King. An Experimental Investigation into Additive Manufacturing-Induced Residual Stresses in 316L Stainless Steel. *Metallurgical and Materials Transactions A*, 45(13):6260–6270, December 2014. ISSN 1073-5623, 1543-1940. doi: 10.1007/s11661-014-2549-x.

[24] Bey Vrancken, Lore Thijs, Jean-Pierre Kruth, and Jan Van Humbeeck. Heat treatment of Ti6Al4V produced by Selective Laser Melting: Microstructure and mechanical properties. *Journal of Alloys and Compounds*, 541:177–185, November 2012. ISSN 09258388. doi: 10.1016/j.jallcom.2012.07.022.

[25] Luke N. Carter, Moataz M. Attallah, and Roger C. Reed. Laser Powder Bed Fabrication of Nickel-Base Superalloys: Influence of Parameters; Characterisation, Quantification and Mitigation of Cracking. In *Superalloys 2012*, pages 577–586. John Wiley & Sons, Ltd, 2012. ISBN 978-1-118-51643-0. doi: 10.1002/9781118516430.ch64. _eprint: https://onlinelibrary.wiley.com/doi/pdf/10.1002/9781118516430.ch64.

[26] Loong-Ee Loh, Chee-Kai Chua, Wai-Yee Yeong, Jie Song, Mahta Mapar, Swee-Leong Sing, Zhong-Hong Liu, and Dan-Qing Zhang. Numerical investigation and an effective modelling on the Selective Laser Melting (SLM) process with aluminium alloy 6061. *International Journal of Heat and Mass Transfer*, 80: 288–300, January 2015. ISSN 00179310. doi: 10.1016/j.ijheatmasstransfer.2014.09.014.

[27] Bo Song, Shujuan Dong, Qi Liu, Hanlin Liao, and Christian Coddet. Vacuum heat treatment of iron parts produced by selective laser melting: Microstructure, residual stress and tensile behavior. *Materials & Design (1980-2015)*, 54:727–733, February 2014. ISSN 0261-3069. doi: 10.1016/j.matdes.2013.08.085.

[28] Lore Thijs, Maria Luz Montero Sistiaga, Ruben Wauthle, Qingge Xie, Jean-Pierre Kruth, and Jan Van Humbeeck. Strong morphological and crystallographic texture and resulting yield strength anisotropy in selective laser melted tantalum. *Acta Materialia*, 61(12):4657–4668, July 2013. ISSN 1359-6454. doi: 10.1016/j.actamat.2013.04.036.

[29] J-P. Kruth, P. Mercelis, J. Van Vaerenbergh, L. Froyen, and M. Rombouts. Binding mechanisms in selective laser sintering and selective laser melting. *Rapid Prototyping Journal*, 11(1):26–36, February 2005. ISSN 1355-2546. doi: 10.1108/13552540510573365.

[30] L. M. Sochalski-Kolbus, E. A. Payzant, P. A. Cornwell, T. R. Watkins, S. S. Babu, R. R. Dehoff, M. Lorenz, O. Ovchinnikova, and C. Duty. Comparison of Residual Stresses in Inconel 718 Simple Parts Made by Electron Beam Melting and Direct Laser Metal Sintering. *Metallurgical and Materials Transactions A*, 46(3):1419–1432, March 2015. ISSN 1073-5623, 1543-1940. doi: 10.1007/s11661-014-2722-2.

[31] Galina Kasperovich, Jan Haubrich, Joachim Gussone, and Guillermo Requena. Correlation between porosity and processing parameters in TiAl6V4 produced by selective laser melting. *Materials & Design*, 105:160–170, September 2016. ISSN 0264-1275. doi: 10.1016/j.matdes.2016.05.070.

[32] R. P. Turner, C. Panwisawas, Y. Lu, I. Dhiman, H. C. Basoalto, and J. W. Brooks. Neutron tomography methods applied to a nickel-based superalloy additive manufacture build. *Materials Letters*, 230: 109–112, November 2018. ISSN 0167-577X. doi: 10.1016/j.matlet.2018.07.112.

[33] M. Strantza, R. K. Ganeriwala, B. Clausen, T. Q. Phan, L. E. Levine, D. Pagan, W. E. King, N. E. Hodge, and D. W. Brown. Coupled experimental and computational study of residual stresses in additively manufactured Ti-6Al-4V components. *Materials Letters*, 231:221–224, November 2018. ISSN 0167-577X. doi: 10.1016/j.matlet.2018.07.141.

[34] R. Laquai, B. R. Müller, G. Kasperovich, J. Haubrich, G. Requena, and G. Bruno. X-ray refraction distinguishes unprocessed powder from empty pores in selective laser melting Ti-6Al-4V. *Materials*

Research Letters, 6(2):130–135, February 2018. ISSN null. doi: 10.1080/21663831.2017.1409288. _eprint: https://doi.org/10.1080/21663831.2017.1409288.

[35] M. Morgano, N. Kalentics, C. Carminati, J. Capek, M. Makowska, R. Woracek, T. Maimaitiyili, T. Shinohara, R. Loge, and M. Strobl. Investigation of the effect of Laser Shock Peening in Additively Manufactured samples through Bragg Edge Neutron Imaging. *Additive Manufacturing*, 34:101201, August 2020. ISSN 2214-8604. doi: 10.1016/j.addma.2020.101201.

[36] Qi Zhang, Jiawen Xie, Zhenyuan Gao, Tyler London, David Griffiths, and Victor Oancea. A metallurgical phase transformation framework applied to SLM additive manufacturing processes. *Materials & Design*, 166:107618, March 2019. ISSN 02641275. doi: 10.1016/j.matdes.2019.107618.

[37] H. S. Tran, J. T. Tchuindjang, H. Paydas, A. Mertens, R. T. Jardin, L. Duchêne, R. Carrus, J. Lecomte-Beckers, and A. M. Habraken. 3D thermal finite element analysis of laser cladding processed Ti-6Al-4V part with microstructural correlations. *Materials & Design*, 128:130–142, August 2017. ISSN 0264-1275. doi: 10.1016/j.matdes.2017.04.092.

[38] Michele Chiumenti, Eric Neiva, Emilio Salsi, Miguel Cervera, Santiago Badia, Joan Moya, Zhuoer Chen, Caroline Lee, and Christopher Davies. Numerical modelling and experimental validation in Selective Laser Melting. *Additive Manufacturing*, 18:171–185, December 2017. ISSN 2214-8604. doi: 10.1016/j.addma.2017.09.002.

[39] Umberto Scipioni Bertoli, Gabe Guss, Sheldon Wu, Manyalibo J. Matthews, and Julie M. Schoenung. In-situ characterization of laser-powder interaction and cooling rates through high-speed imaging of powder bed fusion additive manufacturing. *Materials & Design*, 135:385–396, December 2017. ISSN 0264-1275. doi: 10.1016/j.matdes.2017.09.044.

[40] Claire Bruna-Rosso, Ali Gökhan Demir, and Barbara Previtali. Selective laser melting finite element modeling: Validation with high-speed imaging and lack of fusion defects prediction. *Materials & Design*, 156:143–153, October 2018. ISSN 0264-1275. doi: 10.1016/j.matdes.2018.06.037.

[41] Manyalibo J. Matthews, Gabe Guss, Saad A. Khairallah, Alexander M. Rubenchik, Philip J. Depond, and Wayne E. King. Denudation of metal powder layers in laser powder bed fusion processes. *Acta Materialia*, 114:33–42, August 2016. ISSN 1359-6454. doi: 10.1016/j.actamat.2016.05.017.

[42] Sonny Ly, Alexander M. Rubenchik, Saad A. Khairallah, Gabe Guss, and Manyalibo J. Matthews. Metal vapor micro-jet controls material redistribution in laser powder bed fusion additive manufacturing. *Scientific Reports*, 7(1):4085, June 2017. ISSN 2045-2322. doi: 10.1038/s41598-017-04237-z.

[43] Johannes Trapp, Alexander M. Rubenchik, Gabe Guss, and Manyalibo J. Matthews. In situ absorptivity measurements of metallic powders during laser powder-bed fusion additive manufacturing. *Applied Materials Today*, 9:341–349, December 2017. ISSN 2352-9407. doi: 10.1016/j.apmt.2017.08.006.

[44] Brandon Lane, Shawn Moylan, Eric P. Whitenton, and Li Ma. Thermographic measurements of the commercial laser powder bed fusion process at NIST. *Rapid Prototyping Journal*, 22(5):778–787, January 2016. ISSN 1355-2546. doi: 10.1108/RPJ-11-2015-0161.

[45] Paul A. Hooper. Melt pool temperature and cooling rates in laser powder bed fusion. *Additive Manufacturing*, 22:548–559, August 2018. ISSN 22148604. doi: 10.1016/j.addma.2018.05.032.

[46] Le Tan Phuc and Matteo Seita. A high-resolution and large field-of-view scanner for in-line characterization of powder bed defects during additive manufacturing. *Materials & Design*, 164:107562, February 2019. ISSN 0264-1275. doi: 10.1016/j.matdes.2018.107562.

[47] Sergey A. Shevchik, Giulio Masinelli, Christoph Kenel, Christian Leinenbach, and Kilian Wasmer. Deep Learning for In Situ and Real-Time Quality Monitoring in Additive Manufacturing Using Acoustic Emission. *IEEE Transactions on Industrial Informatics*, 15(9):5194–5203, September 2019. ISSN 1941-0050. doi: 10.1109/TII.2019.2910524.

[48] P. Bidare, R. R. J. Maier, R. J. Beck, J. D. Shephard, and A. J. Moore. An open-architecture metal powder bed fusion system for in-situ process measurements. *Additive Manufacturing*, 16:177–185, August 2017. ISSN 2214-8604. doi: 10.1016/j.addma.2017.06.007.

[49] P. Bidare, I. Bitharas, R. M. Ward, M. M. Attallah, and A. J. Moore. Fluid and particle dynamics in laser powder bed fusion. *Acta Materialia*, 142:107–120, January 2018. ISSN 1359-6454. doi: 10.1016/j.actamat.2017.09.051.

[50] Cang Zhao, Kamel Fezzaa, Ross W. Cunningham, Haidan Wen, Francesco De Carlo, Lianyi Chen, Anthony D. Rollett, and Tao Sun. Real-time monitoring of laser powder bed fusion process using high-speed X-ray imaging and diffraction. *Scientific Reports*, 7(1), December 2017. ISSN 2045-2322. doi: 10.1038/s41598-017-03761-2.

[51] N. D. Parab, C. Zhao, R. Cunningham, L. I. Escano, K. Fezzaa, W. Everhart, A. D. Rollett, L. Chen, and T. Sun. Ultrafast X-ray imaging of laser–metal additive manufacturing processes. *Journal of Synchrotron Radiation*, 25(5):1467–1477, September 2018. ISSN 1600-5775. doi: 10.1107/S1600577518009554.

[52] Chu Lun Alex Leung, Sebastian Marussi, Robert C. Atwood, Michael Towrie, Philip J. Withers, and Peter D. Lee. In situ X-ray imaging of defect and molten pool dynamics in laser additive manufacturing. *Nature Communications*, 9(1), December 2018. ISSN 2041-1723. doi: 10.1038/s41467-018-03734-7.

[53] Nicholas P. Calta, Jenny Wang, Andrew M. Kiss, Aiden A. Martin, Philip J. Depond, Gabriel M. Guss, Vivek Thampy, Anthony Y. Fong, Johanna Nelson Weker, Kevin H. Stone, Christopher J. Tassone, Matthew J. Kramer, Michael F. Toney, Anthony Van Buuren, and Manyalibo J. Matthews. An instrument for in situ time-resolved X-ray imaging and diffraction of laser powder bed fusion additive manufacturing processes. *Review of Scientific Instruments*, 89(5):055101, May 2018. ISSN 0034-6748, 1089-7623. doi: 10.1063/1.5017236.

[54] Eckart Uhlmann, Erwin Krohmer, Felix Schmeiser, Norbert Schell, and Walter Reimers. A laser powder bed fusion system for in situ x-ray diffraction with high-energy synchrotron radiation. *Review of Scientific Instruments*, 91(7):075104, July 2020. ISSN 0034-6748. doi: 10.1063/1.5143766.

[55] C. Kenel, P. Schloth, S. Van Petegem, J. L. Fife, D. Grolimund, A. Menzel, H. Van Swygenhoven, and C. Leinenbach. In Situ Synchrotron X-Ray Diffraction and Small Angle X-Ray Scattering Studies on Rapidly Heated and Cooled Ti-Al and Al-Cu-Mg Alloys Using Laser-Based Heating. *JOM*, 68(3):978–984, March 2016. ISSN 1047-4838, 1543-1851. doi: 10.1007/s11837-015-1774-0.

Bibliography

[56] C. Kenel, D. Grolimund, J. L. Fife, V. A. Samson, S. Van Petegem, H. Van Swygenhoven, and C. Leinenbach. Combined in situ synchrotron micro X-ray diffraction and high-speed imaging on rapidly heated and solidified Ti–48Al under additive manufacturing conditions. *Scripta Materialia*, 114:117–120, March 2016. ISSN 1359-6462. doi: 10.1016/j.scriptamat.2015.12.009.

[57] Haider Ali, Le Ma, Hassan Ghadbeigi, and Kamran Mumtaz. In-situ residual stress reduction, martensitic decomposition and mechanical properties enhancement through high temperature powder bed pre-heating of Selective Laser Melted Ti6Al4V. *Materials Science and Engineering: A*, 695:211–220, May 2017. ISSN 0921-5093. doi: 10.1016/j.msea.2017.04.033.

[58] Reliance Cool Muscle Motor - RCM1. URL https://www.reliance.co.uk/catalogue/cool-muscle-motor/rcm1/.

[59] Ulrich E. Klotz, Dario Tiberto, and Franz Held. Optimization of 18-karat yellow gold alloys for the additive manufacturing of jewelry and watch parts. *Gold Bulletin*, 50(2):111–121, June 2017. ISSN 2364-821X, 2190-7579. doi: 10.1007/s13404-017-0201-4.

[60] M. Colopi, L. Caprio, A. G. Demir, and B. Previtali. Selective laser melting of pure Cu with a 1 kW single mode fiber laser. *Procedia CIRP*, 74:59–63, January 2018. ISSN 2212-8271. doi: 10.1016/j.procir.2018.08.030.

[61] Toshi-Taka Ikeshoji, Kazuya Nakamura, Makiko Yonehara, Ken Imai, and Hideki Kyogoku. Selective Laser Melting of Pure Copper. *JOM*, 70(3):396–400, March 2018. ISSN 1543-1851. doi: 10.1007/s11837-017-2695-x.

[62] HTW Germany. URL http://www.htw-germany.com/products.php5?lang=en&nav0=3&nav1=3.

[63] Bhaskar Dutta and F. H. Froes. *Additive Manufacturing of Titanium Alloys: State of the Art, Challenges, and Opportunities*. BH, Butterworth-Heinemann, an imprint of Elsevier, Amsterdam Boston Heidelberg London, 2016. ISBN 978-0-12-804782-8 978-0-12-804783-5. OCLC: ocn945355171.

[64] Galina Kasperovich and Joachim Hausmann. Improvement of fatigue resistance and ductility of TiAl6V4 processed by selective laser melting. *Journal of Materials Processing Technology*, 220:202–214, June 2015. ISSN 0924-0136. doi: 10.1016/j.jmatprotec.2015.01.025.

[65] Gerrit Ter Haar and Thorsten Becker. Selective Laser Melting Produced Ti-6Al-4V: Post-Process Heat Treatments to Achieve Superior Tensile Properties. *Materials*, 11(1):146, January 2018. ISSN 1996-1944. doi: 10.3390/ma11010146.

[66] A. Zafari and K. Xia. High Ductility in a fully martensitic microstructure: A paradox in a Ti alloy produced by selective laser melting. *Materials Research Letters*, 6(11):627–633, November 2018. ISSN null. doi: 10.1080/21663831.2018.1525773.

[67] Charlotte de Formanoir, Sébastien Michotte, Olivier Rigo, Lionel Germain, and Stéphane Godet. Electron beam melted Ti–6Al–4V: Microstructure, texture and mechanical behavior of the as-built and heat-treated material. *Materials Science and Engineering: A*, 652:105–119, January 2016. ISSN 09215093. doi: 10.1016/j.msea.2015.11.052.

[68] Xinhua Wu, Jing Liang, Junfa Mei, C. Mitchell, P. S. Goodwin, and W. Voice. Microstructures of laser-deposited Ti–6Al–4V. *Materials & Design*, 25(2):137–144, April 2004. ISSN 0261-3069. doi: 10.1016/j.matdes.2003.09.009.

[69] T. Vilaro, C. Colin, and J. D. Bartout. As-Fabricated and Heat-Treated Microstructures of the Ti-6Al-4V Alloy Processed by Selective Laser Melting. *Metallurgical and Materials Transactions A*, 42(10): 3190–3199, October 2011. ISSN 1543-1940. doi: 10.1007/s11661-011-0731-y.

[70] Ruben Wauthle, Bey Vrancken, Britt Beynaerts, Karl Jorissen, Jan Schrooten, Jean-Pierre Kruth, and Jan Van Humbeeck. Effects of build orientation and heat treatment on the microstructure and mechanical properties of selective laser melted Ti6Al4V lattice structures. *Additive Manufacturing*, 5:77–84, January 2015. ISSN 22148604. doi: 10.1016/j.addma.2014.12.008.

[71] A. Zafari, M. R. Barati, and K. Xia. Controlling martensitic decomposition during selective laser melting to achieve best ductility in high strength Ti-6Al-4V. *Materials Science and Engineering: A*, 744:445–455, January 2019. ISSN 0921-5093. doi: 10.1016/j.msea.2018.12.047.

[72] Bo Song, Shujuan Dong, Baicheng Zhang, Hanlin Liao, and Christian Coddet. Effects of processing parameters on microstructure and mechanical property of selective laser melted Ti6Al4V. *Materials & Design*, 35:120–125, March 2012. ISSN 0261-3069. doi: 10.1016/j.matdes.2011.09.051.

[73] Zhonghua Li, Ibrahim Kucukkoc, David Z. Zhang, and Fei Liu. Optimising the process parameters of selective laser melting for the fabrication of Ti6Al4V alloy. *Rapid Prototyping Journal*, 24(1):150–159, November 2017. ISSN 1355-2546. doi: 10.1108/RPJ-03-2016-0045.

[74] Jia Song, Wenheng Wu, Liang Zhang, Beibei He, Lin Lu, Xiaoqing Ni, Qianlei Long, and Guoliang Zhu. Role of scanning strategy on residual stress distribution in Ti-6Al-4V alloy prepared by selective laser melting. *Optik*, 170:342–352, October 2018. ISSN 00304026. doi: 10.1016/j.ijleo.2018.05.128.

[75] H. Shipley, D. McDonnell, M. Culleton, R. Coull, R. Lupoi, G. O'Donnell, and D. Trimble. Optimisation of process parameters to address fundamental challenges during selective laser melting of Ti-6Al-4V: A review. *International Journal of Machine Tools and Manufacture*, 128:1–20, May 2018. ISSN 0890-6955. doi: 10.1016/j.ijmachtools.2018.01.003.

[76] Nikola Kalentics, Andreas Burn, Michael Cloots, and Roland E. Logé. 3D laser shock peening as a way to improve geometrical accuracy in selective laser melting. *The International Journal of Advanced Manufacturing Technology*, 101(5):1247–1254, April 2019. ISSN 1433-3015. doi: 10.1007/s00170-018-3033-3.

[77] Elham Mirkoohi, Daniel E. Seivers, Hamid Garmestani, and Steven Y. Liang. Heat Source Modeling in Selective Laser Melting. *Materials*, 12(13):2052, January 2019. doi: 10.3390/ma12132052.

[78] Haider Ali, Hassan Ghadbeigi, and Kamran Mumtaz. Residual stress development in selective laser-melted Ti6Al4V: A parametric thermal modelling approach. *The International Journal of Advanced Manufacturing Technology*, 97(5):2621–2633, July 2018. ISSN 1433-3015. doi: 10.1007/s00170-018-2104-9.

[79] R. L. Brown and J. C. Richards. CHAPTER 2 - PACKINGS. In R. L. Brown and J. C. Richards, editors, *Principles of Powder Mechanics*, pages 13–39. Pergamon, January 1970. ISBN 978-0-08-006605-9. doi: 10.1016/B978-0-08-006605-9.50006-1.

Bibliography

[80] CXRO X-Ray Interactions With Matter. URL http://henke.lbl.gov/optical_constants/.

[81] A. B. Spierings, M. Voegtlin, T. Bauer, and K. Wegener. Powder flowability characterisation methodology for powder-bed-based metal additive manufacturing. *Progress in Additive Manufacturing*, 1(1):9–20, June 2016. ISSN 2363-9520. doi: 10.1007/s40964-015-0001-4.

[82] F-Theta Lenses Tutorial. URL https://www.thorlabs.com/newgrouppage9.cfm?objectgroup_id=10766.

[83] Sill Optics GmbH & Co. KG - f-theta lenses. URL https://www.silloptics.de/en/products/laser-optics/f-theta-lenses-1.

[84] Mezintel. LabVIEW Queued State Machine Consumer Producer Architecture - Mezintel Inc., December 2016. URL http://www.mezintel.com/blog/labview-queued-state-machine/.

[85] RAYLASE GmbH. URL https://www.raylase.de/.

[86] Industrial Laser Solutions Manufacturer | SPI Fiber Laser Products. URL https://www.spilasers.com/.

[87] LabVIEW 2017 - LabVIEW Wiki. URL https://labviewwiki.org/wiki/LabVIEW_2017.

[88] Slic3r - Open source 3D printing toolbox. URL https://slic3r.org/.

[89] Rodney Boyer, Gerhard Welsch, and E. W. Collings, editors. *Materials Properties Handbook: Titanium Alloys*. ASM International, Materials Park, Ohio, 4. printing edition, 2007. ISBN 978-0-87170-481-8. OCLC: 552237520.

[90] Yoshiki Oshida. 2 - Materials Classification. In Yoshiki Oshida, editor, *Bioscience and Bioengineering of Titanium Materials (Second Edition)*, pages 9–34. Elsevier, Oxford, January 2013. ISBN 978-0-444-62625-7. doi: 10.1016/B978-0-444-62625-7.00002-9.

[91] B. Vrancken, L. Thijs, J. P. Kruth, and J. Van Humbeeck. Microstructure and mechanical properties of a novel β titanium metallic composite by selective laser melting. *Acta Materialia*, 68:150–158, April 2014. ISSN 1359-6454. doi: 10.1016/j.actamat.2014.01.018.

[92] T. Ahmed and H. J. Rack. Phase transformations during cooling in A+β titanium alloys. *Materials Science and Engineering: A*, 243(1):206–211, March 1998. ISSN 0921-5093. doi: 10.1016/S0921-5093(97)00802-2.

[93] Properties of Pure Metals. In ASM Handbook Committee, editor, *Properties and Selection: Nonferrous Alloys and Special-Purpose Materials*, volume 2, page 0. ASM International, January 1990. ISBN 978-1-62708-162-7. doi: 10.31399/asm.hb.v02.a0001117.

[94] G. P. Grabovetskaya, E. N. Melnikova, Yu. R. Kolobov, I. P. Chernov, E. V. Naidenkin, N. N. Nikitenkov, and I. P. Mishin. Evolution of the structural and phase states of a Ti-6Al-4V alloy in forming submicro-crystalline structure with the use of temporary hydrogenation. *Russian Physics Journal*, 49(4):442–447, April 2006. ISSN 1573-9228. doi: 10.1007/s11182-006-0123-8.

[95] Weidong Zeng, Yu Sun, Yuanfei Han, Yongqing Zhao, and Ping Guo. Microstructure-Tensile Properties Correlation for the Ti-6Al-4V Titanium Alloy. *Journal of Materials Engineering and Performance*, 24, April 2015. doi: 10.1007/s11665-015-1437-x.

[96] A. Mertens, S. Reginster, H. Paydas, Q. Contrepois, T. Dormal, O. Lemaire, and J. Lecomte-Beckers. Mechanical properties of alloy Ti–6Al–4V and of stainless steel 316L processed by selective laser melting: Influence of out-of-equilibrium microstructures. *Powder Metallurgy*, 57(3):184–189, July 2014. ISSN 0032-5899, 1743-2901. doi: 10.1179/1743290114Y.0000000092.

[97] Dang Khoa Do and Peifeng Li. The effect of laser energy input on the microstructure, physical and mechanical properties of Ti-6Al-4V alloys by selective laser melting. *Virtual and Physical Prototyping*, 11(1):41–47, January 2016. ISSN 1745-2759, 1745-2767. doi: 10.1080/17452759.2016.1142215.

[98] Usman Ali, Yahya Mahmoodkhani, Shahriar Imani Shahabad, Reza Esmaeilizadeh, Farzad Liravi, Esmat Sheydaeian, Ke Yin Huang, Ehsan Marzbanrad, Mihaela Vlasea, and Ehsan Toyserkani. On the measurement of relative powder-bed compaction density in powder-bed additive manufacturing processes. *Materials & Design*, 155:495–501, October 2018. ISSN 0264-1275. doi: 10.1016/j.matdes. 2018.06.030.

[99] A. A. Coelho. TOPAS and TOPAS-Academic: An optimization program integrating computer algebra and crystallographic objects written in C++. *Journal of Applied Crystallography*, 51(1):210–218, February 2018. ISSN 1600-5767. doi: 10.1107/S1600576718000183.

[100] Johannes Schindelin, Ignacio Arganda-Carreras, Erwin Frise, Verena Kaynig, Mark Longair, Tobias Pietzsch, Stephan Preibisch, Curtis Rueden, Stephan Saalfeld, Benjamin Schmid, Jean-Yves Tinevez, Daniel James White, Volker Hartenstein, Kevin Eliceiri, Pavel Tomancak, and Albert Cardona. Fiji: An open-source platform for biological-image analysis. *Nature Methods*, 9(7):676–682, July 2012. ISSN 1548-7105. doi: 10.1038/nmeth.2019.

[101] G. Tinti, A. Bergamaschi, S. Cartier, R. Dinapoli, D. Greiffenberg, I. Johnson, J. H. Jungmann-Smith, D. Mezza, A. Mozzanica, B. Schmitt, and X. Shi. Performance of the EIGER single photon counting detector. *Journal of Instrumentation*, 10(03):C03011–C03011, March 2015. ISSN 1748-0221. doi: 10.1088/1748-0221/10/03/C03011.

[102] B. D. Cullity and S. R. Stock. *Elements of X-Ray Diffraction: Pearson New International Edition*. Pearson Education Limited, October 2013. ISBN 978-1-292-05255-7.

[103] V. Dyadkin, P. Pattison, V. Dmitriev, and D. Chernyshov. A new multipurpose diffractometer PILA-TUS@SNBL. *Journal of Synchrotron Radiation*, 23(3):825–829, May 2016. ISSN 1600-5775. doi: 10.1107/S1600577516002411.

[104] Fast Azimuthal Integration using Python — pyFAI 0.18.0a0 documentation. URL https://pyfai. readthedocs.io/en/latest/.

[105] Khalid Hellal Harbbi and Ahmed Alaa Ihsan. Studying Variance Method of X-Ray Diffraction Line Profile Then Develop It to Three New Models for Determine New Parameters. *Advances in Physics Theories and Applications*, 49(0):46–56–56, 2015. ISSN 2225-0638. URL https://www.iiste.org/Journals/ index.php/APTA/article/view/26934.

[106] Full width at half maximum. *Wikipedia*, October 2019. URL https://en.wikipedia.org/w/index.php? title=Full_width_at_half_maximum&oldid=923573054. Page Version ID: 923573054.

Bibliography

[107] Y. S. Touloukian, R. K. Kirby, R. E. Taylor, and P. D. Desai. *Thermal Expansion.* Springer US, Boston, MA, 1975. ISBN 978-1-4757-1624-5 978-1-4757-1622-1. doi: 10.1007/978-1-4757-1622-1.

[108] John J. Z. Li, William L. Johnson, and Won-Kyu Rhim. Thermal expansion of liquid Ti–6Al–4V measured by electrostatic levitation. *Applied Physics Letters*, 89(11):111913, September 2006. ISSN 0003-6951. doi: 10.1063/1.2349840.

[109] W. Xu, M. Brandt, S. Sun, J. Elambasseril, Q. Liu, K. Latham, K. Xia, and M. Qian. Additive manufacturing of strong and ductile Ti–6Al–4V by selective laser melting via in situ martensite decomposition. *Acta Materialia*, 85:74–84, February 2015. ISSN 13596454. doi: 10.1016/j.actamat.2014.11.028.

[110] Changjun Han, Yan Li, Qian Wang, Shifeng Wen, Qingsong Wei, Chunze Yan, Liang Hao, Jie Liu, and Yusheng Shi. Continuous functionally graded porous titanium scaffolds manufactured by selective laser melting for bone implants. *Journal of the Mechanical Behavior of Biomedical Materials*, 80: 119–127, April 2018. ISSN 1751-6161. doi: 10.1016/j.jmbbm.2018.01.013.

[111] Punit Kumar, Om Prakash, and Upadrasta Ramamurty. Micro-and meso-structures and their influence on mechanical properties of selectively laser melted Ti-6Al-4V. *Acta Materialia*, 154:246–260, August 2018. ISSN 1359-6454. doi: 10.1016/j.actamat.2018.05.044.

[112] Sabina L. Campanelli, Nicola Contuzzi, Antonio D. Ludovico, Fabrizia Caiazzo, Francesco Cardaropoli, and Vincenzo Sergi. Manufacturing and Characterization of Ti6Al4V Lattice Components Manufactured by Selective Laser Melting. *Materials (Basel, Switzerland)*, 7(6):4803–4822, June 2014. ISSN 1996-1944. doi: 10.3390/ma7064803.

[113] Dylan Agius, Kyriakos Kourousis, and Chris Wallbrink. A Review of the As-Built SLM Ti-6Al-4V Mechanical Properties towards Achieving Fatigue Resistant Designs. *Metals*, 8(1):75, January 2018. ISSN 2075-4701. doi: 10.3390/met8010075.

[114] Nikolay Tolochko, Sergei Mozzharov, Igor Yadroitsev, Tahar Laoui, L. Froyen, Victor Titov, and Michail Ignatiev. Balling processes during selective laser treatment of powders. *Rapid Prototyping Journal*, 10: 78–87, April 2004. doi: 10.1108/13552540410526953.

[115] Tomasz Kurzynowski, Edward Chlebus, Bogumiła Kuźnicka, and Jacek Reiner. Parameters in Selective Laser Melting for processing metallic powders. *Proceedings of SPIE*, 8239:823914, February 2012. doi: 10.1117/12.907292.

[116] Samy Hocine, Helena Van Swygenhoven, Steven Van Petegem, Cynthia Sin Ting Chang, Tuerdi Maimaitiyili, Gemma Tinti, Dario Ferreira Sanchez, Daniel Grolimund, and Nicola Casati. Operando X-ray diffraction during laser 3D printing. *Materials Today*, 34:30–40, April 2020. ISSN 1369-7021. doi: 10.1016/j.mattod.2019.10.001.

[117] Thomas G. Spears and Scott A. Gold. In-process sensing in selective laser melting (SLM) additive manufacturing. *Integrating Materials and Manufacturing Innovation*, 5(1):16–40, December 2016. ISSN 2193-9772. doi: 10.1186/s40192-016-0045-4.

[118] C. Cayron. ARPGE: A computer program to automatically reconstruct the parent grains from electron backscatter diffraction data. *Journal of Applied Crystallography*, 40(6):1183–1188, December 2007. ISSN 0021-8898. doi: 10.1107/S0021889807048777.

[119] Marco Simonelli, Yau Yau Tse, and Chris Tuck. On the Texture Formation of Selective Laser Melted Ti-6Al-4V. *Metallurgical and Materials Transactions A*, 45(6):2863–2872, June 2014. ISSN 1073-5623, 1543-1940. doi: 10.1007/s11661-014-2218-0.

[120] Abaqus Unified FEA - SIMULIA™ by Dassault Systèmes®. URL https://www.3ds.com/products-services/simulia/products/abaqus/.

[121] Samy Hocine, Steven Van Petegem, Ulrich Frommherz, Gemma Tinti, Nicola Casati, Daniel Grolimund, and Helena Van Swygenhoven. A miniaturized selective laser melting device for operando X-ray diffraction studies. *Additive Manufacturing*, 34:101194, August 2020. ISSN 2214-8604. doi: 10.1016/j.addma.2020.101194.

[122] Kenneth C. Mills. *Recommended Values of Thermophysical Properties for Selected Commercial Alloys*. Woodhead, Cambridge, 2002. ISBN 978-1-85573-569-9 978-0-87170-753-6. OCLC: 248239792.

[123] Diego A. De Moraes and Aleksander Czekanski. Parametric Thermal FE Analysis on the Laser Power Input and Powder Effective Thermal Conductivity during Selective Laser Melting of SS304L. *Journal of Manufacturing and Materials Processing*, 2(3):47, September 2018. doi: 10.3390/jmmp2030047.

[124] SAMUEL SUMIN SIH and JOEL W. BARLOW. The Prediction of the Emissivity and Thermal Conductivity of Powder Beds. *Particulate Science and Technology*, 22(4):427–440, October 2004. ISSN 0272-6351. doi: 10.1080/02726350490501682.

[125] T. Hoshino, K. Mito, A. Nagashima, and M. Miyata. Determination of the thermal conductivity of argon and nitrogen over a wide temperature range through data evaluation and shock-tube experiments. *International Journal of Thermophysics*, 7(3):647–662, May 1986. ISSN 1572-9567. doi: 10.1007/BF00502397.

[126] A. V. Gusarov and E. P. Kovalev. Model of thermal conductivity in powder beds. *Physical Review B*, 80(2):024202, July 2009. doi: 10.1103/PhysRevB.80.024202.

[127] Haider Ali. *Evolution of Residual Stress in Ti6Al4V Components Fabricated Using Selective Laser Melting*. Phd, University of Sheffield, August 2017. URL http://etheses.whiterose.ac.uk/18039/.

[128] SIMULIA™ Support Documentation - Dassault Systèmes®. URL https://www.3ds.com/products-services/simulia/services-support/support/documentation/.

[129] Jihong Yang, Shoujin Sun, Milan Brandt, and Wenyi Yan. Experimental investigation and 3D finite element prediction of the heat affected zone during laser assisted machining of Ti6Al4V alloy. *Journal of Materials Processing Technology*, 210(15):2215–2222, November 2010. ISSN 0924-0136. doi: 10.1016/j.jmatprotec.2010.08.007.

[130] John Goldak, Aditya Chakravarti, and Malcolm Bibby. A new finite element model for welding heat sources. *Metallurgical Transactions B*, 15(2):299–305, June 1984. ISSN 1543-1916. doi: 10.1007/BF02667333.

[131] Haijun Gong, Hengfeng Gu, Kai Zeng, J.j.s Dilip, Deepankar Pal, Brent Stucker, Daniel Christiansen, Jack Beuth, and John Lewandowski. Melt Pool Characterization for Selective Laser Melting of Ti-6Al-4V Pre-alloyed Powder. August 2014.

Bibliography

[132] A. C. Jupe, S. R. Stock, P. L. Lee, N. N. Naik, K. E. Kurtis, and A. P. Wilkinson. Phase composition depth profiles using spatially resolved energy dispersive X-ray diffraction. *Journal of Applied Crystallography*, 37(6):967–976, December 2004. ISSN 0021-8898. doi: 10.1107/S0021889804024148.

[133] Ch Genzel, I A. Denks, Rodrigo Coelho, Diana Thomas, Roland Mainz, Daniel Apel, and M Klaus. Exploiting the features of energy-dispersive synchrotron diffraction for advanced residual stress and texture analysis. *Journal of Strain Analysis for Engineering Design*, 46:615–625, September 2011. doi: 10.1177/0309324711403824.

[134] Errol F. I. Roberts and Keith M. Clarke. The colour characteristics of gold alloys. *Gold Bulletin*, 12(1): 9–19, March 1979. ISSN 0017-1557, 2190-7579. doi: 10.1007/BF03215099.

[135] Marina Garcia-Gonzalez, Steven Van Petegem, Nadine Baluc, Samy Hocine, Maxime Dupraz, Fanny Lalire, and Helena Van Swygenhoven. Enhanced precipitate growth at reduced temperatures during chemical ordering in deformed red gold alloys. *Scripta Materialia*, 170:129–133, September 2019. ISSN 1359-6462. doi: 10.1016/j.scriptamat.2019.05.038.

[136] NIST: X-Ray Mass Attenuation Coefficients - Table 3. URL https://physics.nist.gov/PhysRefData/ XrayMassCoef/tab3.html.

[137] EIGER2 X and XE CdTe for Synchrotron. URL /products/eiger2/eiger2-x-xe-cdte-for-synchrotron/.

[138] Haider Ali, Hassan Ghadbeigi, and Kamran Mumtaz. Effect of scanning strategies on residual stress and mechanical properties of Selective Laser Melted Ti6Al4V. *Materials Science and Engineering: A*, 712:175–187, January 2018. ISSN 09215093. doi: 10.1016/j.msea.2017.11.103.

[139] J. Robinson, I. Ashton, P. Fox, E. Jones, and C. Sutcliffe. Determination of the effect of scan strategy on residual stress in laser powder bed fusion additive manufacturing. *Additive Manufacturing*, 23:13–24, October 2018. ISSN 2214-8604. doi: 10.1016/j.addma.2018.07.001.

[140] Shangqin Yuan, Chee Kai Chua, and Kun Zhou. 3D-Printed Mechanical Metamaterials with High Energy Absorption. *Advanced Materials Technologies*, 4(3):1800419, 2019. ISSN 2365-709X. doi: 10.1002/admt.201800419.

[141] Shakeel Safdar, Andrew J. Pinkerton, Lin Li, Mohammed A. Sheikh, and Philip J. Withers. An anisotropic enhanced thermal conductivity approach for modelling laser melt pools for Ni-base super alloys. *Applied Mathematical Modelling*, 37(3):1187–1195, February 2013. ISSN 0307-904X. doi: 10.1016/j. apm.2012.03.028.

[142] Ulrich E. Klotz, Dario Tiberto, and F. J. Held. Additive manufacturing of 18-karat yellow-gold alloys. In *The 30th Santa Fe Symposium on Jewelry Technology, Albuquerque, USA. ISBN*, pages 255–272, 2016. URL http://www.legor.com/uploads/asset/file/738/klotz_eng_2017.pdf.

[143] S. Fürtauer, D. Li, D. Cupid, and H. Flandorfer. The Cu–Sn phase diagram, Part I: New experimental results. *Intermetallics*, 34:142–147, March 2013. ISSN 09669795. doi: 10.1016/j.intermet.2012.10.004.

[144] L.B. Wolff. Polarization-based material classification from specular reflection. *IEEE Transactions on Pattern Analysis and Machine Intelligence*, 12(11):1059–1071, November 1990. ISSN 1939-3539. doi: 10.1109/34.61705.

[145] Sadao Adachi. *The Handbook on Optical Constants of Metals: In Tables and Figures*. World Scientific, Singapore, 2012. ISBN 978-981-4405-94-2. OCLC: 788287106.

[146] Richard P. Feynman, Robert B. Leighton, and Matthew Sands. *The Feynman Lectures on Physics, Vol. II: The New Millennium Edition: Mainly Electromagnetism and Matter*. Basic Books, October 2011. ISBN 978-0-465-02494-0.

[147] N. Saunders and A. P. Miodownik. The Cu-Sn (Copper-Tin) system. *Bulletin of Alloy Phase Diagrams*, 11(3):278–287, June 1990. ISSN 0197-0216. doi: 10.1007/BF03029299.

[148] M Hirabayashi and S Weissmann. Study of CuAu I by transmission electron microscopy. *Acta Metallurgica*, 10(1):25–36, January 1962. ISSN 0001-6160. doi: 10.1016/0001-6160(62)90183-9.

[149] K. Hisatsune, Y. Tanaka, K. Udoh, and K. Yasuda. Three stages of ordering in CuAu. *Intermetallics*, 3(4):335–339, 1994. ISSN 0966-9795. doi: 10.1016/0966-9795(95)97294-B.

[150] H. Okamoto, D. J. Chakrabarti, D. E. Laughlin, and T. B. Massalski. The Au-Cu (Gold-Copper) system. *Journal of Phase Equilibria*, 8(5), October 1987. ISSN 1054-9714. doi: 10.1007/BF02893155.

[151] V. I. Syutkina and E. S. Yakovleva. The Mechanism of Deformation of the Ordered CuAu Alloy. *physica status solidi (b)*, 21(2):465–480, January 1967. ISSN 1521-3951. doi: 10.1002/pssb.19670210204.

[152] N. Kurnakow, S. Zemczuzny, and M. Zasedatelev. The transformations in alloys of gold with copper. *The Journal of the Institute of Metals*, 15(1):305–331, 1916.

[153] Arunachalam. Order-hardening in AuCu. 1967.

[154] Henning. Order-disorder phase transition and stress-induced diffusion in Au-Cu. 2009.

[155] Mushtaq Khan and Phill Dickens. Selective laser melting (SLM) of gold (Au). *Rapid Prototyping Journal*, 18(1):81–94, 2012. URL http://www.emeraldinsight.com/doi/abs/10.1108/13552541211193520.

[156] Damiano Zito, Alessio Carlotto, Alessandro Loggi, Patrizio Sbornicchia, Daniele Maggian, P. Unterberg, M. Fockele, A. Molinari, and I. Cristofolini. Optimization of SLM technology main parameters in the production of gold and platinum jewelry. In *The Santa Fe Symposium on Jewelry Manufacturing Technology*, pages 439–470, 2014.

[157] S. Scudino, C. Unterdörfer, K.G. Prashanth, H. Attar, N. Ellendt, V. Uhlenwinkel, and J. Eckert. Additive manufacturing of Cu–10Sn bronze. *Materials Letters*, 156:202–204, October 2015. ISSN 0167577X. doi: 10.1016/j.matlet.2015.05.076.

[158] Zhongfa Mao, David Z. Zhang, Peitang Wei, and Kaifei Zhang. Manufacturing Feasibility and Forming Properties of Cu-4Sn in Selective Laser Melting. *Materials*, 10(4):333, March 2017. doi: 10.3390/ma10040333.

[159] Zhongfa Mao, David Z. Zhang, Junjie Jiang, Guang Fu, and Peng Zhang. Processing optimisation, mechanical properties and microstructural evolution during selective laser melting of Cu-15Sn high-tin bronze. *Materials Science and Engineering: A*, 721:125–134, April 2018. ISSN 0921-5093. doi: 10.1016/j.msea.2018.02.051.

Bibliography

[160] Joseph R. Davis and ASM International, editors. *Copper and Copper Alloys.* ASM Specialty Handbook. ASM International, Materials Park, Ohio, 1. printing edition, 2001. ISBN 978-0-87170-726-0. OCLC: 248645933.

Samy **Hocine**

Education

PhD in Materials Science and Engineering *Villigen, Switzerland*

École Polytéchnique Fédérale de Lausanne (EPFL) - Paul Scherrer Institut (PSI) *Oct. 2016 - Sept. 2020*

- Specialisation in metal additive manufacturing processing
- Design and assembling of a miniaturised selective laser melting (MiniSLM) machine for *operando* X-ray measurements
- Programming of the software interface to pilot the MiniSLM, and interface with synchrotron beamlines
- Synchrotron X-ray diffraction experiments and diffraction pattern data analysis
- Validation of finite element analysis models with the obtained experimental data
- Supervision of a summer intern and a master's thesis student at PSI

MSc in Mechanical Engineering *Atlanta, USA*

Georgia Institute of Technology *Aug. 2014 - Dec. 2015*

- Major: Micromechanics, Continuum Mechanics, Inelastic Deformations and Structure-Property Relationship in Materials
- Minor: Fracture Mechanics and Fatigue Life
- GPA: 4.0/4.0

MSc in Mechanical and Industrial Engineering *Metz, France*

Arts et Métiers ParisTech *Sept. 2012 - Dec. 2015*

- Major: Mechanics, Material Science, Energy Systems, Industrialisation and Manufacturing Processes
- Second year project: Design and integration of a slug-feeding unit for the Vulcain platform

Publications

Operando X-ray diffraction during laser 3D printing

- Authors: S. Hocine, H. Van Swygenhoven, S. Van Petegem, C. S. T. Chang, T. Maimaitiyili, G. Tinti, D. Ferreira Sanchez, D. Grolimund, N. Casati
- Journal: Materials Today, Volume 34, April 2020, Pages 30-40
- DOI: 10.1016/j.mattod.2019.10.001

A miniaturized selective laser melting device for _operando_ X-ray diffraction studies

- Authors: S. Hocine, S. Van Petegem, U. Frommherz, G. Tinti, N. Casati, D. Grolimund, H. Van Swygenhoven
- Journal: Additive Manufacturing, Volume 34, August 2020, 101194
- DOI: 10.1016/j.addma.2020.101194

Verification of selective laser melting heat source models with operando X-ray diffraction data

- Authors: S. Hocine, H. Van Swygenhoven, S. Van Petegem
- Journal: Additive Manufacturing
- Status: submitted, under review